



**HAL**  
open science

# Stochastic description of rare events for complex dynamics in the Solar System

Éric Woillez

► **To cite this version:**

Éric Woillez. Stochastic description of rare events for complex dynamics in the Solar System. Atmospheric and Oceanic Physics [physics.ao-ph]. Université de Lyon, 2018. English. NNT : 2018LY-SEN046 . tel-01930004

**HAL Id: tel-01930004**

**<https://theses.hal.science/tel-01930004>**

Submitted on 21 Nov 2018

**HAL** is a multi-disciplinary open access archive for the deposit and dissemination of scientific research documents, whether they are published or not. The documents may come from teaching and research institutions in France or abroad, or from public or private research centers.

L'archive ouverte pluridisciplinaire **HAL**, est destinée au dépôt et à la diffusion de documents scientifiques de niveau recherche, publiés ou non, émanant des établissements d'enseignement et de recherche français ou étrangers, des laboratoires publics ou privés.



Numéro National de Thèse : 2018LYSEN046

**THESE de DOCTORAT DE L'UNIVERSITE DE LYON**

opérée par

**l'Ecole Normale Supérieure de Lyon**

**Ecole Doctorale N° 52**

**Physique et astrophysique de Lyon**

**Discipline : Physique**

Soutenue publiquement le 21/09/2018, par :

**Monsieur Eric WOILLEZ**

---

**Stochastic description of rare events for  
complex dynamics in the Solar System**

**Modélisation stochastique d'événements rares dans des  
systèmes dynamiques complexes de notre système solaire**

---

Devant le jury composé de :

Mme Anne LEMAITRE	Professeure, University of Namur, Rapporteur
M. Eric VANDEN-EIJNDEN	Professeur, Courant Institute (New-York), Rapporteur
M. Cristel CHANDRE	DR CNRS, Institut de mathématiques de Marseille, Examineur
M. Jacques LASKAR	DR CNRS, IMCCE, Examineur
M. Alessandro MORBIDELLI	DR CNRS, Observatoire de la côte d'Azur, Examineur
Mme Nelly PUSTELNIK	CR CNRS, ENS de Lyon, Examinatrice
M. Freddy BOUCHET	DR CNRS, ENS de Lyon, Directeur de thèse



# Contents

<b>1</b>	<b>Averaging, stochastic averaging and large deviations</b>	<b>17</b>
1.1	Physical motivations . . . . .	17
1.1.1	Describe the long-term evolution of a system . . . . .	17
1.1.2	Necessity of a probabilistic approach . . . . .	18
1.1.3	The problem of rare events with a large impact: large deviation theory . . . . .	22
1.1.4	About the conventions used in the present manuscript . . . . .	24
1.2	Slow-fast dynamical systems . . . . .	24
1.2.1	Theoretical framework . . . . .	24
1.2.2	Ergodicity and mixing . . . . .	25
1.2.3	Stochastic dynamics of the slow variable: three levels of description . . . . .	31
1.3	Averaging and stochastic averaging . . . . .	33
1.3.1	The averaging principle . . . . .	34
1.3.2	Stochastic averaging in finite time . . . . .	36
1.3.3	Stochastic averaging, case $\bar{b} \equiv 0$ . . . . .	41
1.4	Large deviations and instantons . . . . .	44
1.4.1	Large deviation principle for a probability distribution . . . . .	45
1.4.2	Large deviations for sample paths . . . . .	45
1.4.3	Instantons for large deviations from the averaged dynamics . . . . .	47
1.4.4	Instantons for diffusive processes . . . . .	49
1.5	Example: the overdamped Langevin equation . . . . .	50
<b>2</b>	<b>Stationary state of zonal jets</b>	<b>53</b>
2.1	Introduction . . . . .	53
2.2	The quasilinear barotropic model in the beta plane . . . . .	55
2.2.1	Equations of the model . . . . .	55
2.2.2	Nondimensional equations . . . . .	56
2.3	Reynolds stress from the pseudo-momentum balance . . . . .	57
2.3.1	The pseudo-momentum balance . . . . .	57
2.3.2	Simplification in the inertial limit . . . . .	59
2.3.3	Close equation for the mean flow in the small scale forcing limit . . . . .	62
2.4	Prediction of the stationary velocity profile . . . . .	64
2.4.1	Close equation for the mean velocity profile . . . . .	64
2.4.2	Linear stability of the velocity profile . . . . .	67
2.4.3	Regularization at the extrema of the jets . . . . .	68
2.5	Perspectives . . . . .	69

<b>3</b>	<b>Long-term influence of the asteroids</b>	<b>73</b>
3.1	Introduction and motivations . . . . .	73
3.2	Dynamics of Mars perturbed by a chaotic asteroid . . . . .	75
3.2.1	Simplified Hamiltonian model . . . . .	75
3.2.2	Slow-fast dynamics of the orbital elements . . . . .	76
3.3	Stochastic averaging of the dynamics of the semi-major axis . . . . .	78
3.3.1	Dynamics with rescaled variables . . . . .	78
3.3.2	Stochastic differential equation for the orbital elements . . . . .	79
3.3.3	Diffusion process for the semi-major axis . . . . .	80
3.4	Superdiffusion of the mean longitude of Mars . . . . .	82
3.4.1	Heuristic picture of the mechanism: dispersion is enhanced by the Keplerian flow . . . . .	82
3.4.2	Variance of the mean longitude . . . . .	83
3.4.3	Orders of magnitude for the superdiffusion time . . . . .	84
3.4.4	Conclusion: impact on chaotic motion of the solar system . . . . .	84
<b>4</b>	<b>Obliquity of a Moonless Earth</b>	<b>87</b>
4.1	Introduction: chaotic variations of planetary obliquities . . . . .	87
4.1.1	Motivations . . . . .	87
4.1.2	Chaotic Hamiltonian dynamics . . . . .	89
4.1.3	Slow variations of the frequencies . . . . .	91
4.2	Stochastic dynamics for the long-term evolution of the secular frequencies . . . . .	94
4.2.1	Auto regressive model . . . . .	94
4.2.2	Algorithm . . . . .	94
4.2.3	Results . . . . .	95
4.3	Qualitative picture of the transport mechanism in phase space . . . . .	97
4.3.1	Chaotic regions are created by resonance overlap . . . . .	97
4.3.2	Transitions between chaotic regions . . . . .	99
4.3.3	Averaging of the dynamics: the local diffusive model . . . . .	100
4.3.4	Numerical characterizations of the chaotic regions . . . . .	102
4.3.5	The problem of first entrance times . . . . .	103
4.4	Numerical integrations of the stochastic Hamiltonian dynamics . . . . .	105
4.4.1	Integration with fixed values of the frequencies . . . . .	105
4.4.2	Integration with the reference simulation of the frequencies . . . . .	105
4.4.3	Integration with a large number of realizations of the frequencies fluctuations	106
4.4.4	Discussion . . . . .	106
4.5	Numerical simulations . . . . .	107
4.5.1	Simulations of the stochastic Hamiltonian model . . . . .	108
4.5.2	Simulations of the local diffusive model . . . . .	108
4.5.3	Discussion of the results . . . . .	109
4.6	Conclusion . . . . .	114
<b>5</b>	<b>Instantons for Mercury's dynamics</b>	<b>115</b>
5.1	Introduction: large variations of Mercury's eccentricity . . . . .	115
5.2	Simplified model for a Massless planet . . . . .	117
5.2.1	Secular Hamiltonian for Mercury including the three major resonances . . . . .	117
5.2.2	Resonance map in action space . . . . .	121
5.2.3	The truncated Hamiltonian as a slow variable . . . . .	123
5.2.4	Condition for Mercury's destabilization . . . . .	124
5.3	Diffusion process for the slow variable . . . . .	127

5.3.1	Third order resonances amplitudes . . . . .	127
5.3.2	Stochastic averaging and order of magnitude for the diffusion coefficient .	130
5.3.3	Numerical evaluation of the probability distribution of Mercury's first destabilization time . . . . .	133
5.3.4	Theoretical predictions for the first destabilization time probability dis- tribution . . . . .	133
5.4	Instantons for Mercury . . . . .	137
5.4.1	Short term destabilization probability . . . . .	137
5.4.2	Explicit formulae obtained with the diffusive model . . . . .	137
5.4.3	Comparison with the slow variable trajectories . . . . .	139
5.5	Conclusion and perspectives . . . . .	140
<b>A</b>	<b>Computation of the diffusion coefficient</b>	<b>155</b>
<b>B</b>	<b>Resolution of the diffusion equation</b>	<b>157</b>
<b>C</b>	<b>Resonant part of the BMH Hamiltonian</b>	<b>159</b>



# Remerciements

A la fin de cette thèse, mes pensées vont en premier lieu à mon directeur de thèse Freddy Bouchet, sans qui tout ce travail de recherche n'aurait pas été possible. Freddy m'a non seulement formé au métier de chercheur, mais il m'a aussi donné l'exemple d'un homme rigoureux, curieux, inventif, et surtout profondément humain. Je ne saurais trop le remercier pour ces 4 années de collaboration.

Je dois également beaucoup à tous les professeurs qui m'ont formé pendant mes études supérieures et qui ont joué un grand rôle pour m'aider à devenir un physicien compétent. Je tiens spécialement à mentionner parmi eux Denis Choimet et Jacques Renault, Frédéric Van Wijland, Emmanuel Trizac, Rémi Monasson, Lyderic Bocquet, Jacques Laskar, Stephane Fauve, Ludovic Berthier et Jean-Louis Barrat.

Je tiens à remercier aussi l'ensemble des collègues qui m'ont successivement supportés dans un même bureau, Robin, Anne, Jason, Lucas. J'ai travaillé avec plaisir toutes ces années au laboratoire de physique de l'ENS de Lyon, dans lequel j'ai profité de l'excellente ambiance humaine et d'interactions extrêmement intéressantes avec les autres membres du laboratoire. Je tiens à remercier aussi son directeur, Thierry Dauxois, pour l'attention qu'il porte aux thésards du laboratoire.

Je ne puis écrire cette page de remerciements sans avoir une pensée pour Tomás Tangarife, que nous ne pouvons oublier. Tomás m'a accompagné au début de ma thèse dans mon travail sur les écoulements géophysiques, et tout un pan de ma thèse s'inspire en grande partie de la sienne.

Merci à ma famille et mes parents pour leur soutien tout au long de ces années et qui m'ont accompagné dans tous les moments difficiles.

Enfin, merci à toi Maÿlis, qui a accepté de m'accompagner tout au long de ma vie. Merci pour tes encouragements, ton écoute dans mes moments de doute et ta présence indéfectible à mes côtés, y compris dans mon travail de recherche. Je sais que cette thèse n'aurait pas été si aboutie sans toi.



# Introduction

The discovery that the long-term motion of the solar system is chaotic [47] has also shown the possibility of exceptional structural changes in the system composed of the four terrestrial planets Mercury, Venus, the Earth and Mars. The orbital dynamics of the lightest planet, Mercury, is also the most chaotic one. It can be destabilized in few hundred million years, leading to the ejection of Mercury out of the solar system, or to a collision with Venus or the Earth [58]<sup>1</sup>. Chaotic motion does not only affect planetary orbits, but also their spin axis. Without the stabilizing effect of the Moon, the Earth spin axis orientation could experience very large changes between 0° and 90° with dramatical consequences on the Earth climate [78]. The asteroid belt between Mars and Jupiter is strongly chaotic, and is one limitation for long-term predictions of planetary orbits over few million years. Rare events in the solar system can be also found in the chaotic evolution of the atmosphere of giant gaseous planets, especially Jupiter's atmosphere. The flow in Jupiter's atmosphere has the interesting property to organize in strong eastward and westward parallel currents called *zonal jets*. Although they are very stable, turbulent fluctuations of those jets may lead to the creation or disappearance of a new jet [105].

Jupiter's atmosphere, chaotic motion of Mercury, spin axis dynamics of the Earth without the Moon, chaotic dynamics of asteroids, all these physical systems share one common point: they fall in the vast framework of slow-fast dynamical systems. Moreover, rare events, that is, events occurring with very low probability and causing qualitatively important changes in the system, can be observed for three of them. A generic dynamical system involves a large number of coupled physical phenomena, each of them at their own time and space scale. The interesting property of the four systems considered in this thesis is the existence for each of them of a variable (or a field in case of Jupiter's atmosphere) called the *slow variable*, the dynamics of which evolves on a timescale that is much larger than the other degrees of freedom. The slow variable has the property to control the system's long-term evolution and the possible rare events of its dynamics. The slow variable can have a simple physical interpretation, but this is not always the case. For Jupiter's atmosphere for example, the slow variable is simply the wind velocity averaged over longitude. A lot of work has been required before the beginning of this thesis to identify the small parameter that ensures the timescale separation between variables [12]. For Mercury's dynamics on the contrary, the construction of a good slow variable itself has been a difficult task [7].

In the present manuscript, I explain how the stochastic description of the slow variables allows to predict the system long-term evolution and the probability of rare events. The prediction of rare event probabilities in a complex dynamical system is very difficult. Using direct numerical simulations, the numerical cost of such predictions is prohibitive for systems with a large number of degrees of freedom, such as the ones presented in this thesis. Rare event description has stimulated the development of new theoretical tools on slow fast systems, and a complete class of

---

<sup>1</sup>This discovery has been brought to a larger audience, see [60].

algorithms especially devoted to rare event computations [77, 82, 85]. Even if they considerably increase the efficiency of numerical computations, rare event algorithms only work if we have a very good physical comprehension of the dynamics [66]. For each new physical system, a refined theoretical work is required to identify precisely the physical mechanism leading to the rare event, give the relevant parameters, and find orders of magnitudes. Such a theoretical work is done in the present thesis, for complex dynamics in the solar system. For zonal jets and Mercury's dynamics, I will even show that the complexity of the system can be reduced and that a close equation can be found to describe the long-term dynamics of the slow variable.

My work does not present any new mathematical result about slow-fast dynamical systems. To my knowledge, the originality of the work resides in the fact that it creates a bridge between quite abstract mathematical theorems and concrete real physical systems. I show in particular that the abstract mathematical results about stochastic averaging and large deviation theory (both theory are precisely described in my thesis) give reasonably precise predictions for the systems described above. For the chaotic systems considered in the present manuscript (geophysical flows, chaotic Hamiltonian dynamics), theoretical predictions have been, and still are extremely difficult. Therefore, the results of the present work do not reach the same level of precision as direct numerical simulations. The values of probability distributions obtained with stochastic averaging can be seen as orders of magnitude rather than exact values. For each physical system, I have particularly taken care of emphasizing the physical mechanisms in the problems, which, I think, has as much importance as giving numerical predictions. My work should be understood as a complementary approach to numerical simulations, both of them being necessary to do relevant predictions of rare events. I therefore hope that the results in hydrodynamics and in celestial mechanics obtained in this thesis will be used as a guideline for scientists who would like to conduct more extensive work about these problems.

Let me give now some precisions about the physical phenomena I am interested in.

Numerical integration of the secular equations of motion for the full solar system have shown that the four smallest planets Mercury, Venus, the Earth and Mars have a chaotic dynamics on a timescale of ten million years [47, 48, 93, 51]. This means that chaotic motion increases exponentially any difference in planetary initial conditions and leads to a complete indetermination of planetary positions on a timescale of ten million years. The main consequence of this result is that the solar system's long-term evolution becomes unpredictable after few million years. Major changes in the structure of the inner solar system -the system composed of the four terrestrial planets- can occur on a timescale comparable to the age of the solar system [58]. With the current planetary orbital conditions, the effect of chaos is restricted to slow random evolution of planetary orbital parameters. But it has even been shown that chaotic evolution can drive in very few cases the inner solar system in a regime of large-scale chaos in which collisions between planets are possible [58]. The probability of such a rare event has been estimated about 1% in 5 billion years [58]. The lightest planet Mercury is also the most chaotic one and its dynamics is the key to understand the disintegration of the inner solar system. Fig.(0.0.1) displays the evolution of Mercury's eccentricity for many trajectories with different initial conditions. Abrupt jumps in Mercury's eccentricity can be seen clearly in the figure when the eccentricity crosses a critical value. It has been observed that this event is related to a regime of large-scale chaos in the inner solar system. After many refined studies of Mercury's dynamics [71, 15, 7], we still only have a partial understanding of the destabilization mechanism. It has now been clearly shown that destabilization is related to a resonance between Jupiter's and Mercury's perihelia [15]. Through this resonance, Jupiter can transfer to Mercury the large amount of angular momentum necessary for a large increase in eccentricity. But the mechanism to enter into resonance is less sure. The slow intermediate evolution in Mercury's orbital parameters between

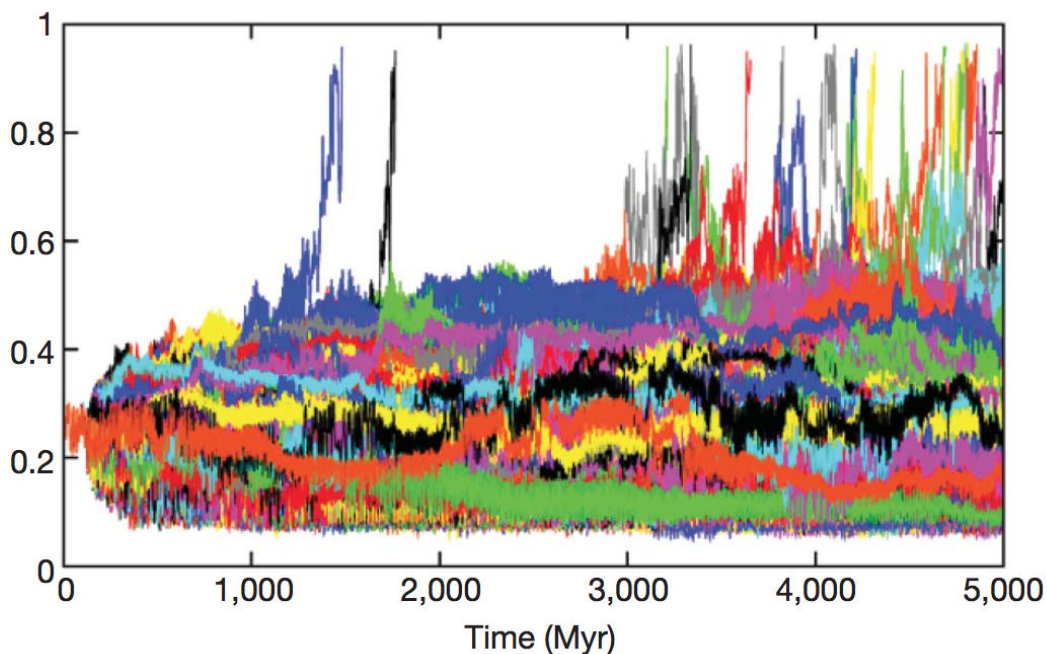


Figure 0.0.1: Mercury’s eccentricity time evolution for different trajectories with close initial conditions. The vertical axis represents the eccentricity value. The simulation shows abrupt jumps in Mercury’s eccentricity for trajectories that cross a threshold value close to 0.6. (Taken from [58])

the current orbital state and the resonant state looks like a random process, the characteristics of which are still debated [7].

The description of rare events in planetary dynamics opens the question of the sources of chaoticity in the solar system. We have just seen that one source of chaoticity is the planetary mutual interactions, and is thus intrinsic to the dynamical system composed of the eight planets. But planetary dynamics is also influenced by external phenomena that act as external sources of chaoticity for the eight planets system. One major source of chaoticity is the asteroid belt between Mars and Jupiter. The asteroid belt contains planetesimals, the mass of which is non-negligible for planetary dynamics (the largest asteroid Ceres has about  $\frac{1}{300}$  Mercury’s mass). Because of asteroid’s mutual interaction, the dynamics of asteroids is much more chaotic than planetary dynamics, and even the trajectories of the largest ones become unpredictable after a few tens thousand years [61]. It can thus be naturally expected that asteroid-planet interactions act as a noise on planetary dynamics and partly contribute to the random evolution of planetary orbital parameters. It has already been observed in numerical simulations of the full solar system including asteroids that they do not affect significantly the long-term intrinsic chaotic evolution [25, 61], but a systematic investigation of their influence has not been done yet. In particular, it was not known whether asteroid’s noisy dynamics could trigger Mercury’s destabilization.

Chaotic motion does not only affect planetary orbits, but also their spin axis [51]. For example, the motion of the Earth spin axis, can be accurately described by a precessional periodic motion of about 26000 years, but the periodic description becomes inadequate for long-term evolution in billions of years. The spin axes of terrestrial planets have chaotic long-

term evolution that can create large variations in their obliquities (the obliquity is the angle between the equatorial plane and the orbital plane) [63]. Therefore none of the current planetary obliquities can be considered as primordial. On the contrary, the initial obliquities values right after solar system's formation could have been very different from now, and driven in their current state by chaotic dynamics and dissipative effects [63, 21]. The amplitude of chaotic evolution is conditioned by the existence of many spin-orbit resonances, that is, resonances between their precession frequency and the characteristic frequencies of their orbital motion. The Earth enjoys exceptional dynamical conditions because the presence of the Moon increases the effective value of its precession frequency compared to a fictitious Earth without Moon [63, 78]. The current Earth thus feels no major spin-orbit resonance and, would the Moon remain with the Earth forever, its spin axis dynamics would be only very weakly chaotic. But due to dissipative tidal effects, the Moon slowly goes away from the Earth and its influence on Earth tides will become negligible in about 4 billion years! During this slow process the Earth precession frequency decreases and will reach spin-orbit resonant conditions [78]. Fig.(0.0.2) displays one possible trajectory of the Earth spin axis in a numerical simulation of 5 billion years. The picture shows that, once the Earth has reached the red chaotic region, its obliquity can suffer very large variations, up to  $90^\circ$ . For example, at the end of the simulation of Fig.(0.0.2), the Earth obliquity is trapped in a chaotic state with its obliquity constantly varying between  $50^\circ$  and  $80^\circ$ . The value of the Earth obliquity determines the mean surface insolation and is thus one of the main factors that influences its climate. Understanding the chaotic variations of planetary obliquities is essential to predict their environmental surface conditions far in the future and in the past.

The recent pictures of Jupiter's atmosphere taken by Juno probe give again an example how beautiful large-scale structures can emerge from the turbulent dynamics of geophysical flows. Two of those pictures are displayed in Fig.(0.0.3). At the top of Jupiter's atmosphere, observations show alternatively red and grey bands which are the signature of strong alternatively eastward and westward parallel currents called *zonal jets*. The flow can also organize in giant cyclones and anti-cyclones like the famous Great Red Spot. Such large-scale atmospheric structures also exist on other giant gaseous planets like Saturn or Uranus [37, 31, 30], although they can be much clearly seen in Jupiter atmosphere. For this reason, Jupiter has become one of the best available experimental setup for physicists studying geophysical turbulent flows [98], and a goal of many space craft missions. The velocity profile of Jupiter jets has been measured many times in 1979 by Voyager 2 and in 2000 by Cassini showing very few changes [81, 87]. The largest scales of the flow are very stable in time and only evolve on a timescale of tens of years. Yet, it is known from experimental and numerical works that the flow can sustain different stable states characterized by a different number of zonal jets [4, 20]. There are strong reasons to believe that Jupiter may have lost one of its jets during the 40's [84, 105], which indicates that transitions between different stable states are possible for Jupiter's atmosphere. The slow evolution of zonal jets is thus crucial to understand Jupiter abrupt climate changes. Also on the Earth, the circumpolar current called the jet stream is an example of a zonal flow. The fluctuating dynamics of this jet, and zonal atmospheric currents at mid-latitudes have a major impact on climate [101], and the transitions between different blocked states is important to understand climate variations [45]

For slow-fast dynamical systems, the theory of averaging, stochastic averaging, as well as the more recent large deviation theory, present rigorous theorems that enable to eliminate the fast variables from the dynamics. The procedure, called adiabatic elimination of fast variables, shows that the long-term evolution of the slow variable can be described by an effective dynamics for the slow variable alone [26, 44, 33]. The adiabatic elimination of fast variables drastically

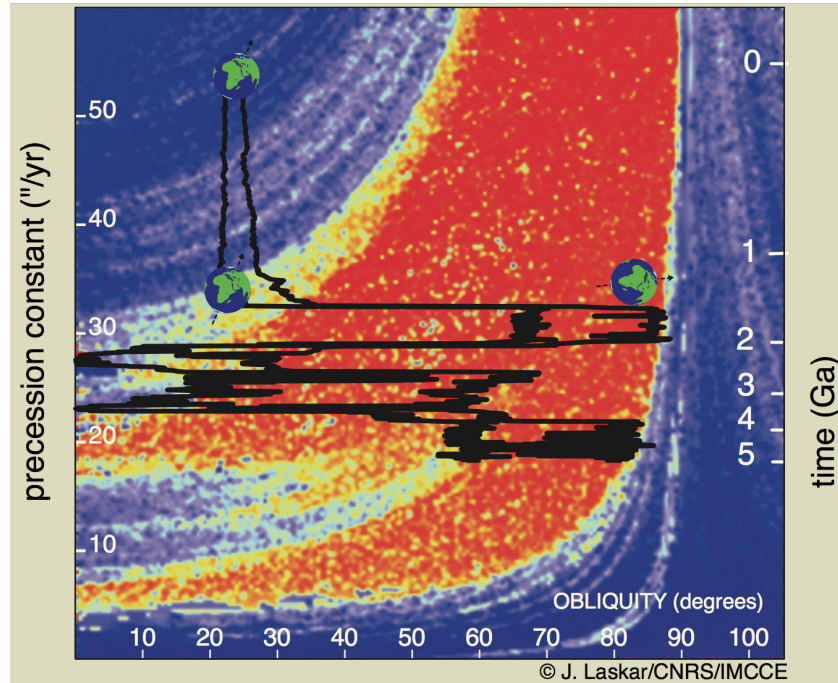


Figure 0.0.2: A possible realization of the Earth spin axis evolution in 5 billion years. The vertical axis represents the Earth precession constant, that conditions its precession frequency. The horizontal axis represents the Earth obliquity (spin axis orientation). The red part of the picture displays the chaotic regions created by the major spin-orbit resonances. When the Moon goes away from the Earth, the value of the precession constant is progressively reduced and the Earth reaches the conditions for large-scale chaotic motion. In the chaotic region, the Earth obliquity can suffer very large variations up to  $90^\circ$ . (Taken from [78])



Figure 0.0.3: Two pictures of Jupiter atmosphere taken by Juno probe. The picture on the left shows three beautiful giant vortices. The picture on the right is a zoom on the mid-latitude zonal jets. More pictures can be found on the Nasa website [1].

reduces the number of degrees of freedom. The price to be paid for such a simplification is to switch from deterministic equations to stochastic processes. Under some conditions about the fast dynamics that will be described below, there exists a stochastic process that gives a description of the long-term asymptotic dynamics of the slow variable fully equivalent to the initial deterministic set of equations.

The type of equations that can be obtained for the slow variable depends on the properties of the fast dynamics -the dynamics obtained with fixed values for the slow variables. The exact hypothesis required for stochastic averaging and large deviations are very subtle and are one of the topic of ergodic theory [43, 44], but they can roughly be summarized in two main hypotheses. First, the dynamics should be *ergodic*, which means that the system's trajectory visits all accessible regions of phase space in finite time [100, 79]. In that case, the long-term effective dynamics of the slow variable is given by the equations of motion averaged over the fast dynamics. The averaging procedure is a very intuitive and very old idea in physics. A famous result in celestial mechanics obtained with the averaging principle is the secular Laplace–Lagrange equations that describe accurately the slow deformations of planetary orbits through mutual gravitational interactions, for times smaller than one million years [75]. Second, the dynamics should be *mixing*. It is difficult to formulate a precise definition of the mixing hypothesis, but the general idea is that a mixing system rapidly “forgets” the memory of its initial condition [8, 100]. The mixing hypothesis allows to go beyond simple averaging. In the limit of large timescale separation between the slow and fast dynamics, stochastic averaging leads to a stochastic process that describes the slow variable's deviations from the averaged dynamics. Two cases should be distinguished.

If the slow variables's dynamics averages to zero, stochastic averaging shows that the slow variable's evolution is given to next order by a stochastic differential equation with a white noise term [33]. The white noise limit is exact for large timescale separation. The stochastic differential equation describes both the law of small and large fluctuations of the slow variable. The model for Mercury's long-term dynamics presented in section 5 is an example for which stochastic averaging gives exactly the limit process for the slow variable.

If the averaged dynamics does not vanishes, no stochastic equation can describe exactly the long-term evolution of the slow variable. Large deviation theory shows that the slow variable's dynamics is given by a stochastic process, and gives an exponential equivalent for its probability distributions [26]. Large deviation theory is currently the most powerful available tool to solve complex out-of-equilibrium problems for which the old statistical theory of equilibrium systems fails [100, 95]. If the averaged dynamics has many stable states, large deviation theory is the suitable tool to compute the probability of random transitions between the different stable states. The slow dynamics of zonal jets in geophysical flows falls in this framework. Large deviation theory could in principle tackle the problem of rare events in the system, that is, predict both the probability of rare transitions between stable states with a different number of jets, and predict the transition path leading from one stable state to the other.

The manuscript begins in section 1 with a theoretical part about slow-fast chaotic dynamical systems. The introduction 1.1 of the theoretical section 1 presents the physical motivations to use stochastic methods for complex physical systems. The introduction 1.1 has been especially written for physicists who are not specialists of statistical physics or stochastic methods. The following of section 1 is more technical. I give a rigorous formulation of the ergodic and mixing hypotheses and the main theorems and proofs of averaging and stochastic averaging for slow-fast dynamical systems. I also briefly describe the part of large deviation theory that deals with instanton dynamics.

The following parts of the manuscript present the results obtained for the four physical

systems I have sketched at the beginning of the introduction. In all systems, averaging, stochastic averaging and large deviation theory can be applied to predict the long-term dynamics using a stochastic description of the slow variables.

In section 2, I study the slow dynamics of zonal jets in geostrophic turbulent flows, coupled with the fast dynamics of turbulent eddies. Although they have been studied for a long time in all theoretical, experimental and numerical aspects, the dynamics of zonal jets remain far from being completely understood. In this work, I use a barotropic model of geostrophic flows within the quasilinear approximation to predict theoretically the zonal structure of the average flow. In the asymptotic limit where the rate of energy injection is small and energy is injected at small scale, I show that the averaged dynamics of the zonal velocity profile  $U$  is given explicitly by the closed equation (2.4.2)

$$\partial_t U - \frac{\epsilon U'''}{U'^2} = -rU,$$

where  $\epsilon$  is the rate of energy injection in  $m^2.s^{-3}$  and  $r$  is the dissipation coefficient in  $s^{-1}$ . In hydrodynamics, it is in general not possible to close exactly the hierarchy for the velocity moments. The above equation is thus one of the very few examples for which the exact closure is possible. The work of part 2 has been published in [103].

The three other sections present the applications in celestial mechanics. The work on Mercury's secular dynamics of chapter 5 has been done in collaboration with the group of Jacques Laskar at the IMCCE who already obtained an estimation of the probability distributions of the planetary orbital parameters over 5 billion years. Those predictions are the result of long-term numerical integrations of the full secular dynamics of the solar system [53]. My approach is more theoretical. I use stochastic averaging and large deviation theory to recover some of the numerical results about the state of the solar system on a timescale of many billion years.

In section 3, I answer the question whether the chaotic dynamics of the asteroid belt has a long-term influence on planetary dynamics. From a completely theoretical approach using stochastic averaging, I find that the asteroids are responsible for a superdiffusion -that is, a diffusion scaling as  $t^{3/2}$  instead of  $\sqrt{t}$  for standard diffusion- of the planetary longitudes on a typical timescale of few million years. A theoretical expression for the typical timescale of longitudes superdiffusion is (3.4.4)

$$\tau_{\text{diff}} \approx \left( \left( \frac{M_S}{m_a} \right)^2 \frac{a_p^3 \tau_\varphi}{\mathcal{G} M_S} \right)^{1/3},$$

where  $m_a$  is the asteroid's mass,  $M_S$  is the mass of the Sun,  $\mathcal{G}$  is Newton's gravitational constant,  $a_p$  is the planet's semi-major axis, and  $\tau_\varphi$  is the Lyapunov time of the asteroid (about 10000 years). The superdiffusion process on planetary longitudes thus confirms from a pure theoretical approach that no ephemerides can be done for times larger than 10 million years. This work has also been published in [102].

Section 4 deals with the chaotic obliquity of a Moonless Earth. I show that the phase space of the spin axis dynamics has three distinct strongly chaotic regions. The spin axis can do rare transitions between these regions, and I give a numerical estimation of the rate of the transition rate between the chaotic regions. This gives access to the probability that the obliquity of the Moonless Earth may have a very large variation from  $0^\circ$  up to  $55^\circ$ . I show that slow chaotic variations of the solar system's fundamental frequencies considerably increases the transition rate. Beyond the particular problem of the spin axis dynamics, this work proposes a new transport mechanism in chaotic symplectic maps depending on slow stochastic parameters, and gives some theoretical results about transport rates.

Last, section 5 studies Mercury's chaotic long-term (secular) dynamics. Using the simple model proposed in [7], I use stochastic averaging to compute theoretically the probability distribution of Mercury's first destabilization time. I show that Mercury's long-term chaotic dynamics can be modeled by a Brownian trajectory in a bounded domain. I could obtain a theoretical order of magnitude for the diffusion coefficient that is in accordance with numerical results. In particular, the theoretical expression for the diffusion coefficient shows that the system is very sensitive to Mercury's initial conditions. Mercury's orbital destabilization could not happen in a few billion years if Mercury's current eccentricity would be reduced only by 20% . One interesting consequence of the stochastic model is the existence of an instanton mechanism for short-term destabilizations of Mercury's orbit. This shows that large deviation theory can predict the probability of an early disintegration of the inner solar system through planetary collisions before its predicted disappearance when the Sun will become a red giant.

# Chapter 1

## Averaging, stochastic averaging and large deviations

### 1.1 Physical motivations

#### 1.1.1 Describe the long-term evolution of a system

A simple observation that surely every physicist has done in his life is that phenomena occurring in nature are very complex. They involve a large number of degrees of freedom, in general in a nonlinear chaotic dynamics that cannot be solved analytically. Only in laboratories do physicists design artificially simple experimental setups to isolate one particular phenomenon, that can be explained with reasonably simple models. It is very rare that a simple model could grasp the whole diversity inherent to a natural system. For example, the room of  $45 \text{ m}^3$  in which I am working contains approximately  $2.5 \cdot 10^{25}$  molecules of gas evolving with a Hamiltonian dynamics and interacting through elastic collisions. Solving the complete dynamics of the particles is completely out of range of our present computers, and will surely remain out of range in the future.

Have a look at the very challenging problem of predicting climate evolution on our planet. Climate scientists have built very complex computer programs to study the long-term evolution of the Earth's climate. Some climate models account as many as possible of the different phenomena involved in the problem, such as the dynamics of the Earth fluid envelops oceans and atmosphere, the presence of clouds, the insolation, coupling with vegetation, etc... To model oceans and atmosphere dynamics, climate model solve the Navier–Stokes equations in the regime of high Reynolds number. This task is however out of range of current computers and a simplified version of the Navier–Stokes equations is effectively implemented. Even with this simplification, the best simulations actually reach a Reynolds number about  $10^5$  [104, 39] whereas the Reynolds number of the atmosphere is many orders of magnitude larger, about  $10^9$ . The largest experimental setup of fluid dynamics in laboratories hardly reaches a Reynolds number of  $10^6$  [97, 106]. As a matter of fact, it would cost more energy for computers to solve the Navier–Stokes equations for the oceans dynamics with the real Reynolds number than the complete energy dissipated by the ocean dynamics itself!

Computational limitations can also arise for dynamical systems with much less degrees of freedom than hydrodynamics. This is the case of celestial mechanics for example. Celestial mechanics has long been the most famous area of physics for the precision of its theoretical predictions. A lot of work has been devoted in the past trying to predict the exact position

of celestial objects (planets, comets, asteroids), far in the future or in the past. The best ephemerides we are currently able to do range up to a few million years [56], a timescale that, however impressive it looks, remains much lower than the age of the solar system itself. Long-term exact predictions of the structure of the solar system fail because of the chaotic nature of the dynamics of planets [47, 48, 93]. A statistical prediction of the orbital elements of planets over 5 billion years has been done [53, 58] at the price of six months of numerical computations on the powerful computers JADE at CINES. This illustrates the fact that, even for real systems with a moderate number of degrees of freedom, long-term predictions can become a formidable task.

The evolution of a very large system is often dominated by a few global variables that characterize the system at the macroscopic level. Earth's climatic conditions for example, can be described by some global informations such as the averaged temperature, the main atmospheric and oceanic currents (golf stream, Kuroshio, jet stream, latitudinal position of Hadley cells...), seasonal variations. Knowing all those global variables, one can say to have a reasonably good description of climate on the Earth. In such a complex system, not all degrees of freedom have the same importance: large scale structures are more important than small scales, long term variations are more important than rapid oscillations. To know the Earth's mean surface insolation for example, astronomers only need the value of the slowly varying orbital elements eccentricity  $e$  and inclination  $i$  of the Earth and can forget the exact longitude of the planet on its orbit.

It is thus very interesting for long-term predictions of a complex physical system to try to describe only the dynamics of some global variables with a slow evolution, without solving the dynamics of a large number of fast evolving variables. This can be achieved using the averaging procedure. The general idea of the averaging technique consists in averaging the influence of the fast variables in the dynamics of the slow variables. The procedure leads to a set of closed equations that describes the dynamics of the slow variables alone, and can be solved independently of the dynamics of the fast variables. For physical systems with a very large number of degrees of freedom, averaging leads to a drastic reduction of the number of degrees of freedom. The final set of equations is suitable for an analytic treatment, or if it is too complex, for a numerical resolution. The set of equations obtained through averaging describes the *averaged* behavior of the system. In celestial mechanics for example, the secular equations describing the long-term evolution of the planets are obtained by averaging the planetary mutual interactions over the Keplerian dynamics [75].

However, the averaging procedure gives a set of *deterministic* equations, that does not take into account possible random fluctuations of the system's dynamics. In physical systems where fluctuations play a major role, we have to go beyond such a simple averaged description. The next two sections will show the importance of random fluctuations of a system and the impact of dynamical large deviations away from the averaged behavior.

### 1.1.2 Necessity of a probabilistic approach

As we have seen in the previous section, the long term evolution of a system can be partly predicted by averaging the dynamics of fast degrees of freedom and keeping only the averaged motion of slow degrees of freedom. Reducing the description of a dynamics to its average may sometimes lead to excellent predictions (as for the secular equations for the solar system) but much more often this description is a too rough approximation. The average description does not take into account the intrinsic *randomness* of a physical system. A real system has always fluctuations away from its averaged dynamics, and in some systems, those fluctuations cannot be neglected. We have to take them into account by a stochastic description of the dynamics. The fluctuating dynamics of a large particle in a bath of smaller particles, called *Brownian*

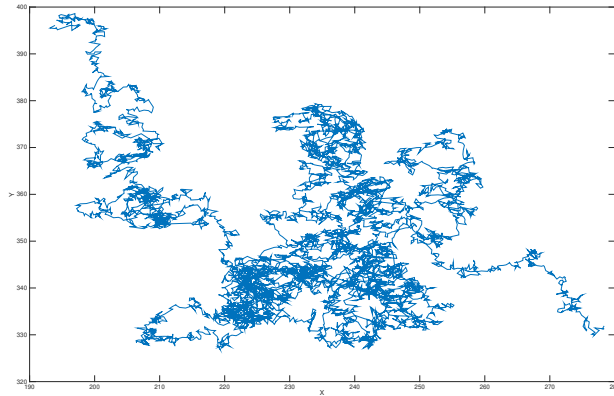


Figure 1.1.1: The reader should not be mistaken: this is not the map of Europe! This is the trajectory of a  $2\mu\text{m}$  particle in a bath. The erratic motion of the particle is an example of Brownian motion.

*motion*, is an excellent example of a system in which random fluctuations cannot be neglected. The large particle feels the collisions with other particles of the bath, and each collision creates a small displacement of the large particle. Those displacements are extremely small compared to the particle size, and because no direction is preferred during the collisions, they average to zero. The averaged displacement of the particle is zero, and however, the accumulation in time of a large number of small random displacements create a large displacement away from the averaged position. A real trajectory of a Brownian particle of size  $2\mu\text{m}$  observed on the microscope is displayed in Fig.(1.1.1).

Describing the dynamics of such a motion has been a very difficult task in the past, both for the physical comprehension of such an erratic motion, and for the mathematical formulation of the equations of motion. The first stochastic differential equation dates back to Louis Bachelier in the context of mathematical models of financial markets [3]. At that time, the formulation of a stochastic equation could be considered as a conceptual breakthrough. The work of Louis Bachelier was totally ignored, although it contains the first theory of Brownian motion that has been independently formulated few years later by Paul Langevin. At the end of the *XIX<sup>th</sup>* century, the theory of Markov processes did not enjoy its current popularity, and physicists were rather used to describe all natural phenomena by deterministic equations. And indeed, it is really not obvious to understand how a system that obeys to deterministic equations of motion at the microscopic level can become a stochastic system at the macroscopic level. In order to understand this transition, one has to understand the properties of a chaotic system. The stochastic description of the dynamical system at large scale comes from the chaotic properties of the dynamics at small scale.

The fundamental property of chaotic systems is that two trajectories with arbitrarily small difference in their initial conditions separate exponentially fast with time. Two trajectories with very close initial conditions do not remain close forever, but the distance between them instead becomes comparable to the size of the system after a characteristic time  $\tau_L$  called the *Lyapunov time* of the system. In real dynamical systems, the initial position is known with some uncertainty. Moreover, the system can feel the influence of some external phenomena that create a small deviation of the system from its predicted trajectory. For timescales that are

much larger than the Lyapunov time, the trajectory can be considered as a random path. The path probability distribution reflects the uncertainty in the initial position, and the uncertainty about “hidden degrees of freedom” that may also influence the motion. In Brownian motion for example, the Lyapunov time of the bath is much smaller than the typical observation time of the large particle, that’s why the large particle’s motion can be described by a stochastic trajectory. Even if the stochastic differential equations have been used for a long time by physicist in an intuitive manner, the mathematical framework and the rigorous connection between stochastic equations and chaotic dynamical motion was very difficult to build and came only very recently.

Which physical information do we get by predicting probability distributions for a system? There are two answers to this question.

For some systems, the probability distribution is directly related to a physical state. Let us take an example to illustrate this point. If one tosses independently  $N$  coins, where  $N$  is a large number, (this was the experiment done by Bernoulli who laid the fundamental laws of probability theory), the ratio  $\frac{n}{N}$  between the number  $n$  of coins falling onto heads and the total number of coins can be approximated by the probability of heads. This result is called the law of large numbers. It means that probability theory is able to predict the statistics of a large number of repeated independent experiments. Although probability theory has been first designed to maximize the gain in games of chance, it turns out that it can be applied to physical systems as well. Some real phenomena in nature do correspond to a large number of independent realizations of an experiment. In Fig.(1.1.2), we display the dispersion of the ash cloud after an eruption of the Chaitén volcano in Chile. Predicting the dispersion of dusts and gas is of great importance as it directly impacts environmental conditions and human life in the neighborhood. Polluting particles in a turbulent flow can be considered to have no interactions, and their trajectories are thus independent. The trajectory of each particle is a random trajectory independent from the other. The trajectories of polluting particles are similar to the coins falling onto head or tail in the sense that they represent independent realizations of an experiment. One could *in principle* predict the concentration of pollutants in the flow by computing the trajectories probability distribution (this is, however, a very difficult task because one has to solve the advection-diffusion equation in a turbulent flow).

For some other physical systems, the probability distribution gives informations about the system’s history. For systems in which we only have one single realization of the dynamics, and none other, the probability distribution does not represent a physical state. This is the case for planetary dynamics for example. We only have one Earth, and there will never be different independent realizations of its trajectory. The probability distribution gives informations about the apparition frequency of a physical state. Over a time  $T$  of observation, the probability distribution gives an estimation of the time  $T_{A_0}$  over which a physical quantity  $A$  has taken the value  $A_0$ . When the observation time becomes very long, the ratio  $\frac{T_{A_0}}{T}$  converges to the probability of  $A_0$ . In the context of planetary dynamics, the probability distributions predict statistics of planetary orbital states in the solar system, since its formation. Fig.(1.1.3) displays the chaotic evolution of the planetary eccentricities over 25 billion years. The computation of probability distributions of planetary orbits gives access to the time statistics of their eccentricities. The planetary eccentricity is directly related to the mean surface insolation and thus to the living conditions on its surface. The time statistics of the Earth’s eccentricity bring a crucial information for understanding the environmental conditions and the development of life on our planet since its formation.

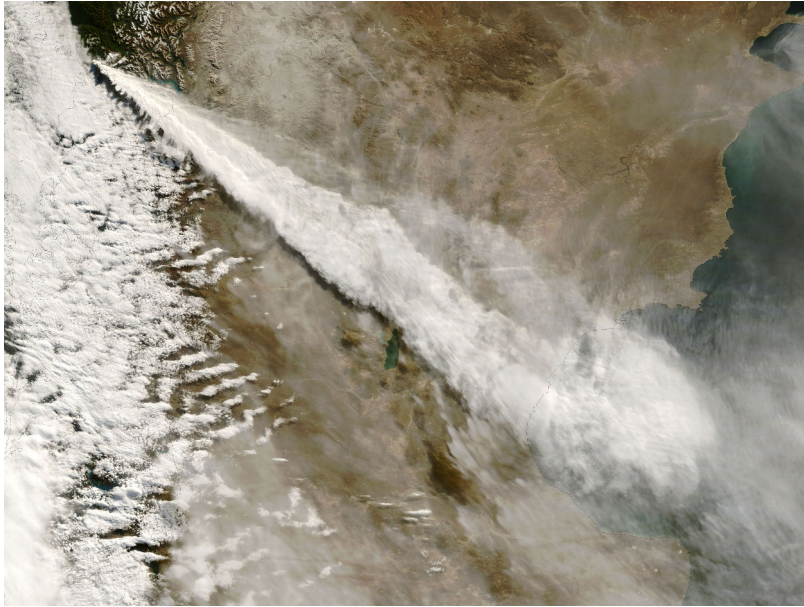


Figure 1.1.2: Ash cloud from the 2008 eruption of Chaitén volcano, Chile, stretching across Patagonia from the Pacific to the Atlantic Ocean. (Wikipedia.org)

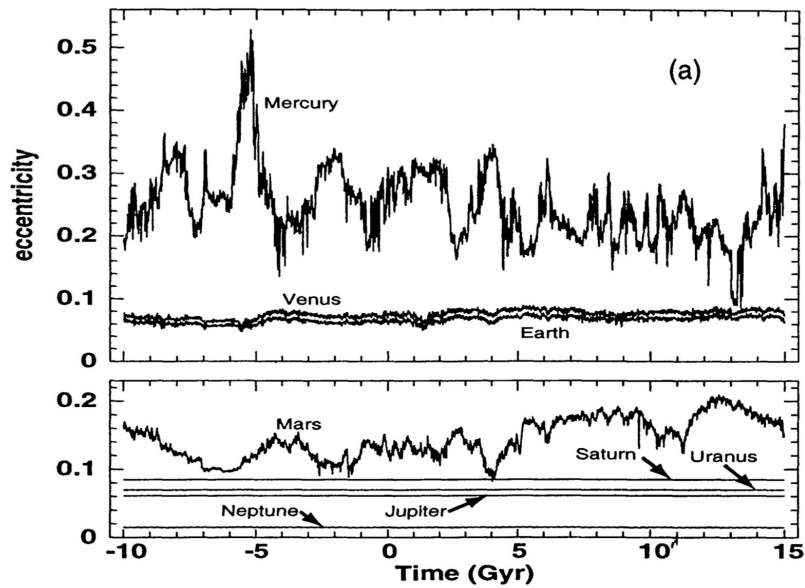


Figure 1.1.3: Chaotic evolution of the eccentricities of the planets in the Solar system over 25 billion years. The simulation shows that the chaos is much more important for the small planets in the inner solar system, in particular for Mercury. (taken from [50])

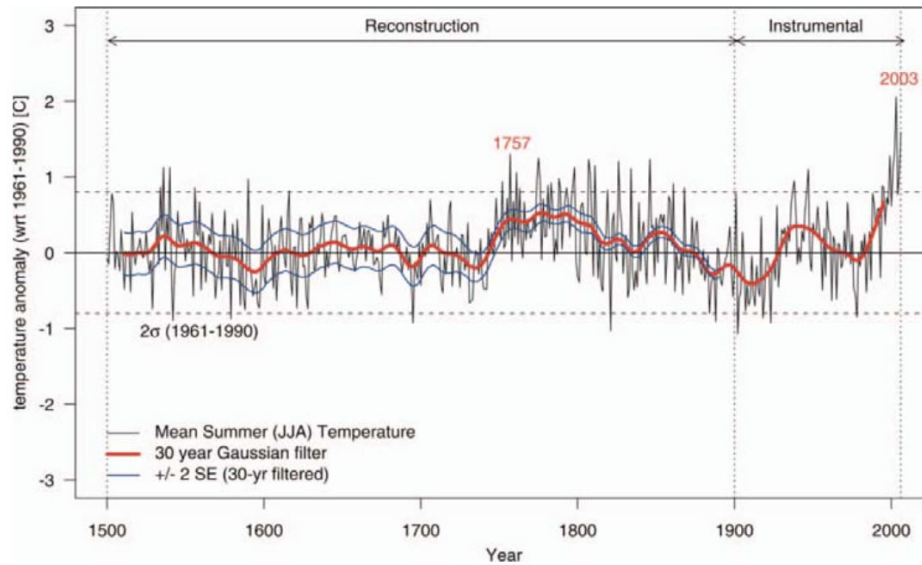


Figure 1.1.4: The temperature anomaly averaged over June, July and August (JJA) and averaged over Europe. The anomaly is defined with respect to the average temperature over the 1961-1990 period. (taken from [32])

### 1.1.3 The problem of rare events with a large impact: large deviation theory

We have seen in sections 1.1.1 and 1.1.2 that the time evolution of slow variables in a complex physical system can be represented by an averaged dynamics, and random fluctuations around the average. The averaged trajectory does not necessarily corresponds to a trajectory observed in the real system: the real trajectories differ from the averaged trajectory because of random dynamical fluctuations. In some physical systems, the averaged dynamics has an attractor. An attractor is a trajectory with the particular property that the system will come back close to this trajectory after any small fluctuation. In physical systems with attractors, the real trajectories remain close to the averaged trajectory with very high probability. Any fluctuation of the system far away from its averaged behavior is possible but very unlikely. A very large fluctuation of a physical system, much larger than the typical fluctuations observed around the average, is what we call a *rare event*.

Even if very large fluctuations of a physical system are very rare, it would be a mistake to believe that we can in general neglect them. The rare events are also the ones that have the most physical impact on the system, that's why it is worth studying them. In 2003, a heat wave in western Europe led to the death toll of more than 70 000 [83]. Fig.(1.1.4) shows the temperature anomaly over Europe averaged over the three months of Summer June, July and August. The temperature has typical variations around the averaged temperature. For Europe, the standard deviation of the June-July-August temperature is about  $1^\circ$ . An exceptional event happened in summer 2003 since the averaged temperature anomaly exceeded  $1.9^\circ$  in Europe, which is about two times greater than the standard deviation. In Switzerland where the heat wave had its maximal amplitude, the temperature anomaly even reached  $5.5^\circ$  [32].

A heat wave like the one occurring in 2003 is a very rare event, and yet, its probability is

high enough for it to be observed at human-life timescale. This means that similar heat waves may happen again in some years. They are random events, and cannot be foreseen far in the future, but we can have an idea of the typical time we have to wait before observing a new heat wave of the same magnitude. The waiting time between two consecutive heat waves is called the *return time*. A major result of the theory of rare events -also called *large deviation theory*- is to be able to compute efficiently the probability distribution of this return time. There are many technical questions to be solved before we are able to predict the return time probability of heat waves and other extreme climatic phenomena with major impact on human's life. The aim of large deviation theory applied to natural systems is to give precisely the return time probability of extreme event, and being better prepared to face them.

After a very large fluctuation, the system does not always come back to its initial stable state. There are examples of natural systems in which many stable states are possible. In that case, a rare event may even lead to the complete destabilization of the system and the reorganization in a new stable state. Let us give a few examples.

In the present thesis, we will be concerned with the possible increase in the eccentricity of Mercury to very high values ( $e > 0.7$ ). This event is a rare event with major impact over the structure of our inner solar system. When the eccentricity of Mercury is too high, its orbit can cross the orbit of Venus and the Earth and the planet may then be completely ejected from the solar system, or collide with Venus or the Earth [54, 58]. After such an event, the structure of the inner solar system would be completely changed to a new state, with a possibly fewer number of planets. This example shows how a rare event leads the system to evolve in an irreversible way and change completely its structure.

In economy, the dynamics of stock prices is often represented by a stochastic process with jumps. A financial crisis sometimes occur, because of a very large and unexpected breakdown of the prices on the financial markets. Such a crisis happened for example in 2008 with a major impact over the economies of all countries in the world. This crisis could be managed thanks to the intervention of the states and the financial markets can be said to have returned in a stable state with small fluctuations. The financial crisis of 1929 is an example in close history where a financial crisis could not be rapidly tackled, especially in Germany, and led to a complete geopolitical reorganization in Europe. One can also think of population dynamics, in which ecological bursts or extinction of species can be observed.

Financial crises, biological crises can be extremely harmful for human societies and for the living conditions of all species on our planet. The aim of large deviation theory does not reduce to predict the extreme events probabilities. As we will explain in section 1.4, a rare event occurs randomly, but once it occurs, it is predictable. We cannot predict with the theory *when* a rare event will occur, but we can predict *how* it will occur. This gives us an extraordinary advantage: if we compare the situation to that of a general that has to face a powerful attack, we are in the situation where the general does not know when he will be attacked, but he knows which path and which weapons the enemy will use to attack his army. In war, this advantage is often sufficient to win the battle, even with very inferior military strengths. The study of rare events thus opens the possibility to intervene to avoid or to stop efficiently disastrous physical phenomena, or if they cannot be avoided, to protect human life from them.

In the very classical problem of a Brownian particle in a potential well, the path chosen by the particle to escape is predicted by large deviation theory. Assume now that a stochastic model similar to that of Brownian motion could be efficiently applied to financial markets, we could in principle extend large deviation theory to predict the path leading to financial crises. This knowledge would greatly help the states to stabilize their financial markets and avoid catastrophic crises. For climate phenomena or population dynamics, it is hopeless to think that we will be able to avoid catastrophic events in the near future. Would large deviation theory be

able to predict the statistics of extreme climate phenomena, and predict their climatic conditions, it would also be helpful to protect ourselves from their consequences. Those last sentences sound like speculations rather than precise statements given the current state-of-the-art in rare event predictions, but it gives an idea about how promising and useful could be future research in large deviation theory.

### 1.1.4 About the conventions used in the present manuscript

All stochastic differential equations are written with the Itô convention, except explicit mention of the contrary. As this work is intended for an audience beyond the field of statistical physics, I have chosen to write the stochastic differential equations using the Gaussian white noise term  $\xi(t)$  instead of the increment  $dW$  of the Wiener process. That is, the stochastic differential equation

$$\dot{X} = a(X) + \sigma(X)\xi(t),$$

is equivalent to

$$dX = a(X)dt + \sigma(X)dW.$$

Throughout the text, the notation “ $f :=$ ” means that the right-hand side of the equality is the definition of  $f$ . The notation “ $f \equiv$ ” means that  $f$  is identically equal to the right-hand side of the equality. In chapter 1,  $\epsilon$  always represents a small nondimensional parameter.  $\epsilon$  should not be confused with  $\varepsilon$ . The notation  $\varepsilon$  is used in chapter 2 for the energy injection rate in the flow (expressed in  $m^2s^{-3}$ ), and in chapter 4 to refer to the Earth obliquity.

## 1.2 Slow-fast dynamical systems

### 1.2.1 Theoretical framework

In the present work, we will be dealing with a slow-fast dynamical system of the form [26, 43, 44, 79]

$$\dot{X}_\epsilon = b(X_\epsilon, y) \tag{1.2.1}$$

$$\dot{y} = \frac{1}{\epsilon}f(X_\epsilon, y) \tag{1.2.2}$$

In the dynamical system (1.2.1-1.2.2), the variables  $\{X_\epsilon, y\}$  refer to the solution of the differential equation for a given value of  $\epsilon$ . In the following, we will be interested in the convergence of the solution  $X_\epsilon$  for  $\epsilon \rightarrow 0$ . We should have also written  $y_\epsilon$  for the fast variable, but we choose to omit the subscript  $\epsilon$ . The variables  $\{X_\epsilon, y\}$  can be finite or infinite dimensional.  $\epsilon$  is a small non-dimensional parameter. We call  $X_\epsilon$  the *slow variable* of the dynamical system, whereas  $y$  is called the *fast variable*. The fundamental assumption about the dynamical system (1.2.1-1.2.2) is the existence of a *timescale separation* between the slow and the fast variables in the limit  $\epsilon \rightarrow 0$ . For infinite dimensional systems, the timescale separation hypothesis is not always satisfied, even in the small  $\epsilon$  limit. For some complex systems for example, there can be a continuous range of timescales in the dynamics such that even the definition of a “slow variable” is impossible (as in three-dimensional turbulent flows for example). If the timescale separation between the variables  $X_\epsilon$  and  $y$  exists, then the typical time for  $y$  variations vanishes when  $\epsilon \rightarrow 0$ .

The aim of the following sections 1.3 and 1.4 is to derive an effective dynamics for the slow variable in the asymptotic limit  $\epsilon \rightarrow 0$ .

Dynamical systems of the form (1.2.1-1.2.2) have been thoroughly studied both by physicists and mathematicians because of their theoretical importance and the wide range of applications to concrete physical systems. In their most general form (1.2.1-1.2.2), where the slow and the fast variables are fully coupled, theorems on the dynamics of the slow variable in the asymptotic limit  $\epsilon \rightarrow 0$  are extremely hard to obtain. A lot of work has been done in [26, 42] in the simpler case where the dynamics (1.2.2) does not depend on  $X_\epsilon$  and is a Markov process satisfying a stochastic differential equation. Those results were then generalized by [44] for fully coupled slow-fast dynamics. Those recent results were obtained for systems where the fast process is a chaotic dynamics satisfying some hypothesis (hyperbolic chaotic systems), and do no longer require that the fast dynamics is stochastic. This can be considered a major theoretical advance for applications to real physical systems because in nature, the fundamental equations of motion for classical (not quantum!) systems are the deterministic Newton's equations. Many authors have shown that there is no fundamental difference between a complex chaotic dynamics and a stochastic dynamics. This idea heuristically explains why the asymptotic dynamics of the slow variable is exactly the same both when the fast variable is described by a stochastic dynamics and by a deterministic chaotic dynamics.

The works on slow-fast dynamical systems [26, 43, 44, 79] give different levels of description for the slow dynamics, depending on the properties of the fast dynamics. We can distinguish two cases for the fast dynamics:

1. The dynamics of the fast variable is only **ergodic**. To say it shortly, this means that the trajectory  $y(t)$  visits all accessible regions of phase space. Under this hypothesis, the dynamics of  $X_\epsilon$  converges as  $\epsilon \rightarrow 0$  to an averaged dynamics, but does not behave like a stochastic variable. The averaging theorem will be explained in section 1.3.1.
2. The dynamics of the fast variable is **ergodic** and **mixing**. The mixing property means that on a timescale that we call  $\tau_m$ , the system loses the memory of its initial condition. A mixing system is necessarily ergodic. However, the mixing time  $\tau_m$  does not always corresponds to the typical time in which the system visits the entire phase space. The system can be ergodic on a much smaller timescale than  $\tau_m$ . Section 3 gives a concrete example of a dynamical system where the timescales for ergodicity and mixing are different. It often happens that the mixing time  $\tau_m$  is of the order of the Lyapunov time  $\tau_L$  in chaotic dynamical systems, and that both times can be assimilated. If the dynamics (1.2.2) is mixing, the stochastic averaging theorems given in sections 1.3.2-1.3.3 state that the solution  $X_\epsilon$  follows a stochastic differential equation in the small  $\epsilon$  limit. The case of a mixing fast dynamics will be very interesting for physical applications, because it allows to go beyond the simple averaged description of the slow variable.

Before we turn to the exact formulation of averaging and stochastic averaging, we will explain more precisely in the next section the meaning of *ergodic* and *mixing*. My aim is to give an intuitive comprehension rather than a complete mathematical definition of those two properties. For a more complete discussion, we refer the reader to [86, 28, 22].

## 1.2.2 Ergodicity and mixing

We consider in the present section the dynamics of the fast variable alone on the timescale  $\epsilon$

$$\dot{y} = f(X, y). \quad (1.2.3)$$

In equation (1.2.3), the slow variable  $X$  is fixed at a given value. We assume that the dynamical system (1.2.3) is ergodic and mixing. The ergodicity or mixing properties can be quite easily proven for Markov chains. For chaotic dynamical systems however, those properties are so

difficult to prove that it has only been done for very simple dynamics (hard disks in two dimensions for example [91]). For most chaotic dynamical systems, ergodicity and mixing remain assumptions that are well satisfied for practical purposes.

Let us give an intuitive picture of the mixing property. For mixing dynamics, the different parts of the trajectory  $y(t)$  can be considered as uncorrelated. Otherwise stated, there exists a timescale  $\tau_m$  for which two different states  $y(t_1)$  and  $y(t_2)$  with  $|t_1 - t_2| > \tau_m$  can be considered as independent and identically distributed random variables. Have a look at Fig.(1.2.1). We divide the trajectory in pieces  $[t_i, t_{i+1}]$  of length  $\tau_m$ . The variables  $\{y(t_1), y(t_2), \dots\}$  behave as independent random variables with identical distribution  $\rho_s(X, y)$ , where  $\rho_s$  is the unique invariant measure of the dynamics (1.2.3). We recall here that an invariant measure of a dynamical system, or a stochastic process, is equivalently called a stationary distribution: it is a probability distribution that does not evolve in time with the considered dynamics. A mathematical definition will be given in (1.2.10).

From the property, we can derive the asymptotic law of any integral of the form

$$\int_0^T b(X, y(t)) dt, \quad (1.2.4)$$

where the function  $b$  is continuous. The ergodic property states that the time average of  $b(X, y(t))$  is identical to its average in probability. This means that for any initial condition  $y(0)$

$$\frac{1}{T} \int_0^T b(X, y(t)) dt \xrightarrow{T \rightarrow +\infty} \int b(X, y) \rho_s(X, y) dy. \quad (1.2.5)$$

The convergence in (1.2.5) can be seen as a property similar to the law of large numbers in probability theory. Please note that the convergence (1.2.5) does not require the mixing hypothesis, this is a consequence of ergodicity alone. Thus, property (1.2.5) still holds if the system is ergodic but not mixing.

The mixing property gives further information about the convergence of the time integral (1.2.4). The integral in (1.2.4) can be seen as a sum of i.i.d random variables. A generalization of the central limit theorem to continuous set of random variables states that the integral (1.2.4) converges in law as  $T \rightarrow \infty$  to a Gaussian distribution. Let us define  $\bar{b}(X) := \int b(X, y) \rho_s(X, y) dy$  as the average of  $b$ , and subtract  $b$  from its average  $\tilde{b}(X) := b(X, y) - \bar{b}(X)$ . As a consequence of the mixing hypothesis, probability distribution of the variable

$$\frac{1}{\sqrt{T}} \int_0^T \tilde{b}(X, y(t)) dt \quad (1.2.6)$$

converges as  $T \rightarrow +\infty$  to a Gaussian distribution independently from the initial condition  $y(0)$  (see e.g. [33] chapter 8). The convergence of probability distributions is called the convergence *in law*. The Gaussian asymptotic distribution of (1.2.6) is entirely characterized by its correlation matrix

$$\begin{aligned} A(X) &:= \lim_{T \rightarrow \infty} \frac{1}{T} \int_0^T \int_0^T \tilde{b}(X, y(t)) \tilde{b}^T(X, y(t')) dt dt' \\ &= \lim_{T \rightarrow \infty} \frac{1}{T} \int_{-\infty}^{+\infty} ds \int_0^T dt \tilde{b}(X, y(t)) \tilde{b}^T(X, y(t+s)) \mathbf{1}[-s < t < T-s]. \end{aligned}$$

Thanks to the ergodic hypothesis, the first integral over  $t$  converges as  $T \rightarrow \infty$  to

$$\frac{1}{T} \int_0^T dt \tilde{b}(X, y(t)) \tilde{b}^T(X, y(t+s)) \mathbf{1}[-s < t < T-s] \xrightarrow{T \rightarrow +\infty} \mathbb{E} \left[ \tilde{b}(X, y(0)) \tilde{b}^T(X, y(s)) \right].$$

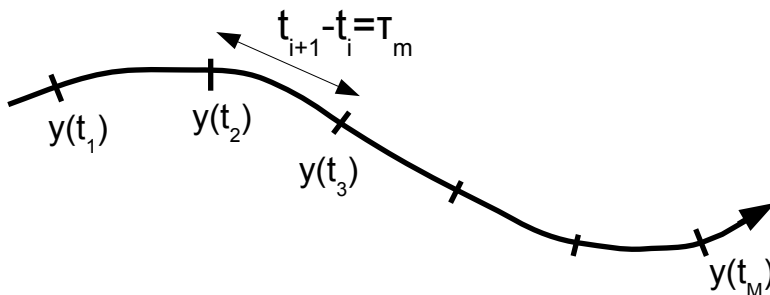


Figure 1.2.1: Decomposition of the trajectory  $y(t)$  in independent random variables.

And thus the correlation matrix writes

$$\begin{aligned} A(X) &= \int_{-\infty}^{+\infty} \mathbb{E} \left[ \tilde{b}(X, y(0)) \tilde{b}^T(X, y(s)) \right] ds, \\ &= 2 \int_0^{+\infty} \mathbb{E} \left[ \tilde{b}(X, y(0)) \tilde{b}^T(X, y(s)) \right] ds, \end{aligned} \quad (1.2.7)$$

where the last equality is obtained by symmetry with respect to time reversal of the correlation function  $\mathbb{E} \left[ \tilde{b}(X, y(0)) \tilde{b}^T(X, y(s)) \right]$ .

The equivalence (1.2.5) between time and probability average, and the convergence of the time integral (1.2.6) to a Gaussian distribution are the two fundamental properties of mixing systems that we will use in section 1.3 to derive averaging and stochastic averaging theorems. In the remaining part of this section, we discuss more precisely the concepts of ergodicity and mixing. In particular, we explain more precisely the intuitive picture of Fig.(1.2.1) and we explain in which sense a mixing dynamics can be considered as a Markov chain. The two following paragraphs are not necessary for the comprehension of the manuscript. The reader can skip them and read directly section 1.2.3.

**Fokker-Planck equation and invariant measure.** For simplicity, we only explain the concept of the invariant measure in the framework of Markov chains, and we use the Fokker-Planck equation. The whole discussion can be extended to dynamical systems of type (1.2.3) using the mathematical framework of distributions and weak convergence.

Let  $\rho(X, y, t)$  be the probability to find the dynamical system in state  $y$  at time  $t$ , for a given value  $X$  of the slow variable. The Fokker-Planck equation corresponds to the continuity equation for the probability distribution  $\rho$  [33]

$$\partial_t \rho + \nabla_y (j[\rho]) = 0, \quad (1.2.8)$$

where  $j[\rho]$  is the probability flux, that can be expressed from the dynamics (1.2.3) as a linear operator over  $\rho$ . We also introduce the Fokker-Planck linear operator  $\mathcal{L}_X[\rho] := -\nabla_y (j[\rho])$ . The Fokker-Planck equation (1.2.8) then writes

$$\partial_t \rho = \mathcal{L}_X[\rho]. \quad (1.2.9)$$

As the dynamics (1.2.3) depends on  $X$ , the linear Fokker-Planck operator  $\mathcal{L}_X$  also depends on  $X$ . An invariant measure  $y \rightarrow \rho_s(X, y)$  of the dynamical system (1.2.3) is a stationary solution of equation (1.2.9), that is

$$\mathcal{L}_X [\rho_s] = 0. \quad (1.2.10)$$

In particular, if the initial distribution of the Markov process is chosen to be the invariant measure, the system has no time evolution, it is trapped in a stationary state.

**The ergodic hypothesis.** There are many equivalent definitions of ergodicity for a deterministic dynamical system or a stochastic process. We propose in the following two equivalent definitions and show the physical implications of ergodicity (see e.g. [100], chapter 2).

Let  $A$  be a region in phase space. Considering a time interval  $[0, T]$ , we call  $T_A$  the time spent by the system  $y(t)$  in region  $A$ .  $T_A$  can thus be defined by

$$T_A := \int_0^T \mathbf{1}[y(t) \in A] dt.$$

The function  $\mathbf{1}[y(t) \in A]$  takes the value 1 if  $y(t)$  is in  $A$ , zero otherwise. A dynamical system will be defined as ergodic if, for very large times, the fraction of time spent by the system in  $A$  corresponds to the probability of the system to be in  $A$  in stationary state. This property writes

$$\lim_{T \rightarrow +\infty} \frac{T_A}{T} = \int_A \rho_s(X, y) dy. \quad (1.2.11)$$

Property (1.2.11) has to be true for almost any initial condition  $y_0$  of the fast dynamics. The property (1.2.11) of ergodic systems means that the statistics over time are given equivalently by the stationary probability distribution. Intuitively, we can say that the ergodic hypothesis will be satisfied if the system can explore fast enough the entire accessible phase space whatever the initial condition. In the context of slow-fast dynamical system, fast enough means that the exploration of phase space has to occur before any significant variation of the variable  $X$ . If this is not the case, the system cannot be considered as ergodic on the timescale of the slow variable and the averaging over the fast variable  $y$  will only occur over a fraction of phase space, not the entire phase space.

A dynamical system is for example not ergodic when the phase space is partitioned into two or more distinct regions  $C_1, C_2, \dots$  that are not connected by the dynamics (1.2.3). The system may then be ergodic in  $C_1$ , and in  $C_2$  separately, but not on  $C_1 \cup C_2$ , because there is no possible transition from  $C_1$  to  $C_2$ . The situation is illustrated in Fig.(1.2.2). The system has many different invariant measures  $\rho_s^1, \rho_s^2, \dots$  associated with the different regions.  $\rho_s^i$  is nonzero in region  $C_i$  and zero everywhere else.

Hence, an equivalent definition of ergodicity may be written:

*The dynamics has one single non-trivial invariant measure.*

If the phase space is connected, but the typical time for transitions between different regions  $C_i$  is longer or of the same order as the time of a significant variation of  $X$ , the fast system is not ergodic at the scale of the slow variable (even if it is ergodic from a strict mathematical point of view). This shows that for real physical slow-fast system, one has to be very careful that averaging might not be possible because the fast system is trapped for a long time in some subregion of phase space.

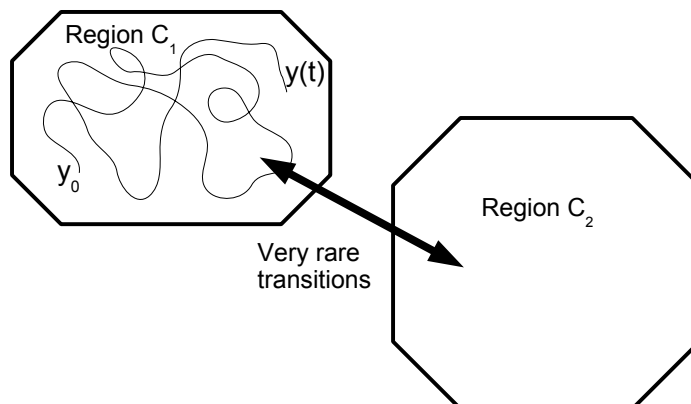


Figure 1.2.2: Schematic representation of a non ergodic process. The phase space has two disconnected regions and the dynamics can hardly escape from one region to the other.

**The mixing hypothesis.** A dynamical system is called mixing by analogy with the behavior of a mixture in a pot when someone turns a spoon inside. Consider for example a drop of red paint in a pot of white paint. After many turnover of the spoon, the red paint is stretched in thinner and thinner filaments (see Fig.1.2.3) until both color are eventually mixed, when the human eye cannot differentiate them. The same happens for a mixing chaotic dynamics.

To compare the picture (1.2.3) of mixing occurring in a real natural flow with the mixing occurring in chaotic dynamical system, we display some images of the phase space  $[0, 2\pi] \times [0, 1]$  of the dynamical system defined by the Hamiltonian [51]

$$H_E = \frac{\alpha}{2} p^2 + \sqrt{(1-p^2)} \sum_{k=1}^{13} \alpha_k \sin(\nu_k t + q + \varphi_k) \quad (1.2.12)$$

The Hamiltonian (1.2.12) will be used in chapter 4 to study the long term variations of the Earth obliquity.  $(p, q)$  is the set of canonical variables,  $t$  is the time and all other coefficients are external parameters. The Hamiltonian (1.2.12) has one degree of freedom and depends explicitly on time, it thus defines a chaotic dynamics for the variables  $(p, q)$ . To show how mixing occurs in the system, we perform a direct numerical integration of Hamilton's equations. We start from a uniform distribution over the line displayed in the left panel of Fig.(1.2.4), and let the system evolve according to Hamilton's equations. Using a try and error algorithm [90], we are able to track the folding of the line for a long time, and resolve the thin filaments and lobes that are created by the mixing of the distribution. The evolution of the line distribution function is displayed in the left panel of Fig.(1.2.4). One clearly sees that the initially localized distribution spreads on the  $(p, q)$  plane because of the thin structures that are created at small scales. For ergodic Hamiltonian dynamics, the invariant measure is the uniform measure because the Hamiltonian flow conserves the areas (the Hamiltonian flow is called *symplectic*). In Fig.(1.2.4), the distribution becomes more and more uniform. The initial distribution converges to the uniform distribution in a weak sense: the distribution can be considered as uniform when the separation between the filaments happens at a scale that is smaller than the smallest physical scale we are able to observe.

To formulate more clearly the mixing hypothesis, consider an initial probability distribution  $\rho_0(y)$  almost entirely concentrated around an initial state  $y_0$ . Take for example a step function



Figure 1.2.3: Picture of red paint in white paint after partial mixing.

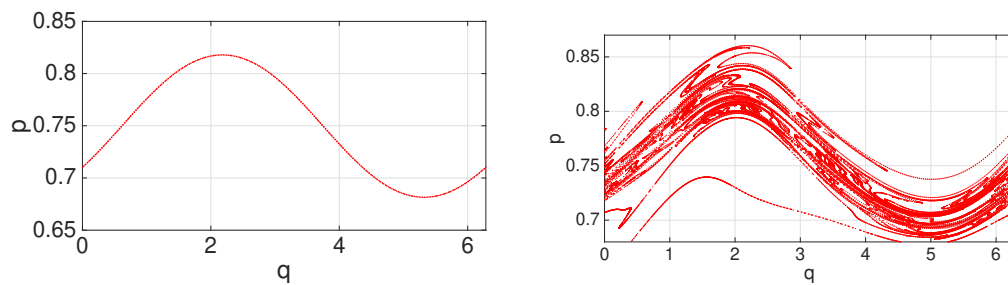


Figure 1.2.4: Simulation of the Hamiltonian dynamics (1.2.12). The left panel represents the initial distribution of trajectories. The right panel displays the distribution of trajectories after many turnover times of the dynamics. One can clearly see that the initial line is distorted and creates thin filaments and lobes.

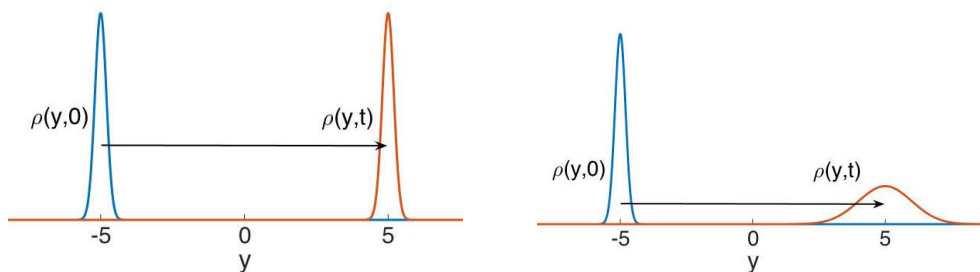


Figure 1.2.5: The left picture shows the probability distribution evolution in an ergodic system without mixing. The right picture shows the same evolution in an ergodic and mixing system.

of infinitesimal extension  $\delta > 0$ ,

$$\rho_0(y) := \frac{1}{\delta^N} \mathbf{1}[\|y - y_0\| < \delta], \quad (1.2.13)$$

where  $N$  is the dimension of space, and  $\|y\|$  is the Euclidean norm of a vector. Then, let the initial distribution (1.2.13) evolve with the probability flow according to the Fokker–Planck equation (1.2.9) (or according to Liouville’s equation for a dynamical system). When the system satisfies the mixing hypothesis, the initial distribution (1.2.13) converges in a large time compared to the mixing time  $\tau_m$  to the invariant measure of the system

$$\rho(X, y, t) \underset{t \gg \tau_m}{\approx} \rho_s(X, y). \quad (1.2.14)$$

In particular, the convergence in (1.2.14) does not depend on the initial distribution  $\rho_0$ . A mixing dynamical system is necessarily ergodic, not the reverse. As a consequence, it has a well defined unique invariant measure  $\rho_s$ . In Fig.(1.2.5), we show qualitatively the difference between an ergodic but non-mixing system, and a mixing system. Starting from a very localized distribution (1.2.13) in an ergodic system, the distribution is carried throughout phase space, but does not spread. After a very large time, the distribution can be found around some value  $y_1 \neq y_0$  but it remains localized around  $y_1$ . The system is reversible, and keeps the memory of its initial condition: knowing the value  $y_1$  at time  $t$ , we can come back to the initial value  $y_0$ .

The situation is very different in a mixing system. A mixing system is irreversible: starting from a very localized distribution, the distribution spreads all over phase space and converges to the invariant measure. This corresponds to the right picture of Fig.(1.2.5). One can see that after some time  $t \sim \tau_m$ , it is impossible to know what was the initial condition. The system could have started from every point in phase space because every initial distribution relaxes to the invariant measure.

The mixing dynamical system has thus the qualitative properties of a discrete Markov chain. Suppose that the system is located in a state  $y$  with some uncertainty  $\delta y$ . After a long time  $t$  compared to  $\tau_m$ , the system can be found in any state  $y(t)$  with probability  $\rho_s$ . The trajectory can thus be decomposed in a number of independent variables as shown in Fig.(1.2.1).

### 1.2.3 Stochastic dynamics of the slow variable: three levels of description

We now summarize the main theorems we will give about the slow-fast dynamical system (1.2.1-1.2.2). Fig.(1.2.6) displays a typical example of the slow variable trajectory in a slow-fast system.

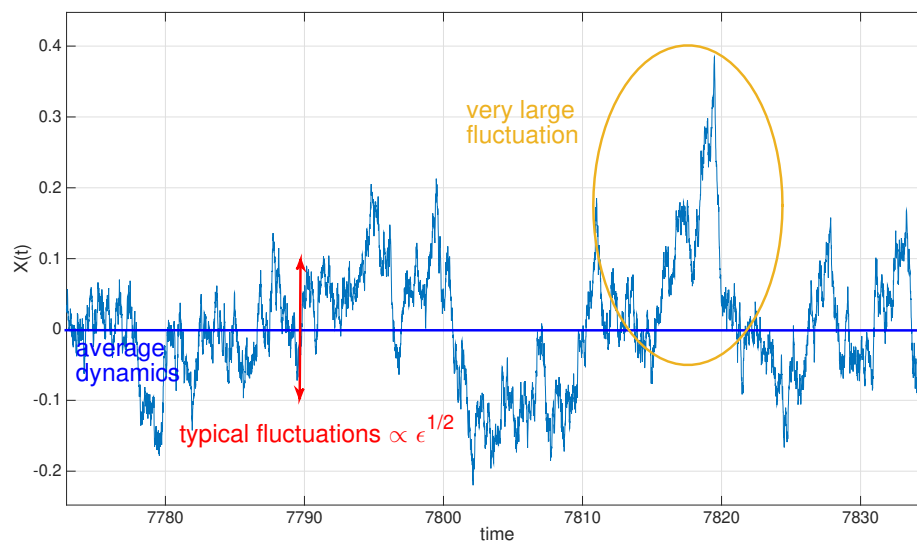


Figure 1.2.6: The picture is an illustration of the asymptotic dynamics of a slow variable in a slow-fast system. For a very large timescale separation, the slow process converges to its average with Gaussian fluctuations of order  $\sqrt{\epsilon}$  around the average. The picture also displays an example of a very large fluctuation, which is very rare in the limit  $\epsilon \rightarrow 0$ . The probability of large fluctuations are predicted by the large deviation theory.

The trajectory  $X_\epsilon(t)$  in Fig.(1.2.6) has zero time average. When  $\epsilon$  goes to zero, the fluctuations of  $X_\epsilon(t)$  become smaller and smaller around the average. This result is a consequence of the *averaging principle* (see section 1.3.1)

$$X_\epsilon \xrightarrow{\epsilon \rightarrow 0} \bar{X}, \quad (1.2.15)$$

where  $\bar{X}(t)$  is the trajectory of the slow variable averaged over the dynamics of the fast variable.

The averaging principle (1.2.15) gives a rather crude approximation of the real trajectory, even in the limit  $\epsilon \rightarrow 0$ . As can be seen in Fig.(1.2.6), the dynamics of the slow variable fluctuates around the average trajectory. The *stochastic averaging theorem* gives a precise estimation of the fluctuations of  $X_\epsilon - \bar{X}$ . The stochastic averaging theorem states that  $u_\epsilon := \frac{X_\epsilon - \bar{X}}{\sqrt{\epsilon}}$  follows asymptotically a stochastic differential equation where the noise is a Gaussian white noise process

$$\dot{u} = a(\bar{X})u + \sigma(\bar{X})\xi(t). \quad (1.2.16)$$

For the precise expression of the coefficients  $a$  and  $\sigma$ , the reader is referred to section 1.3.2. The stochastic averaging theorem shows that typical fluctuations of the slow variable around its average are Gaussian, and are of order  $\sqrt{\epsilon}$ . This result also gives the rate of convergence in the averaging principle (1.2.15). The simulation in Fig.(1.2.6) was done with  $\epsilon = 0.01$ , and thus the typical fluctuations observed are of order of 0.1.

Last, Fig.(1.2.6) shows a very large fluctuation away from zero, much larger than  $\sqrt{\epsilon}$ . Such a fluctuation is very rare because the system displayed in Fig.(1.2.6) has the property that the dynamics always tends to bring back the system to its equilibrium position  $X = 0$ . *Large deviation theory* is able to give an estimation of the probability of such rare events. Large deviation theory predicts that such large fluctuations are exponentially few probable as  $\epsilon \rightarrow 0$ , that's why they are much less observed than the typical fluctuations of order  $\sqrt{\epsilon}$ . For this process, the stationary probability  $\mathbb{P}_\epsilon(X)$  to observe the system in state  $X$  is asymptotically

$$\mathbb{P}_\epsilon(X) \underset{\epsilon \rightarrow 0}{\asymp} e^{-\frac{X^2}{2\epsilon}}. \quad (1.2.17)$$

The asymptotic relation (1.2.17) is not exactly an asymptotic equivalence. The precise meaning of the relation  $\asymp$  will be given in section 1.4. The large deviation principle is the most powerful tool we currently have to describe the stochastic dynamics of a slow variable. In fact, we will also explain in section 1.4 that large deviation theory does not only predict the probability of large fluctuations, but also the path -called *instanton*- chosen by the system to realize a large fluctuation. The instanton theory, which is a consequence of large deviation theory, is of paramount importance for physical systems in general, and for the applications presented in this thesis, and will thus be described in section 1.4.

### 1.3 Averaging and stochastic averaging

In the following sections 1.3.1,1.3.2 and 1.3.3, we give the theorems of averaging and stochastic averaging for slow-fast systems of type (1.2.1-1.2.2). For each theorem, we give two different proofs, one based on asymptotic analysis of stochastic integrals, and one based on an asymptotic expansion of the Fokker-Planck equation. The first proof uses analysis methods (as in [26]), and the second one algebraic methods (as in [79]). Both methods are complementary to each other, and give completely equivalent results. The reader might prefer one or the other depending on its own mathematical affinities.

### 1.3.1 The averaging principle

Consider the slow-fast dynamical system (1.2.1-1.2.2). Assume that for each  $X \in \mathbb{R}^N$ , the fast dynamics (1.2.2) is ergodic, and let  $\rho_s(X, y)$  be its invariant measure. We define the new vector field  $\bar{b}$  by the relation

$$\bar{b}(X) := \int b(X, y) \rho_s(X, y) dy. \quad (1.3.1)$$

Then for all  $T > 0$  the solution  $X_\epsilon(t)$  of the slow-fast system converges in law to the trajectory of the average dynamics on the time interval  $[0, T]$ :

$$X_\epsilon \xrightarrow[\epsilon \rightarrow 0]{} \bar{X}, \quad (1.3.2)$$

with

$$\dot{\bar{X}} = \bar{b}(\bar{X}). \quad (1.3.3)$$

To say it in a more rigorous way, the convergence in law of  $X_\epsilon$  to  $\bar{X}$  means that for all  $\delta > 0$  we have

$$\mathbb{P} \left\{ \sup_{t \leq T} |X_\epsilon(t) - \bar{X}(t)| > \delta \right\} \xrightarrow[\epsilon \rightarrow 0]{} 0. \quad (1.3.4)$$

Some additional hypothesis on the regularity of  $b$  are required to derive the result (1.3.4), we refer the reader to the chapter 2 of [26].

**Formal proof using the integral increment** To prove the result (1.3.2), we rewrite the slow fast system (1.2.1-1.2.2) in a slightly different but equivalent form

$$\dot{X} = b \left( X, y \left( \frac{t}{\epsilon} \right) \right), \quad (1.3.5)$$

$$\dot{y} = f(X, y). \quad (1.3.6)$$

We omit in the proof the subscript  $\epsilon$  for clarity. Equation (1.3.5) for the evolution of the slow variable also writes in its integral form

$$X(T) = X_0 + \int_0^T b \left( X(t), y \left( \frac{t}{\epsilon} \right) \right) dt.$$

We chose an increment of time such that the slow variable does not change significantly during the time  $\Delta T$ . We define the integral increment of  $X$  by

$$\Delta X := \int_0^{\Delta T} b \left( X(t), y \left( \frac{t}{\epsilon} \right) \right) dt. \quad (1.3.7)$$

The main idea of the proof consists in studying the asymptotic behavior of the integral increment (1.3.7) when  $\epsilon$  goes to zero. The trajectory  $X(t)$  over  $[0, T]$  is composed by the sum of a large number of integral increments, that's why the asymptotic trajectory of  $X$  on a finite time interval can be derived from the asymptotic behavior of its integral increments.

With the change of variable  $t \leftarrow \frac{t}{\epsilon}$  in the integral (1.3.7) we get

$$\Delta X := \Delta T \frac{\epsilon}{\Delta T} \int_0^{\frac{\Delta T}{\epsilon}} b(X(\epsilon t), y(t)) dt. \quad (1.3.8)$$

Because the slow variable  $X$  has no significant changes during the time  $\Delta T$ , we can approximate the function  $X(\epsilon t)$  in (1.3.8) by its initial value  $X(0)$ . Then, for any fixed value  $X(0)$ , the ergodic hypothesis implies the convergence (1.2.5) of the time average of  $b$ , which gives

$$\frac{\epsilon}{\Delta T} \int_0^{\frac{\Delta T}{\epsilon}} b(X(0), y(t)) dt \xrightarrow{\epsilon \rightarrow 0} \bar{b}(X(0)),$$

where the field  $\bar{b}$  is given by (1.3.1). This means that

$$\Delta X \xrightarrow{\epsilon \rightarrow 0} \bar{b}(X(0))\Delta T.$$

The convergence is valid for any increment  $\Delta X$  of the trajectory with starting point  $X(t)$ . This shows that the asymptotic trajectory of  $X$  follows the equation

$$\Delta X(t) = \bar{b}(X(t))\Delta t,$$

and this gives the result (1.3.3).

**Formal proof using asymptotic expansion of the Fokker-Planck equation** The probability distribution  $\rho(X, y, t)$  of the dynamical system (1.2.1-1.2.2) satisfies the Fokker-Planck equation

$$\partial_t \rho = \mathcal{L}_1(\rho) + \frac{1}{\epsilon} \mathcal{L}_2(\rho),$$

where  $\mathcal{L}_1, \mathcal{L}_2$  are the Fokker-Planck operators associated to the dynamics of  $X$  and  $y$  respectively. The explicit expression of both operators can depend on  $X$  and  $y$ . To find the asymptotic behavior of the distribution  $\rho$ , we formally expand  $\rho$  in power of  $\epsilon$

$$\rho(X, y, t) := \rho_0(X, y, t) + \epsilon \rho_1(X, y, t) + \dots$$

To leading order in  $\epsilon$  we obtain the equation for  $\rho_0$

$$\mathcal{L}_2(\rho_0) = 0. \tag{1.3.9}$$

This relation implies that  $\rho_0$  is a stationary solution of the Fokker-Planck equation for the fast variable. Because of the ergodicity hypothesis, equation (1.3.9) has a unique solution which is the invariant measure  $\rho_s(X, y)$ . We thus define a new distribution  $\tilde{\rho}_0$  by

$$\rho_0(X, y, t) := \tilde{\rho}_0(X, t) \rho_s(X, y). \tag{1.3.10}$$

Please note that  $\tilde{\rho}_0$  is the marginal distribution over  $X$  at order 0,  $\tilde{\rho}_0 := \int \rho_0(X, y, t) dy$ . The fact that the joint probability distribution can be written to leading order in the form (1.3.10) has a clear physical interpretation: the fast variable has time to reach a quasi-static equilibrium with the slow variable.

At next order in  $\epsilon$ , we obtain

$$\partial_t \rho_0 = \mathcal{L}_1(\rho_0) + \mathcal{L}_2(\rho_1). \tag{1.3.11}$$

Because the Fokker-Planck operator is the divergence of the probability current  $j[\rho]$ , we have  $\mathcal{L}_2(\rho_1) = \nabla_y j[\rho_1]$ , and thus  $\int \mathcal{L}_2(\rho_1) dy = 0$ . The integration of equation (1.3.11) over  $y$ , with the relation  $\int \rho_s(X, y) dy = 1$ , gives

$$\partial_t \tilde{\rho}_0 = \int \mathcal{L}_1(\rho_0) dy. \tag{1.3.12}$$

With the explicit expression  $\mathcal{L}_1(\rho_0) = -\nabla_X (b(X, y)\tilde{\rho}_0(X, t)\rho_s(X, y))$  the right-hand side of (1.3.12) becomes

$$\begin{aligned} \int \mathcal{L}_1(\rho_0)dy &= -\nabla_X \left( \tilde{\rho}_0(X, t) \int b(X, y)\rho_s(X, y)dy \right), \\ &= -\nabla_X (\tilde{\rho}_0(X, t)\bar{b}(X)). \end{aligned}$$

The equation for the marginal distribution  $\tilde{\rho}_0$  thus writes

$$\partial_t \tilde{\rho}_0(X, t) = -\nabla_X (\bar{b}(X)\tilde{\rho}_0(X, t)). \quad (1.3.13)$$

Equation (1.3.13) is the Fokker–Planck equation for the average dynamics (1.3.3). We have thus “formally” proven that  $X \xrightarrow{\epsilon \rightarrow 0} \bar{X}$  in law.

### 1.3.2 Stochastic averaging in finite time

The aim of stochastic averaging theorems is to describe the fluctuations of  $X_\epsilon$  around the averaged trajectory  $\bar{X}$ . The fundamental assumption of those theorems is the mixing hypothesis for the fast dynamics. We will prove in the following that the slow variable has small fluctuations of typical size  $\sqrt{\epsilon}$  around  $\bar{X}$ .

We define a new variable

$$u_\epsilon := \frac{X_\epsilon - \bar{X}}{\sqrt{\epsilon}}.$$

We assume that for any  $X \in \mathbb{R}^N$  the dynamics of the fast variable

$$\dot{y} = f(X, y)$$

is mixing. In particular all correlation functions of the fast variable  $y$  decrease fast enough with time (the meaning of “fast enough” can be precisely defined, see [26])

$$\mathbb{E} [b(X, y(t))b^T(X, y(0))] - \mathbb{E} [b(X, y(t))]\mathbb{E} [b^T(X, y(0))] \xrightarrow{t \rightarrow +\infty} 0.$$

For all practical purposes, stochastic averaging for the slow variable will be valid over times  $t \gg \tau_m$ . For chaotic systems where the mixing time is of the same order as the Lyapunov time  $\tau_L$ , stochastic averaging can be applied for timescales  $t \gg \tau_L$ .

We can now formulate the first theorem of stochastic averaging. For all finite  $T > 0$  the fluctuations  $u_\epsilon(t)$  of the slow variable converge in law over the time interval  $[0, T]$  to the function  $u_0(t)$  that satisfies the stochastic differential equation

$$\dot{u}_0 = a(\bar{X})u_0 + \sigma(\bar{X})\xi(t). \quad (1.3.14)$$

The stochastic product has to be understood with the Itô convention. The matrix coefficients  $a(\bar{X})$  and  $\sigma(\bar{X})$  in equation (1.3.14) are given by the Green–Kubo formulae

$$\sigma(X)\sigma^T(X) = 2 \int_0^{+\infty} \mathbb{E} [\tilde{b}(X, y(t))\tilde{b}^T(X, y(0))] dt, \quad (1.3.15)$$

$$a_{ij}(X) = \frac{\partial}{\partial X_j} \int b^i(X, y)\rho_s(X, y)dy = \frac{\partial \bar{b}}{\partial X_j}(X). \quad (1.3.16)$$

In expression (1.3.15),  $^T$  stands for the transposition operator of a matrix or a vector, and the new field  $\tilde{b}$  is the dynamical field  $b$  with subtraction of its average  $\tilde{b}(X, y) := b(X, y) - \bar{b}(X)$ .

The asymptotic limit (1.3.14) is valid for finite times. In particular, the convergence of  $u_\epsilon$  implies that the variable  $X_\epsilon$  remains close to  $\bar{X}$  in finite time. However, the theorem of this section does not provides any result about the variations of  $X_\epsilon$  for large times. The variations of  $X_\epsilon$  for finite time has typical amplitude  $\sqrt{\epsilon T}$ . This means that the variations can become very large for  $T \propto \frac{1}{\epsilon}$ . The example of Brownian motion in Fig.(1.1.1) shows that the variations of the slow variable can deviate far away from its averaged position. With no attractor, the limit (1.3.14) does not provide enough informations about the possible large fluctuations of  $X(t)$  for times of order  $\frac{1}{\epsilon}$ . In the particular case  $\bar{b} = 0$ , it is possible to derive a stochastic differential equation for the slow variable, valid for timescales of order  $\frac{1}{\epsilon}$ . This case is of major interest for this thesis and will be treated in section (1.3.3).

**Formal proof using the integral increment** The proof of the asymptotic equation (1.3.14) for  $u_0$  follows the same method as the proof of the averaging theorem of section 1.3.1. We omit the subscript  $\epsilon$  for clarity. We have to derive, as  $\epsilon$  goes to zero, the limit of the integral increment of  $u$

$$\Delta u = \frac{1}{\sqrt{\epsilon}} \int_0^{\Delta T} b \left( X(t), y_X \left( \frac{t}{\epsilon} \right) \right) dt - \frac{1}{\sqrt{\epsilon}} \int_0^{\Delta T} \bar{b}(\bar{X}(t)) dt. \quad (1.3.17)$$

The notation  $y_X(t)$  is used to remember that the fast process depends explicitly on  $X$ .

We then introduce in (1.3.17) the average of  $b(X(t), y_X(\frac{t}{\epsilon}))$ , and we decompose the increment  $\Delta u$  as

$$\begin{aligned} \Delta u &= \frac{1}{\sqrt{\epsilon}} \int_0^{\Delta T} \left\{ b \left( X(t), y_X \left( \frac{t}{\epsilon} \right) \right) - \int b(X(t), y) \rho_s(X(t), y) dy \right\} dt \\ &+ \frac{1}{\sqrt{\epsilon}} \int_0^{\Delta T} \left\{ \int b(X(t), y) \rho_s(X(t), y) dy - \int b(\bar{X}(t), y) \rho_s(\bar{X}(t), y) dy \right\} dt. \end{aligned} \quad (1.3.18)$$

The increment  $\Delta u$  is composed of two terms. The first one is

$$\Delta u_1 := \frac{1}{\sqrt{\epsilon}} \int_0^{\Delta T} \left\{ b \left( X(t), y_X \left( \frac{t}{\epsilon} \right) \right) - \int b(X(t), y) \rho_s(X(t), y) dy \right\} dt.$$

With the change of variable  $t \leftarrow \frac{t}{\epsilon}$  and the approximation that  $X(\epsilon t) \approx X(0)$  we get

$$\Delta u_1 := \sqrt{\epsilon} \int_0^{\frac{\Delta T}{\epsilon}} \tilde{b}(X(0), y_X(t)) dt. \quad (1.3.19)$$

The integrand  $\tilde{b}(X(0), y_X(t))$  in (1.3.19) is a function of  $y_X(t)$ , with zero mean. Thanks to the hypothesis that the dynamics of  $y$  is mixing, the integral in (1.3.19) can be considered as a sum of independant and identically distributed random variables with zero mean. In the present context we can apply the central limit theorem to the continuous distribution of the random variables  $\left\{ \tilde{b}(X(0), y_X(t)) \right\}_{t \in [0, \Delta T/\epsilon]}$ . The result is that the continuous sum of random variables

$$\sqrt{\frac{\epsilon}{\Delta T}} \int_0^{\frac{\Delta T}{\epsilon}} \tilde{b}(X(0), y_X(t)) dt$$

converges as  $\epsilon \rightarrow 0$  to a Gaussian distribution with zero mean and variance

$$\Delta u_1^2 = 2 \int_0^{+\infty} \mathbb{E} \left[ \tilde{b}(X(0), y(t)) \tilde{b}^T(X(0), y(0)) \right] dt.$$

Therefore, on the timescale of the slow variable, the increment  $\Delta u_1$  is completely equivalent in law to

$$\Delta u_1 \xrightarrow[\epsilon \rightarrow 0]{\text{in law}} \sigma(X(0))\Delta W,$$

where  $\sigma$  is given by 1.3.15 and  $\Delta W$  is a Gaussian random variable with zero mean and variance  $\Delta T$ .

We now turn to the second part of the integral increment in (1.3.18)

$$\Delta u_2 := \frac{1}{\sqrt{\epsilon}} \int_0^{\Delta T} \left\{ \int b(X(t), y) \rho_s(X(t), y) dy - \int b(\bar{X}(t), y) \rho_s(\bar{X}(t), y) dy \right\} dt.$$

As the difference between  $X$  and  $\bar{X}$  is of the order  $\sqrt{\epsilon}$ , we can expand the integral  $\int b(X(t), y) \rho_s(X(t), y) dy$  around  $\bar{X}$ , this gives

$$\begin{aligned} \Delta u_2 &= \frac{1}{\sqrt{\epsilon}} \int_0^{\Delta T} \frac{\partial}{\partial \bar{X}_i} \left\{ \int b(\bar{X}(t), y) \rho_s(\bar{X}(t), y) dy \right\} (X_i(t) - \bar{X}_i(t)) dt + o(X - \bar{X}), \\ &= \int_0^{\Delta T} \frac{\partial \bar{b}}{\partial \bar{X}_i} (\bar{X}(t)) u_i(t) dt + o(\sqrt{\epsilon}). \end{aligned}$$

with implicit summation over the index  $i$ . To order  $\Delta T$ , we get

$$\Delta u_2 \approx a(\bar{X}(0)) u(0) \Delta T,$$

with the matrix  $a$  given by (1.3.16). Finally, neglecting all terms of higher orders in  $\epsilon$  and  $\Delta T$ , we obtain the following asymptotic expansion for the increment

$$\Delta u \xrightarrow[\epsilon \rightarrow 0]{} a(\bar{X}(0)) u(0) \Delta T + \sigma(X(0)) \Delta W. \quad (1.3.20)$$

The last step is to notice that  $X(0) = \bar{X}(0) + \sqrt{\epsilon}u(0)$ , such that we can replace  $\sigma(X(0))$  by  $\sigma(\bar{X}(0))$  in the limit (1.3.20). We finally obtain

$$\Delta u \xrightarrow[\epsilon \rightarrow 0]{} a(\bar{X}(0)) u(0) \Delta T + \sigma(\bar{X}(0)) \Delta W.$$

which is valid for every value  $\bar{X}(0)$ . This proves that the function  $u(t)$  satisfies the stochastic differential equation (1.3.14) in the limit of vanishing  $\epsilon$ .

**Formal proof using the asymptotic expansion of the Fokker-Planck equation** The proof using the Fokker-Planck equation is quite long and can be found in [33, 10]. We give below the sketch of the calculations to be done. In the following, we use the convention of implicit summation over multiple indices.

The first step of the proof consists in expanding the slow-fast dynamical system around  $\bar{X}(t)$  to obtain a system of equations for the dynamics of  $(u, y)$ . With straightforward computations, we get

$$\begin{aligned} \dot{u} &= \frac{1}{\sqrt{\epsilon}} \tilde{b}(\bar{X}, y) + \frac{\partial \tilde{b}}{\partial X_j}(\bar{X}, y) u_j + O(\sqrt{\epsilon}), \\ \dot{y} &= \frac{1}{\epsilon} f(\bar{X}, y) + \frac{1}{\sqrt{\epsilon}} \frac{\partial f}{\partial X_j}(\bar{X}, y) u_j + O(1), \end{aligned}$$

with implicit summation over the index  $j$ . The Fokker–Planck operators  $\mathcal{L}_1, \mathcal{L}_2$  associated with the dynamics of  $u$  and  $y$  respectively, can also be expanded in powers of  $\epsilon$  as

$$\begin{cases} \mathcal{L}_1 &= \frac{1}{\sqrt{\epsilon}}\mathcal{L}_1^\alpha + \mathcal{L}_1^\beta + \sqrt{\epsilon}\mathcal{L}_1^\gamma + \dots \\ \mathcal{L}_2 &= \frac{1}{\epsilon}\mathcal{L}_2^\alpha + \frac{1}{\sqrt{\epsilon}}\mathcal{L}_2^\beta + \mathcal{L}_2^\gamma + \dots \end{cases} \quad (1.3.21)$$

and the probability distribution  $\rho$  as

$$\rho(u, y, t) := \rho_0(u, y, t) + \sqrt{\epsilon}\rho_1(u, y, t) + \epsilon\rho_2(u, y, t) + \dots$$

The reader has to take care of the fact that all explicit expressions of the Fokker–Planck operators in (1.3.21) involve the variables  $u, y$  and  $t$  because of the function  $\bar{X}(t)$  which is an input in the system. The procedure now consists in collecting the equations at successive orders of  $\epsilon$ .

The equation to leading order shows that the distribution  $\rho_0$  writes

$$\rho_0(u, y, t) = \tilde{\rho}_0(u, t)\rho_s(\bar{X}(t), y), \quad (1.3.22)$$

where  $\rho_s(X, y)$  is as before the invariant measure of the fast process for a given value  $X$ . The decomposition of  $\rho_0$  in (1.3.22) means that the fast variable has time to reach the quasi-static equilibrium with the slow process.

To next order we get

$$\mathcal{L}_2^\alpha(\rho_1) = -\mathcal{L}_1^\alpha(\rho_0) - \mathcal{L}_2^\beta(\rho_0). \quad (1.3.23)$$

To solve the latter equation and express the distribution  $\rho_1$  as a function of  $\rho_0$ , we have to check that the solvability condition is satisfied

$$\int \mathcal{L}_1^\alpha(\rho_0)dy = 0. \quad (1.3.24)$$

The explicit expression  $\int \mathcal{L}_1^\alpha(\rho_0)dy = -\frac{\partial}{\partial u} \left\{ \tilde{\rho}_0(u, t) \int \tilde{b}(\bar{X}, y) \rho_s(\bar{X}, y)dy \right\}$  shows that the solvability condition (1.3.24) is satisfied because  $\tilde{b}$  has zero mean. We may then invert the operator  $\mathcal{L}_2^\alpha$  in relation (1.3.23). The explicit expression for  $\rho_1$  is thus

$$\rho_1 = \int_0^{+\infty} e^{s\mathcal{L}_2^\alpha} (\mathcal{L}_1^\alpha(\rho_0)) ds + \int_0^{+\infty} e^{s\mathcal{L}_2^\alpha} (\mathcal{L}_2^\beta(\rho_0)) ds.$$

Finally, the equation at next order gives us the dynamics of  $\tilde{\rho}_0$

$$\partial_t \tilde{\rho}_0 = \int \mathcal{L}_1^\alpha(\rho_1)dy + \int \mathcal{L}_1^\beta(\rho_0)dy. \quad (1.3.25)$$

The second term of (1.3.25) is the simplest one, it gives the following drift term in the equation for  $X$

$$\int \mathcal{L}_1^\beta(\rho_0)dy = -\frac{\partial}{\partial u_i} \left\{ u_j \tilde{\rho}_0(u, t) \int \frac{\partial b^i}{\partial X_j}(\bar{X}, y) \rho_s(\bar{X}, y) dy \right\} \quad (1.3.26)$$

The second term is a bit more subtle. It is composed of the two different contributions

$$\int \mathcal{L}_1^\alpha(\rho_1)dy = \int_0^{+\infty} ds \left\{ \int \mathcal{L}_1^\alpha e^{s\mathcal{L}_2^\alpha} (\mathcal{L}_1^\alpha(\rho_0)) dy \right\} + \int_0^{+\infty} ds \left\{ \int \mathcal{L}_1^\alpha e^{s\mathcal{L}_2^\alpha} (\mathcal{L}_2^\beta(\rho_0)) dy \right\}.$$

To compute the term

$$\int \mathcal{L}_1^\alpha e^{s\mathcal{L}_2^\alpha} (\mathcal{L}_1^\alpha(\rho_0)) dy = \frac{\partial}{\partial u_i} \frac{\partial}{\partial u_j} \left\{ \tilde{\rho}_0(u, t) \left\{ \int \tilde{b}^i(\bar{X}, y) e^{s\mathcal{L}_2^\alpha} \tilde{b}^j(\bar{X}, y) \rho_s(\bar{X}, y) \right\} \right\}, \quad (1.3.27)$$

we use the adjoint of the Fokker–Planck operator  $(\mathcal{L}_2^\alpha)^\dagger$  in the integral over  $y$ . We then use the nontrivial property that

$$e^{s(\mathcal{L}_2^\alpha)^\dagger} [\tilde{b}^i(\bar{X}, y)] = \mathbb{E}_y [\tilde{b}^i(\bar{X}, y(s))],$$

where  $y(s)$  is the value of the flow at time  $s$  with initial condition  $y(0) = y$ . This shows that

$$\int \tilde{b}^i(\bar{X}, y) e^{s\mathcal{L}_2^\alpha} \tilde{b}^j(\bar{X}, y) \rho_s(\bar{X}, y) = \mathbb{E} [\tilde{b}^i(X, y(s)) \tilde{b}^j(X, y(0))]. \quad (1.3.28)$$

Equations (1.3.27),(1.3.28) give the result

$$- \int_0^{+\infty} ds \left\{ \int \mathcal{L}_1^\alpha e^{s\mathcal{L}_2^\alpha} (\mathcal{L}_1^\alpha(\rho_0)) dy \right\} = \frac{\partial}{\partial u_i} \frac{\partial}{\partial u_j} \left\{ \tilde{\rho}_0(u, t) \left\{ \int_0^{+\infty} \mathbb{E} [\tilde{b}^i(X, y(s)) \tilde{b}^j(X, y(0))] ds \right\} \right\}.$$

This term corresponds to the white noise  $\sigma(\bar{X})\xi(t)$  in equation (1.3.14).

The most difficult term is

$$\int_0^{+\infty} ds \left\{ \int \mathcal{L}_1^\alpha e^{s\mathcal{L}_2^\alpha} (\mathcal{L}_2^\beta(\rho_0)) dy \right\} = \frac{\partial}{\partial u_i} \left\{ \tilde{\rho}_0(u, t) \left\{ \int_0^{+\infty} ds \int \tilde{b}^i(\bar{X}, y) e^{s\mathcal{L}_2^\alpha} \frac{\partial}{\partial y_j} \left\{ u_k \frac{\partial f^j}{\partial \bar{X}_k}(\bar{X}, y) \rho_s(\bar{X}, y) \right\} dy \right\} \right\}.$$

Using again the property

$$e^{s(\mathcal{L}_2^\alpha)^\dagger} [\tilde{b}^i(\bar{X}, y)] = \mathbb{E}_y [\tilde{b}^i(\bar{X}, y(s))],$$

we can write

$$\begin{aligned} \int_0^{+\infty} ds \left\{ \int \mathcal{L}_1^\alpha e^{s\mathcal{L}_2^\alpha} (\mathcal{L}_2^\beta(\rho_0)) dy \right\} &= \frac{\partial}{\partial u_i} \left\{ \tilde{\rho}_0(u, t) u_k \left\{ \int_0^{+\infty} ds \int \mathbb{E}_y [\tilde{b}^i(\bar{X}, y(s))] \frac{\partial}{\partial y_j} \left\{ \frac{\partial f^j}{\partial \bar{X}_k}(\bar{X}, y) \rho_s(\bar{X}, y) \right\} dy \right\} \right\} \\ &= - \frac{\partial}{\partial u_i} \left\{ \tilde{\rho}_0(u, t) u_k \left\{ \int_0^{+\infty} ds \int \frac{\partial}{\partial y_j} \mathbb{E}_y [\tilde{b}^i(\bar{X}, y(s))] \frac{\partial f^j}{\partial \bar{X}_k}(\bar{X}, y) \rho_s(\bar{X}, y) dy \right\} \right\} \end{aligned} \quad (1.3.29)$$

This identity shows that the term  $\int_0^{+\infty} ds \left\{ \int \mathcal{L}_1^\alpha e^{s\mathcal{L}_2^\alpha} (\mathcal{L}_2^\beta(\rho_0)) dy \right\}$  adds a drift term to the stochastic equation (1.3.14) which explicit expression is

$$\int_0^{+\infty} ds \int \frac{\partial}{\partial y_j} \mathbb{E}_y [\tilde{b}^i(\bar{X}, y(s))] \frac{\partial f^j}{\partial \bar{X}_k}(\bar{X}, y) \rho_s(\bar{X}, y) dy.$$

Such an expression can be found for example in [10]. Some additional work is needed to show that the last expression, together with (1.3.26), simplifies to give the coefficient  $a$ .

Let us come back to (1.3.29) and use the relation

$$\begin{aligned} \frac{\partial}{\partial y_j} \left\{ \frac{\partial f^j}{\partial \bar{X}_k}(\bar{X}, y) \rho_s(\bar{X}, y) \right\} &= \frac{\partial}{\partial \bar{X}_k} \frac{\partial}{\partial y_j} \left\{ f^j(\bar{X}, y) \rho_s(\bar{X}, y) \right\} - \frac{\partial}{\partial y_j} \left\{ f^j(\bar{X}, y) \frac{\partial \rho_s}{\partial \bar{X}_k}(\bar{X}, y) \right\}, \\ &= - \frac{\partial}{\partial y_j} \left\{ f^j(\bar{X}, y) \frac{\partial \rho_s}{\partial \bar{X}_k}(\bar{X}, y) \right\}, \end{aligned} \quad (1.3.30)$$

where the last equality is obtained because the invariant measure satisfies

$$\frac{\partial}{\partial y_j} \left\{ f^j(\bar{X}, y) \rho_s(\bar{X}, y) \right\} = 0.$$

An integration by part in (1.3.29) using (1.3.30) gives

$$\int_0^{+\infty} ds \left\{ \int \mathcal{L}_1^\alpha e^{s\mathcal{L}_2^\alpha} \left( \mathcal{L}_2^\beta(\rho_0) \right) dy \right\} = \frac{\partial}{\partial u_i} \left\{ \tilde{\rho}_0(u, t) u_k \left\{ \int_0^{+\infty} ds \int f^j(\bar{X}, y) \frac{\partial}{\partial y_j} \mathbb{E}_y \left[ \tilde{b}^i(\bar{X}, y(s)) \right] \frac{\partial \rho_s}{\partial \bar{X}_k}(\bar{X}, y) dy \right\} \right\} \quad (1.3.31)$$

The Feynman-Kac formula also implies that

$$f^j(\bar{X}, y) \frac{\partial}{\partial y_j} \mathbb{E}_y \left[ \tilde{b}^i(\bar{X}, y(s)) \right] = \frac{\partial}{\partial s} \mathbb{E}_y \left[ \tilde{b}^i(\bar{X}, y(s)) \right],$$

and thus

$$\int_0^{+\infty} f^j(\bar{X}, y) \frac{\partial}{\partial y_j} \mathbb{E}_y \left[ \tilde{b}^i(\bar{X}, y(s)) \right] ds = \int \tilde{b}^i(\bar{X}, y') \rho_s(\bar{X}, y') dy' - \tilde{b}^i(\bar{X}, y).$$

using the last equality in (1.3.31), we finally get

$$\int_0^{+\infty} ds \left\{ \int \mathcal{L}_1^\alpha e^{s\mathcal{L}_2^\alpha} \left( \mathcal{L}_2^\beta(\rho_0) \right) dy \right\} = -\frac{\partial}{\partial u_i} \left\{ \tilde{\rho}_0(u, t) u_k \left\{ \int \tilde{b}^i(\bar{X}, y) \frac{\partial \rho_s}{\partial \bar{X}_k}(\bar{X}, y) dy \right\} \right\}. \quad (1.3.32)$$

One can then check that both terms (1.3.26) and (1.3.32) combine to give the total drift  $a(\bar{X})$  in (1.3.16).

### 1.3.3 Stochastic averaging, case $\bar{b} \equiv 0$

In section 1.3.2, we have seen that the real trajectory  $X_\epsilon(t)$  can deviate from the averaged trajectory  $\bar{X}(t)$  with Gaussian fluctuations of the order  $\sqrt{\epsilon}$ . This result is valid for any finite time  $T$ . Long-term predictions for the dynamics are much more difficult, and the long-term behavior partly depends on the structure of the averaged field  $\bar{b}$ . We show in this section that a stochastic equation for  $X_\epsilon$  can be derived in the particular case  $\bar{b} \equiv 0$ . Consider equation (1.3.14) for the fluctuations with  $\bar{X} = 0$  and  $a \equiv 0$ . The variable  $X_\epsilon(t)$  satisfies the free diffusion equation

$$\dot{X}_\epsilon(t) \underset{\epsilon \rightarrow 0}{\sim} \sqrt{\epsilon} \sigma(0) \xi(t). \quad (1.3.33)$$

In equation (1.3.33), the dynamics of  $X_\epsilon$  is a free diffusion process, and can thus reach very high values on a timescale of order  $\frac{1}{\epsilon}$ . Over the timescale  $\frac{1}{\epsilon}$ , the fluctuations of  $X_\epsilon$  cannot be described by a power expansion of  $b$  and equation (1.3.14) breaks down.

The aim of the present section is thus to derive a new stochastic averaging theorem in the case  $\bar{b} \equiv 0$  ([79], chapter 11). The theorem of this section will be particularly useful for applications in celestial mechanics (see sections 3 and 5). In celestial mechanics, the time evolution of action variables is a periodic function of the canonical angles that averages to zero over the fast motion.

We assume now that the dynamical field  $b$  averages to zero over the fast variable

$$\bar{b} := \int b(X, y) \rho_s(X, y) dy \equiv 0.$$

The new timescale of evolution for  $X$  will be of order  $\frac{1}{\epsilon}$ . We thus write the system (1.2.1-1.2.2) on the new timescale as

$$\dot{X}_\epsilon = \frac{1}{\epsilon} b(X_\epsilon, y), \quad (1.3.34)$$

$$\dot{y} = \frac{1}{\epsilon^2} f(X_\epsilon, y). \quad (1.3.35)$$

We assume that for each fixed value of  $X$ , the fast process defined by the equation

$$\dot{y} = f(X, y)$$

is mixing, and we call  $\tau_m$  its mixing time. The stochastic description of the slow variable is only valid for timescales much larger than  $\tau_m$ .

Then for all  $T > 0$ , the slow process  $X_\epsilon(t)$  converges in law over the time interval  $[0, T]$  to the process  $X_0(t)$  that satisfies the stochastic differential equation

$$\dot{X}_0 = \gamma(X_0) + \sigma(X_0)\xi(t). \quad (1.3.36)$$

If the fast process is symmetric w.r.t. time reversal, the matrix coefficient  $\sigma$  in (1.3.36) is given by the Green–Kubo formula

$$\sigma(X)\sigma^T(X) = 2 \int_0^{+\infty} \mathbb{E} [b(X, y(t))b^T(X, y(0))] dt. \quad (1.3.37)$$

In the fast process is not time reversal symmetric,  $\sigma\sigma^T$  is given by the symmetric part of the matrix (1.3.37). Contrary to the first stochastic averaging theorem (1.3.14), the vector coefficient  $\gamma$  does not have any simple expression. The coefficient  $\gamma$  creates a drift term in the equation for  $X_0$ . Physically, it is important to understand that the drift term comes from correlations between the fast and the slow variables. In equation (1.3.14), the correlations between  $X$  and  $y$  could be neglected because they would only create a correction of order  $\epsilon$  to the dynamical field  $\bar{b}$ . When  $\bar{b}$  is zero, the correction of order  $\epsilon$  is important over times of order  $\frac{1}{\epsilon}$ .

Only in the simple case of one dimensional fast process that does not depend on  $X$ , we do recover an explicit expression for the drift (see [33], chapter 8)

$$\gamma(X) = \int_0^{+\infty} \mathbb{E} [\partial_X b(X, y(t))b(X, y(0))] dt. \quad (1.3.38)$$

For a fully coupled dynamics as (1.3.34-1.3.35), the computation of the coefficient  $\gamma$  should be done in each particular case using one of the two techniques of algebra or analysis described below in the proof.

Equation (1.3.36) is an exact limit in law. It describes completely the long-term distribution of  $X_\epsilon$ , and there is no need to resort to large deviation theory.

**Proof using the Fokker-Planck equation** Contrary to what was done in section (1.3.2), we only give here the proof using asymptotic expansion of the Fokker–Planck equation. This method is the only one I know that leads to explicit although quite abstract expressions for the coefficient  $\gamma$  in (1.3.36).

We use the results (1.3.10-1.3.11-1.3.12) obtained in the proof for the averaging principle. Because of the assumption that  $\bar{b} \equiv 0$ , the term in the right-hand side of (1.3.12) vanishes. We get the equation

$$\partial_t \tilde{\rho}_0 = 0.$$

The expansion of the distribution in powers of  $\epsilon$  does not provide any information about the time evolution of  $\rho$ . To be consistent, we have to use a multiscale expansion instead. We assume that  $\rho$  now depends on all timescales  $\epsilon t, \epsilon^2 t, \dots$ , that is

$$\rho(X, y, t) = \tilde{\rho}_0(X, \epsilon t, \epsilon^2 t \dots) \rho_s(X, y) + \epsilon \rho_1(X, y, \epsilon t, \epsilon^2 t \dots) + O(\epsilon^2).$$

The distribution  $\rho_1$  satisfies the equation

$$\mathcal{L}_2(\rho_1) = -\mathcal{L}_1(\rho_0),$$

which gives after inverting the Fokker–Planck operator

$$\rho_1 = \int_0^{+\infty} e^{t' \mathcal{L}_2} \mathcal{L}_1(\rho_0) dt'. \quad (1.3.39)$$

The next order in  $\epsilon$  gives the time evolution of  $\rho_0$  on the timescale  $\frac{1}{\epsilon}$ . The equation is

$$\partial_{t_1} \rho_0 = \mathcal{L}_1(\rho_1) + \mathcal{L}_2(\rho_2),$$

where  $t_1$  is the time variable  $\epsilon t$ . After integration over  $y$ , this equation becomes

$$\partial_{t_1} \tilde{\rho}_0 = \int \mathcal{L}_1(\rho_1) dy. \quad (1.3.40)$$

We have to evaluate the right-hand side of (1.3.40) using (1.3.39). The expression writes explicitly

$$\int \mathcal{L}_1(\rho_1) dy = \int_0^{+\infty} dt' \nabla_X \left\{ \int dy b(X, y) e^{t' \mathcal{L}_2} \nabla_X \{b(X, y) \rho_s(X, y) \tilde{\rho}_0\} \right\}. \quad (1.3.41)$$

We then use the adjoint  $\mathcal{L}_2^\dagger$  of the Fokker–Planck operator and the relation

$$e^{t \mathcal{L}_2^\dagger} b(X, y) = \mathbb{E}_y [b(X, y(t))].$$

The value  $y(t)$  in the average should be understood as the trajectory of the fast process at time  $t$  starting from  $y(0) = y$ . The reader has to take care that the fast process depends also on  $X$ ! Finally, we can write equation (1.3.40) as

$$\begin{aligned} \partial_{t_1} \tilde{\rho}_0 = & - \nabla_X \left\{ \left\{ \int_0^{+\infty} dt' \int dy (\nabla_X \mathbb{E}_y [b(X, y(t'))]) b(X, y) \rho_s(X, y) \right\} \tilde{\rho}_0 \right\} \\ & + \nabla_X \nabla_X \left\{ \left\{ \int_0^{+\infty} dt' \int dy \mathbb{E}_y [b(X, y(t'))] b^T(X, y) \rho_s(X, y) \right\} \tilde{\rho}_0 \right\}. \end{aligned}$$

The second term gives the diffusion coefficient (1.3.37). The first term gives an abstract expression for the drift

$$\gamma(X) = \int_0^{+\infty} dt' \int dy (\nabla_X \mathbb{E}_y [b(X, y(t'))]) b(X, y) \rho_s(X, y). \quad (1.3.42)$$

When the fast process does not depend on  $X$ , in one dimension, we get the much simpler expression

$$\gamma(X) = \int_0^{+\infty} ds \mathbb{E} [\partial_X b(X, y(s)) b(X, y(0))].$$

The explicit expressions for the drift and the diffusion coefficient involve correlations functions of the fast process. The mixing hypothesis is crucial to ensure the convergence of the time integrals in (1.3.42). For mixing chaotic dynamics, correlations functions usually decay exponentially fast as  $e^{-\frac{t}{\tau_L}}$  where  $\tau_L$  is the Lyapunov time of the fast process. The decay of all correlation functions is one of the necessary hypotheses of stochastic averaging, which is satisfied in practice by mixing chaotic systems.

When the fast process does not depend on  $X$ , and in the one dimensional case, the process 1.3.36 can be written as

$$\dot{X}_0 = \sigma(X_0) \circ \xi(t),$$

where the stochastic product has to be understood with the Stratanovitch convention. In the multidimensional case, there are some corrections to the Stratanovitch product [41].

## 1.4 Large deviations and instantons

It has been shown in section 1.3.3 that the long-term evolution of the slow process  $X_\epsilon$  can be described by a stochastic differential equation when the averaged dynamics vanishes. The fact that the long-term dynamics of  $X_\epsilon$  is given by a such simple mathematical object as a close stochastic differential equation is exceptional. No equivalent simple result exists when  $\bar{b}$  is non zero. The slow trajectory remains most of the time close to the averaged trajectory  $\bar{X}(t)$ , and its fluctuations around  $\bar{X}(t)$  are typically Gaussian fluctuations of typical amplitude  $\sqrt{\epsilon}$ . This kind of fluctuations are described by equation (1.3.14). Yet, the long-term dynamical behavior does not reduce to the small Gaussian fluctuations around the averaged trajectory. Fluctuations of order one can carry  $X_\epsilon$  far away from  $\bar{X}$ . Such a large fluctuation is displayed in Fig.(1.2.6). A large fluctuation is always a rare event in the system because  $X_\epsilon$  has to overcome the repelling force of the averaged dynamics through an exceptional fluctuation. The rare events have to be taken into account in the dynamical description of  $X_\epsilon$ , in the infinite time limit. There is in general no complete expression for the probability distribution of the small and large fluctuations of  $X_\epsilon$ . As will be shown in this section, large deviation theory gives an exponential equivalent for the probability distribution of any path  $X_\epsilon(t)$ .

Consider again the slow-fast process (1.2.1-1.2.2). The joint process  $(X_\epsilon(t), y(t))$  can be a dynamical system, or any other kind of Markov process. The variable  $X_\epsilon(t)$  is not a Markov process because it keeps memory of its trajectory through coupling with the variable  $y$ . The averaging theorems presented in section 1.3 show that in the limit of very large timescale separation between the two processes and with the hypothesis of ergodicity of the fast process, the slow process  $X_\epsilon(t)$  can be described *alone* by a Markov process. This means that for any  $t' > t$ , the conditional probability  $\mathbb{P}_\epsilon(X(t')|X(t), y(t))$  does no longer depend on  $y(t)$

$$\mathbb{P}_\epsilon(X(t')|X(t), y(t)) \xrightarrow{\epsilon \rightarrow 0} \mathbb{P}_0(X(t')|X(t)). \quad (1.4.1)$$

The convergence (1.4.1) is satisfied even if the fast process is ergodic but not mixing.

To describe the time evolution of the process  $X_\epsilon(t)$  in the small  $\epsilon$  limit, we introduce  $\mathbb{P}_\epsilon\left(\frac{\Delta X}{\Delta T}|X\right)$ , the conditional probability to observe a increment  $\Delta X$  during a time  $\Delta T$  starting from  $X$ . In the limit  $\epsilon \rightarrow 0$ , property (1.4.1) states that this probability does not depend on  $y$ .

The averaging principle (1.3.2) and the stochastic averaging theorems of sections 1.3.2 and 1.3.3 can be seen as asymptotic expansions of the probability  $\mathbb{P}_\epsilon\left(\frac{\Delta X}{\Delta T}|X\right)$ . The averaging theorem states that

$$\mathbb{P}_\epsilon\left(\frac{\Delta X}{\Delta T}|X\right) \xrightarrow{\epsilon \rightarrow 0} \delta\left(\frac{\Delta X}{\Delta T} - \bar{b}(X)\right).$$

Thus, the averaging theorem gives the limit in law of the probability  $\mathbb{P}_\epsilon\left(\frac{\Delta X}{\Delta T}|X\right)$ . Stochastic averaging gives an equivalent of  $\mathbb{P}_\epsilon\left(\frac{\Delta X}{\Delta T}|X\right)$  when  $\epsilon$  goes to zero. The averaging theorem (1.3.14) states that *if  $X$  is close to  $\bar{X}$  and  $\Delta X$  is close to zero*, then the equivalent in (1.4.1) is Gaussian and

$$\mathbb{P}_\epsilon\left(\frac{\Delta X}{\Delta T}|X\right) \underset{\epsilon \rightarrow 0}{\sim} \frac{1}{\sqrt{2\pi\epsilon\sigma^2(\bar{X})\Delta T}} e^{-\frac{(\Delta X - (\Delta X))}{2\epsilon\sigma^2(\bar{X})\Delta T}}. \quad (1.4.2)$$

In the present section, we will show that we can give the exponential equivalent of  $\mathbb{P}_\epsilon\left(\frac{\Delta X}{\Delta T}|X\right)$  for every value of  $X$ , using large deviation theory. We will see that the distribution  $\mathbb{P}_\epsilon\left(\frac{\Delta X}{\Delta T}|X\right)$  has the asymptotic general form

$$\mathbb{P}_\epsilon\left(\frac{\Delta X}{\Delta T}|X\right) \underset{\epsilon \rightarrow 0}{\sim} C_\epsilon(X) e^{-\frac{1}{\epsilon}\mathcal{L}\left(\frac{\Delta X}{\Delta T}, X\right)\Delta T},$$

where  $C_\epsilon(X)$  is the normalization constant. The equivalent (1.4.2) corresponds to a quadratic approximation of the function  $\mathcal{L}$  close to  $\bar{X}$ . In general,  $\mathcal{L}$  is not a quadratic function and only the exact expression of  $\mathcal{L}$  gives the correct asymptotic expression for  $\mathbb{P}_\epsilon$ .

### 1.4.1 Large deviation principle for a probability distribution

In this section, we give the precise definition of the large deviation principle.

A probability distribution  $\mathbb{P}_\epsilon(z)$  with  $z \in \mathbb{R}^N$ , depending on a small parameter  $\epsilon$ , satisfies a large deviation principle when there exists a function  $I(z)$  such that

$$-\epsilon \ln \mathbb{P}_\epsilon(z) \xrightarrow{\epsilon \rightarrow 0} I(z). \quad (1.4.3)$$

The function  $I$  is called the large deviation rate function. The notation

$$\mathbb{P}_\epsilon(z) \underset{\epsilon \rightarrow 0}{\asymp} e^{-\frac{1}{\epsilon} I(z)}$$

equivalently means that  $\mathbb{P}_\epsilon$  satisfies the large deviation principle (1.4.3). The consequence of the large deviation principle is that there exists a function  $C_\epsilon(z)$  such that  $\mathbb{P}_\epsilon(z) = C_\epsilon(z) e^{-\frac{1}{\epsilon} I(z)}$  where the function  $C_\epsilon(z)$  has subexponential growth with  $\epsilon$ .  $C_\epsilon(z)$  will be called the prefactor of the large deviation principle (1.4.3).

We now assume that  $C_\epsilon$  is continuous and that the rate function  $I$  is twice differentiable and has one single maximum at  $z^*$ .  $\mathbb{P}_\epsilon(z)$  is a probability distribution and thus satisfies the normalization condition  $\int \mathbb{P}_\epsilon(z) dz = 1$ . When  $\epsilon$  goes to zero, the Laplace principle gives the following asymptotic equivalent for  $\int \mathbb{P}_\epsilon(z) dz$

$$\int \mathbb{P}_\epsilon(z) dz \underset{\epsilon \rightarrow 0}{\sim} C_\epsilon(z^*) \frac{(2\pi\epsilon)^{N/2}}{\sqrt{|\det I''(z^*)|}} e^{-\frac{1}{\epsilon} I(z^*)}, \quad (1.4.4)$$

where  $z^*$  is the maximum of the rate function  $I$ , and  $I''(z^*)$  is the Hessian matrix of  $I$  at  $z^*$ . The normalization condition for  $\mathbb{P}_\epsilon$  with the asymptotic equivalent (1.4.4) shows that

1.  $I(z^*) = 0$  and  $I \geq 0$ ,
2.  $C_\epsilon(z^*) \underset{\epsilon \rightarrow 0}{\sim} \frac{\sqrt{|\det I''(z^*)|}}{(2\pi\epsilon)^{N/2}}$ .

The first property is generic of every rate function  $I$ . The second property gives the expression of the prefactor to leading order in  $\epsilon$  when  $I$  is twice differentiable.

### 1.4.2 Large deviations for sample paths

The aim of large deviation theory is to predict the probability distribution  $\mathbb{P}_\epsilon(X, t)$  of the slow variable  $X_\epsilon(t)$  at any time  $t$ . We will see in the present section that large deviation theory gives much more information than the distribution  $\mathbb{P}_\epsilon(X, t)$ . Large deviation theory does not only predict the probability distribution, but it also predict the probability of any *path*  $[X(t)]_{t \in [0, T]}$ . In the following,  $\mathbb{P}_\epsilon(X, t)$  will denote the probability of a single state  $X$ , whereas  $\mathbb{P}_\epsilon[X(t)]$  will denote the probability of a path.

For a fixed value of  $X$ , consider the increment of the slow variable during a small interval of time  $\Delta T$

$$\Delta X := \int_0^{\Delta T} b\left(X, y\left(\frac{t}{\epsilon}\right)\right) dt. \quad (1.4.5)$$

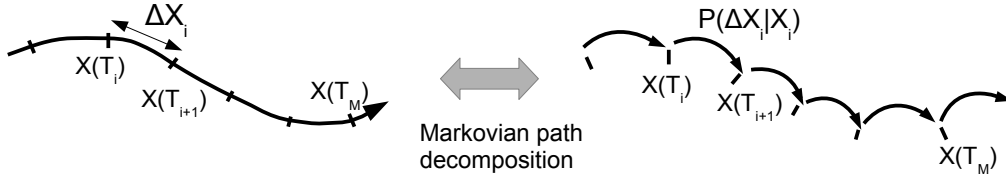


Figure 1.4.1: Decomposition of the path  $X(t)$  into a discrete Markov chain.

In the definition (1.4.5), the fast process  $y(t)$  follows the differential equation

$$\dot{y}(t) = f(X, y(t))$$

with the same fixed value  $X$  of the slow variable. (1.4.5) can be equivalently written

$$\frac{\Delta X}{\Delta T} := \frac{\epsilon}{\Delta T} \int_0^{\Delta T/\epsilon} b(X, y(t)) dt.$$

This shows that the asymptotic probability of  $\frac{\Delta X}{\Delta T}$  when  $\epsilon \rightarrow 0$  is given by the asymptotic behavior for large times of the time average

$$\frac{1}{T} \int_0^T b(X, y(t)) dt.$$

Because of the ergodic hypothesis, the above integral does not depend on  $y(0)$  for large values of  $T$ . We now do the stronger assumption that this integral satisfies a large deviation principle as  $T \rightarrow \infty$ . Equivalently, we assume that for every value of  $X$ , the increment (1.4.5) satisfies the large deviation principle

$$\mathbb{P}_\epsilon \left( \frac{\Delta X}{\Delta T} | X \right) \underset{\epsilon \rightarrow 0}{\asymp} e^{-\frac{1}{\epsilon} \mathcal{L} \left( \frac{\Delta X}{\Delta T}, X \right) \Delta T}. \quad (1.4.6)$$

Consider now a full path  $[X(t)]_{t \in [0, T]}$ . The path can be divided a large number  $M$  of small intervals  $\Delta T_i := [T_i, T_{i+1}]$ . For each of those intervals, we note  $X_i$  the value of  $X$  at time  $T_i$  and  $\Delta X_i$  the increment between  $T_i$  and  $T_{i+1}$ . The decomposition of the path is illustrated on Fig.(1.4.1).

From the Markov chain rule, we can write the probability of the path as

$$\mathbb{P}_\epsilon [X(t)] = \prod_{i=1}^M \mathbb{P}_\epsilon \left( \frac{\Delta X_i}{\Delta T_i} | X_i \right). \quad (1.4.7)$$

In the limit  $\epsilon \rightarrow 0$ , the large deviation property (1.4.6) implies that the whole path probability satisfies the large deviation principle

$$\mathbb{P}_\epsilon [X(t)] \underset{\epsilon \rightarrow 0}{\asymp} e^{-\frac{1}{\epsilon} \sum_{i=1}^M \mathcal{L} \left( \frac{\Delta X_i}{\Delta T_i}, X_i \right) \Delta T_i}. \quad (1.4.8)$$

In the limit of vanishing  $\Delta T_i$ , the sum  $\sum_{i=1}^M \mathcal{L} \left( \frac{\Delta X_i}{\Delta T_i}, X_i \right) \Delta T_i$  becomes an integral over time, and the large deviation principle (1.4.8) becomes

$$\mathbb{P}_\epsilon [X(t)] \underset{\epsilon \rightarrow 0}{\asymp} e^{-\frac{1}{\epsilon} \int_0^T \mathcal{L}(\dot{X}(t), X(t)) dt}. \quad (1.4.9)$$

The large deviation rate function for a path is thus a functional of the path that we call *action* by analogy with the classical action of analytical mechanics. Using this analogy,  $\mathcal{L}$  is called the *Lagrangian*. The action is defined as

$$\mathcal{A}[X(t)] := \int_0^T \mathcal{L}(\dot{X}(t), X(t)) dt. \quad (1.4.10)$$

The large deviation principle for paths relies on the property that the limit  $\epsilon \rightarrow 0$  and  $\Delta T \rightarrow 0$  in the Markov chain rule (1.4.7) do commute, at least at the exponential level. In the case of fully coupled slow-fast dynamical systems, the proof of a large deviation principle has only been recently proven in [44, 99].

The Lagrangian  $\mathcal{L}$  is a large deviation rate function, and thus it has to satisfy the generic properties of those functions. This means that  $\mathcal{L} \geq 0$  and that the minimum of  $\mathcal{L}$  over  $\dot{X}$  is zero. The averaging principle of section 1.3.1 shows that

$$\mathcal{L}(\dot{X}(t), X(t)) = 0 \iff \dot{X}(t) = \bar{b}(X(t)). \quad (1.4.11)$$

The action (1.4.10) is a positive functional that only vanishes over the trajectories of the averaged dynamics.

### 1.4.3 Instantons for large deviations from the averaged dynamics

In this section, we will explain the origin of the large deviations from the averaged dynamics that we already observed in section 1.2.3. The large deviation principle for sample paths obtained in (1.4.9) has many important consequences for the phenomenology of the slow variable's stochastic trajectories.

Consider fixed initial and final values  $X_s, X_f$  and the ensemble of all paths  $[X(t)]$  starting at  $X(0) = X_s$  and ending at  $X(T) = X_f$ . The large deviation principle (1.4.9) shows that the probability distribution of the paths  $\mathbb{P}_\epsilon[X(t)]$  is maximal on the particular path  $\tilde{X}(t)$  where the action is maximal. In the limit  $\epsilon \rightarrow 0$ , the probability distribution  $\mathbb{P}_\epsilon[X(t)]$  has a very small extension around the path  $\tilde{X}(t)$ . Qualitatively, all the paths joining  $X_s$  and  $X_f$  observed in the system are very close to the path  $\tilde{X}(t)$ . The typical deviations from  $\tilde{X}(t)$  are only of order  $\sqrt{\epsilon}$ . The situation is illustrated in Fig.(1.4.2). The most probable path  $\tilde{X}(t)$  joining  $X_s$  and  $X_f$  is called an *instanton*.

Suppose now that you want to compute the transition probability  $\mathbb{P}_\epsilon(X_f, T|X_s, 0)$  to reach  $X_f$  at time  $T$  starting from  $X_s$ . The transition probability is the sum of the probabilities of all possible paths, and can thus be expressed as the path integral

$$\mathbb{P}_\epsilon(X_f, T|X_s, 0) = \int \mathcal{D}[X(t)] \mathbb{P}_\epsilon[X(t)], \quad (1.4.12)$$

where  $\mathcal{D}[X(t)]$  is the measure over the space of absolutely continuous paths from  $X_s$  to  $X_f$ . The large deviation principle (1.4.9) shows that the probability of transition (1.4.12) also satisfies a large deviation principle

$$\mathbb{P}_\epsilon(X_f, T|X_s, 0) \underset{\epsilon \rightarrow 0}{\asymp} \int \mathcal{D}[X(t)] e^{-\frac{1}{\epsilon} \mathcal{A}[X(t)]}. \quad (1.4.13)$$

Using the Laplace principle in the path integral (1.4.13), we finally give the large deviation principle for the transition probability in its most useful form

$$\mathbb{P}_\epsilon(X_f, T|X_s, 0) \underset{\epsilon \rightarrow 0}{\asymp} e^{-\frac{1}{\epsilon} S(X_f, T)}, \quad (1.4.14)$$

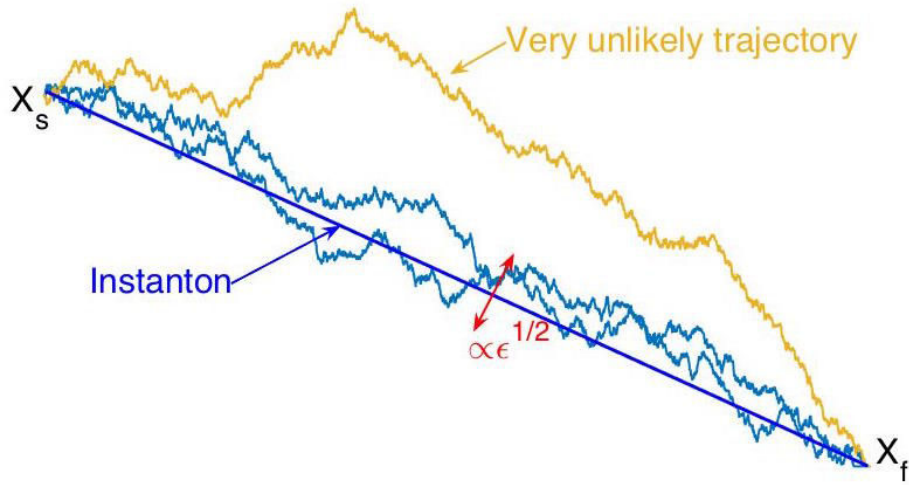


Figure 1.4.2: The instanton path  $\tilde{X}$  together with typical paths joining  $X_s$  to  $X_f$ . The yellow trajectory deviates much from the instanton and has thus a such small probability that it will never be observed (on the picture, the dynamics has been biased to obtain the yellow trajectory).

with the function  $\mathcal{S}$  given by

$$\mathcal{S}(X_f, T) := \mathcal{A}[\tilde{X}(t)]. \tag{1.4.15}$$

The function  $\mathcal{S}$  is thus the minimum of the action functional, and the minimum is reached on the instanton path.

In the following paragraph, we briefly describe the case where the averaged dynamical field  $\bar{b}$  is nonzero. To keep the discussion as simple as possible, we assume that the dynamics has one single stable critical point  $X_0$ . In the following,  $X_0$  will be called the attractor of the system.

When the system has reached a statistically stationary state, it spends most of the time around the attractor  $X_0$  with small fluctuations of order  $\sqrt{\epsilon}$  around  $X_0$ . However, the example of section 1.2.3 has shown the possibility to have fluctuations of order one away from the attractor  $X_0$ , with very small probability. We now explain that both the probability of those events, and the path chosen by the dynamical system to realize them, can be predicted with large deviation theory.

The stationary probability (or invariant measure) to find the system in the state  $X_f$  can be seen as the limit of infinite time of the transition probability  $\mathbb{P}_\epsilon(X_f, T|X_0, 0)$ . We call  $\mathbb{P}_\epsilon^\infty(X_f)$  the stationary measure. It can be expected in the present context in which the dynamics  $\bar{b}$  has a single attractor, that the limits  $T \rightarrow \infty$  and  $\epsilon \rightarrow 0$  commute at the level of large deviations. This property is no longer true for dynamics with many attractors [17]. We thus consider the path integral (1.4.13), where the integration is done over paths starting at  $X_0$  at  $T \rightarrow -\infty$  and ending at  $X_f$  at  $T = 0$ . The large deviation principle for the invariant measure writes

$$\mathbb{P}_\epsilon^\infty(X_f) \underset{\epsilon \rightarrow 0}{\asymp} e^{-\frac{1}{\epsilon}V(X_f)},$$

where  $V$  is called the *quasipotential* of the sytem

$$V(X_f) := \mathcal{A}[\tilde{X}(t)],$$

where the instanton path  $\tilde{X}(t)$  now satisfies  $\tilde{X}(0) = X_f$  and  $\tilde{X}(t) \xrightarrow[t \rightarrow -\infty]{} X_0$ . The instanton starting at the attractor is called a *fluctuation path*.

The fluctuation path is defined as the path of minimal action, in the limit where the transition occurs for an infinite time. However, we have seen in section 1.2.3 that the transition effectively happens in short time, that is, in a typical time of same order as the typical time of the average dynamics  $\bar{b}$ . To do a large fluctuation, the system has to move for a long distance oppositely to the dynamics  $\bar{b}$ . It is thus much more advantageous from the point of view of probabilities, to do this fluctuation quite fast, to minimize the time spent far away from the attractor. A typical fluctuation path reaching  $X_f$  at  $t = 0$ , performs most of its displacement in a small interval of time of order one, and generically relaxes exponentially to  $X_0$  when  $t$  goes to  $-\infty$ .

We have seen in the present section that the phenomenology of large fluctuations of the slow variable can be explained by a large deviation principle for the probability distribution of the paths  $X(t)$ . The transition probability  $\mathbb{P}(X_f, T | X_s, 0)$  and the most probable path of the system can be determined by minimizing an action functional (1.4.10). The problem thus reduces to the computation of the Lagrangian of the action, and then minimize the action to find the instanton. It is beyond the scope of this thesis to describe all the techniques and theorems used to compute the action. The complete theory of large deviations for slow-fast dynamical systems can be found for example in [26].

#### 1.4.4 Instantons for diffusive processes

This section is devoted to large deviations in the case  $\bar{b} = 0$ . We already explained in section 1.3.3 that the case  $\bar{b} = 0$  is very different from the case  $\bar{b} \neq 0$ , because we have to consider the slow variable on the timescale  $\frac{1}{\epsilon}$  as described by the system of equations (1.3.34-1.3.35). With  $\bar{b} = 0$ , we have seen that the slow process follows a stochastic differential equation (1.3.36) in the limit  $\epsilon \rightarrow 0$ . Equation (1.3.36) is an exact asymptotic equivalent of the slow process on a timescale of order  $\frac{1}{\epsilon}$ , not an approximation. Because the drift term is of same order as the stochastic term, the system is not confined in the vicinity of the attractors. Therefore, each state can be visited by the slow variable with a probability of order one. The probability  $\mathbb{P}_\epsilon(X_f, T | X_s, 0)$  to observe a transition from  $X_s$  to  $X_f$  has thus no reason to be small. We show in this section that the phenomenology of instantons can be recovered for fast transitions from  $X_s$  to  $X_f$ .

For simplicity, we consider the case where the diffusion coefficient  $\sigma$  in equation (1.3.36) does not depend on  $X$ . The argument we give below can be generalized to space dependent diffusion coefficients with the Hamiltonian formalism that we do not describe in this thesis.

From equation (1.3.36), the probability of any path  $X(t)$  joining  $X_s$  to  $X_f$ , in the limit  $\epsilon \rightarrow 0$ , is given by

$$\mathbb{P}_0[X(t)] \propto e^{-\frac{1}{2\sigma^2} \int_0^T \|\dot{X} - \gamma(X)\|^2 dt}. \quad (1.4.16)$$

Let  $L$  be the distance between  $X_s$  and  $X_f$ . With the change of variable  $t = Ts$  and  $X(t) := LX'(s)$  in the time integral (1.4.16), we get

$$\mathbb{P}_0[X(t)] \propto e^{-\frac{L^2}{2\sigma^2 T} \int_0^1 \|\dot{X}' - \frac{T}{L} \gamma(X')\|^2 ds}. \quad (1.4.17)$$

Two different time scales appear in the integral (1.4.17). The drift term  $\gamma(X')$  is homogeneous to a velocity, and gives thus a important contribution over a typical time  $\frac{L}{|\gamma|}$ , where  $|\gamma|$  is a typical value for  $\gamma(X')$ . The noise gives a contribution over the typical diffusion time  $\frac{L^2}{\sigma^2}$ . We

consider the probability to do a transition from  $X_s$  to  $X_f$  in a time small compared to both the diffusion time  $\frac{L^2}{\sigma^2}$  and the drift time  $\frac{L}{|\gamma|}$ . The drift term  $\frac{T}{L}\gamma(X')$  can thus be neglected in (1.4.17) and the nondimensional parameter  $\frac{L^2}{\sigma^2 T}$  appearing in front of the integral is small. The expression of the transition probability (1.4.17) in the limit  $T \rightarrow 0$  satisfies the large deviation principle

$$\mathbb{P}_0[X(t)] \underset{T \rightarrow 0}{\asymp} e^{-\frac{L^2}{2\sigma^2 T} \int_0^1 \|\dot{X}'\|^2 ds}. \quad (1.4.18)$$

The instanton can be defined as the path with minimal value of the action  $\int_0^1 \|\dot{X}'\|^2 ds$ , which is simply the straight trajectory

$$\tilde{X}(t) = \left(1 - \frac{t}{T}\right) X_s + \frac{t}{T} X_f. \quad (1.4.19)$$

The large deviation principle (1.4.18) should be considered cautiously. The white noise limit for the slow process (1.3.36) is only valid for  $\frac{1}{\epsilon} \gg 1$ . We have explained that the white noise limit is a consequence of the central limit theorem for continuous set of variables. The implicit assumption of this result is that  $T \gg \tau_m$ , where  $\tau_m$  is the mixing time (or Lyapunov time for chaotic processes) of the fast dynamics  $\dot{y} = f(X, y)$ . The large deviation principle (1.4.18) is thus valid in the limit of small times provided the considered timescale still satisfies  $\frac{L^2}{\sigma^2} \gg T \gg \tau_m$ . For times of same order as  $\tau_m$ , we expect the large deviation principle (1.4.18) to be valid with a modified expression of the action. In particular, instantons are not necessarily straight lines when  $\frac{T}{\tau_m}$  is of order one.

## 1.5 Example: the overdamped Langevin equation

The Langevin equation is a very classical model describing the random dynamics of a large particle in a bath of smaller particles. The bath at temperature  $T$  exerts a random force on the large particle. Because of the timescale separation between the dynamics of the large particle and the dynamics of the bath particles, the random force can be represented with an excellent approximation by a Gaussian white noise. The Langevin equation writes

$$\begin{aligned} \dot{x} &= v \\ m\dot{v} &= -\nabla V(x) - m\gamma v + \sqrt{2m\gamma k_B T} \xi(t) \end{aligned} \quad (1.5.1)$$

where  $v$  is the velocity of the particle,  $V(x)$  is an external potential,  $k_B$  is the Boltzmann constant and  $\gamma$  is the friction coefficient. The noise amplitude is related to the friction coefficient through Einstein's fluctuation-dissipation relation. When the external force  $-\nabla V(x)$  is zero, the Langevin equation is one of the very few examples of stochastic differential equations that can be solved explicitly.

For most practical cases, the inertia of the particle can be neglected because the particle's velocity evolves on a time  $\tau_v := \frac{1}{\gamma}$  much smaller than the typical time of diffusion over a distance  $L$ ,  $\tau_L := \sqrt{\frac{mL^2}{k_B T}}$ . The limit  $\frac{1}{\gamma} \ll \sqrt{\frac{mL^2}{k_B T}}$  is called the *overdamped limit*, and corresponds to the situation where the velocity relaxes very fast compared to the time of diffusion in space. In this limit,  $x$  is a slow variable in the problem, and its dynamics can be described by a closed stochastic differential equation

$$\dot{x} = -\frac{1}{m\gamma} \nabla V(x) + \sqrt{2D} \xi(t) \quad (1.5.2)$$

Equation (1.5.2) is the overdamped Langevin equation. It can be obtained simply by neglecting the inertial term in the equation (1.5.1) for the velocity.  $D := \frac{k_B T}{m\gamma}$  is the diffusion coefficient.

The overdamped Langevin equation is now used in many areas of physics, not only to describe classical Brownian motion, but also more complex systems in bacteria motility or polymer dynamics. For some of these systems, the diffusion coefficient in (1.5.2) depends on space. In that case, the friction  $\gamma$  depends also on space because of fluctuation-dissipation relations. For space dependent diffusion coefficients, the noise term  $\sqrt{2D(x)}\xi(t)$  is not well defined, because the stochastic product can be interpreted with different conventions.

This problem has been already solved quite long ago using the techniques of adiabatic eliminations of fast variables [88]. To obtain the overdamped Langevin equation with a space-dependent friction coefficient, one has to start from the Langevin equation (1.5.1) in which the noise can be understood without ambiguity, and take properly the limit  $\frac{1}{\gamma(x)} \rightarrow 0$ . Using Itô convention for stochastic equations, we get

$$\dot{x} = -\frac{1}{m\gamma(x)}\nabla V(x) + \nabla D(x) + \sqrt{2D(x)}\xi(t) \quad (1.5.3)$$

The fact that the diffusion coefficient depends on space adds a drift term  $\nabla D(x)$  in the equation. Physically, this term can be interpreted as an entropic force that pushes the particle in regions of high diffusion coefficient. The particle goes in regions where it can move faster. In the following, we will explicitly derive equation (1.5.3) using the techniques of stochastic averaging presented in section 1.3.

**Explicit derivation of the overdamped limit of the Langevin equation** We start from the Langevin equation (1.5.1) with a space dependent friction  $\gamma(x)$  and we consider the limit of fast relaxation of the velocity  $\frac{1}{\gamma(x)} \rightarrow 0$ . The small parameter in the problem is the ratio between the slow time scale  $\tau_x$  and the fast time scale  $\tau_v$ . The equation for the fast process can be written as

$$\dot{v} = -\frac{1}{m}\nabla V(x) - \gamma(x)v + \sqrt{2\gamma(x)\frac{k_B T}{m}}\xi(t) \quad (1.5.4)$$

The averaging principle presented in section 1.3.1 states that the slow process  $x(t)$  converges to the process  $\bar{x}(t)$  satisfying the equation

$$\dot{\bar{x}}(t) = \langle v \rangle_{\bar{x}}(t),$$

where  $\langle v \rangle_{\bar{x}}$  is the average of the velocity for a fixed value of the position  $x = \bar{x}$ . Taking the stochastic average of equation (1.5.4) we get

$$\langle \dot{v} \rangle = -\frac{1}{m\gamma(x)}\nabla V(x) - \langle v \rangle,$$

because the noise  $\xi(t)$  averages to zero. This shows that the stationary mean velocity is

$$\langle v \rangle = \frac{1}{m\gamma(x)}\nabla V(x),$$

and thus  $\langle v \rangle \xrightarrow[\gamma(x) \rightarrow +\infty]{} 0$ .

The averaging principle states that the diffusion process  $x(t)$  is constant on the time scale  $\tau_L := \sqrt{\frac{mL^2}{k_B T}}$ . The average of the velocity comes to order  $\frac{1}{\gamma}$  in the equation for the slow variable. This means that the contribution of the stochastic terms comes to the same order as the average

$\langle v \rangle$  in the equation for  $x$ . To find the limit of the slow process  $x(t)$ , we thus have to go beyond the averaging principle and perform a stochastic averaging of the fast process. The Langevin equation falls in the framework of slow-fast dynamical systems with  $\bar{b} \equiv 0$  described in section 1.3.3. The theorem states that the slow process  $x(t)$  converges in law to a stochastic process given by the Itô stochastic differential equation

$$\dot{x} = a(x) + \sqrt{2D(x)}\xi(t),$$

where  $a(x)$  is the drift, and the diffusion coefficient  $D(x)$  is given by the Green-Kubo formula (1.3.37)

$$D(x) = \int_0^{+\infty} \langle v(t)v(0) \rangle_x dt. \quad (1.5.5)$$

Let  $C_x(t) := \langle v(t)v(0) \rangle_x$  be the correlation function of the fast process with fixed value of  $x$ . Multiplying equation (1.5.4) by  $v(0)$  and taking the stochastic average, we find that  $C$  satisfies the equation

$$\dot{C}_x(t) = -\gamma(x)C_x(t).$$

And thus

$$\begin{aligned} C_x(t) &= \langle v^2 \rangle e^{-\gamma(x)t}, \\ &= \frac{k_B T}{m} e^{-\gamma(x)t}. \end{aligned}$$

The expression of the diffusion coefficient (1.5.5) is

$$D(x) = \frac{k_B T}{m\gamma(x)}.$$

The explicit expression for the drift  $a$  can be computed using equation (1.3.42) with  $b(x, v) := v$ ,  $\rho_s(v) = \sqrt{\frac{m}{2\pi k_B T}} e^{-\frac{1}{2} \frac{mv^2}{k_B T}}$ , and equation (1.5.4). This computation requires some work but presents no major difficulty.

However, we want to emphasize that the drift term  $\nabla D$  in the overdamped Langevin equation comes from the correlation between the fast and the slow process. This can be seen from equation (1.5.4). The average of equation (1.5.4) gives

$$\langle \dot{v}(t) \rangle = -\frac{1}{m} \langle \nabla V(x(t)) \rangle - \langle \gamma(x(t))v(t) \rangle. \quad (1.5.6)$$

Using the previous equation, we can expand  $x(t)$  around its average as  $x(t) = \langle x(t) \rangle + \int_0^t \tilde{v}(s) ds$ , where  $\tilde{v}(s) := v(s) - \langle v \rangle$ . To leading order in  $x - \langle x \rangle$ , equation (1.5.6) writes

$$\langle \dot{v}(t) \rangle = -\frac{1}{m} \nabla V(\langle x \rangle) - \gamma(\langle x \rangle) \langle v \rangle(t) - \gamma'(\langle x \rangle) \int_0^t \langle \tilde{v}(s)\tilde{v}(t) \rangle ds.$$

Finally, with the approximation  $\int_{-\infty}^0 \langle \tilde{v}(s)\tilde{v}(0) \rangle ds = \frac{k_B T}{m\gamma(\langle x \rangle)}$ , we find that the stationary average of the velocity writes

$$\langle v \rangle = -\frac{1}{m\gamma(\langle x \rangle)} \nabla V(\langle x \rangle) - \frac{k_B T}{m} \frac{\gamma'(\langle x \rangle)}{\gamma^2(\langle x \rangle)}.$$

The argument above has no pretension to be rigorous. We give it to show how the correlations between the slow and the fast variable give a contribution to the drift in the stochastic equation for the slow variable. We believe this physical interpretation is not obvious from the multiscale expansion in the Fokker-Planck equation.

In slow-fast processes where  $\bar{b} \neq 0$ , the correction to the drift coming from correlations is negligible because the correction comes at order  $\epsilon$  whereas the fluctuations  $X_\epsilon - \bar{X}$  around the average trajectory are of order  $\sqrt{\epsilon}$ .

## Chapter 2

# Stationary state of barotropic zonal jets in the inertial limit

### 2.1 Introduction

An interesting property of two dimensional turbulent flows is their inverse energy cascade from small scales to large scales. This inverse energy cascade is responsible for the self organization of the flow into large scale coherent structures that evolve much slower than the small scale velocity fluctuations called “eddies”. Among those structures, giant vortices and zonal jets have raised strong interest in the scientific community. Both structures are observed in the atmosphere of gaseous planets [37, 31, 30], and in particular on Jupiter (see Fig.(2.1.1)). The atmosphere of Jupiter is a three-dimensional flow, it can be thus surprising to invoke the properties of two-dimensional turbulence to explain the large scale structures of the flow. The probe *Juno* that has been orbiting around Jupiter since 2016 gives us a large amount of data to understand the interior structure of Jupiter. In particular, precise measurements of the gravitational field indicates that the zonal jets observed at the surface of Jupiter extend deep inside the planet, up to thousands of kilometers [40]. The fact that the winds at Jupiter’s surface can be well understood within the the framework of two-dimensional geostrophic turbulence is then not due to the confinement of winds in a thin layer at the top of the atmosphere (as was first proposed by [35]). It would rather be explained by the very fast rotation of the planet that creates a Coriolis force depending on the latitude. This effect - called the  $\beta$  effect - led the physicist Friedrich Busse to introduce in 1976 a deep layer model for the atmosphere of Jupiter, but leads qualitatively to the same conclusions as the thin layer model, because the  $\beta$  effect forces the flow to be mainly barotropic (without vertical component). As the ratio between vertical and horizontal velocities is very small for the top atmosphere of Jupiter, the atmosphere dynamics is qualitatively well understood within the framework of two-dimensional geostrophic turbulence in a  $\beta$  plane that we use in the present work [80]. More refined models are however needed if one wants to understand the quantitative features of Jupiter’s zonal jets [68, 89].

Before the *Juno* probe, the data collected by the probes *Gallileo* and *Cassini* during their close encounter with Jupiter allow us to have a high resolution of the dynamics of the upper layers of Jupiter’s atmosphere, and measure the magnitude of zonal jets velocity. The observations from *Voyager* and *Cassini* are displayed in Fig.(2.1.1). Not only do we have access to the velocity of zonal winds that form the large red and grey bands at the surface, but we also have a lot of images of the smaller vortices imbedded in the flow. Those vortices are related with vertical motion in the atmosphere. The wind fluctuations are continuously injecting energy in the zonal

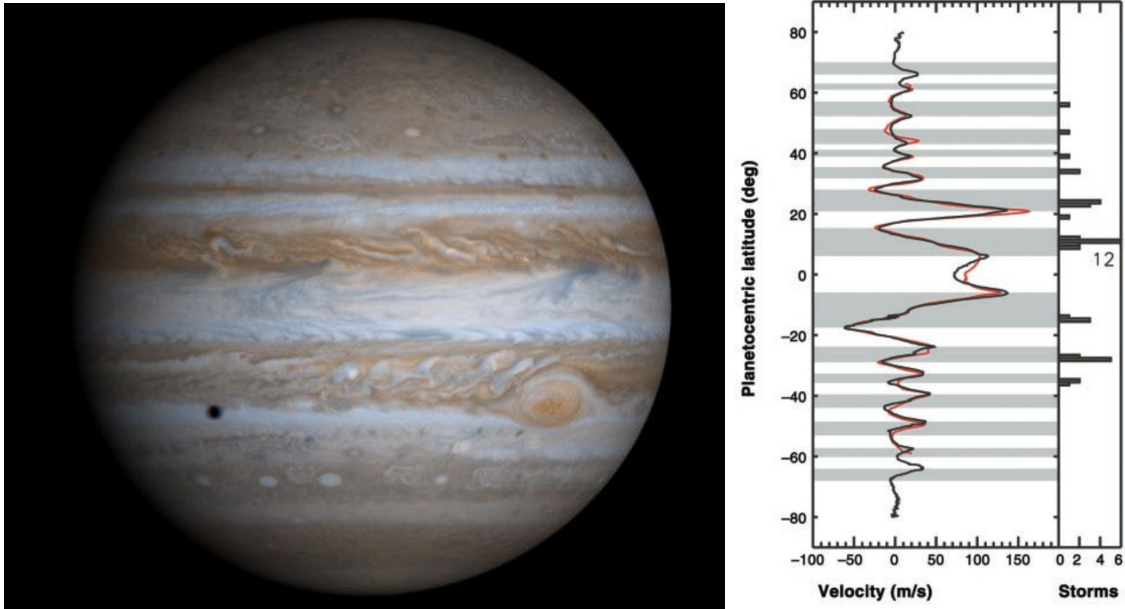


Figure 2.1.1: Left: A picture of Jupiter showing the zonal winds and the great red spot. Right: Measurements of the zonal velocity component (jets) at the surface of Jupiter by the probes Voyager 2 (1979) and Cassini (2000). The measurements show that zonal jets are very stable structures that evolve on a much longer timescale than the small-scale eddies at the surface.

component [38, 87], and equilibrate the dissipation mechanisms. Thanks to the astronomical observations, we can estimate the magnitude of the parameters used in nonequilibrium models. It comes out that, provided we use the model of barotropic flow in a  $\beta$  plane for Jupiter, the relevant regime should be a limit of small scale forcing and weak energy injection.

In the limit where energy is injected at small scale, with weak energy injection and dissipation rate (inertial and small scale forcing limit), we will see in section 2.2.2 that there is a timescale separation between the dynamics of the zonal component of the velocity, the jets, and the dynamics of eddies. The two-dimensional geostrophic flow in a  $\beta$  plane has the structure of a slow-fast dynamical system, where the zonal velocity component  $U$  plays the role of the slow variable, and the eddies play the role of fast variables. The aim of the present work is to apply the averaging principle to obtain a close equation for the dynamics of zonal jets. The main result shows that explicit analytical expressions can be found for the velocity profile  $U$  in the inertial and small scale forcing limit. Our result predicts the existence of jets as stable attractors for the averaged dynamics of  $U$ .

## 2.2 The quasilinear barotropic model in the beta plane

### 2.2.1 Equations of the model

We start from the equations for a barotropic flow on a periodic beta plane with stochastic forces

$$\begin{aligned}\partial_t V + V \cdot \nabla V &= -rV - \frac{1}{\rho} \nabla P + \beta y \begin{pmatrix} V_y \\ -V_x \end{pmatrix} + \sqrt{2\varepsilon} f \\ \nabla V &= 0\end{aligned}\tag{2.2.1}$$

where  $V := \begin{pmatrix} V_x \\ V_y \end{pmatrix}$  is the two dimensional velocity field. In real geophysical flows, energy is injected at small scale by multiple and complex phenomena among which are the baroclinic and convective instabilities. In the model (2.2.1), the small scale energy injection is created by the stochastic term  $\sqrt{2\varepsilon}f$ .  $f$  is a stochastic force, that we assume white in time, i.e  $\mathbb{E}[f(r, t)f(r, t')] = \delta(t - t')C_f(r, r')$ . We choose a normalization for the force correlation function  $C_f$ , such that  $\varepsilon$  is the rate of energy injection in the flow per unit of mass:  $\varepsilon$  has dimensions  $m^2 s^{-3}$ . In the following, we will always assume that there is no direct energy injection in the zonal velocity profile, i.e that  $\frac{1}{L_x} \int dx f(r, t) = 0$ . We call  $L_f$  the typical scale at which energy is injected. We thus implicitly assume that the Fourier spectrum of  $C_f$  is mainly concentrated at the wavevector  $\frac{2\pi}{L_f}$ . Energy is dissipated at large scale by the linear friction  $-rV$  that models the Eckman drag [9]. We recall here that  $\beta$  is the derivative of the Coriolis parameter which comes from the fact that the Coriolis force projected on a plane tangent to the sphere depends on the north-south coordinate  $y$ .

The main idea is then to separate the flow  $V$  in two parts,  $V(r, t) = U(y, t)e_x + \begin{pmatrix} u(r, t) \\ v(r, t) \end{pmatrix}$ .

The mean velocity  $Ue_x = \langle V \rangle$  is defined as the zonal average of the velocity field. More precisely, we assume that the mean flow is parallel and we take  $U(y)e_x = \frac{1}{L_x} \int dx V(x, y)$ . The bracket  $\langle \rangle$  refers to the zonal average.

In this paper, we will refer to  $U$  indifferently as the *mean flow* or *zonal flow*. The fluctuating part  $(u, v)$  of the velocity field is often called the “eddies”. Let us emphasize here that our aim is not to determine how the mean velocity profile becomes a parallel shear flow, but we assume that the mean flow has this shape and we want then to study the dynamics of the zonal component. It is an empirical evidence that this is indeed the case for many regimes of the barotropic flow equation, especially when  $\beta$  is strong enough. Those regimes are of interest for geophysical applications as illustrated by Jupiter or Saturn [13]. We note also that the mean flow is not always zonal, especially for small or vanishing values of  $\beta$  [14].

Using this decomposition and the continuity equation, the equation for the mean velocity  $U$  becomes

$$\partial_t U + \partial_y \langle uv \rangle = -rU.\tag{2.2.2}$$

Equation (2.2.2) shows that the mean flow is forced by the divergence of the Reynolds stress  $\partial_y \langle uv \rangle$ . The Reynolds stress is defined as the zonal average of the product of the velocity components  $u$  and  $v$ . As will be shown below, the dynamics of  $u, v$  are described by stochastic differential equations, and evolve on a much smaller timescale than the timescale of evolution of  $U$ . Equation (2.2.2) is that of a slow variable coupled to a set of fast variables and falls thus perfectly in the framework of fully coupled slow-fast dynamical systems described in section 1.2.1. The aim of the present work reduces to describing the *averaged* dynamics of zonal jets, not the fluctuations nor the large deviations from the average. For that purpose, we only need to apply the averaging principle on the slow dynamics of  $U$ . We will study the dynamics of the

stochastic average of the zonal flow  $\bar{U} := \mathbb{E}[U]$ , defined by the equation

$$\partial_t \bar{U} + \partial_y \mathbb{E}[\langle uv \rangle] = -r\bar{U}. \quad (2.2.3)$$

The averaged dynamics of zonal flows is thus completely determined by the zonal and stochastic average of the Reynolds stress  $\mathbb{E}[\langle uv \rangle]$ . In general, it is not possible to obtain explicit expressions for the Reynolds stress without strong approximations, except in very particular configurations [92]. The aim of the present work is to compute explicitly the average of the Reynolds stress in some asymptotic limits of the parameters. In the following of this chapter, we will abusively use the bracket  $\langle \rangle$  for both the zonal and stochastic average, and  $U$  will refer to the averaged zonal flow  $\bar{U}$ . In section 2.5, we will come back to equation (2.2.2) and show, as a perspective of the work, how it is possible to go beyond the averaging principle and describe the fluctuations of the zonal flow  $U$ .

## 2.2.2 Nondimensional equations

The first step to do mathematical treatment of equations (2.2.1) is to chose length and time scales to write nondimensional equations. There is no classical way of rescaling in the literature. We chose here to set temporal and spatial units such that the mean kinetic energy  $\frac{\varepsilon}{r} = 1$ , and  $\beta = 1$  (please see [12] for more details, or [13] page 2-3 for comparison with other common nondimensionalization of the equations). Of course, the length  $L$  of the domain could have been used as the reference length scale. In that case,  $\beta$  gives approximately the number of jets in the domain. For giant gaseous planets as Jupiter for example, the number of jets can be quite large, and then, with  $L = 1$ ,  $\beta$  is a large parameter in the problem. The use of  $\beta$  as a reference of units is equivalent to chose the width of a single jet as the reference of lengths. To say it heuristically, we consider the flow “at the scale of a jet”. The choice to set the mean kinetic energy to 1 implies that the mean square of the zonal velocity, defined by the relation  $\frac{1}{2}U_{rms}^2 := \frac{1}{2}\langle U^2 \rangle$ , satisfies  $\frac{1}{2}U_{rms}^2 \equiv \frac{\varepsilon}{r} \equiv 1$ .

Finally, we eliminate the pressure term by taking the rotational of the first equation of (2.2.1). The nondimensional equations are

$$\begin{aligned} \partial_t \Omega + V \cdot \nabla \Omega &= -\alpha \Omega - V_y + \sqrt{2\alpha} \eta \\ \nabla V &= 0, \end{aligned} \quad (2.2.4)$$

where  $\eta = \nabla \wedge f$ . There are now two nondimensional parameters in the problem.  $\alpha := r \sqrt{\frac{\sqrt{2}}{U_{rms} \beta}}$  is a nondimensional parameter although we will often refer to it as the “friction”. The second nondimensional parameter is the typical wavevector  $K := \frac{2\pi}{L_f} \sqrt{\frac{\sqrt{2}\beta}{U_{rms}}}$  of the stochastic forcing. It defines the ratio between the scale at which energy is injected and the scale of the jets. A third nondimensional parameter that does not appear explicitly is the reduced length  $L \sqrt{\frac{U_{rms}}{\sqrt{2}\beta}}$  of the domain. This last parameter will play no role in our computations because it only sets the boundary conditions of the problem. In particular, it controls the number of jets in the domain. We assume in the present work that the domain is much larger than the width of a jet such that the boundary conditions play a minor role.

The Gaussian stochastic term  $\eta$  is defined through its correlation function  $\langle \eta(r, t) \eta(r', t') \rangle = C(r - r') \delta(t - t')$ . We assume that  $C$  is statistically homogeneous such that it depends only on the difference  $r - r'$ . As a correlation function,  $C$  is a definite positive function and has to satisfy the following properties: let us call  $\hat{C}_{k,l}$  the Fourier coefficients of  $C$

$$C(x, y) := \sum_{k,l} \hat{C}_{k,l} e^{ikx + ily} \quad (2.2.5)$$

and  $\mathbf{k}^2 := k^2 + l^2$ , then the function  $\hat{C}_{k,l}$  is real and positive. All along this chapter,  $k$  will be the  $x$  component of the wavevector and  $l$  will be its  $y$  component. Moreover, if we assume the symmetry  $x \rightarrow -x$  and  $y \rightarrow -y$ , the function  $\hat{C}_{k,l}$  is symmetric wrt  $k \rightarrow -k$  and  $l \rightarrow -l$ . The constrain that the mean kinetic energy is one writes  $\frac{1}{2} \iint dk dl \frac{\hat{C}_{k,l}}{K^2} = 1$ . From now on, the computations will be done with nondimensional quantities. If we want to write a result in its dimensional formulation, we will reintroduce the dimensions of  $[\frac{\varepsilon}{r}] = m^2 \cdot s^{-2}$  and  $[\beta] = m^{-1} s^{-1}$ .

In the following we are precisely interested in the small  $\alpha$  regime. In the asymptotic limit  $\alpha \rightarrow 0$ , the nonlinear terms in the equation for the velocity fluctuations can be neglected. This approximation is called the *quasilinear approximation*. We will not develop the full justification of the quasilinear approximation here, the interested reader is referred to [12]. Let us simply recall the steps leading to the equations with quasilinear approximation. First, we notice that the strength of the noise in equation (2.2.4) is of order  $\sqrt{\alpha}$ . As fluctuations are sheared and transferred to the largest scales on a timescale of order one, this is a natural hypothesis to expect fluctuations  $(u, v)$  to be of the same order of magnitude. This was proven to be self-consistent in [12]. We do the substitution  $(u, v) \rightarrow \sqrt{2\alpha}(u, v)$  in equation (2.2.4). The eddy-eddy interaction terms (that is, the nonlinear terms in  $u, v$ ) are of order  $\alpha^{\frac{3}{2}}$ , and can then be neglected. We are left with the set of equations

$$\partial_t U = -\alpha [\partial_y \langle uv \rangle + U] \quad (2.2.6)$$

$$\partial_t \omega + U \partial_x \omega + (\beta - U''')v = -\alpha \omega + \eta \quad (2.2.7)$$

where we have introduced  $\omega = \partial_x v - \partial_y u = \Delta \psi$ , the vorticity of the fluctuations.

Equation (2.2.6) shows that the typical timescale for the the mean flow evolution is  $\frac{1}{\alpha}$ . In the limit  $\alpha \rightarrow 0$ , we thus have a clear timescale separation between the dynamics of the velocity fluctuations (also called the dynamics of eddies), and the dynamics of the zonal flow. Using the timescale separation, we consider that  $U$  is a constant field in the second equation (2.2.7), and we solve  $\omega(t)$  for a given velocity profile  $U$ . The equation for eddies dynamics becomes linear because  $U$  is considered as a given field. Such a timescale separation is observed for example on Jupiter where the typical time of eddies evolution ranges from few days to few weeks whereas significant changes in the mean flow are only detected over decades. (see e.g [81]).

## 2.3 Reynolds stress from the pseudo-momentum balance

### 2.3.1 The pseudo-momentum balance

The quasilinear equations conserve energy and enstrophy as the full Navier-Stokes equations do. One of the key relation we will use in this paper comes from the enstrophy balance for the eddies,

$$\frac{1}{2} \partial_t \langle \omega^2 \rangle + (U''' - \beta) \langle v\omega \rangle = -\alpha \langle \omega^2 \rangle + \frac{1}{2} C(0).$$

We recall that the bracket  $\langle \rangle$  refers both to the zonal and stochastic average. As we assume a timescale separation between the zonal flow and fluctuation dynamics, we are interested in the long-term behavior of the latter equation. When the vorticity fluctuations  $\omega$  reach its stationary distribution, we have the equality

$$\langle v\omega \rangle = \frac{1}{U''' - \beta} \left[ \alpha \langle \omega^2 \rangle - \frac{1}{2} C(0) \right]. \quad (2.3.1)$$

Equation (2.3.1) will be a key formula for our work. Indeed, using the incompressibility condition, we have the equality  $\langle v\omega \rangle = -\partial_y \langle uv \rangle$ . One can notice looking at (2.3.1) that in the

absence of dissipation and forcing, we have  $\langle v\omega \rangle = 0$ . In steady state without dissipation and forcing, waves have no effects on the mean flow. This result is classically known in the literature as the non acceleration theorem (see [34] p 537 or [2] for a more complete description). It is then natural to expect that any forcing on the mean flow should come from the nonconservative processes which are here only a linear friction and an enstrophy injection at small scales (we could have added in the equations a viscous term that would have given an additional term in the enstrophy balance). Without the nonconservative processes, the left-hand side of equation (2.2.7) conserves the pseudomomentum  $\int \frac{\langle \omega^2 \rangle}{U'' - \beta}$ . If  $U'' - \beta$  has constant sign in the flow, the conservation of the pseudomomentum does not allow any instability to occur and the flow is stable. This is called the Rayleigh-Kuo criterion for shear flows stability. If  $U'' - \beta$  somewhere vanishes in the flow, an instability may or may not exist. The fact that  $U'' - \beta$  vanishes is a necessary condition for instability, not a sufficient one. In equation (2.3.1), the right-hand side is not defined where  $U'' = \beta$ . The denominator is zero but the numerator also vanishes. Indeed, for  $U'' = \beta$ , equation (2.2.7) reduces to free transport of the fluctuations and can be solved directly giving the relation  $\alpha \langle \omega^2 \rangle - \frac{1}{2}C(0) = 0$ . In general, the Reynolds stress divergence remains finite except perhaps at some particular places in the flow. This will be discussed in section 2.5.

Equation (2.3.1) gives us a way to compute the Reynolds stress that forces the mean flow:

- We solve the linear equation (2.2.7) and compute the average  $\langle \omega^2 \rangle$  as a function of  $U$ .
- Then we can use this expression to close the first equation (2.2.6), and discuss possible stationary profile  $U$ .

Of course things will not be that easy because the dynamics of  $\omega$  is given by a partial differential equation, and there are no reasons why we could find any simple expression of  $\langle \omega^2 \rangle$  in general. First we can take advantage of the invariance along the  $x$  direction by taking the Fourier transform of (2.2.7) in  $x$ . The Fourier transform in  $y$  does not provide an obvious simplification because the profile  $U$  depends on  $y$ . However, we can use the linearity of equation (2.2.7) to express the solution as the sum of particular solutions for independent stochastic forcing fields  $\eta_l(y, t)$ . Each of these fields has a correlation function  $c_l(y) = e^{ily}$ , this means that their correlation function is  $\mathbb{E}[\eta_l(y, t)\eta_l(y', t)] = e^{il(y-y')}\delta(t-t')$ . We take the Fourier transform in  $x$  defined by  $\omega_k(y) := \frac{1}{L_x} \int dx \omega(x, y) e^{-ikx}$  with  $k$  taking the values  $\frac{2\pi}{L_x}n$ ,  $n$  is an integer.  $\omega_{k,l}(y, t)$  is then defined as the function  $\omega_k(y, t)$  that is solution of (2.2.7) with a stochastic forcing field with only one Fourier component  $(k, l)$ . We then obtain

$$\langle v\omega \rangle = \frac{1}{U'' - \beta} \sum_{k,l} \frac{\hat{C}_{k,l}}{2} [2\alpha \langle |\omega_{k,l}|^2 \rangle - 1], \quad (2.3.2)$$

where the positive constants  $\hat{C}_{k,l}$  are defined by (2.2.5). Be careful that the bracket  $\langle |\omega_{k,l}|^2 \rangle$  in formula (2.3.2) denotes a stochastic averaging, because the zonal average is already taken into account by the sum over all vectors  $k$ . The vorticity  $\omega_{k,l}(y, t)$  is the solution of the stochastic partial differential equation

$$\partial_t \omega_{k,l} + ikU\omega_{k,l} + ik(\beta - U'')\psi_{k,l} = -\alpha\omega_{k,l} + \eta_l. \quad (2.3.3)$$

As the reader would have notice, we try to reduce the problem by expressing the solution as the sum of particular problem that we hope to be much simpler. Now we have to find an expression for  $\omega_{k,l}$  instead of the full solution  $\omega$ . We will go one step further and show that the

stochastic problem described by the two equations (2.3.2-2.3.3) reduces in fact to a *deterministic one*, following [12]. Equation (2.3.3) can be formally written as

$$\partial_t \omega_{k,l} + L_k[\omega_{k,l}] = -\alpha \omega_{k,l} + \eta_l,$$

where

$$L_k[\omega_{k,l}] = ikU\omega_{k,l} + ik(\beta - U^n)\psi_{k,l} \quad (2.3.4)$$

is a linear operator for a given mean velocity field  $U$ . Then we use the fact that the noise  $\eta_{k,l}$  is white in time and has an exponential correlation function  $c_l(y) = e^{ily}$  to express the quantity  $\langle |\omega_{k,l}|^2 \rangle$  as

$$\langle |\omega_{k,l}|^2 \rangle = \int_{-\infty}^0 dt e^{2\alpha t} |e^{tL_k}[c_l]|^2. \quad (2.3.5)$$

This formula should be understood as follows:  $e^{tL_k}[c_l]$  is the solution at time  $t$  of the *deterministic equation*  $\partial_t \omega_d + L_k[\omega_d] = 0$  with initial condition  $c_l := y \rightarrow e^{ily}$ . The subscript  $d$  will mean that we are dealing with the solution of a deterministic equation. The exponential  $e^{\alpha t}$  ensures the convergence of this integral. The great advantage to have reduced the stochastic problem to a deterministic one is that we now have to solve an hydrodynamic problem, the propagation of a vorticity fluctuation in a shear flow, a problem for which much has already been done in the literature.

### 2.3.2 Simplification in the inertial limit

Expression (2.3.5) is still complicated because it requires to know the behavior of the solution  $e^{tL_k}[c_l]$  up to times of order  $\frac{1}{\alpha}$ . Two parameters can be used to further simplify the problem, the vector  $\mathbf{k} = (k, l)$  and the damping  $\alpha$ . In the present work, we are considering the asymptotic limit  $\alpha \rightarrow 0$  that ensures a timescale separation between the zonal flow dynamics, and the eddies dynamics. The limit  $\alpha \rightarrow 0$  is called the inertial limit because the fluctuating field is free to evolve without damping. It corresponds to fully turbulent regimes. A rough estimation the parameters  $\alpha$  on Jupiter (assuming of course that our model could be valid to describe the behavior of Jupiter's jets) shows that  $\alpha \approx 10^{-3}$  and corresponds thus to the limit  $\alpha \rightarrow 0$ .

We have to compute (2.3.2-2.3.5)

$$2\alpha \langle |\omega_{k,l}|^2 \rangle = 2\alpha \int_{-\infty}^0 dt e^{2\alpha t} |e^{tL_k}[c_l]|^2, \quad (2.3.6)$$

where  $e^{tL_k}[c_l] := \omega_d$  is the solution of the deterministic equation

$$\begin{aligned} \partial_t \omega_d + ikU\omega_d + ik(\beta - U^n)\psi_d &= 0 \\ (\partial_y^2 - k^2)\psi_d &= \omega_d \end{aligned} \quad (2.3.7)$$

with initial condition  $c_l(y) = e^{ily}$ . We will first assume there are no neutral nor unstable modes solutions of (2.3.7). First, we do the change of time scale  $\alpha t \rightarrow t$  in the integral of (2.3.6). It gives us

$$2\alpha \langle |\omega|^2 \rangle = 2 \int_{-\infty}^0 dt e^{2t} \left| e^{\frac{t}{\alpha} L_k}[c_l] \right|^2. \quad (2.3.8)$$

When  $\alpha$  goes to zero, the term  $e^{\frac{t}{\alpha} L_k}[c_l]$  is the long time limit of the solution of (2.3.7). We use the nontrivial result of [11] that there exists a function  $\omega_d^\infty(y)$  such that  $\omega_d(y, t) \underset{t \rightarrow \infty}{\sim} \omega_d^\infty(y) e^{-ikUt}$  when there are no neutral nor unstable modes. Hence  $\left| e^{\frac{t}{\alpha} L_k}[c_l] \right| \rightarrow |\omega_d^\infty(y)|$ , and the presence

of the exponential  $e^{2t}$  in the integral of (2.3.8) ensures the convergence of the whole integrand. This proves that without neutral modes

$$2\alpha \langle |\omega|^2 \rangle \xrightarrow{\alpha \rightarrow 0} |\omega_d^\infty|^2.$$

Let us add again the subscripts  $k, l$  for  $\omega_{k,l}^\infty$  to recall that the asymptotic vorticity function depends on the Fourier mode. The correlation  $\langle v\omega \rangle$  writes in the limit  $\alpha \rightarrow 0$

$$\langle v\omega \rangle = \frac{1}{U'' - \beta} \sum_{k,l} \frac{\hat{C}_{k,l}}{2} [|\omega_{k,l}^\infty|^2 - 1]. \quad (2.3.9)$$

An interesting remark can be made from the above computations: when  $\alpha$  becomes small, the enstrophy term  $\langle \omega^2 \rangle$  diverges as  $\frac{1}{\alpha}$ , but as the Reynolds stress divergence expression (2.3.2) involves  $\alpha \langle \omega^2 \rangle$ , it converges. Such a compensation can be seen as necessary in order to fulfill the pseudomomentum balance.

In this subsection, we will summarize the main result obtained by Bouchet and Morita [11] that allows us to compute the function  $\omega_{k,l}^\infty$  involved in the Reynolds stress divergence (2.3.9).  $\omega_{k,l}^\infty$  gives then an easy access to the small  $\alpha$  limit.

We start from equation (2.3.7) that describe the linear evolution of a perturbation  $\omega(y, t)e^{ikx}$  of meridional wave number  $k$ , and streamfunction  $\psi(y, t)e^{ikx}$ . The idea is to transform equation (2.3.7) into an inhomogeneous Rayleigh equation, as classically done, and then to study its asymptotics solutions close to the real axis, which is the limit  $\epsilon \rightarrow 0$ , with the notations below. We introduce the function  $\varphi_\epsilon(y, c)$  which is the Laplace transform of the stream function  $\psi(y, t)$  i.e  $\varphi_\epsilon(c) := \int_0^\infty dt \psi(y, t) e^{-ik(c+i\epsilon)t}$ . To avoid any confusion, we stress that  $\epsilon$  will always denote in this section a small parameter and not the energy injection rate. Using the same notations as in [11], the equation for  $\varphi_\epsilon$  is

$$\left( \frac{d^2}{dy^2} - k^2 \right) \varphi_\epsilon(y, c) + \frac{\beta - U''(y)}{U(y) - c - i\epsilon} \varphi_\epsilon(y, c) = \frac{\omega(y, 0)}{ik(U(y) - c - i\epsilon)}, \quad (2.3.10)$$

with the boundary conditions that  $\varphi_\epsilon$  vanishes at infinity. We do not have an infinite flow in the  $y$  direction, but as already stated, we consider the properties of the flow at the scale of one jet, and assume that there is a large number of jets in the domain. The choice to take vanishing boundary conditions at infinity is done for convenience and it is expected that this particular choice does not modify the physical behavior of the perturbation.

For all  $\epsilon > 0$  the function  $\varphi_\epsilon$  is well defined. The inhomogeneous Rayleigh equation (2.3.10) is singular for  $\epsilon = 0$  at any critical point (or critical layer)  $y_c$  such that the zonal flow velocity is equal to the phase speed:  $U(y_c) = c$ . One can show that  $\varphi_\epsilon$  has a limit denoted  $\varphi_+$  when  $\epsilon$  goes to zero. The function  $\omega^\infty$  is then given by

$$\omega^\infty(y) = ik(U''(y) - \beta)\varphi_+(y, U(y)) + \omega(y, 0), \quad (2.3.11)$$

see [11]. The function  $\omega^\infty$  depends on the Laplace transform of the stream function but for a phase velocity  $c$  equal to the zonal velocity at latitude  $y$ . From a mathematical point of view, it corresponds to the value of  $\varphi_+$  exactly at its singularity. The singularity in equation (2.3.10) is of degree one (proportional to  $\frac{1}{y}$ ) except at the extrema  $y_c$  of the jets where  $U'(y_c) = 0$  and where the singularity is of degree two. A singularity of order two would create a divergence for the solution, but it happens that the numerator in (2.3.10) vanishes at such points and the solution is still defined at the extrema of a jet. A nontrivial consequence of that is

$$\omega^\infty(y_c) = 0$$

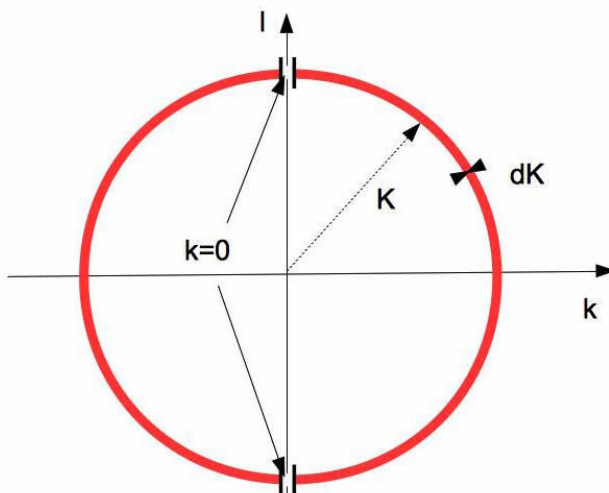


Figure 2.3.1: Fourier spectrum of the stochastic forcing field.

at all critical latitudes  $y_c$  where  $U' = 0$ . This result, called depletion of vorticity fluctuations at the jet critical points in [11], has important physical consequences that influence the dynamics of a jet.

As described in [11], using formula (2.3.10) and (2.3.11), one can numerically compute the function  $\omega^\infty$ : we first have to solve a set of boundary value problems for ordinary differential equations parameterized by  $c$  and  $\epsilon$  to obtain a family of solutions  $\varphi_\epsilon(c)$ . Then we evaluate, for small enough  $\epsilon$  each solution  $\varphi_\epsilon(c)$  at the value  $y_c$  satisfying  $U(y_c) = c$ . This method is much faster and has less numerical cost than computing the long time evolution of the partial differential equation (2.3.7).

Expressions (2.3.9) and (2.3.11) give the theoretical expression of the Reynolds stress divergence  $\langle v\omega \rangle$  in the inertial limit. However, the result still depends on the function  $\varphi_+$  defined in (2.3.11), for which we do not have any explicit expression. So far, we did not study the influence of the second nondimensional parameter in the problem, the wavevector  $K$ , that gives the characteristic scale at which energy is injected in the flow. In the present work, we will assume a spectrum in the form of an annulus of radius  $K$ . Fig.(2.3.1) displays the spectrum of the stochastic forcing field in Fourier space. Note that the value  $k = 0$  is excluded because we assume that no energy is directly injected in the zonal flow  $U$ .

An order of magnitude of the nondimensional wavevector  $K$  is given by the ratio between the width of a jet and the scale at which energy is injected in the barotropic flow. In the atmosphere of Jupiter, the scale of energy injection is approximately given by the size of the storms at the surface. Fig.(2.3.2) displays a picture of such a storm together with a picture of the equatorial jet of Jupiter. The storms have a typical spatial extension of 1000 Km, whereas the width of the main jets is about 20000 Km. The nondimensional parameter  $K$  is thus larger than 10. This is the motivation to consider the asymptotic regime  $K \gg 1$  called the *small scale forcing regime*. We show in the next section that an explicit expression can be found for the Reynolds stress divergence in the limit  $K \rightarrow +\infty$ , and we give a close equation satisfied by the mean flow  $U$ .

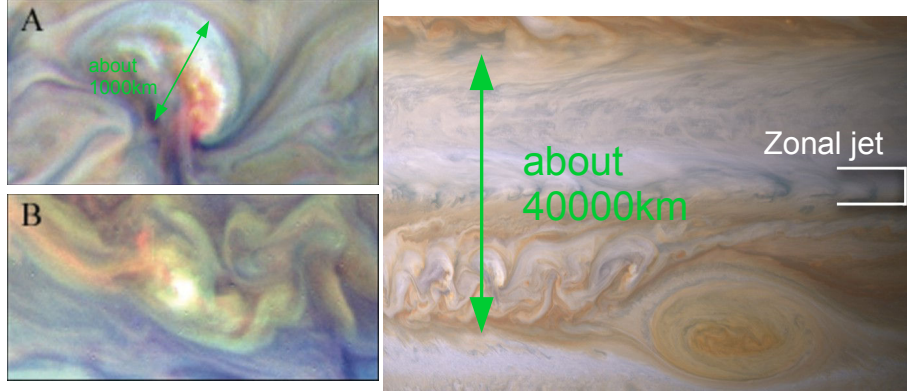


Figure 2.3.2: Pictures of a typical storm at the surface of Jupiter (left), and of the equatorial zonal jet of Jupiter (right). The storms have a spatial extension much smaller than the width of jets.

### 2.3.3 Close equation for the mean flow in the small scale forcing limit

We now consider the limit of small scale forcing  $K \rightarrow \infty$ . The calculations are rather technical and can be skipped in the first lecture.

We start from equation (2.3.10) that describes the inertial behavior of a deterministic evolution of a perturbation  $\omega(y, 0)$  when  $\epsilon$  vanishes. Using the Green function  $H_k(y)$  of  $(\partial_y^2 - k^2)$  we write

$$\varphi_\epsilon(y, c) = (U''(y) - \beta) \int dy' H_k(y') \frac{\varphi_\epsilon(y - y', c)}{U(y - y') - c - i\epsilon} + \int dy' H_k(y') \frac{\omega(y - y', 0)}{ik(U(y - y') - c - i\epsilon)}.$$

Now we make the change of variable  $Y = ky'$ . The Green function has the scaling  $H_k(y') := -\frac{1}{2k} H_0(Y)$ . Recalling that  $\varphi_+(y, c) = \lim_{\epsilon \downarrow 0} \varphi_\epsilon(y, c)$ , it follows

$$\varphi_+(y, c) = -\frac{(U''(y) - \beta)}{2k^2} \lim_{\epsilon \rightarrow 0} \int dY H_0(Y) \frac{\varphi_\epsilon(y - \frac{Y}{k}, c)}{U(y - \frac{Y}{k}) - c - i\epsilon} - \frac{1}{2ik^3} \lim_{\epsilon \rightarrow 0} \int dY H_0(Y) \frac{\omega(y - \frac{Y}{k}, 0)}{U(y - \frac{Y}{k}) - c - i\epsilon}. \quad (2.3.12)$$

We are implicitly making the assumption that  $\frac{1}{k} := \tan \theta$  is finite and thus  $K \rightarrow \infty$  implies  $k \rightarrow \infty$ . Let us recall here that it is crucial to take the limit  $\epsilon \rightarrow 0$  first before  $K \rightarrow \infty$  because  $\epsilon$  plays exactly the role of the linear friction  $\alpha$ . As we are in the inertial regime, we have to take a vanishing friction first. In [11], it is shown that the function  $\varphi_\epsilon$  has a finite limit  $\varphi_+$ .

Consider now the magnitude of both terms in the right-hand side of (2.3.12). The first term depends on  $\varphi_+$  and the other depends on the initial condition  $\omega(y, 0)$ . The initial condition is of order 1, and the second term will thus be of order  $\frac{1}{k^3}$ . As a consequence, the first term in the asymptotic expansion of  $\varphi_+$  will be of order  $\frac{1}{k^3}$ . The first term in the right-hand side of (2.3.12) gives the order  $\frac{1}{k^5}$  of the asymptotic expansion and is thus negligible. We write

$$\varphi_+(y, c) \underset{K \rightarrow \infty}{\sim} -\frac{1}{2ik^3} \lim_{\epsilon \rightarrow 0} \int dY H_0(Y) \frac{\omega(y - \frac{Y}{k}, 0)}{U(y - \frac{Y}{k}) - c - i\epsilon}. \quad (2.3.13)$$

Combining equations (2.3.11) and (2.3.13) we find that

$$|\omega^\infty(y)|^2 \underset{K \rightarrow \infty}{\sim} |\omega(y, 0)|^2 - \frac{U'' - \beta}{k^2} \mathcal{R}e \left\{ \lim_{\epsilon \rightarrow 0} \int dY H_0(Y) \frac{\omega^*(y, 0) \omega(y - \frac{Y}{k}, 0)}{U(y - \frac{Y}{k}) - U(y) - i\epsilon} \right\}.$$

The final step is to replace  $\omega(y, 0) = e^{iy}$ , and  $H_0(Y) = e^{-|Y|}$ . We use also the Sokhotski–Plemelj formula:  $\lim_{\epsilon \rightarrow 0} \frac{1}{x - i\epsilon} = i\pi\delta(x) + \mathcal{P}\left(\frac{1}{x}\right)$ , to obtain

$$\begin{aligned} |\omega^\infty(y)|^2 &\underset{K \rightarrow \infty}{\sim} |\omega(y, 0)|^2 - \frac{U'' - \beta}{k^2} \mathcal{R}e \left\{ \lim_{\epsilon \rightarrow 0} \int dY e^{-|Y|} \frac{e^{-iY \tan \theta}}{U(y - \frac{Y}{k}) - U(y) - i\epsilon} \right\} \\ &\underset{K \rightarrow \infty}{\sim} |\omega(y, 0)|^2 - \frac{U'' - \beta}{k^2} \mathcal{R}e \left\{ i\pi \int dY e^{-|Y|} e^{-iY \tan \theta} \delta \left( U \left( y - \frac{Y}{k} \right) - U(y) \right) \right\} \\ &\quad - \frac{U'' - \beta}{k^2} \mathcal{R}e \left\{ \mathcal{P} \left\{ \int dY e^{-|Y|} \frac{e^{-iY \tan \theta}}{U(y - \frac{Y}{k}) - U(y)} \right\} \right\} \\ &\underset{K \rightarrow \infty}{\sim} |\omega(y, 0)|^2 - \frac{U'' - \beta}{k^2} \mathcal{P} \left\{ \int dY e^{-|Y|} \frac{\cos(Y \tan \theta)}{U(y - \frac{Y}{k}) - U(y)} \right\}, \end{aligned}$$

where we have used that the term  $i\pi \int dY e^{-|Y|} e^{-iY \tan \theta} \delta \left( U \left( y - \frac{Y}{k} \right) - U(y) \right)$  is purely imaginary. Injecting this result in (2.3.9) gives the contribution of one Fourier mode  $k, l$  with  $\frac{k}{l} = \tan \theta$  to the Reynolds stress divergence

$$\mathcal{R}e \langle v_\theta^* \omega_\theta \rangle \underset{K \rightarrow \infty}{\sim} - \frac{\hat{C}_{k,l}}{2k^2} \mathcal{P} \left\{ \int dY e^{-|Y|} \frac{\cos(Y \tan \theta)}{U(y - \frac{Y}{k}) - U(y)} \right\}. \quad (2.3.14)$$

We then use the limit  $k \rightarrow +\infty$  to expand the mean flow  $U(y - \frac{Y}{k})$  in the vicinity of  $y$ . This gives

$$\begin{aligned} &\mathcal{P} \left\{ \int dY e^{-|Y|} \frac{\cos(Y \tan \theta)}{U(y - \frac{Y}{k}) - U(y)} \right\} \\ &= \lim_{\eta \rightarrow 0} \int_{-\infty}^{-\eta} dY e^{-|Y|} \frac{\cos(Y \tan \theta)}{U(y - \frac{Y}{k}) - U(y)} + \int_{\eta}^{+\infty} dY e^{-|Y|} \frac{\cos(Y \tan \theta)}{U(y - \frac{Y}{k}) - U(y)} \\ &= \int_0^{+\infty} dY e^{-|Y|} \cos(Y \tan \theta) \left\{ \frac{1}{U(y - \frac{Y}{k}) - U(y)} + \frac{1}{U(y + \frac{Y}{k}) - U(y)} \right\} \\ &= \int_0^{+\infty} dY e^{-|Y|} \cos(Y \tan \theta) \left\{ \frac{U(y - \frac{Y}{k}) + U(y + \frac{Y}{k}) - 2U(y)}{(U(y - \frac{Y}{k}) - U(y))(U(y + \frac{Y}{k}) - U(y))} \right\} \\ &\xrightarrow[k \rightarrow \infty]{} \frac{U''}{U'^2} \int_0^{+\infty} dY e^{-|Y|} \cos(Y \tan \theta) = \frac{U''}{U'^2} \frac{1}{1 + \tan^2 \theta}. \end{aligned}$$

We have used that  $U(y - \frac{Y}{k}) + U(y + \frac{Y}{k}) - 2U(y) \sim U'' \frac{Y^2}{k^2}$  and  $(U(y - \frac{Y}{k}) - U(y))(U(y + \frac{Y}{k}) - U(y)) \sim -U'^2 \frac{Y^2}{k^2}$ . We get with (2.3.14)

$$\mathcal{R}e \langle v_\theta^* \omega_\theta \rangle \underset{K \rightarrow \infty}{\sim} \frac{\hat{C}_{k,l}}{2k^2} \frac{U''}{U'^2} \frac{1}{1 + \tan^2 \theta} = \frac{\hat{C}_{k,l}}{2K^2} \frac{U''}{U'^2}. \quad (2.3.15)$$

The choice to set the mean kinetic energy to 1 implies  $\frac{1}{2} \iint dk' dl' \frac{\hat{C}_{k',l'}}{K'^2} = 1$ . The integration of (2.3.15) over the whole spectrum gives the result

$$\langle v\omega \rangle \xrightarrow[\alpha \rightarrow 0, K \rightarrow +\infty]{} \frac{U''}{U'^2}. \quad (2.3.16)$$

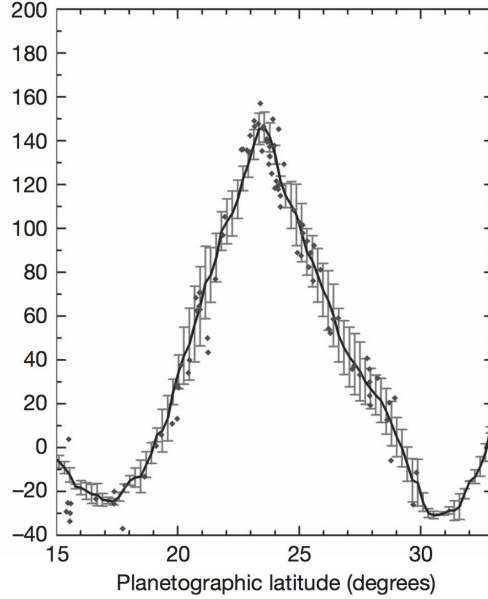


Figure 2.3.3: The 23° N zonal jet of Jupiter.

The computation of the asymptotic expansion of  $\langle v\omega \rangle$  in the limit  $K \rightarrow +\infty$  shows that the result (2.3.16) can be only valid if  $\frac{kU'}{U''} \rightarrow \infty$ . As  $U'$  vanishes at the extremum of the jet, there should exist a small region of size  $\frac{1}{K}$  in the vicinity of the extremum where this calculation breaks down. The formula can only be valid for strictly monotonic profiles or for the monotonic part between two extrema of a jet. Jets have nonmonotonic velocity profiles  $U$ . We display in Fig.(2.3.3) one of the jets of Jupiter at 23° of latitude. Fig.(2.3.3) shows the existence of a cusp at the extremum of the jet. The extremum is a place where the velocity profile has a structure at scale  $\frac{1}{K}$ . At the extremum, the asymptotic value of the Reynolds stress is no longer valid, and a refined calculation is required to find the structure of the mean flow at its extremum.

In the inertial limit, and with small scale forcing, we have shown that the Reynolds stress does not depend on the Fourier spectrum of the stochastic forcing field, provided it injects energy at small scale. It is worth to emphasize that our results are asymptotic results. The behavior may be really different for finite friction and finite  $K$ . The work done in [92] shows that the shape of the stochastic forcing matters in the general case.

## 2.4 Prediction of the stationary velocity profile

### 2.4.1 Close equation for the mean velocity profile

With the asymptotic result (2.3.16), we are now able to derive a close equation for the mean velocity profile  $U$ . Relation (2.3.16) together with  $\langle v\omega \rangle = -\frac{\partial}{\partial y} \langle uv \rangle$  gives an explicit expression for the Reynolds stress divergence in the inertial small scale forcing limit

$$\frac{\partial}{\partial y} \langle uv \rangle = -\frac{U''}{U'^2},$$

where  $U'$  and  $U''$  respectively are the first and second partial derivatives of  $U$  w.r.t. the spatial coordinate  $y$ . Writing the previous relation with dimensional variables gives

$$\frac{\partial}{\partial y} \langle uv \rangle = -\frac{\varepsilon U''}{U'^2}. \quad (2.4.1)$$

Relation (2.4.1) is the main result of this chapter. It shows that it is possible to give an explicit expression of the Reynolds stress in the considered asymptotic limit. As already mentioned in the introduction 2.1, it is very rare to be able to close exactly the equation for the mean flow  $U$ , except in very particular configurations. Using the explicit expression for the Reynolds stress divergence in equation (2.2.2) we obtain the following close equation for  $U$

$$\partial_t U - \frac{\varepsilon U''}{U'^2} = -rU. \quad (2.4.2)$$

From the latter result, we deduce that the stationary velocity profile  $U_0$  satisfies the equation

$$\frac{\varepsilon U_0''}{U_0'^2} = rU_0. \quad (2.4.3)$$

Equation (2.4.3) surprisingly has a Newtonian structure: multiplying both sides by  $U_0'$  and integrating over  $y$ , we find explicitly

$$\frac{1}{2}U_0^2 - \frac{\varepsilon}{r} \ln(|U_0'|) = C, \quad (2.4.4)$$

where  $C$  is a constant of integration.

In equation (2.4.4), the function  $x \rightarrow -\frac{\varepsilon}{r} \ln(|x|)$  plays the role of a potential. The dynamics defined by (2.4.4) is completely similar to a particle moving in a potential with equation

$$\frac{1}{2}\dot{x}^2 + V(x) = C,$$

with the potential  $V(x) := -\frac{\varepsilon}{r} \ln(|x|)$ . The only difference is that the roles of  $U$  and  $U'$  are exchanged compared to the role of  $x$  and  $\dot{x}$  for a particle in a potential. The situation is represented in Fig.(2.4.1).

Whatever the value of the constant  $C$ , the velocity profile  $U$  always diverges. The derivative  $U_0'$  cannot change sign. There are two classes of solutions: solutions with  $U_0' > 0$  and solutions with  $U_0' < 0$ . The two classes of solutions correspond to the two sides of a jet. The solution of equation (2.4.4) is represented in Fig.(2.4.2). Equation (2.4.4) predicts that zonal jets are composed by a succession of diverging velocity profiles, with successively increasing and decreasing values of the velocity. The side with increasing velocity of a jet is totally independent of the side with decreasing velocity. The velocity profiles of westward and eastward jets are symmetric, with in both cases a diverging value of the velocity at the extremum. Such a velocity profile of course is not realistic because the velocity of zonal winds have finite values.

The fact that equation (2.4.4) predicts divergent velocity profiles means that some of our hypotheses are broken at the extrema of zonal jets, and that an other mechanism of regularization takes place. In section 2.4.3, we explain which physical mechanisms prevent the divergence of the velocity. By taking those physical mechanisms into account, it is possible to get realistic jets that correspond to the observations at the surface of Jupiter. In the following, of the present section, we discuss the meaning of the result (2.4.1) in term of the energy balance.

After integration over  $y$ , equation (2.4.1) can be written as

$$U' \langle uv \rangle = \varepsilon. \quad (2.4.5)$$

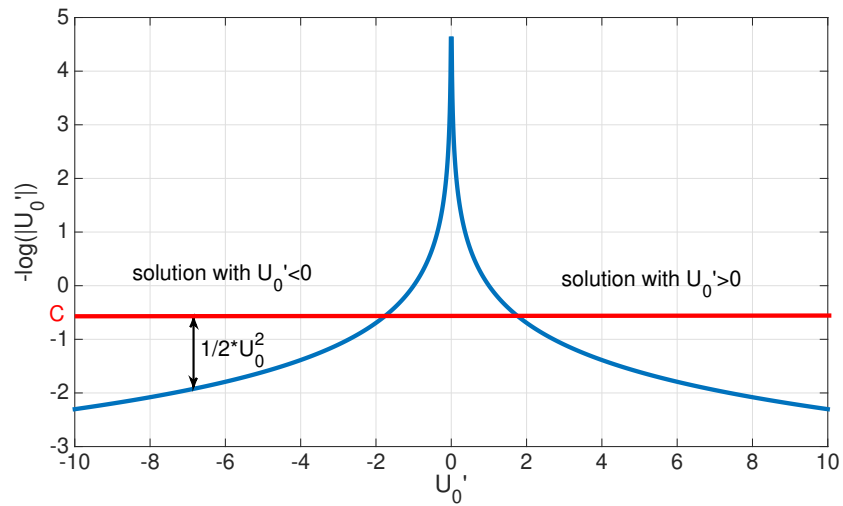


Figure 2.4.1: The stationary zonal flow satisfies a Newtonian equation similarly to a particle in a potential. Whatever the value of the integration constant  $C$ , two classes of solutions exist: one profile has an increasing velocity, the other one has a decreasing velocity.

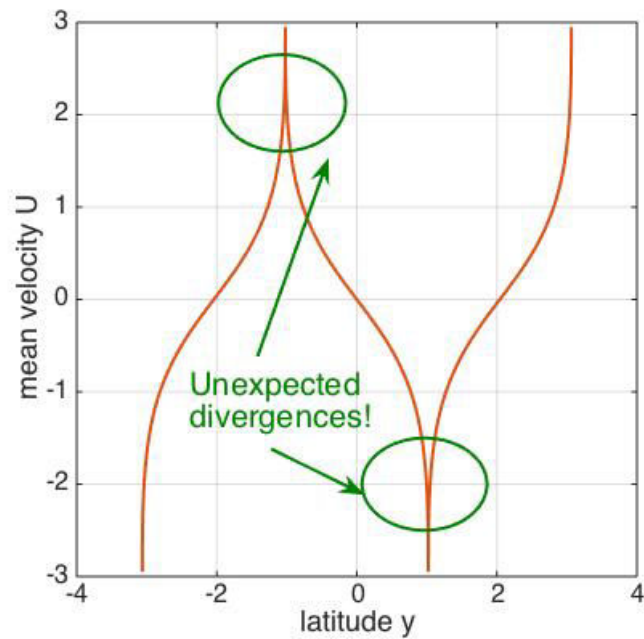


Figure 2.4.2: The stationary velocity profile of the zonal flow predicted by equation (2.4.4), in the inertial small scale forcing limit. Equation (2.4.4) predicts symmetric eastward and westward jets, with diverging values of the velocity at the extrema.

The constant of integration has no physical meaning, and can be set to zero. We now discuss equation (2.4.5):  $\varepsilon$  is the rate of energy injection in the flow. From the energy balance, the term  $U' \langle uv \rangle$  can be interpreted as the rate of energy transferred from the small-scale eddies to the mean flow. Relation (2.4.5) thus means that all energy injected at small scale is transferred *locally* to the largest scale of the flow. This can be explained by the limits  $\alpha \rightarrow 0$  and  $K \rightarrow +\infty$ . The inertial limit  $\alpha \rightarrow 0$  corresponds to a vanishing value of the friction coefficient  $r$ . In the limit of vanishing friction, the system has no time to dissipate energy at small scale. All energy is transferred to the largest scale before being dissipated. The small scale forcing limit  $K \rightarrow +\infty$  prevents energy transfers between the different parts of the flow. The velocity fluctuations at latitude  $y$  only interact with the flow in a small region of size of order  $\frac{1}{K}$  around. Thus, spatial energy transfer is impossible and energy has to be transferred to the mean flow at the same latitude  $y$ . For the velocity fluctuations, the mean flow at scale  $\frac{1}{K}$  looks like a parabolic profile with derivative  $U'(y)$  and second derivative  $U''(y)$ , that's why the asymptotic development of the Reynolds stress divergence is expressed in terms of  $U'$  and  $U''$ .

To sum up this idea, we can say that the energy transfer is local in physical space, but nonlocal in Fourier space. Energy is transferred directly from the scale  $\frac{1}{K}$  to the mean flow through direct interaction between the mean flow and the eddies, and not through an inverse energy cascade in Fourier space. Energy transfer is possible only if  $U' \neq 0$ . At the extrema of the jets, expression (2.4.5) breaks because direct energy transfer from small scale to the mean flow is impossible.

### 2.4.2 Linear stability of the velocity profile

We now turn to the question whether the stationary velocity profile  $U_0$  predicted by (2.4.4) is an attractor for the average dynamics (2.4.2). We thus study the stability of the profile displayed in Fig.(2.4.2). We will try to give a qualitative argument to explain why the profile of Fig.(2.4.2) is stable for the dynamics (2.4.2). Let  $U_0(y)$  be the stationary velocity profile predicted by equation (2.4.4). We study the linearized dynamics of (2.4.4) around  $U_0$ . Injecting  $U_0 + \delta U$  in equation (2.4.2) and keeping only the linear terms in  $\delta U$  gives

$$\delta \dot{U} = \frac{\varepsilon}{U_0'^2} \delta U'' + \frac{2\varepsilon U_0''}{U_0'^3} \delta U' - r \delta U. \quad (2.4.6)$$

Equation (2.4.6) has the general form

$$\delta \dot{U} = \varepsilon a_2(y) \delta U'' + \varepsilon a_1(y) \delta U' - r \delta U, \quad (2.4.7)$$

where  $a_1(y) := \frac{1}{U_0'^2}$ ,  $a_2(y) := \frac{2U_0''}{U_0'^3}$  are some functions depending on the stationary solution  $U_0(y)$ . The growth of the perturbation  $\delta U$  is the result of the effect of three terms: the term in  $\delta U''$  is a diffusive term, the term in  $\delta U'$  makes the solution propagate on the  $y$ -axis, and the last term is a linear damping. For the question of stability, the sign of the diffusion coefficient  $a_2$  in front of  $\delta U''$  is crucial. From the expression  $a_1(y) := \frac{1}{U_0'^2}$ , we deduce that the diffusion coefficient in equation (2.4.7) is always strictly positive, which means that the perturbation  $\delta U$  is always damped, whatever the wavevector of the perturbation.

Let us summarize what we found in this section. We studied the limit  $\alpha \rightarrow 0$  and  $K \rightarrow \infty$  for the dynamics of the velocity fluctuations. We found that the Reynolds stress divergence can be expressed in terms of the zonal flow  $U$  and its derivatives, which allows to write a *closed* PDE for the dynamics of  $U$ . We solved the stationary equation for  $U$  and found that two solutions can exist. One solution has an increasing velocity  $U_0$ , the other one has decreasing  $U_0$ . Both

solutions diverge in a finite length. Jets are given by the juxtaposition of divergent profiles. (see Fig.(2.4.2)). With a qualitative argument, we explained why the stationary profile  $U_0$  is linearly stable. For real flows, such divergences cannot occur. When  $K$  is finite, there should be a regularizing mechanism at scale  $\frac{1}{K}$  that stops the growth of the mean velocity profile and regularizes the solution  $U_0$  at scale  $\frac{1}{K}$ . “Cusps” of typical size  $\frac{1}{K}$  should be created at places where the solution  $U_0$  is diverging, as shown on the  $23^\circ$  eastward jet of Jupiter in Fig.(2.3.3). However, this is only one part of the mechanism. On Jupiter as well as in numerical simulations, cusps can be observed only for the eastward part of the flow. For the westward part, the flow is more parabolic with a curvature close to  $\beta$ . In section 2.4.3, we will explain why a cusp cannot occur for westward jets. Let us now precise that a cusp for a westward jet violates the Rayleigh-Kuo criterion for stability whereas a cusp on eastward jets does not. The mechanism for the formation of a parabolic profile is the hydrodynamic instability.

### 2.4.3 Regularization at the extrema of the jets

We have seen in section 2.4.1 that the formula (2.3.16)  $\langle v\omega \rangle = -\frac{U''}{U'^2}$  gives a divergent mean velocity profile and we discussed that this formula can only be valid in the limit  $\frac{kU'}{U''} \rightarrow \infty$ . It is thus natural to think that the asymptotic convergence (2.3.16) for the divergence of the Reynolds stress is valid between the extrema of the jet, but not around the extrema. In a region of size  $\frac{1}{K}$  around the extremum, another mechanism should take place to stop the growth of the jet. On Jupiter, the data collected by Galileo and Cassini probes shown in Fig.(2.1.1), indicate that the eastward jets have “cusps”, while westward jets seem smoother. We first discuss eastward jet cusps.

Looking more precisely at the cusp in Fig.(2.3.3), we see that its size is approximately 1 degree i.e a scale of  $\sim 1000$  km. The cusp has thus approximately the size  $\frac{1}{K}$ . The observation is consistent with the intuitive idea that the cusp should be regularized at a scale of order  $1/K$ . the question is then: can we have a cusp, i.e a zonal structure at scale  $\frac{1}{K}$ , solution of the stationary equation

$$\langle v\omega \rangle (U_0) = rU_0,$$

in the limit  $K \rightarrow \infty$  ?

The idea is to take equation (2.3.10) and study the asymptotic behavior of the solution after changing the scale  $y \leftarrow Ky$ . We do not detail the calculations. it can be shown that the rescaled zonal velocity profile  $\tilde{U}(y) = U(\frac{y}{K})$  has a finite limit when  $K$  goes to infinity. We were not able to compute analytically the asymptotic profile  $\tilde{U}$ . However, the phenomenon of depletion of vorticity at the stationary stream lines discovered in [11] gives a very simple expression for the Reynolds stress divergence just at the critical latitude  $y_c$  where  $U'(y_c) = 0$ . We get

$$\langle v\omega \rangle (y_c) = -\frac{\varepsilon K^2}{\tilde{U}_0''(y_c)}. \quad (2.4.8)$$

From equation (2.4.8), we find that the cusp should satisfy the relation (still with dimensional variables)

$$U_0(y_c) = -\frac{\varepsilon K^2}{rU_0''(y_c)}. \quad (2.4.9)$$

The relation is a general property of a stationary jet profile. It relates the strength of a jet to its curvature, and the physical parameters  $\varepsilon, r$  and  $K$ . It does not depends on the detailed shape of the spectrum of the stochastic forcing.

At a formal level, nothing in the equations considered so far seems to make any difference between the eastward part of a jet and its westward component. The parameter  $\beta$  is the only term in the set of equations (2.2.6-2.2.7) that breaks the eastward-westward symmetry, but it disappears from the asymptotic expression (2.3.16) when  $K \rightarrow +\infty$ . However, if we look at the jets observed on Jupiter displayed in Fig.(2.1.1), we see a clear asymmetry between eastward and westward jets, especially at high latitudes. Numerical simulations of the barotropic model also shows the eastward-westward asymmetry. Of course, numerical simulations always include a small scale dissipation (usually an hyperviscosity), but as this viscosity is small, we expect the results to be close to those of our model. In [19] for example, the curvature at the eastward jet is almost exactly  $\beta$  and seems to be trapped at this value whatever large the coefficients  $K$  and  $\frac{1}{\alpha}$  are.

Observations show that zonal jets seem to satisfy the Rayleigh-Kuo criterion of hydrodynamic stability. The Rayleigh-Kuo criterion states that if the inequality  $\beta - U'' > 0$  is satisfied everywhere in the flow, the flow cannot have an hydrodynamic instability (see e.g [80]). The Rayleigh-Kuo criterion gives a sufficient condition for the mean flow  $U$  to be stable, but it is not a necessary condition. There are examples of stable flows violating the Rayleigh-Kuo criterion. For what concerns zonal jets, we have seen numerically that a very localized hydrodynamic instability grows at the extremum of the westward jet as soon as the curvature of the extremum is larger than  $\beta$ . The unstable mode of the hydrodynamic instability stops the growth of the jet and keeps the curvature  $U''$  to a value very close to  $\beta$ . This shows that westward jets are marginally stable in the sense that the curvature of the westward extremum equilibrates to a value close to  $\beta$  at which the damping effect of the hydrodynamic instability is balanced by the force of the Reynolds stress divergence.

## 2.5 Perspectives

The barotropic equations in a  $\beta$  plane (2.2.1) can lead to formation and equilibration of zonal jets. Those jets are in an out-of-equilibrium steady state that results in a balance between energy injection at small scale and linear friction that dissipates energy at the largest scale. After rescaling the equations, two nondimensional parameters remain,  $\alpha$  and  $K$ , where  $\alpha$  gives the magnitude of energy injection and dissipation and  $\frac{1}{K}$  gives the scale of the stochastic forcing. The velocity profile of zonal jets  $U(y)$  obeys equation (2.2.2). This equation shows that the dynamics of zonal jets is governed by the Reynolds stress divergence  $\partial_y \langle uv \rangle$ , that can be computed from the equation for the velocity fluctuations. In the inertial limit  $\alpha \rightarrow 0$ , there is a clear timescale separation between the dynamics of the jets and the dynamics of the velocity fluctuations. The dynamics of zonal jets falls thus in the framework of slow-fast dynamical systems described in chapter 1.

The aim of the present work was to apply the averaging principle to the dynamics of zonal jets, to find a close equation for the averaged zonal velocity profile  $\bar{U}(y)$  (see equation (2.2.3)). We have shown that an analytical expression, as a function of  $\bar{U}$ , can be found for the Reynolds stress divergence in the small scale forcing limit  $K \rightarrow +\infty$ . The result is a close equation that predicts the existence of jets, and shows that jets are attractors of the averaged dynamics. From astronomical observations on Jupiter, we believe that both limits  $\alpha \rightarrow 0$  and  $K \rightarrow \infty$  are relevant to describe planetary flows and that the present work should find applications for the atmosphere of giant gaseous planets.

The present work was thought to be the first step toward a general comprehension of the statistical properties of zonal jets. What we have done here is to compute the averaged Reynolds stress  $\mathbb{E}[\langle uv \rangle]$  w.r.t the realizations of the stochastic force, to show that zonal jets are stable attractors of the averaged dynamics of jets. However, it is known from numerical simulations

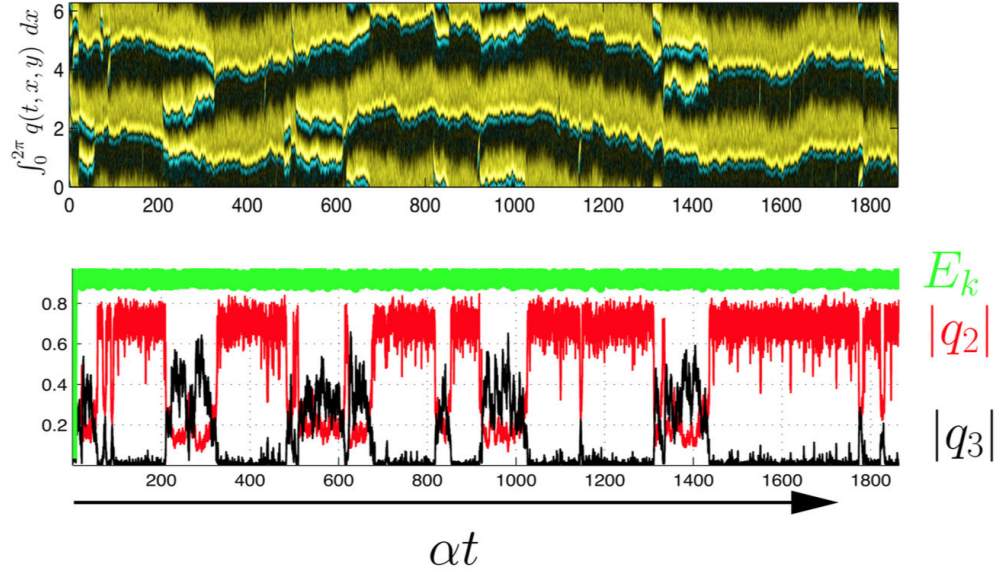


Figure 2.5.1: Direct numerical simulation of the stochastic quasigeostrophic barotropic equations. (Eric Simonnet) Top panel: spatio-temporal diagram of the zonally averaged vorticity. Bottom panel: time series of the vorticity Fourier components. When the flow is in the two-jets configuration, the Fourier mode  $q_2$  dominates, and when the flow has three jets, the mode  $q_3$  dominates. Rare transitions between the three and two jets configurations can be clearly seen.

that the mean flow  $U$  can have many stationary state with different numbers of jets [20, 24]. With stochastic forcing, transitions between the different attractors can be observed in the flow. The transitions are very rare in the sense that they happen on a timescale much longer than the typical timescale of evolution of zonal jets. Fig.(2.5.1) shows the result of a direct numerical simulation of the stochastic quasigeostrophic barotropic equations by Eric Simonnet. The top panel is a spatio-temporal diagram of the zonally averaged vorticity and the bottom panel is a time series of the vorticity Fourier components. When the flow is in the two-jets configuration, the Fourier mode  $q_2$  dominates, and when the flow has three jets, the mode  $q_3$  dominates. Rare transitions between the three and two jets configurations can be clearly seen.

To understand the rare transitions between states with a different number of jets, one would have to go beyond the averaging procedure and study also the fluctuations and large deviations of the Reynolds stress. Large deviation theory is in principle able to predict the probability of rare transitions between many-jets states [94], and predict the instanton path chosen by the flow to realize the fast and abrupt transitions (displayed in Fig.(2.5.1)). Private discussions with Eric Simonnet and Freddy Bouchet led us to believe that the creation of a new jet begins with a nucleus of inverse curvature at the extremum of the westward jet. On the contrary, the disappearance of a jet happens on a different path, with a fusion of two neighboring eastward jets and annihilation of the westward jet between them. The fact that analytical expressions can be found for the Reynolds stress in the small scale forcing limit is an encouraging result, and prompt us to look also for analytical results for the transitions between many-jets states. Rare events such as the creation or annihilation of a jet happen in real physical systems, not only in numerical simulations. On Jupiter, there are some clues that one jet has been lost in

the past, which indicates that transitions similar to those observed in our numerical simulations could really happen. Numerical work is in progress to study the appearance or disappearance of a jet using special algorithms designed for the computation of rare events. In this domain, the numerical simulations have a head start on theoretical works, and much remains to be done to fully understand the stochastic dynamics of large scales in a 2D turbulent flow.



## Chapter 3

# Long-term influence of the asteroids on the dynamics of Mars

### 3.1 Introduction and motivations

The numerical integration of the secular and full equations of motion for the eight planets of the solar system including the moon [47, 93] has shown that the solar system is chaotic and its Lyapunov time  $\tau_i$  has been estimated around 10 Myr. The chaos is significant enough such that a single integration of the equations of motion is not at all representative of the state of the solar system after a few 10 Myr. One property of chaotic motion is that it increases exponentially any difference in the initial positions of the planets. Therefore, an error of few meters in the initial positions of the planets leads on tens of Myr time scale to a complete indetermination on the actual position of the planets.

The eight planets of the solar system represent a dynamical system in the form

$$\frac{dx}{dt} = f_0(x) + \eta f_1(x). \quad (3.1.1)$$

In equation (3.1.1),  $x$  is a vector of  $2 \times 3 \times 8$  dimensions gathering all action-angle variables of the planets. The zeroth order dynamics defined by

$$\frac{dx}{dt} = f_0(x) \quad (3.1.2)$$

is the Keplerian dynamics. To zeroth order in the masses of the planets, the resolution of equation (3.1.2) shows that the trajectories of planets are ellipses where the position of the Sun is one of the focus of the ellipses. (3.1.2) is an integrable Hamiltonian dynamics. In the full dynamics (3.1.1),  $\eta$  is a small parameter and  $\eta f_1(x)$  is the perturbative function coming from the gravitational interactions between the planets. Because of the perturbative function  $\eta f_1(x)$ , the dynamical system (3.1.1) is no longer integrable, it is chaotic. Numerical simulations of the full equations of motion for the solar system without averaging were done by [93, 65] to build precise ephemeris for the Earth. They show that the Lyapunov time of the complete dynamics (3.1.1) has a Lyapunov time of same order as  $\tau_i \approx 10$  Myr computed with the secular equations. Chaotic motion is intrinsic to the dynamics of the planets, because of their mutual interactions. In particular, the dynamics is chaotic even without taking into account the external perturbations to the system, among which are the asteroids, the comets, the tidal effects, the radiative pressure of the Sun, etc...

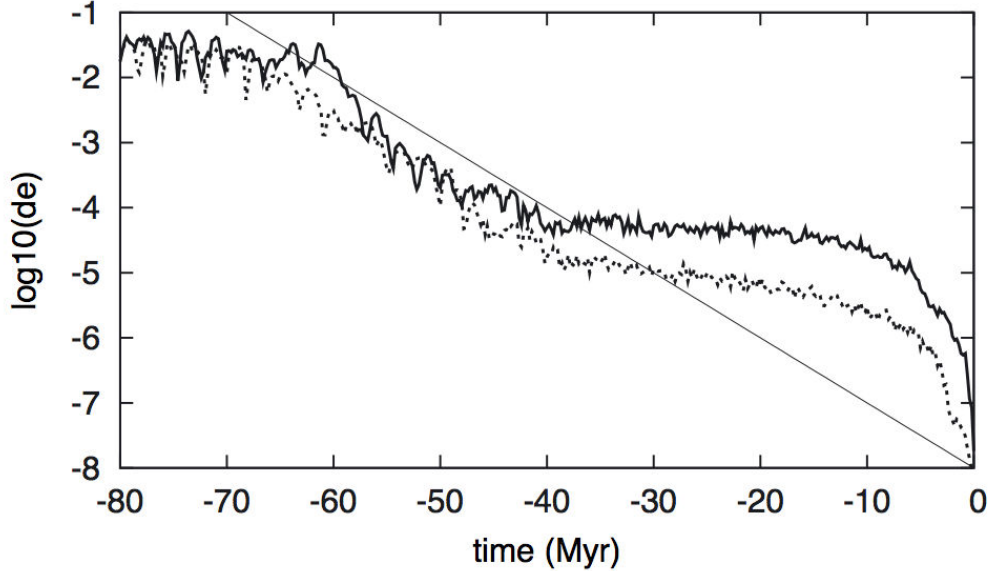


Figure 3.1.1: Evolution of the Earth's eccentricity uncertainty  $\delta e(t)$  without asteroids mutual interaction (dotted line), and with asteroids mutual interaction (solid line). The straight line represents the secular chaotic behavior with Lyapunov time of 10 Myr (taken from [61]).

Among all possible external perturbations to the dynamics (3.1.1), rough orders of magnitude suggest that the asteroids should be the main one. Taking the external influence of asteroids on the dynamics of planets, the system (3.1.1) is modified in

$$\frac{dx}{dt} = f_0(x) + \eta f_1(x) + \epsilon g(x, t), \quad (3.1.3)$$

where  $\epsilon \ll 1$  is a small parameter related to the mass of the asteroids, and the term  $\epsilon g(x, t)$  represent the gravitational interaction between planets and asteroids. Numerical simulations of the dynamics of the solar system including the asteroids, compared to others without asteroids [61], show that asteroids can indeed change the secular behavior of planetary orbits, however it has been observed that simulations with asteroids do not affect significantly the Lyapunov time of the solar system. Fig.(3.1.1) shows the increasing difference in eccentricity  $\delta e(t)$  between two trajectories of the Earth with close initial conditions [61]. The difference increases exponentially with time, which is characteristic of chaotic systems. One numerical integration (dotted line) is done without asteroids mutual interactions, and the other one (solid line) with asteroids mutual interactions. Without mutual interactions, , asteroids are about ten times less chaotic than with mutual interactions. In both cases, one can see on Fig.(3.1.1) that the influence of asteroids do not affect the Lyapunov time of 10 Myr computed without asteroids. This means that the Lyapunov time of the full system (3.1.3) with external perturbation from the asteroids has the same Lyapunov time  $\tau_i$  as the intrinsic dynamics (3.1.1).

The same numerical integrations in [61] have shown that the dynamics of asteroids is chaotic with a Lyapunov time  $\tau_\varphi \simeq 10^4$  yr, thus much smaller than the Lyapunov time of 10 Myr of the planets. The dynamics of asteroids is mixing, with a mixing time  $\tau_\varphi$  much smaller than  $\tau_i$ . The stochastic averaging theorems of section 1.3 state that the asteroids should act as a white noise on the dynamics of planets, on the Myr timescale. The aim of the present work is thus to study

the external perturbation of asteroids on the planetary dynamics, using the tools of stochastic averaging. More precisely, we look at the dynamical system

$$\frac{dx}{dt} = f_0(x) + \epsilon g(x, t). \quad (3.1.4)$$

The dynamics (3.1.4) where we have suppressed planetary mutual interactions, allows us to study the asteroids as an external source of chaos for the planets. In equation (3.1.4), chaotic motion is only due to the influence of asteroids. Let us call  $\tau_e$  ( e for *external* ) its Lyapunov time. We show that the chaotic dynamical system (3.1.4) is equivalent on the Myr timescale to the stochastic dynamics

$$\frac{dx}{dt} = f_0(x) + \xi(x, t), \quad (3.1.5)$$

where  $\xi(x, t)$  is a white noise, which amplitude can be expressed with the properties of  $g(x, t)$  with a Green-Kubo formula. Once the system (3.1.4) has been written as a stochastic process (3.1.5), it is quite easy to give the order of magnitude of  $\tau_e$ . Equations (3.1.1-3.1.4) define two different regimes depending on the Lyapunov times  $\tau_i$  and  $\tau_e$  :

1. The regime  $\tau_i \ll \tau_e$  defines a regime of intrinsic chaos. On a time of order of the internal Lyapunov time  $\tau_i$ , the effect of the external perturbation  $\epsilon g$  is small. Thus, the probability distributions of the variable  $x$  are essentially the same, to leading order in  $\epsilon$ , for the full system (3.1.3) and for the intrinsic dynamics (3.1.1).
2. If on the contrary  $\tau_e \ll \tau_i$ , then the external perturbation creates chaos in the integrable system, in the sense that the system loses the memory of its initial condition before the intrinsic chaos can develop. For intermediate times between  $\tau_e$  and  $\tau_i$ , the complete dynamics (3.1.3) can thus be described by a stochastic process, and the probability distributions may be strongly influenced by the external perturbation.

Using the present framework, our question formulates in a very simple way. Let the complete set of equations (3.1.3) be the equations for planetary motion of the solar system perturbed by the asteroid belt. Are we in the regime of *dominant intrinsic chaos* with  $\tau_i \ll \tau_e$  or in the regime of *external source of chaos* with  $\tau_e \ll \tau_i$ ? What is then the order of magnitude of  $\tau_e$  describing the interactions between asteroids and planets?

As we have suppressed planetary mutual interactions in equation (3.1.4), we can consider the influence of asteroids on each planet independently. In the present work, we have applied stochastic averaging on the dynamics of Mars, which is the closest planet to the asteroid belt and mostly feels the influence of asteroids. The method can be applied straightforwardly to other planets, using the correct orbital elements.

## 3.2 Dynamics of Mars perturbed by a chaotic asteroid

### 3.2.1 Simplified Hamiltonian model

For times smaller than the Lyapunov time of the solar system, the secular motion of planetary orbits is very accurately described by the periodic solution of the Laplace–Lagrange equations. Except for the smallest planet Mercury, the planetary orbital elements eccentricities and inclinations remain very small (less than 0.15 for the eccentricity, and less than 10 degrees for the inclination) in the Myr time scale [53]. The computations to be performed in the following could be done without fundamental difficulties for elliptic and inclined trajectories. However solving the equations for the elliptic motion is technically much more tedious than for restricted

Asteroid	non-dimensional mass $\epsilon = \frac{m}{M_S}$	semi-major axis (u.a)	eccentricity	inclination	Lyapunov time $\tau_\varphi$ (yr)
Ceres	$4.7 * 10^{-10}$	2.8	0.076	11 °	28900
Vesta	$1.35 * 10^{-10}$	2.4	0.09	7 °	14282
Pallas	$1.05 * 10^{-10}$	2.7	0.23	35 °	6283

Table 3.1: Physical properties of the main asteroids of the belt, Ceres, Vesta and Pallas.  $M_S$  is the mass of the sun. The Lyapunov times are taken from [61]

planar and circular motions, and it would not change the orders of magnitude to leading order in eccentricities and inclinations. To study the order of magnitude of the perturbation induced by the asteroids on the planets, we introduce a simplified model where the orbits of celestial bodies are circular and coplanar. To describe the motion of the planet Mars, we thus keep only the two orbital elements mean longitude  $\lambda$  and semi-major axis  $a$ . Most of the mass of the asteroids only comes from the contribution of the largest ones Ceres, Vesta and Pallas (the three largest asteroids represent about 58 % of the total mass of all asteroids). The physical properties of those three asteroids is summarized in table 3.1. In our simplified model, we thus only retain the planet Mars and one asteroid. Asteroids have chaotic motions because of gravitational perturbation by the planets, but also because of interactions between each other (in particular close encounters) as shown by [61]. They are thus not independent. Yet, their motions are decorrelated after the Lyapunov time  $\tau_\varphi$ , that's why, on the Myr timescale, we do the hypothesis that the perturbation of asteroids are independent. We thus add the individual contributions of each asteroid in the final result to obtain the right order of magnitude. The simplified model of the planet Mars perturbed by one asteroid is described by the Hamiltonian

$$H = -\frac{\mathcal{G}M_S m_p}{2a_p} - \frac{\mathcal{G}M_S m}{2a} - \frac{\mathcal{G}m m_p}{|a_p e^{i\lambda} - a e^{i\varphi}|},$$

where  $M_S, m_p, m$  stand for the masses of the Sun, Mars, and the asteroid respectively,  $\lambda, \varphi$  are the mean longitudes of Mars and the asteroid, and  $a_p$  and  $a$  their respective semi-major axis. The Sun is considered as fixed. This means that we only retain the direct term of the perturbative function and we take the real mass  $m$  instead of the reduced mass  $\frac{1}{\beta} = \frac{1}{m} + \frac{1}{M_S}$ .

### 3.2.2 Slow-fast dynamics of the orbital elements

In physical units, it is difficult to see whether there is a small parameter in the problem. The stochastic averaging techniques require to clearly identify a timescale separation between a slow and a fast variable. Therefore, we rescale all physical variables. The mass of the sun is taken as the unit mass,  $M_S = 1$ , and the reduced mass  $\epsilon := \frac{m}{M_S}$  of the asteroid is thus very small (table 3.1). Then we change the units for time and length, the astronomic unit (1  $UA$ ) is the new length scale, and we choose the new unit of time such that  $\mathcal{G}M_S = 1$ . Finally, let  $\Lambda := \epsilon_p \sqrt{a_p}$  be the canonical momentum associated to  $\lambda$  (we call  $\epsilon_p := \frac{m_p}{M_S}$  the reduced mass of Mars), we do the canonical change of variables  $H \leftarrow \frac{H}{\epsilon_p}, \Lambda \leftarrow \frac{\Lambda}{\epsilon_p}$ .

In the work of [61], the orbits of asteroids have been shown to be chaotic and the Lyapunov time  $\tau_\varphi$  has been computed numerically. The Lyapunov time  $\tau_\varphi$  corresponds to exponential separation for the longitudes  $\varphi(t)$  of asteroids. The Lyapunov times for the three main asteroids are given in table 3.1. In the present model of planet Mars perturbed by one asteroid, it is the chaos of the asteroid's motion that breaks the periodic Keplerian regular motion of Mars. Of course the chaotic motion of the asteroid does not come from the influence of Mars alone,

but rather from interaction and close encounters with other asteroids and on the influence of the giant planets. The retroactive influence of Mars on the asteroid can be considered as negligible compared to the influence of Jupiter or Saturn, and the interaction with Mars cannot substantially change the characteristics of the orbit of the asteroid, in particular its Lyapunov time. That's why we do not solve the equations of motion for the asteroid. To capture the physical phenomena coming from the gravitational interaction between Mars and the asteroid, the trajectory of the asteroid has to be considered as an input function in the model which physical properties are given by more precise numerical studies. We thus take the semi-major axis  $a$  as a constant and the longitude of the asteroid  $\varphi(t)$  as a function of time with correlation time of the order of the Lyapunov time  $\tau_\varphi$ . The trajectory of Mars in our model is a functional of the trajectory  $\varphi(t)$  of the asteroid. The reader should always bear in mind that those strong hypothesis are done to the aim of giving orders of magnitude and not precise quantitative results.

The Hamiltonian of the simplified model we study writes in nondimensional variables

$$H(\Lambda, \lambda, t) := -\frac{1}{2\Lambda^2} - \frac{\epsilon}{|\Lambda^2 e^{i\lambda} - a e^{i\varphi(t)}|}. \quad (3.2.1)$$

The Hamiltonian (3.2.1) does not conserve the total energy and angular momentum of the asteroid and Mars. But to first order in  $\epsilon$ , energy and angular momentum are the ones given by the Keplerian orbit and depend thus only on the canonical momentum  $\Lambda$ . Our model is consistent if the change in energy and angular momentum occurs on a time scale much larger than the time we are considering for the perturbation of Mars. This point will be checked a posteriori in section 3.4.3 when we will obtain the time  $\tau_{diff}$  over which the perturbation of Mars becomes large.

From the Hamiltonian (3.2.1), we get the set of Hamilton equations for  $\lambda, \Lambda$  as

$$\begin{aligned} \frac{d\lambda}{dt} &= n_p(\Lambda) + \epsilon \frac{\partial G}{\partial \Lambda}(\Lambda, \lambda - \varphi(t)) \\ \frac{d\Lambda}{dt} &= -\epsilon \frac{\partial G}{\partial \lambda}(\Lambda, \lambda - \varphi(t)), \end{aligned} \quad (3.2.2)$$

where we have introduced the Keplerian pulsation  $n_p(\Lambda) := \frac{1}{\Lambda^3}$  and the gravitational interaction  $G(\Lambda, \lambda - \varphi) := \frac{-1}{|\Lambda^2 e^{i(\lambda - \varphi)} - a|}$ . The set of equations (3.2.2) is a perfect slow-fast dynamical system, where the longitudes  $\lambda, \varphi$  of Mars and the asteroid respectively are the fast variables, and the semi-major axis of Mars is the slow variable. From equations (3.2.2), we know that the semi-major axis of Mars evolves on a timescale larger than  $\frac{1}{\epsilon}$ , which corresponds to about one billion year. The mixing time of the dynamics of the asteroid is of order of 10 000 yr, which is thus much smaller than the time of evolution of  $a$ . The timescale separation between the mixing time and the time of evolution of  $a$  satisfies the hypotheses required to do stochastic averaging on the semi-major axis, which is the aim of the next section 3.3.

In the final paragraph of this section, we discuss more precisely in which sense the position of Mars should be considered as a stochastic variable associated to a probability distribution. What is usually done in numerical simulations of chaotic planetary motion is to choose a large number of initial conditions differing only by a small shift in the initial position. Because of chaos, the different trajectories do not stay close together but separate exponentially fast on a timescale given by the Lyapunov exponent. After sufficiently long time compared to the Lyapunov time, the positions of all trajectories give a distribution. This distribution is an estimation of all possible positions that could be reached from a uniform distribution on a very small set of initial conditions. In this sense, it is a probability distribution. In the simplified model (3.2.1), we do not fix the initial position of the asteroid. We study the motion of Mars for

different possible realizations of the function  $\varphi(t)$  and we take for  $\varphi(0)$  a uniform distribution over the range  $[0, 2\pi]$ . This choice is done because the incertitude on the longitude of the asteroid becomes total after a time large enough compared to the Lyapunov time  $\tau_\varphi$ . The position of Mars has a probability distribution because it is conditioned by the realizations of the stochastic function  $\varphi(t)$ . We really emphasize that the trajectories of Mars will not separate exponentially with time, as would have been the case if we had just consider a set of very close initial conditions for the position of Mars and one single function  $\varphi(t)$ . In our model,  $\varphi(t)$  is a random function with a probability distribution  $\mathbb{P}[\varphi]$ . Given this probability distribution, we want to obtain the probability distribution of the canonical variables  $\Lambda, \lambda$ . Instead of an exponential separation, we will get a diffusive behavior as will be shown in the next section.

### 3.3 Stochastic averaging of the dynamics of the semi-major axis

#### 3.3.1 Dynamics with rescaled variables

For technical reasons, it is convenient to consider the variable  $p := n_p(\Lambda)$  instead of  $\Lambda$  and write the Hamilton equations (3.2.2) as

$$\begin{aligned}\dot{\lambda} &= p + \epsilon \frac{\partial G}{\partial \Lambda}(\Lambda, \lambda - \varphi(t)) \\ \dot{p} &= -\epsilon \frac{\partial n_p}{\partial \Lambda}(\Lambda) \frac{\partial G}{\partial \lambda}(\Lambda, \lambda - \varphi(t)).\end{aligned}\tag{3.3.1}$$

It is physically clear that to zeroth order in  $\epsilon$ , the motion of  $(p, \lambda)$  is simply a linear flow, with  $p = p(0)$  and  $\lambda(t) = \lambda(0) + p(0)t$ . Equations are then invariant with the change of variables  $p \leftarrow p - p(0)$ ,  $\lambda \leftarrow \lambda - p(0)t$ , provided the function  $\varphi(t)$  is also changed as  $\varphi(t) \leftarrow \varphi(t) - p(0)t$ . This change of variables means that we integrate out the Keplerian motion of Mars and the new function  $\varphi(t)$  represents the difference between the mean longitude of the asteroid and the Keplerian mean longitude of Mars.

Now comes a subtle point: the aim of our calculations is to give an order of magnitude of the influence of the asteroid on the dynamics of Mars. We will not apply brute stochastic averaging as described in section 1.3.3, because averaging on the longitude of Mars would completely hide the stochastic effect of the asteroid on the longitude of Mars. It is not obvious on which timescale the motion of the longitude of Mars will be perturbed. It should scale with  $\epsilon$  but we still do not know the precise scaling at this step of the calculation. Following the method proposed in [46], we thus introduce *a priori* an exponent  $\alpha > 0$  and rescale the time according to  $t' = \epsilon^\alpha t$ . The case  $\alpha = 1$  corresponds to the timescale of the slow variable. With  $\alpha < 1$ , we will find the right timescale at which the longitude of Mars feels the stochastic effect of the asteroid. The variables  $\lambda$  and  $p$  are also rescaled according to  $\lambda'(t) = \lambda\left(\frac{t}{\epsilon^\alpha}\right)$  and  $p'(t) = \frac{1}{\epsilon^\alpha} p\left(\frac{t}{\epsilon^\alpha}\right)$  and  $\Lambda'(t) = \Lambda\left(\frac{t}{\epsilon^\alpha}\right)$ . The equations for the rescaled variables are

$$\begin{aligned}\dot{\lambda}' &= p' + \epsilon^{1-\alpha} \frac{\partial G}{\partial \Lambda} \left( \Lambda', \lambda' - \varphi \left( \frac{t}{\epsilon^\alpha} \right) \right) \\ \dot{p}' &= -\epsilon^{1-2\alpha} \frac{\partial n_p}{\partial \Lambda}(\Lambda') \frac{\partial G}{\partial \lambda} \left( \Lambda', \lambda' - \varphi \left( \frac{t}{\epsilon^\alpha} \right) \right).\end{aligned}\tag{3.3.2}$$

In the next section, we show how the stochastic averaging theorem of section 1.3.3 can give stochastic equations equivalent to (3.3.2). From the stochastic set of equation, we can choose the value of the exponent  $\alpha$  to find the relevant timescale on which diffusion occurs.

### 3.3.2 Stochastic differential equation for the orbital elements

To go one step further, we have to find the asymptotic behavior of the two functions  $\frac{\partial G}{\partial \lambda}(\Lambda', \lambda' - \varphi(\frac{t}{\epsilon^\alpha}))$  and  $\frac{\partial G}{\partial \Lambda}(\Lambda', \lambda' - \varphi(\frac{t}{\epsilon^\alpha}))$  in the limit  $\epsilon \rightarrow 0$ . The limit is not at all trivial. The averaging principle states that the oscillating function  $\frac{\partial G}{\partial \lambda}(\Lambda', \lambda' - \varphi(\frac{t}{\epsilon^\alpha}))$  should be averaged over the distribution of the fast angle  $\varphi$ . However, it happens that the function  $\frac{\partial G}{\partial \lambda}$  is periodic in  $\varphi$ , and its average over a uniform distribution of  $\varphi$  is zero. The averaging principle only tells us that the semi-major axis is invariant to main order in  $\epsilon$ .

The semi-major axis is called an *adiabatic invariant*, it means that it is a conserved quantity of the averaged dynamics. It is known since a long time in celestial mechanics that the semi-major axis is conserved by the secular equations to first order (and even to second order) in the planetary masses. The result is known in celestial mechanics as the Laplace theorem (and the Poisson theorem for the second order in the masses). To obtain a non trivial variation of the semi-major axis, we have to go to next order, beyond the averaging principle, and do stochastic averaging.

The average of the dynamics over the fast angle vanishes  $\overline{\frac{\partial G}{\partial \lambda}} = 0$ . This corresponds to the case of stochastic averaging with  $\bar{b} = 0$  described in section 1.3.3. The stochastic averaging theorem requires the fast dynamics to be mixing. This hypothesis is satisfied because the dynamics of the asteroid is chaotic with the Lyapunov time  $\tau_\varphi$ . Stochastic averaging can be applied provided the considered timescale is much longer than the mixing time  $\tau_\varphi$ . In dimensional variables, this condition would write  $\frac{\tau_\varphi}{T_p} \ll \frac{1}{\epsilon^\alpha}$ , with  $T_p$  the Keplerian period of Mars. The condition has to be checked a posteriori with the value of the exponent  $\alpha$ .

The theory of stochastic averaging in the case  $\bar{b} = 0$  shows that the function  $\frac{\partial G}{\partial \lambda}(\Lambda', \lambda' - \varphi(\frac{t}{\epsilon^\alpha}))$  is equivalent (it is said to be equivalent *in law*) to the stochastic process (see expression 1.3.36)

$$\frac{\partial G}{\partial \lambda} \left( \Lambda', \lambda' - \varphi \left( \frac{t}{\epsilon^\alpha} \right) \right) \underset{\epsilon \rightarrow 0}{\sim} \epsilon^{\alpha/2} \left[ A(\Lambda') + \sqrt{\sigma^2(\Lambda')} \xi(t) \right], \quad (3.3.3)$$

where  $\xi(t)$  is the normal Gaussian white noise,  $\langle \xi(t) \xi(t') \rangle = \delta(t - t')$ . As we said in section 1.3.3, there is in general no simple expression for the drift  $A$  (we call the drift  $A$  to avoid any confusion with the semi-major axis) for a fully coupled slow-fast system. In the present work, we neglect the retroaction of Mars on the asteroid. This assumption means that the fast dynamics is decorrelated from the slow process, and equation (1.3.38) gives then an explicit expression for the drift. The coefficients  $a$  and  $\sigma$  are given in terms of the correlation function of  $\frac{\partial G}{\partial \lambda}$  by

$$\begin{aligned} A(\Lambda') &= \int_0^{+\infty} dt \left\langle \frac{\partial^2 G}{\partial \Lambda \partial \lambda}(\Lambda', \lambda' - \varphi(t)) \frac{\partial G}{\partial \lambda}(\Lambda', \lambda' - \varphi(0)) \right\rangle, \\ \sigma^2(\Lambda') &= 2 \int_0^{+\infty} dt \left\langle \frac{\partial G}{\partial \lambda}(\Lambda', \lambda' - \varphi(t)) \frac{\partial G}{\partial \lambda}(\Lambda', \lambda' - \varphi(0)) \right\rangle. \end{aligned} \quad (3.3.4)$$

It should be noticed that the function  $G$  depends on the variable  $\lambda - \varphi$ , and as a result, the coefficients expressed in (3.3.4) do not depend on  $\lambda'$ . On the contrary, the function  $\frac{\partial G}{\partial \Lambda}$  in the dynamics of  $\lambda'$  in equation (3.3.2) is not periodic in  $\varphi$  and a simple averaging principle is enough to give the equivalent

$$\frac{\partial G}{\partial \Lambda} \left( \Lambda', \lambda' - \varphi \left( \frac{t}{\epsilon^\alpha} \right) \right) \underset{\epsilon \rightarrow 0}{\sim} \left\langle \frac{\partial G}{\partial \Lambda} \right\rangle(\Lambda),$$

where the average  $\langle \rangle$  is done over  $\varphi$ .

Altogether, we can give a *stochastic* equivalent of the system of equations (3.3.2)

$$\begin{aligned}\dot{\lambda}' &= p' + \epsilon^{1-\alpha} \left\langle \frac{\partial G}{\partial \Lambda} \right\rangle (\Lambda') \\ \dot{p}' &= -\epsilon^{1-\frac{2}{3}\alpha} \frac{\partial n_p}{\partial \Lambda} (\Lambda') \left[ A(\Lambda') + \sqrt{\sigma^2(\Lambda')} \xi(t) \right].\end{aligned}\tag{3.3.5}$$

In the first equation of (3.3.5), the perturbation appears at order  $\epsilon^{1-\alpha}$ , whereas in the second equation it is  $\epsilon^{1-\frac{2}{3}\alpha}$ . As  $\alpha > 0$ , the term in the equation for  $p'$  is dominant. We choose the value  $\alpha = \frac{2}{3}$ , because it is the only choice of  $\alpha$  that gives a non trivial finite limit to the set of equations (3.3.5) when  $\epsilon \rightarrow 0$ . We can then drop the term  $\epsilon^{1-\alpha} \left\langle \frac{\partial G}{\partial \Lambda} \right\rangle (\Lambda)$  in the first equation. Forgetting the primes for the variables  $\lambda'$  and  $p'$  we finally write the stochastic equations for the dynamics of Mars perturbed by an asteroid

$$\begin{aligned}\dot{\lambda} &= p \\ \dot{p} &= -\frac{\partial n_p}{\partial \Lambda} (\Lambda) A(\Lambda) + \frac{\partial n_p}{\partial \Lambda} (\Lambda) \sqrt{\sigma^2(\Lambda)} \xi(t).\end{aligned}\tag{3.3.6}$$

The last set of equations describes to main order the diffusion of the canonical variables  $\lambda$  and  $\Lambda$  over a timescale  $\frac{1}{\epsilon^{2/3}}$ .

### 3.3.3 Diffusion process for the semi-major axis

The aim of the present section is to give the consequences of equations (3.3.6) on the semi-major axis of Mars. In particular, we evaluate the order of magnitude of the diffusion coefficient and we give the timescale for diffusion in physical units.

The difficult task is the computation of the diffusion coefficient  $\sigma^2$  in (3.3.4), because it involves the correlation function of the derivative of  $G$ . The full computation is reported in appendix A. The computation depends only on an averaging over the phase of the asteroid. As the motion of the asteroid is a chaotic function for which we do not have an analytic expression, we have to do an hypothesis on how the phase  $\varphi$  of the asteroid differs from a simple Keplerian motion. We have to take into account that the Lyapunov time of the phase is given by  $\tau_\varphi$ . To perform the computation, we assume that the perturbation of the phase of the asteroid is similar to a Brownian motion  $W\left(\frac{t}{\tau_\varphi}\right)$ . However we strongly emphasize that this particular ansatz for the perturbation of the asteroid is chosen to perform analytic calculations, but while the exact result will depend on the particular expression of  $\varphi$ , the order of magnitude of the result will not. Our result will thus give the correct order of magnitude of the diffusion coefficient as a function of the correlation time  $\tau_\varphi$  of  $\varphi$ .

The important result of the calculation of appendix A is to show how the diffusion coefficient  $\sigma^2(\Lambda)$  scales with  $\tau_\varphi$ . We have explained in the theoretical discussion about mixing systems in section 1.2.2 that diffusion only occurs if the motion of the asteroid decorrelates fast enough. It is therefore natural to expect that the diffusion coefficient is larger when  $\tau_\varphi$  is smaller. On the contrary, if the motion of the asteroid is regular, there is no diffusion at all, the diffusion coefficient should be zero for infinite  $\tau_\varphi$ . A rough order of magnitude for the diffusion coefficient  $\sigma^2(\Lambda)$  from the formula (A.0.2) of appendix A writes in non dimensional variables

$$\sigma^2(\Lambda) \propto \frac{|G|^2}{(n_p - \nu)^2 \tau_\varphi},\tag{3.3.7}$$

where  $|G|$  is the typical order of magnitude of the function  $G$ ,  $n_p$  is the Keplerian pulsation of Mars,  $\nu$  is the Keplerian pulsation of the asteroid, and  $\tau_\varphi$  is the Lyapunov time of the asteroid,

all expressed in unit of time period of Mars. If we restrict ourselves to times that are short, or of the order of the diffusion timescale, there is no need to evaluate the drift  $A(\Lambda)$ . The diffusion process has typical growth  $\propto \sqrt{t}$  compared to the growth  $\propto t$  for the drift, and the drift does not influence diffusion for short times  $t$ .

We summarize the results by saying that the effect of the chaotic asteroid on the planet Mars is similar to a white noise process acting on the semi-major axis  $a_p$  of Mars. The equation for  $a_p$  can be deduced from equation (3.3.6) and the relation

$$\begin{aligned} \dot{p} &= \frac{\partial n_p}{\partial \Lambda} \dot{\Lambda}, \\ &= \frac{\partial n_p}{\partial \Lambda} \frac{\dot{a}_p}{2\sqrt{a_p}}. \end{aligned} \quad (3.3.8)$$

The stochastic equation for the semi-major axis  $a_p$  writes

$$\frac{da_p}{dt} = \sqrt{D}\xi(t), \quad (3.3.9)$$

where the order of magnitude of  $D$  can be written in nondimensional units using equations (3.3.6),(3.3.7),(3.3.8) and  $|G| \approx \frac{\epsilon}{|a_p - a|}$

$$D \propto \epsilon^2 \frac{4a_p}{|a_p - a|^2 (n_p - \nu)^2 \tau_\varphi}. \quad (3.3.10)$$

Then, we come back to dimensional variables. The length scale is the astronomical unit, we call it  $L$ . The unit of time is given by  $\frac{L^{3/2}}{\sqrt{\mathcal{G}M_s}}$ , and we have  $\epsilon := \frac{m}{M_s}$ . The dimension of  $D$  is  $[L]^2[T]^{-1}$ . The dimensional form of  $D$  is then simply obtained by multiplying the nondimensional result (3.3.10) by  $L^3 \times \frac{\mathcal{G}M_s}{L^3}$ , which gives

$$D \propto 4 \left( \frac{m}{M_s} \right)^2 \frac{\mathcal{G}M_s a_p}{|a_p - a|^2 (n_p - \nu)^2 \tau_\varphi}. \quad (3.3.11)$$

Equations (3.3.9) and (3.3.11) are the first important physical result of this chapter. They give the quantitative stochastic effect of the asteroid belt on the semimajor axis of Mars, with the influence of the relevant parameters. Equation (3.3.9) can be considered as a deviation from the theorem of Poisson that states that the semi-major axis is constant for the averaged equations up to second order in the masses. Equation (3.3.11) gives the main physical parameters that influence the diffusion time. The diffusion coefficient is very small because it is proportional to the square of the small parameter  $\frac{m}{M_s} < 10^{-9}$ . The Lyapunov time of the asteroid appears at the denominator of the expression of  $D$ , which confirms the fact that the noise created by the asteroid is larger when the asteroid is more chaotic. One last important remark is the presence of the difference  $n_p - \nu$  between the Keplerian pulsations of Mars and the asteroid. The result is valid because there is no resonance of first order between Mars and the asteroid. The presence of resonances in the fast dynamics of a slow-fast system can completely change the expression of the diffusion coefficient, and require a special care. An example of resonances in the fast dynamics will be encountered in the secular dynamics of Mercury studied in chapter 5.

From the diffusion coefficient (3.3.11) we can build a typical time of diffusion of the semi-major axis

$$\tau_{a_p} \propto \frac{a_p^2}{D} \approx 10^{22} yr \quad (3.3.12)$$

The time  $\tau_{a_p}$  is much larger than the age of the solar system. The semi-major axis of Mars can thus be considered as constant on the Gyr timescale. However, the result does not mean that asteroids have no significant effect on the dynamics of planets. Section 3.4 will show that the main stochastic effect of asteroids is on the longitude of Mars, not its semi-major axis.

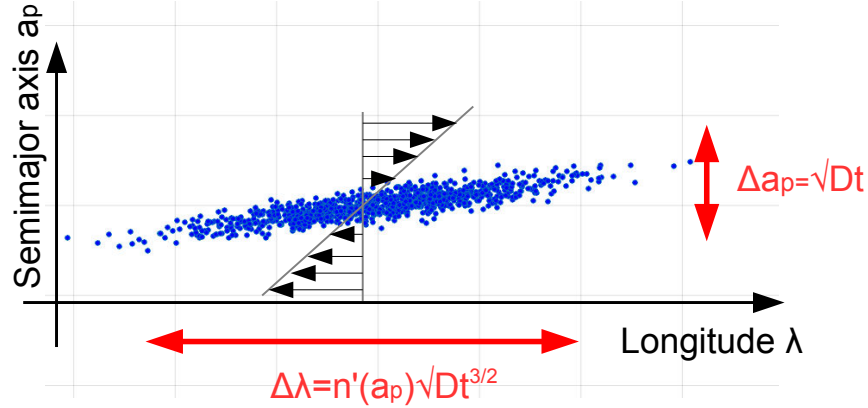


Figure 3.4.1: Dispersion of particles in a channel. The flow is indicated with arrows.

## 3.4 Superdiffusion of the mean longitude of Mars

### 3.4.1 Heuristic picture of the mechanism: dispersion is enhanced by the Keplerian flow

Although the results of the last section could seem very technical at first sight, the underlying physical mechanism is very simple. Let us give a simple picture to understand the result (3.3.6). We represent the Keplerian dynamics of Mars in Fig.(3.4.1) by a parallel flow in a channel. The velocity of the flow is given by the Keplerian pulsation  $n_p(\Lambda)$ , and depends explicitly on the coordinate  $\Lambda$ . We represent in Fig.(3.4.1) the difference in velocity  $n_p(\Lambda) - n_p(\Lambda_0) \approx \frac{\partial n_p(\Lambda_0)}{\partial \Lambda}(\Lambda - \Lambda_0)$  as a linear velocity profile in the channel.

At  $t = 0$ , particles are released in the middle of the channel at  $\Lambda = \Lambda_0$ . The particles represent the different trajectories of Mars with close initial conditions. Particles diffuse along the  $\lambda$ -direction and the  $\Lambda$ -direction. Along the  $\Lambda$ -direction, we have a simple diffusion according to equation (3.3.6) and  $\Delta\Lambda(t) \propto \sqrt{t}$ . Along the  $\lambda$ -direction, the flow amplifies the diffusion: particles going up at  $\Lambda$  feel a velocity  $\frac{\partial n_p(\Lambda_0)}{\partial \Lambda}(\Lambda - \Lambda_0)$  and are carried forward in the  $\lambda$ -direction, whereas those going down at  $-\Lambda$  feel the velocity  $-\frac{\partial n_p(\Lambda_0)}{\partial \Lambda}(\Lambda - \Lambda_0)$  and are carried backward in the  $\lambda$ -direction.

Altogether, if at time  $t$  particles have diffused over a range  $\Delta\Lambda$ , the dispersion along  $\lambda$  scales like  $\Delta\lambda = \frac{\partial n_p(\Lambda_0)}{\partial \Lambda} \Delta\Lambda t$ , and since  $\Delta\Lambda \propto \sqrt{t}$  we find that  $\Delta\lambda \propto \frac{\partial n_p(\Lambda_0)}{\partial \Lambda} t^{\frac{3}{2}}$ . A diffusion scaling with  $t^{\frac{3}{2}}$  is an example of what we call a “superdiffusion”, it is illustrated on Fig. (3.4.1).

Because of the superdiffusion mechanism, the dispersion of trajectories of Mars occur much faster for the longitude than for the semi-major axis. The diffusion time we found in (3.3.12) is much too large to be relevant over the Gyr timescale, but we show in the following that the superdiffusion time of the mean longitude is small enough to have an impact on physical observations.

Let us conclude this section by a remark. The superdiffusion mechanism, that is, diffusion scaling with  $t^{3/2}$  has been known for long in hydrodynamics with the name Taylor-Aris dispersion. In chaotic Hamiltonian systems, its importance has already been recently noticed by [46]. Some physicists in celestial mechanics had also noticed the phenomenon with the propagation of numerical errors in simulations [16]: the error grows much faster for the angle than for the action variable.

### 3.4.2 Variance of the mean longitude

We have noticed in section 3.3.3 that the diffusion time of the semi-major axis is much larger than the age of the solar system. Over the Gyr timescale, the action variable  $\Lambda$  can be considered constant in equation (3.3.6). The system has an exact solution. From the integration of (3.3.6), we deduce that the probability distribution of  $\lambda$  is a Gaussian law. We can now compute its variance w.r.t the realizations of the noise  $\xi$ . The term  $-\frac{\partial n_p}{\partial \Lambda}(\Lambda)A(\Lambda)$  will give a deterministic contribution on  $\lambda$  scaling like  $t^2$ . The interesting part comes from the white noise, because it makes the probability distribution of  $\lambda$  spread over time. From integration of the second equation of (3.3.6) we get

$$p(t) = -\frac{\partial n_p}{\partial \Lambda}(\Lambda)A(\Lambda)t + \frac{\partial n_p}{\partial \Lambda}(\Lambda)\sqrt{\sigma^2(\Lambda)}W(t),$$

where  $W$  is the standard Brownian motion (also called the Wiener process). The mean longitude can be expressed as the integral of  $p$

$$\lambda(t) = \lambda(0) - \frac{\partial n_p}{\partial \Lambda}(\Lambda)A(\Lambda)t^2 + \frac{\partial n_p}{\partial \Lambda}(\Lambda)\sqrt{\sigma^2(\Lambda)}\int_0^t W(s)ds. \quad (3.4.1)$$

From the last expression, we get the variance of the probability distribution of  $\lambda$

$$\begin{aligned} V_\lambda(t) &:= \mathbf{E}[\lambda^2(t)] - \mathbf{E}[\lambda(t)]^2 \\ &= \left(\frac{\partial n_p}{\partial \Lambda}(\Lambda)\right)^2 \sigma^2(\Lambda) \int \int ds ds' \mathbf{E}[W(s)W(s')] \\ &= \left(\frac{\partial n_p}{\partial \Lambda}(\Lambda)\right)^2 \sigma^2(\Lambda) \int \int ds ds' \inf(s, s') \\ &= \frac{1}{3} \left(\frac{\partial n_p}{\partial \Lambda}(\Lambda)\right)^2 \sigma^2(\Lambda) t^3. \end{aligned}$$

This proves that  $\lambda$  is “*superdiffusive*”, because the variance grows like  $t^3$  instead of  $t$  for standard Brownian motion. We can define the timescale of superdiffusion  $\tau_{diff}$  through the relation

$$\Delta\lambda(t) = \left(\frac{t}{\tau_{diff}}\right)^{\frac{3}{2}}, \quad (3.4.2)$$

with the explicit expression of  $\tau_{diff}$  given by

$$\tau_{diff} = \left(\frac{1}{3}\epsilon^2 \left(\frac{\partial n_p}{\partial \Lambda}\right)^2 \sigma^2(\Lambda)\right)^{-1/3}. \quad (3.4.3)$$

Equation (3.4.2) is the mathematical justification of the superdiffusion process described in section 3.4.1. But we even obtain a more precise result than the simple scaling of  $\Delta\lambda$ : equation (3.4.1) shows that the mean longitude is the integral of a Brownian motion. From this result, we can obtain all statistics about the stochastic process  $\lambda(t)$ , including its full probability distribution. In dimensional variables, the expression 3.4.3 of the superdiffusion time becomes

$$\tau_{diff} \propto \left(\left(\frac{m_a}{M_S}\right)^2 \frac{\mathcal{G}M_S}{a_p^3 \tau_\varphi}\right)^{-1/3}. \quad (3.4.4)$$

Asteroid	nondimensional mass $\epsilon \times 10^{10}$	Lyapunov time (yr) $\tau_\varphi$	$\tau_{diff}$ (Myr)	extrinsic Lyapunov time $\tau_e$ (Myr)
Ceres	4.7	28900	22	25
Vesta	1.3	14282	24	23
Pallas	1.05	6283	33	36
total 3 asteroids	7.05	-	17	18

Table 3.2: Effect of the three largest asteroids on the mean longitude of Mars

A final remark will conclude this subsection: the asymptotic result (3.3.3) shows that the interaction with chaotic asteroids is equivalent to a white noise force acting on the planet, on a time scale much larger than the Lyapunov time  $\tau_\varphi$  of the asteroid. (3.3.4) give the properties of the noise, and is the starting point to study the order of magnitude of the noise amplitude, which is done in the next section. Our computation thus gives a theoretical ground to the model studied in [46] of an integrable dynamics perturbed by a white noise, and the correct order of magnitude for the diffusion coefficient  $\sigma^2$  in Eq. (3.3.4) .

### 3.4.3 Orders of magnitude for the superdiffusion time

With the results of appendix A, we are able to give the order of magnitude for the diffusion time of the mean longitude of Mars. On timescales longer than their respective Lyapunov time, the motion of the asteroids can be considered as statistically independent. The perturbations of the asteroids on Mars can thus be considered separately. This allows to give an estimation of the total perturbation.

Table (3.2) is the second important quantitative result of this work. It gives an estimation of the time we have to wait before seeing a noticeable influence of the three largest asteroids on the mean longitude of Mars. The diffusion time  $\tau_{diff}$  depends strongly both on the mass of the asteroid and on the Lyapunov time  $\tau_\varphi$  of the asteroid. In particular we see that Ceres and Vesta seem to have similar effects on Mars because Ceres is much larger, but is also much less chaotic than Vesta. We also report in the last column of table (3.2) the extrinsic Lyapunov time  $\tau_e$  of planets perturbed by the asteroid belt. It is defined as the inverse of the largest Lyapunov exponent of the dynamical system (3.2.2). Physically, it corresponds to the typical time of exponential separation of two close initial conditions in (3.2.2) for the mean longitude of Mars. We do not report details about the computation of  $\tau_e$  because the method is very similar to the computation of  $\tau_{diff}$  and is already explained in the work of [46]. The result is

$$\tau_e = \left( \frac{1}{3} \epsilon^2 \left( \frac{\partial n_p}{\partial \Lambda} \right)^2 2 \int_0^{+\infty} dt \left\langle \frac{\partial^2 G}{\partial \lambda^2} (\Lambda, \lambda(t) - \varphi(t)) \frac{\partial^2 G}{\partial \lambda^2} (\Lambda, \lambda(0) - \varphi(0)) \right\rangle \right)^{-1/3}. \quad (3.4.5)$$

The expression of  $\tau_e$  is very similar to that of  $\tau_{diff}$ , but it involves the correlation function of the second derivatives of  $G$  instead of the first derivatives for  $\tau_{diff}$ . This explains why the orders of magnitude for  $\tau_e$  and  $\tau_{diff}$  in table 3.2 are roughly the same.

### 3.4.4 Conclusion: impact on chaotic motion of the solar system

The present work has shown that the main stochastic effect of asteroids on planetary motion occurs on the time evolution of the mean longitudes. We have shown that the variance of the mean longitude of Mars grows like  $t^{3/2}$  because of the superdiffusion mechanism. The superdiffusion mechanism is an additional mechanism to the usual exponential separation of trajectories

observed in chaotic systems. We believe this mechanism could be observed in numerical simulations.

Consider a number of numerical simulations of the dynamics of Mars and the asteroid belt. If one takes different but very close initial conditions for the planet Mars and exactly *the same* initial conditions for the asteroids, the trajectories of Mars separate exponentially fast with Lyapunov time  $\tau_e$ . This means that for times smaller than  $\tau_e$  we have

$$\Delta\lambda(t) \simeq \Delta\lambda_0 \exp\left(\frac{t}{\tau_e}\right), \quad (3.4.6)$$

where  $\Delta\lambda$  is the difference in mean longitude between two trajectories of Mars. On the contrary, if one simulates the system with *different* initial conditions for the asteroids, but the same initial condition for the planet Mars, the trajectories of Mars in the different simulations separate as

$$\Delta\lambda(t) \simeq \left(\frac{t}{\tau_{diff}}\right)^{3/2}. \quad (3.4.7)$$

because of the superdiffusion mechanism. Now, the simulation can start with *both* different initial conditions for Mars and the asteroids. Table (3.2) shows that  $\tau_e$  and  $\tau_{diff}$  are of the same order of magnitude. Then the trajectories of Mars will also separate following the power law

$$\Delta\lambda(t) \simeq \Delta\lambda_0 + \left(\frac{t}{\tau_{diff}}\right)^{3/2}, \quad (3.4.8)$$

because the superdiffusion mechanism overcomes the exponential divergence for small times  $t < \tau_e$ . This is illustrated on Fig.(3.4.2). This explains why the superdiffusion mechanism is more relevant than exponential separation for the computation of the probability distribution of planetary mean longitudes. The mechanism that causes superdiffusion of longitudes is the perturbation by the asteroids of the planetary semi-major axis, which is an adiabatic invariant of the secular equations of the solar system. Even if the simplified model considered in this work does not take into account secular evolution of the orbital elements eccentricities and inclination, the superdiffusion of the longitudes should not be broken by the secular motion of orbits, and the orders of magnitude of table (3.2) should be the relevant ones.

The superdiffusion timescale for the planetary longitudes, of order of 10 Myr, is of the same order of magnitude as the Lyapunov time  $\tau_i$  of planetary secular motion in the inner solar system, as given by [47]. The superdiffusion of longitudes does not affect the secular chaos in the solar system, because the secular equations do not involve the planetary longitudes. As a natural extension of our work, we have shown that asteroids create another superdiffusion mechanism at the level of the secular equations, which affects the time evolution of planetary eccentricities and inclinations. With a very similar procedure as the one used in this chapter, the ‘‘secular’’ timescale for superdiffusion can be computed theoretically (see [102]). The result shows that the secular timescale for superdiffusion is much larger than the age of the solar system, and that the superdiffusion mechanism is thus negligible compared to the exponential separation of trajectories due to secular chaos. We thus conclude that the long-term probability distributions of planetary orbital parameters should be the same with, and without taking the asteroids into account.

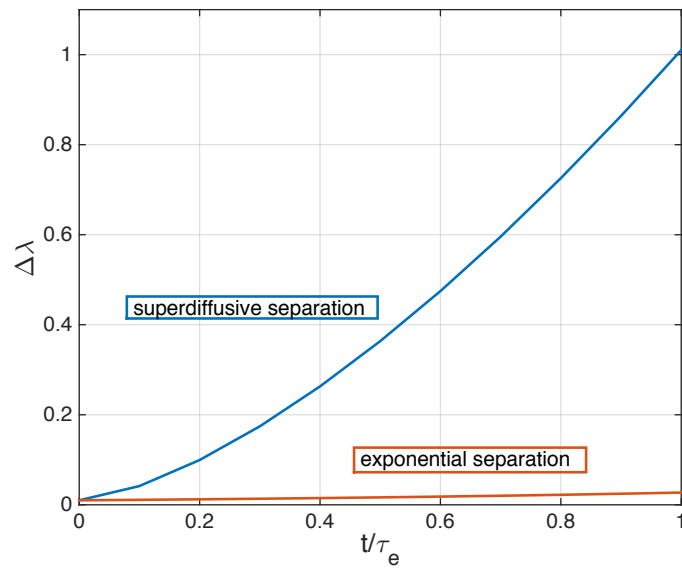


Figure 3.4.2: Separation between the trajectories of Mars with close initial conditions. The superdiffusion mechanism represented by the blue curve gives a separation scaling as a power-law  $\left(\frac{t}{\tau_{diff}}\right)^{3/2}$ . The chaos in the system separates two trajectories exponentially fast as displayed by the red curve. Here we have chosen an initial separation  $\Delta\lambda_0 \approx 0.01$ .

## Chapter 4

# Large variations of the obliquity of a Moonless Earth

### 4.1 Introduction: chaotic variations of planetary obliquities

The Earth spin axis is currently tilted of  $23^\circ$ . The angle between the spin axis and a vertical axis (w.r.t. the orbital plane) is called the obliquity, and noted  $\varepsilon$ . The tilt is responsible for the existence of seasons on our planet, and the value of the obliquity is directly related (with geometrical effects) to the duration of the day, seasons, and mean surface insolation. The spin axis does not always keep the same orientation in space. It has a precessional motion called precession of the equinoxes, similar to the one observed for a top. The precession is due to the torque exerted by the Moon and the Sun because of the non-spherical shape of the Earth. The precession of the Earth is illustrated on figure 4.1.1.

Neglecting all other influences, the spin axis dynamics is described by the Hamiltonian

$$H_E = \alpha \frac{p^2}{2}$$

where  $\alpha$  is the precession constant,  $p := \cos \varepsilon$  is the action variable, and  $q$  is the conjugated precession angle. The explicit expression for the precession constant  $\alpha$  involves the coefficients of the Earth matrix of inertia, such that the precession constant would be zero for a perfectly spherical Earth. To zeroth order, the spin axis dynamics is integrable, and its motion is simply given by

$$\dot{q} = \alpha p.$$

With the current value of the precession constant  $\alpha = 55''/yr$  and  $\varepsilon = 23^\circ$ , the precession period is  $\frac{2\pi}{\alpha \cos \varepsilon} \approx 25900$  years.

But coupling between the spin axis dynamics and the slow variations of the Earth orbital plane creates resonances in the dynamics. The real spin axis dynamics is chaotic and its long term evolution is not given by the simple precessional motion at fixed obliquity value. The chaotic variations of the Earth spin axis is the topic of the present section.

#### 4.1.1 Motivations

A recent work by [63] investigated how long term perturbations by other planets could affect the obliquities and precession rates of all planets in the inner solar system. Combining an analysis

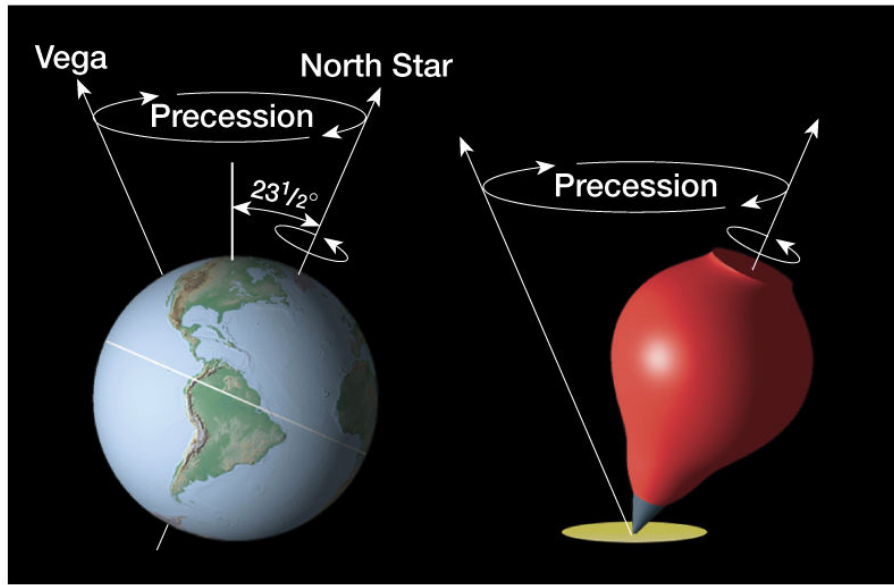


Figure 4.1.1: Illustration of the precession motion of the Earth spin axis. The precession is similar to the one observed for a spinning-top. Its period is about 25900 years.

of the fundamental frequencies of the planetary orbital plane motion (frequency map analysis) with numerical integration of the equations of motion, [63] was able to predict the location of strongly chaotic regions for some values of the precession constant  $\alpha$  of the planets. The main conclusion of this work is that the current planetary obliquities in the solar system are the result of long-term chaotic variations. The current obliquities of terrestrial planets cannot be considered as primordial. This explains the apparently puzzling value of the obliquities of some planets like Venus. Venus is the only planet that has a retrograde rotation, that is, the value of its obliquity is close to  $180^\circ$ . Different mechanisms, including the dissipative effects due to the very dense atmosphere of the planet, have been necessary to drive the planet from its primordial rotation state to the current one. However, the precise work by [21] has shown that chaotic evolution allows Venus spin axis to flip for a large set of initial conditions. Chaotic evolution is thus a fundamental mechanism to understand the rotational states of planets a long time after the formation of the solar system.

The case of the Earth is of particular interest, because it is the only planet that has a satellite with such a large mass ratio. The tides exerted by the Moon on the Earth are of similar order of magnitude as the ones exerted by the Sun. The presence of the Moon increases the effective value of the precession constant compared to a Moonless Earth ( $\alpha = 54.93$  arcsec/yr for the Earth with the Moon, less than 20 arcsec/yr without the Moon). The consequence is that the present obliquity of the Earth is trapped in a very stable region of phase space, and its obliquity is very well approximated by a periodic function of time composed of the precession of the equinoxes and a nutation of about  $2.6^\circ$ . On the contrary, the phase space of the Moonless Earth is divided into strongly chaotic regions created by resonance overlap, separated by regular regions. In a subsequent work, [78] also investigated the future of the Earth taking into account

the progressive separation from the Moon. It was shown with a set of 500 numerical simulations over 5 Gyr, that the Earth could reach an obliquity close to  $90^\circ$  after sufficient increase in the Earth-Moon distance. However, [70] conducted three simulations for the dynamics of the spin axis of the Earth with initial conditions without the Moon, and with initial obliquities located in the three strongly chaotic regions of phase space. Transport is very fast within those three strongly chaotic regions, but much slower in other regions of phase space. Over the age of the solar system, none of the three Moonless Earth leaves the strongly chaotic region in which it had started. Many astrophysicists now believe that large variations of a moonless Earth are possible, but occur in a typical time of many Gyr, and are thus difficult to observe with direct numerical simulations [67]. The aim of the present work is to confirm the existence of trajectories of the moonless Earth with large variations of its obliquity and give the order of magnitude of the transition rate of the obliquity from  $0^\circ$  to  $90^\circ$ .

### 4.1.2 Chaotic Hamiltonian dynamics

A simplified but realistic model for the dynamics of the spin axis of the Earth is given by the Hamiltonian [63]

$$H_E = \frac{\alpha}{2} p^2 + 2\sqrt{(1-p^2)} \sum_{k=1}^{13} \alpha_k \nu_k \sin(\nu_k t + q + \varphi_k). \quad (4.1.1)$$

With the current value  $\alpha = 54.93'' \text{yr}^{-1}$ , the Earth lies in a very stable region of phase space and large variations of its obliquity are impossible. But without the Moon, the precession constant  $\alpha$  of the Earth would be roughly reduced to  $20'' \text{yr}^{-1}$ . Because of dissipative tidal effects, the Moon goes away from the Earth, and the value of the effective precession constant of the Earth-Moon system is continuously reduced and will eventually reach the asymptotic value of  $20'' \text{yr}^{-1}$  when the Moon will be far enough from the vicinity of the Earth. The thirteen parameters  $\{\alpha_k, \nu_k, \varphi_k\}$  come from the quasiperiodic representation of the time evolution of the inclination of the Earth. In particular, some of the frequencies  $\nu_k$  are part of the fundamental frequencies of the Laplace-Lagrange secular system. The  $\alpha_k$  are nondimensional parameters that quantify the extension of chaotic regions. The parameters can be considered as fixed on a timescale of few Myr. These parameters are of small amplitude (see table (4.1)), which means that the Hamiltonian (4.1.1) is a weakly chaotic system.

The simple Hamiltonian (4.1.1) has one degree of freedom, and depends on time through a set of thirteen frequencies, which create resonances and chaotic motion in some regions of phase space. The amplitude of chaotic motion depends on whether the system lies in a region of resonance overlap, or, to say it equivalently, if its precession frequency  $\alpha$  is close to the values of the frequencies  $\nu_k$ . It has first been shown empirically by Chirikov that strong chaotic motion takes place if the fundamental frequency of the system is simultaneously close to at least two resonant frequencies. The criterion is very efficient to detect a priori the presence of chaotic regions and is now widely used with the name of *criterion of resonance overlap*.

Using the empirical Chirikov criterion of resonance overlap, we can draw a representation of chaotic regions in the plane of parameters  $(\varepsilon, \alpha)$ . We do not give here the technical details of the computations of the localization of the chaotic regions. The result is displayed in Fig.(4.1.2). The figure only displays the chaotic regions coming from resonances of first and second order, because the amplitude of higher order resonances is much smaller. Fig.(4.1.2) looks very similar to the precise map of chaotic regions obtained by frequency analysis by [63, 78]. This confirms that the criterion of resonance overlap can be used to predict qualitatively the presence or the absence of strongly chaotic regions in phase space.

From Fig.(4.1.2) we are able to predict the qualitative features of the dynamics of the obliquity of the Earth without the Moon, that is, for a value of the precession constant  $\alpha \approx 20''/\text{yr}$ .

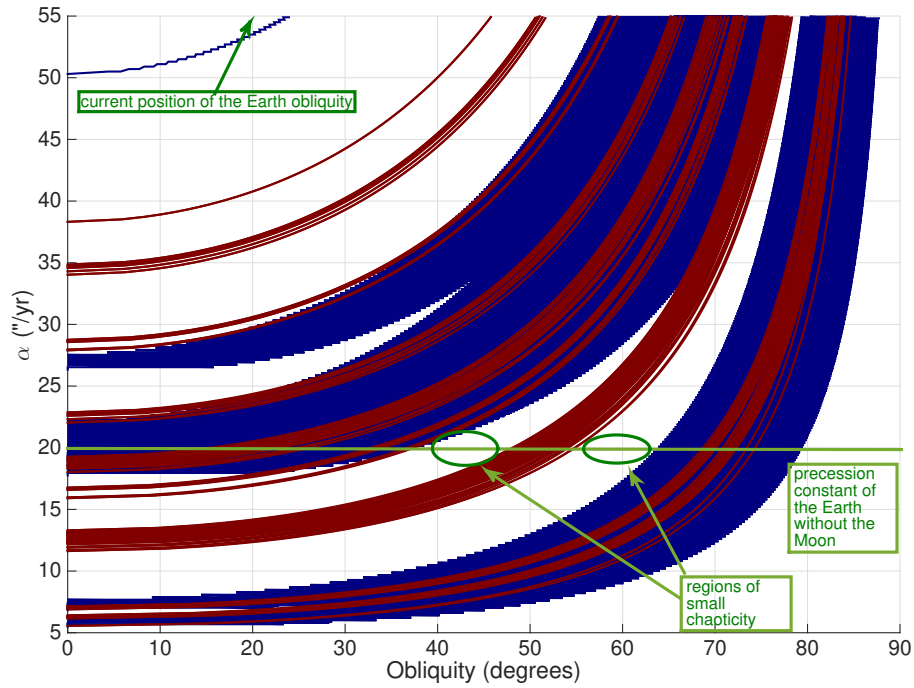


Figure 4.1.2: Representation of the chaotic regions in the plane  $(\varepsilon, \alpha)$ . The regions in blue correspond to first order resonances, the regions in red to second order resonances. Higher order resonances are not represented. The regions remaining in white are far away from the main resonances and are thus more regular. We obtained the figure from pure theoretical considerations and found that it is in agreement with the one obtained in [63] through frequency map analysis.

In Fig.(4.1.2), the green line of constant parameter  $\alpha = 20''/yr$  intersects three strongly chaotic regions: one between  $0^\circ$  and  $40^\circ$ , one around  $50^\circ$ , and one beyond  $65^\circ$ . Those three regions are separated by two more regular regions. We can then predict the following qualitative behavior: the Earth without the Moon can display very large variations of its obliquity up to about  $40^\circ$ , but has to cross two regular regions to reach a value close to  $80^\circ$ . We have confirmed this qualitative picture by a direct numerical simulation of the Hamiltonian dynamics (4.1.1). We integrated 86000 trajectories with initial conditions around  $\varepsilon = 10^\circ$ , using a Runge-Kutta algorithm of order 4. We found that transitions across the regular regions are possible but very rare, because we observed only around ten transitions between  $\varepsilon = 10^\circ$  and  $\varepsilon = 50^\circ$  within 300 Myr. This is an indication that, although very weakly chaotic, the two regions around  $45^\circ$  and  $60^\circ$  can be crossed, which means that no close periodic trajectories (KAM tori) subsist in those two regions.

The previous discussion aimed at showing that the question of the large variations of the spin of the Earth without the Moon is a classical problem of chaotic transport in a dynamical system, and is related to the existence or the breaking of KAM tori [69]. To reach a high value of its obliquity, the system has to jump from the first chaotic region  $\varepsilon \leq 40^\circ$  to the second region  $\varepsilon \approx 50^\circ$ , and then from the second to the third  $\varepsilon \geq 65^\circ$ . Between each of these regions, it has to cross a weakly chaotic region. Would KAM tori subsist in those regular regions (which is not the case here), the transitions would be impossible. If the KAM tori are just broken (this is what is called in the literature a ‘‘cantori’’), transitions are possible but extremely rare, that’s why the question to know if the Earth without the Moon can reach a high value of its obliquity has been for some time not obvious [70, 67].

The transitions between the three different chaotic regions can be considered as rare events for the system. The next section shows how the problem of large variations of the Moonless Earth is related to the theory of slow-fast dynamical systems.

### 4.1.3 Slow variations of the frequencies

Since the discovery that the solar system is chaotic [48, 47] with a Lyapunov time of about 10 Myr, it is known that the periodic solution of Laplace–Lagrange cannot represent accurately the secular variations of planetary orbits on the Myr timescale. The method of frequency analysis with the NAFF algorithm [57, 49] gives the instantaneous values of the fundamental frequencies of secular motion. The fundamental frequencies evolve in the Myr time scale, that is, on a time much larger than the typical period of secular motion. The chaotic secular motion of the planets can be represented by the periodic solution of Laplace–Lagrange with slow variations of the secular frequencies.

As an example, Fig.(4.1.3) shows the time variations of the secular frequencies  $\{s_i\}_{i=1..4}$  in a numerical simulation of the secular dynamics of the solar system over 500 Myr [65]. It can be clearly seen that the variations of the secular frequencies in the Gyr time-scale cannot be neglected. Although the relative variations of  $s_3$  and  $s_2$  are quite weak, of the order of 1%, those of  $s_1$  and  $s_4$  are much more important and are close to 10% for  $s_1$ . The secular frequencies variations have an important impact on the dynamics of the spin axis of the Earth. As explained in section 4.1.2, the amplitude of the chaotic regions depends on resonance overlap and thus on the values of the frequencies  $\{\nu_i\}$ . When those frequencies slowly vary with time, chaotic regions created by resonance overlap may be created, or disappear. The presence of KAM tori in phase space is also very sensitive to the exact value of the resonant frequencies. Any realistic model for the long-term variations of the obliquity of the Earth has to take into account the slow variations of the fundamental frequencies of the solar system.

Considering this new aspect of the dynamics, we propose to consider that the thirteen frequencies appearing in the Hamiltonian (4.1.1) depend slowly on time, that is, we write the

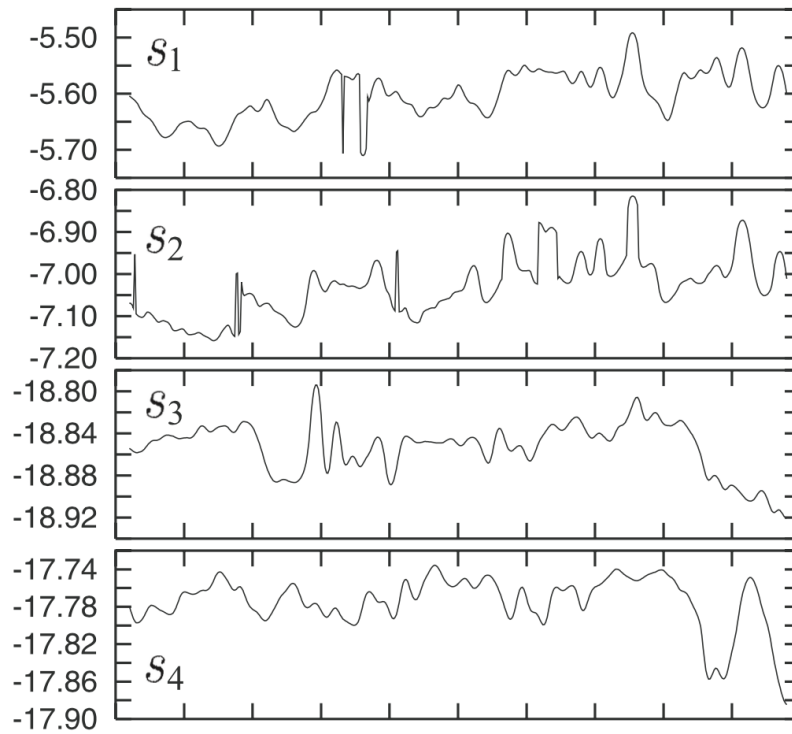


Figure 4.1.3: Time variations of the secular frequencies  $s_1$ ,  $s_2$ ,  $s_3$  and  $s_4$  recorded in a numerical simulation of the full solar system's dynamics over 500 Myr. The time interval on the horizontal axis is 50 Myr. The frequencies are given in arcsec/yr. Taken from [65]

Hamiltonian as

$$\mathcal{H}(p, q, t) = \alpha \frac{p^2}{2} + \sqrt{1 - p^2} \sum_{k=1}^{13} \alpha_k \nu_k(\eta t) \sin \left( q - \int_0^t \nu_k(\epsilon s) ds + \varphi_k \right). \quad (4.1.2)$$

In the new Hamiltonian (4.1.2), the functions  $\nu_k(t)$  are stochastic functions that model the chaotic variations of the secular frequencies. Let us emphasize this point: the functions  $\nu_k(t)$  are not deterministic functions of time. A polynomial representation of the time variations of the frequencies of the solar system has been proposed by [27] to construct planetary ephemerides. It is only valid over 40 Myr because it represents the deterministic variations of the frequencies, and those variations cannot be predicted much longer than the Lyapunov time of the solar system. We need a representation of the frequencies variations that is valid over the Gyr timescale. On such a timescale, much longer than the Lyapunov time of the chaotic dynamics of the solar system, the chaotic variations of the fundamental frequencies are hardly distinguishable from stochastic variations. The validity of a stochastic representation has to be understood in a statistical sense: we are looking for a stochastic representation of the frequencies that has the same stationary probability distribution, correlation time, and statistics of increments. We will explain in Section (4.2) how the numerical data obtained in [65] can be used to construct a stochastic model of the frequency variations.

The small parameter  $\eta$  quantifies the timescale separation between the precession motion of the Earth spin axis and the variations of the secular frequencies. A value of the precession constant  $\alpha = 20$  arcsec/yr corresponds to a period  $T_\alpha = 60000$  yr. On the other hand, the typical timescale of variation of the secular frequencies is 10 Myr. The small parameter  $\epsilon$  can then be estimated around

$$\epsilon \approx \frac{6 \cdot 10^4}{10^7} \approx 6 \cdot 10^{-3}.$$

The aim is to use the Hamiltonian with stochastic frequencies (4.1.2) to make a probabilistic description of the long-term variations of the obliquity of the Earth without the Moon. More precisely, we want to compute the probability distribution function (PDF) of the time  $\tau$  required to reach for the first time an obliquity of  $80^\circ$  starting from an obliquity at its actual value  $23^\circ$ . We focus on two questions: can the transition happen within a time shorter than the life time of the solar system? What is the “path” followed by the system in phase space to do this transition? What is the influence of the variations of the fundamental frequencies  $\nu_k$  in the probability of transition?

As a matter of fact, we could not solve completely the problem for the obliquity of the Earth with the Hamiltonian model (4.1.2). The main reason is that we could not give a satisfactory stochastic representation of the frequencies  $\nu_k(t)$  because of a lack of empirical data. We can not state that the model presented in the present work gives the precise numerical values for the probability distributions of the spin axis of the Earth, and for the probabilities of large variations of the obliquity. The scope of the present work rather consists in showing a new mechanism of transport in Hamiltonian systems. In this section, we study the particular example of the spin axis of the Earth to find the generic properties of transport in phase space for a chaotic Hamiltonian dynamics of 1.5 degrees of freedom depending on slow stochastic parameters. The Hamiltonian (4.1.2) has the general form

$$H(p, q, t, \nu(\epsilon t)), \quad (4.1.3)$$

where  $\epsilon \ll 1$  is a small parameter, and  $\nu(t)$  is a  $p$ -dimensional stochastic parameter. We show how averaging can be applied to systems of type (4.1.3) to compute the long-term diffusion in phase space.

## 4.2 Stochastic dynamics for the long-term evolution of the secular frequencies

In this section, we will try to build a realistic stochastic model for the long-term variations of the frequencies  $\nu_k(t)$  in the Hamiltonian (4.1.2). The model we propose is fully empirical, and is based on the numerical data obtained by the team of Jacques Laskar at the IMCCE (see Fig.(4.1.3)). The stochastic model can then be used as an input in the Hamiltonian dynamics of the spin axis of the Earth.

### 4.2.1 Auto regressive model

The fundamental assumption of our model is that the variations of the secular frequencies of the solar system can be described by an auto-regressive signal perturbed by a white noise. Let  $y_n$  be a discrete signal, for example an evaluation at discrete times of one of the frequencies  $s_{1-6}$ . We assumed that there exist an integer  $M$  and some real parameters  $\{b, a_1 \dots a_M\}$  such that the signal  $y_n$  follows the auto-regressive relation

$$y_{n+1} = b + \sum_{k=1}^M a_k y_{n+1-k} + \xi_n. \quad (4.2.1)$$

In Equation (4.2.1), the term  $\xi_n$  is a random variable with some probability distribution  $w(\xi)$ . All variables  $\xi_n$  have the same distribution  $w(\xi)$ , and are uncorrelated,  $\langle \xi_n \xi_{n'} \rangle = 0$  for  $n \neq n'$ .

Let us discuss the meaning of Equation (4.2.1). The number of coefficients  $M$  determines the length over which the signal is correlated. If  $M = 1$  for example, it means that the signal is a Markov process where the next step is only determined by the present state. For a more general signal, we assume that the signal has finite correlations of length  $M$ . The noise random variables  $\xi_n$  model the chaos in the system. In signal processing, one usually wants to recover a ground signal perturbed by noise coming from the environment. In our case, the noise is created by the chaos inside the system, therefore we don't want to get rid of the noise, but on the contrary extract the random variables  $\xi_n$  and find their probability distribution  $w(\xi)$ .

We do not give a fundamental justification why the signal of the secular frequencies could be described by an Equation like (4.2.1). The auto-regressive model (4.2.1) is purely empirical, and we want to evaluate empirically the coefficients  $\{b, a_1 \dots a_M\}$  and the probability distribution  $w(\xi)$  from the signal itself. It may seem quite disturbing to assume the relation (4.2.1) for the frequencies of the solar system, because the signal of the frequencies might not be stationary, the coefficients  $\{b, a_1 \dots a_M\}$  might depend on the signal  $y_n$  through a nonlinear relation, ..etc. However, an empirical auto-regressive model like (4.2.1) is already used in different fields of physics and can give very realistic predictions. In the following, we describe the method we used to build the model (4.2.1) for the secular frequencies of the solar system.

### 4.2.2 Algorithm

The curves of the secular frequencies  $g_{1-8}$  and  $s_{1-8}$  are given in [65] over 500 Myr. Only the frequencies  $s_{1-4}$  are interesting for the spin axis dynamics. As a first step, we have discretized the signals keeping only a value each 5 Myr. The Lyapunov time of the solar system is of the order of 10 Myr [47], and thus random changes in the secular frequencies should occur over the same timescale. To discretize the signal of the frequencies, we have chosen a time step comparable to the Lyapunov time of the solar system to be consistent with Equation (4.2.1) where the noise terms  $\xi_n$  at each time step are uncorrelated. The result is a discrete sequence  $y_n$  of length 100, giving the variations of the frequencies over 500 Myr.

The next step is to evaluate the parameters  $\{b, a_1, \dots, a_M\}$  from the signal. This is a well known problem in signal processing, and it can be solved using the Levinson--Dublin algorithm [36]. The Levinson--Dublin algorithm, gives the best possible value of  $M$  and an estimation of  $\{b, a_1, \dots, a_M\}$ , assuming that the signal to analyze is of the form (4.2.1). The algorithm extracts from the signal  $y_n$  the “deterministic part”  $\tilde{y}_n$ , which is the value that would take  $y_n$  without noise  $\tilde{y}_{n+1} = b + \sum_{k=1}^M a_k y_{n+1-k}$ , and the difference between the deterministic part and the real signal  $\xi_n := y_{n+1} - \tilde{y}_{n+1}$ . The difference  $\xi_n$  is interpreted as the “noise” in the signal.

Once we have extracted the noise signal  $\xi_n$ , we want to find a stochastic model for the noise, and thus find out which can be its probability distribution  $w(\xi)$ . This is the difficult point, because the signal has only 100 values, and is too small to give a precise estimation of the distribution function  $w(\xi)$ . An example of the empirical distribution of the noise for the frequency  $s_3$  is represented by the histogram  $h(\xi)$  of Fig.(4.2.1). Although it is not possible to fit consistently the histogram of Fig.(4.2.1), it is possible to exclude possible shapes of the probability distribution  $w(\xi)$ . The distribution of the noise  $w(\xi)$  cannot follow a power law as  $w(\xi) \propto \frac{1}{|\xi|^\alpha}$  for some real exponent  $\alpha > 1$ , because we do not observe in the histogram  $h(\xi)$  the “fat tails” characteristics of power law distributions. To confirm this point, we simulate a distribution of 100 random variables following a power law  $\frac{1}{|\xi|^\alpha}$ , for different values of  $\alpha$ . None of the power law distribution could be compared to the histogram  $h(\xi)$ . Another possibility could be to fit the histogram  $h(\xi)$  with a Gaussian law  $w(\xi) \propto e^{-\frac{\xi^2}{2i^2}}$ . However, the best Gaussian fit of  $h(\xi)$  do not reproduce the tails of the empirical distribution. We have concluded that a possible distribution for  $w(\xi)$  could be a exponential law of parameter  $\lambda$ , that is

$$w(\xi) = \frac{1}{2\lambda} e^{-\frac{|\xi|}{\lambda}}. \quad (4.2.2)$$

The conclusion is that the variations of the frequencies  $s_{1-4}(t)$  of the solar system can be modeled by an auto-regressive process (4.2.1) with exponential noise distribution (4.2.2). All parameters of the model,  $M$ ,  $\{b, a_1 \dots a_M\}$ , and  $\lambda$  are given for each secular frequency in Table (4.1). We emphasize once more that the model (4.2.1) should not be taken as rigorous in the sense that it has no precise theoretical justification derived from Hamilton’s equations. It is purely empirical, and it has to be compared to the numerical results obtained with complete simulations of the dynamics of the Solar system.

### 4.2.3 Results

With the stochastic model (4.2.1) and the parameters of Table (4.1), it is possible to give different realizations of the frequencies  $s_{1-4}(t)$ , considered as stochastic functions of time. For example, let us consider a new realization  $\tilde{s}_1(t)$  of  $s_1(t)$ . From Table (4.1), we have  $M = 1$ . We take the same initial value  $\tilde{s}_1(-250)$  and  $s_1(-250)$  at -250 Myr, and then we generate the sequence of  $\tilde{s}_1$  with the auto-regressive model, having one value each 5 Myr. The result is a discrete sequence  $\tilde{s}_1$  of length 100. According to the work of [27], the variations of the secular frequencies can be very accurately represented over 40 Myr by a polynomial approximation using the Chebychev polynomials. This means in particular that the secular frequencies can be represented by regular functions on the Myr timescale. To generate a consistent continuous realization  $\tilde{s}_1(t)$ , we thus interpolate the 100-values sequence obtained with the auto-regressive model using the “spline” function of Matlab, which is a local cubic polynomial interpolation.

We generated with the same method different realizations of  $s_2, s_3, s_4$ . On Fig.(4.2.2), we display the frequency curves  $s_{1-4}$  obtained by [65] in blue, together with a realization of our stochastic autoregressive model in red. The stochastic auto-regressive model generates consistent

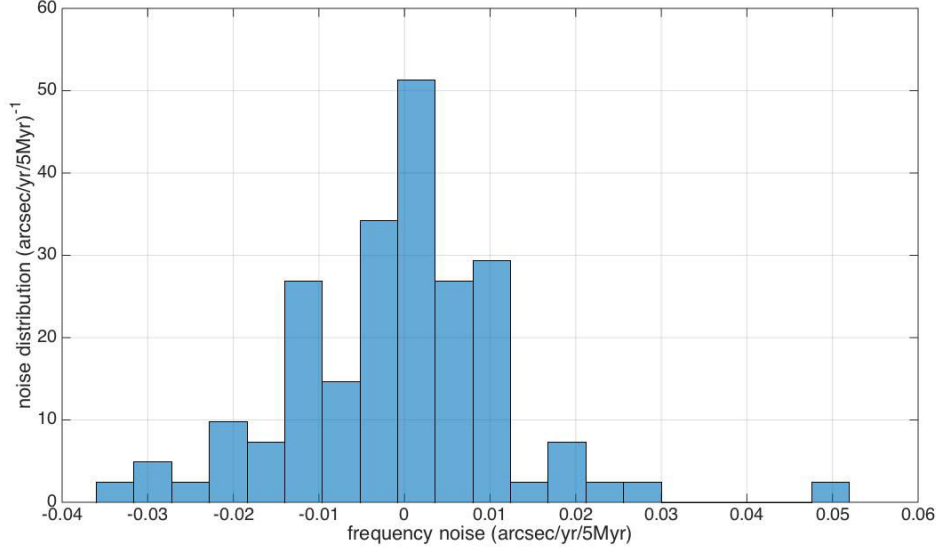


Figure 4.2.1: Probability distribution of noise in the secular frequency  $s_3$ . The noise term creates a variation of the secular frequency of few hundredths of arcsec/yr each 5 Myr.

realizations  $\tilde{s}_{1-4}(t)$  of the secular frequencies  $s_{1-4}(t)$  in the sense that the stochastic realization looks very similar to the real frequency curves obtained by numerical simulations. It is sometimes not easy to distinguish at the first look the real frequency curve from its stochastic realization. The stochastic realization  $\tilde{s}_i(t)$  of a frequency curve  $s_i(t)$  has variations of the same order of magnitude occurring over the same timescale.

However, the stochastic auto-regressive model (4.2.1) has some limitations and cannot reproduce all characteristics of the true signal. In particular, it is not able to reproduce very abrupt variations of the frequencies. There are some sharp peaks in the frequency curves, especially in  $s_1$  and  $s_2$ , that will never appear in the stochastic realization, because the timescale for variation of the frequency in the auto-regressive model is 5 Myr. Another feature to distinguish the stochastic realizations  $\tilde{s}_{i=1..4}(t)$  from the curves  $s_{i=1..4}(t)$  obtained by numerical simulations is that the step size of 5 Myr is clearly visible in the stochastic realizations, whereas in the numerical curves, there are sometimes larger intervals without any significant frequency variations.

One should thus not expect the stochastic auto-regressive model (4.2.1) to give real realizations of the secular frequency variations in the solar system, that is, realizations one would obtain in a direct numerical simulations of the full solar system with some initial conditions of the planets. The red curves on Fig.(4.2.2) should be thought of as an imitation of the real chaotic dynamics of the solar system. The great interest of the stochastic auto-regressive model is that, once it is calibrated with the good choice of parameters, it can give very fast a large number of realizations of the secular frequency curves, without the need to resort to heavy numerical simulations of the solar system. I will now use the imitations of the secular frequency curves given by equation (4.2.1) as an input in the stochastic Hamiltonian model (4.1.2) for the spin of the Earth.

In the present section, I have built a stochastic model for the long-term variations of the frequencies  $s_{1-4}(t)$ , which are four of the thirteen frequencies  $\nu_k(t)$  of the Hamiltonian (4.1.2).

frequency	$M$	$(a_i)_{i=1..M}$	$b$ (arcsec/yr)	$\lambda$ (arcsec/yr)
$s_1$	1	0.7653	-1.3156	0.02
$s_2$	1	0.8105	-1.3324	0.03
$s_3$	4	0.9410   -0.3202   0.3604   -0.1596	-3.3634	0.01
$s_4$	2	1.0521   -0.3253	-4.8563	0.01

Table 4.1: Parameters of the stochastic autoregressive model (4.2.1).

I could not apply the same model to the nine remaining frequencies, because there is at the time being no recording of the time evolution of those frequencies on the Gyr timescale. I have therefore chosen to keep constant the nine frequencies for which I do not have a stochastic model. I therefore cannot state that the numerical simulations performed with the model (4.1.2) are realistic. Yet, I believe that the model (4.1.2) with stochastic representation of the frequencies  $s_{1-4}(t)$  gives the right orders of magnitude for the probability distribution functions of the spin of the Earth because the spin axis dynamics is mainly sensitive to the variations of the frequencies  $s_3$  and  $s_4$ , and much less to the other frequencies.

### 4.3 Qualitative picture of the transport mechanism in phase space

Before turning to direct numerical simulations, we explain in this section the transport mechanism in phase space  $(p, q)$ . We show in particular that the large variations of the obliquity of the Earth is related to slow distortions of the chaotic structure of the phase space, due to the slow chaotic frequency variations.

#### 4.3.1 Chaotic regions are created by resonance overlap

Table (4.2) gives the numerical values of the parameters  $\{\alpha_k, \nu_k, \varphi_k\}$  of the Hamiltonian (4.1.2). The parameters  $\nu_k$  of table (4.2) are the values of the frequencies at  $t = 0$ . The parameters are computed using the results obtained in [51] with frequency map analysis, although more precise values could be found in [65]. The fundamental frequency of the unperturbed dynamics is  $\alpha p$ . Therefore, the ratio  $\frac{\nu_k}{\alpha}$  gives the localization of the resonances in  $p$ -space. Table (4.2) shows that the thirteen frequencies are divided in two clusters: one cluster of 6 frequencies is located in the region  $p > 0.96$  (or equivalently  $\epsilon < 14^\circ$ ), and the other one is composed of 6 frequencies located in the region  $p < 0.40$  (or equivalently  $\epsilon > 67^\circ$ ). The two clusters of frequencies create two separated regions of large scale chaos in phase space. They are called in the following “region 1” and “region 2” respectively, and are the two main chaotic regions created by the overlap of resonances of first order. They correspond to the blue regions in Fig.(4.1.2). Another chaotic region is located around  $p = 0.5$  (or equivalently  $\epsilon = 60^\circ$ ) and is created by the overlap of the resonances of second order. The resonances of second order are given by the average of all couples of resonances of first order  $\left\{ \frac{\nu_i + \nu_j}{2} \right\}_{i,j=1..13}$ . This chaotic region is called “region 3” in the following.

In Fig.(4.3.1), we have represented two pictures to help the reader understand the chaotic structure of phase space. On the left, we have represented the eyes of the four main resonances in red. The resonances are located at the values  $p_k = -\frac{\nu_k}{\alpha}$ , with  $\alpha = 55/3$  "/yr. All the regions of phase space covered by the eyes are strongly chaotic. Additionally to the two main chaotic regions, the resonances of second order create a chaotic band of large extension in the middle

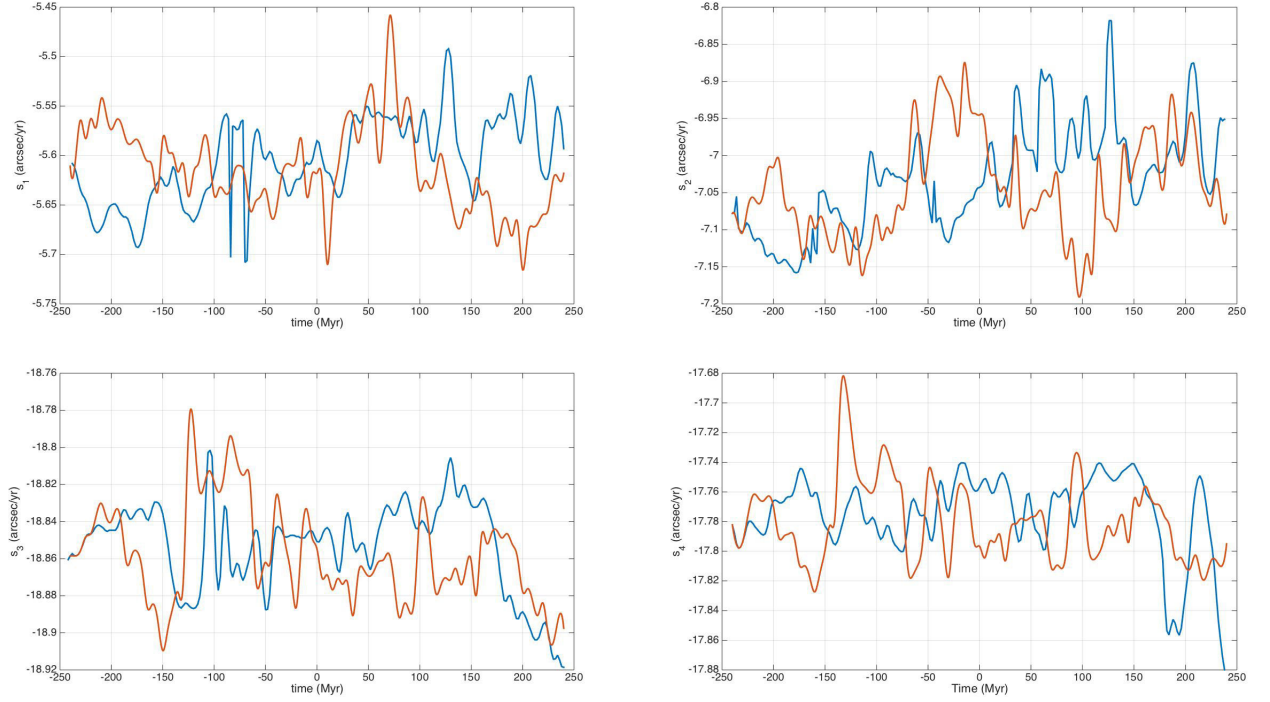


Figure 4.2.2: Variations of the secular frequencies  $s_{1-4}$  over 500 Myr (blue curves). On each graph, we plotted one realization of the stochastic auto-regressive model (4.2.1) for the considered secular frequency (red curves).

k		$\nu_k$ (arcsec/yr)	$\alpha_k \times 10^3$	$\phi_k$ ( $^\circ$ )
1	$s_3$	-18.8504	8.841679	151.724
2	$s_4$	-17.7544	4.017321	199.002
3		-18.3016	2.698497	176.641
4	$s_6$	-26.3302	1.334632	37.294
5	$s_1$	-5.6128	5.040585	270.479
6		-19.3997	1.525373	305.514
7	$s_2$	-7.0772	3.454670	9.899
8		-19.1251	0.894284	46.398
9		-6.9564	1.971634	199.316
10		-7.2037	1.604732	176.470
11		-6.8283	1.637102	233.037
12		-5.4892	1.506215	289.422
13	$s_6 - g_6 + g_5$	-50.3021	0.002138	120.161

Table 4.2: Numerical values used for the parameters in the Hamiltonian (4.1.2). The values are taken from [51]. The reader should be careful that the definition of the parameters  $\alpha_k$  in the present table is different from the ones given in [51]. The parameters are ordered with decreasing values of the product  $\alpha_k \nu_k$  such that the frequencies at the top of the table contribute more to chaotic motion than those at the bottom.

of phase space. The three chaotic regions are separated by two regular bands, in which the transport is only possible through the weak chaos created by higher order resonances, of much smaller amplitudes. On the right of Fig.(4.3.1), we have represented the bands associated to the chaotic regions 1,2 and 3. The regions of weak chaos, which we call the “regular” regions, are labelled as regions 4 and 5. Within the bands 1,2 and 3, chaos is strongly developed, and the system is thus rapidly carried throughout the band. The bands are separated by regions 4 and 5 of much weaker chaos: the system can hardly cross those regular regions, and therefore the migration between one band to the other is very slow.

### 4.3.2 Transitions between chaotic regions

The important point to emphasize is that Fig.(4.3.1) is not static: the frequencies  $\nu_k$  are slowly varying around their mean values  $\nu_k^*$ , with stochastic variations defined by an auto-regressive model of the form (4.2.1). These slow variations of the frequencies imply that the transport in phase space does not only happen through the well known “chaotic diffusion” observed in chaotic maps (e.g the standard map, see [69] chapter 5). It also comes from two other mechanisms that we now describe qualitatively:

1. The chaotic regions themselves are moving in phase space. The displacement is illustrated by the vertical arrows in Fig.(4.3.1). If the system is in one of those chaotic regions, it is carried together with the region upwards or downwards. At any time, it can leave the region and enter in the regular part of phase space. But depending on when the system leaves the region, it can be carried up or down far away from its initial position. This kind of transport is referred to as “transport of the first type”, it is specific to chaotic Hamiltonians.
2. Chaotic diffusion in the regions of weak chaos is enhanced by the slow stochastic variations of the fundamental frequencies. As a result, no KAM tori can subsist in the regular regions 4 and 5 of Fig.(4.3.1). Even if it is away from the resonances, the system will diffuse through phase space because of the slow stochastic deformation of the orbits of the regular regions. This type of transport can be found for both integrable and chaotic Hamiltonian dynamics and is referred to as “transport of the second type”.

Depending on the parameters of the map, one of the two mechanisms described above overcomes the other and is the main mechanism responsible for the transport through phase space. The dominant mechanism of transport depends on the typical amplitude of the variations of  $\nu_k(t)$ . For large variations of  $\nu_k$ , transport of the first type is dominant (the precise the meaning of “large” will become clear in sections 4.4 and 4.5). For the dynamics of the Earth spin axis, section 4.4 will show that we are in the regime for which both transport mechanisms approximately contribute at equal rate. Therefore, we were not able to do theoretical predictions of transport rates for the Earth spin axis. We introduce in section 4.5 a simpler Hamiltonian model for which transport of the first type is dominant and transport rates can be recovered from averaging techniques.

Let us focus for the moment on the Moonless Earth. The system starts at  $p = 0.92$  ( $\varepsilon = 23^\circ$ ) in region 1. It can reach a value close to  $p = 0$  through successive jumps from one region to the other, until it eventually reaches the chaotic region 2. To illustrate the transport mechanism, we have represented in Fig.(4.3.2) the different steps of the transport. We have labelled the chaotic and regular regions the same way as in Fig.(4.3.1). First, one fluctuation downwards of the frequencies of the first cluster brings the chaotic region 1 and the system together around  $p = 0.7$ . Then, region 1 moves upward again, but the system leaves the chaotic region and is thus trapped in region 4. A simultaneous displacement upwards of the frequencies brings the

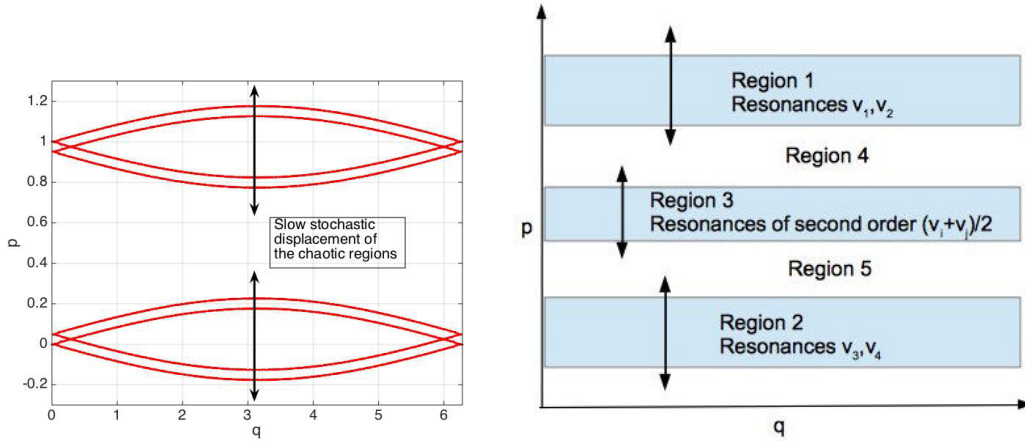


Figure 4.3.1: Schematic representation of the chaotic structure of the phase space for the Hamiltonian (4.1.2).

region 3 of second order resonances upwards, and it captures the system. The system has thus passed from region 1 to region 3 thanks to the fluctuations of the frequencies. It then passes from region 3 to region 2 by a similar trajectory of the frequencies: it is transported downward and dropped in region 5 and an eventual displacement upward of region 2 captures it and brings it to  $p = 0$ .

The mechanism of transport we just described, composed of successive jumps between regions of different types, is typical to go from  $p$  close to 1 to  $p$  close to zero, in the regime where chaotic diffusion in the regular regions is negligible. As the reader would have surely noticed, it does not really matter where the system is exactly located when it is inside a chaotic region of type 1,2 or 3. The mixing in those strongly chaotic regions is so fast compared to the timescale for frequencies variations, that the system has time to explore the whole region before any significant displacement of the region. To say it another way, the underlying Hamiltonian dynamics is not important to determine the characteristics of transports. In fact, only two properties of the dynamics matter. The first one is the conservation of area which is characteristic of Hamiltonian dynamics (it is sometimes said that the Hamiltonian flow is a symplectic transformation). The conservation of area implies that the stationary measure is uniform for ergodic Hamiltonian flows. The second one is that the phase space is partitioned into several strongly mixing regions (where chaos is strongly developed), separated by regular regions. The two properties are generic of Hamiltonian systems of 1.5 degrees of freedom, that's why the mechanism of transport described here for the obliquity of the Earth could be found in any symplectic maps with slowly varying parameters. Those two properties prompted us to perform a kind of “averaging” of the Hamiltonian dynamics and build an even simpler, fully stochastic model, that we call the *local diffusive model*.

### 4.3.3 Averaging of the dynamics: the local diffusive model

The local diffusive model is a purely stochastic model built from the Hamiltonian model (4.1.2) with slow chaotic frequencies. The idea is to average the dynamics over an intermediate time which is much longer than the timescale of the Hamiltonian dynamics, but smaller than the timescale for chaotic variations of the frequencies. As the timescale of the Hamiltonian dynamics

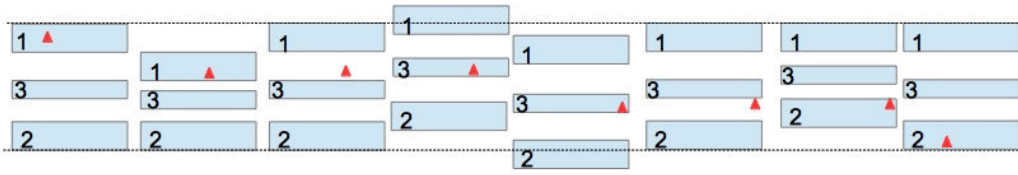


Figure 4.3.2: Example of a trajectory in the Hamiltonian stochastic model (4.1.2). The system, represented by the red triangle, has a transition from region 1 to region 2 through successive jumps between the chaotic regions. See explanations on page 99.

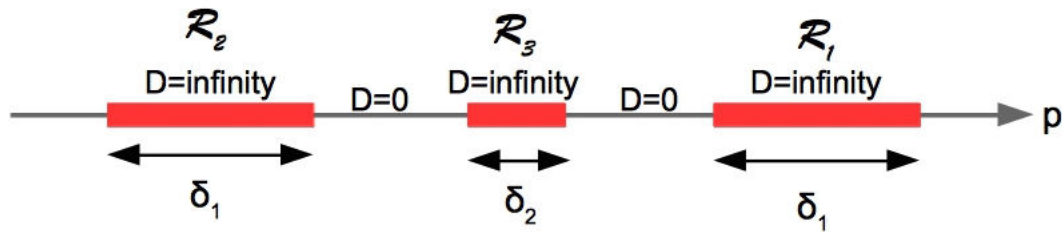


Figure 4.3.3: Schematic representation of the local diffusive model. The regions 1,2 and 3 with infinite diffusion coefficients are displayed by the red rectangles.

is typically of order  $\frac{1}{\alpha}$ , the averaging procedure is done over a time  $\tau_{av}$  satisfying

$$\frac{1}{\alpha} \ll \tau_{av} \ll \frac{1}{\epsilon\alpha}. \tag{4.3.1}$$

On the timescale  $\tau_{av}$ , the Hamiltonian dynamics is mixing in the chaotic regions. The strong chaos separates the neighboring trajectories exponentially fast. The Lyapunov time of region 1 has been estimated in [67] to 1 Myr. On a timescale  $\tau_{av}$  larger than 1 Myr, the system has thus completely “forgotten” its initial condition. This means that if the system has an initial condition inside the chaotic region 1 of Fig.(4.3.2) (for example), it can be anywhere inside the region 1 after a time  $\tau_{av}$ . On the other hand, we assume that the chaos is weak enough in the regular regions 4 and 5 of Fig.(4.3.2) such that the system does not diffuse in phase space within the time  $\tau_{av}$ .

The local diffusive model of second order is represented in Fig.(4.3.3). It consists of three patches of infinite diffusion coefficient  $D$  in  $p$ -space. Two of them have an extension  $\delta_1$ , and correspond on Fig.(4.3.1) to the chaotic regions 1 and 2 of main resonances. The third one has a smaller extension  $\delta_2$  and corresponds to region 3 of second order resonances in Fig.(4.3.1). We assume that chaotic transport is negligible away from the resonances of first and second orders, that’s why we set the diffusion coefficient to zero out of the diffusive patches. The infinite diffusive patches are then moved according to the frequency dynamics.

The solution cannot be represented any more by a trajectory, but only through the probability distribution  $\rho_\nu(p, t)$  to find the system at impulsions  $p$  at time  $t$ , given a realization of the stochastic process  $\nu(t)$ . Let  $\delta_i$  be the extension of the  $i$ -th diffusive region that we call  $\mathcal{R}_i$ . The

diffusive region  $\mathcal{R}_i$  then covers the interval  $[\nu_i - \delta_i/2, \nu_i + \delta_i/2]$ . If the impulsion  $p$  is out of all diffusive regions, the function  $\rho_\nu(p, t)$  remains the same at step  $t + dt$ . If  $p$  is inside the diffusive region  $\mathcal{R}_i$ , the probability distribution at step  $t + dt$  is the average of the probability distribution over the whole region. The dynamics of the distribution  $\rho_\nu(p, t)$  can be implemented following the equations

$$\rho_\nu(p, t + dt) = \begin{cases} \frac{1}{\delta_i} \int_{\nu_i(t) - \delta_i/2}^{\nu_i(t) + \delta_i/2} \rho_\nu(p', s) dp' & \text{if } p \text{ is in region } \mathcal{R}_i \\ \rho_\nu(p, t) & \text{otherwise} \end{cases} \quad (4.3.2)$$

The consequence of Equation (4.3.2) is that at each step, the probability distribution is constant over each region  $\mathcal{D}_i$ . But as the reader can see on Equation (4.3.2), the region  $\mathcal{D}_i$  is moving because of the variations of the frequencies  $\{\nu_i\}_{i=1..13}$ . Therefore, at the next step, the average is performed over a region which has slightly moved during the time step  $dt$ .

In this section, we have set up the mathematical framework we work on. We have two models at hand: the first model is a Hamiltonian model (4.1.2) depending on time and on slowly varying frequencies. The second model is completely stochastic, and can be thought of as the ‘‘averaging’’ of the first model. It is called the local diffusive model, and defined by equation (4.3.2). The great interest of the local diffusive model is that it is completely stochastic, and thus much simpler to study than the first model, which still keeps the complexity inherent to a chaotic dynamics.

We still did not explain under which conditions the local diffusive model gives relevant predictions for Hamiltonian dynamics. Section 4.5 shows that the local diffusive model (4.3.2) is valid when transport is completely dominated by the mechanism of slow displacement of the chaotic regions, what we have called ‘‘transport of the first type’’. Transport of the first type is dominant when the amplitude of frequency variations is of same order as the gap between two neighboring chaotic regions. This will also be illustrated in section 4.5.

#### 4.3.4 Numerical characterizations of the chaotic regions

To put on a rigorous basis the ideas of sections (4.3.1-4.3.2), we first have to define properly the ‘‘regions’’ of phase space. What are exactly the frontiers of the ‘‘chaotic regions’’? The difficult point is that the frontiers of chaotic regions in this problem are *not* given by an equation  $p = \text{constant}$ . The frontiers can be seen as curves in phase space, whose shape depends also on time.

Consider again the Hamiltonian (4.1.1), in which the parameters are constant. There exists a canonical transformation  $(p, q) \rightarrow (P, Q)$  such that the Hamiltonian (4.1.1) becomes

$$H(P, Q) = \alpha \frac{P^2}{2} + H_{pert}^{(2)}(P, Q, t), \quad (4.3.3)$$

where  $H_{pert}^{(2)}(P, Q, t)$  is the part of the Hamiltonian that contains resonances of second order. The canonical change of variable can be achieved using the classical technique of Lie transforms close to the identity. In particular,  $H_{pert}^{(2)}$  is of much smaller amplitude than the part  $H_{pert}^{(1)}(p, q, t) := \sqrt{(1-p^2)} \sum_{k=1}^{13} \alpha_k \nu_k \sin(\nu_k t + q + \varphi_k)$  in the initial Hamiltonian (4.1.1) because it is composed of a sum of terms of amplitudes  $\{\alpha_i \alpha_j\}_{i,j=1..13}$  and higher order terms of smaller amplitudes. If we neglect the part  $H_{pert}^{(2)}$  in (4.3.3), it turns out that the quantity  $\alpha \frac{P^2}{2}$  is conserved, and thus  $P$  is conserved. The canonical variable  $P$  can be considered as an integral of motion to first order in the parameters  $\alpha_k$ . It is the best integral of motion we can build when the system is away

from the first order resonances.  $P$  is thus an excellent candidate to define the frontiers of the chaotic regions 1 and 2. The explicit expression of  $P$  to first order in  $\alpha_k$  is

$$P(p, q, t) := p + \sqrt{1 - p^2} \sum \frac{\alpha_k \nu_k}{\alpha p + \nu_k} \sin(q + \nu_k t + \phi_k) + O(\|\alpha_k\|^2). \quad (4.3.4)$$

We define the frontiers of a chaotic region by the equation

$$P(p, q, t) = \bar{P}.$$

$\bar{P}$  is a constant that has to be computed for each chaotic region 1,2 and 3. In the present work, we only study the transitions from region 1 to region 3. To find the values of  $\bar{P}$  that correspond to the upper frontier of region 3, we perform two numerical simulations. We integrate 1848 trajectories with close initial conditions inside the region 1, and the same for region 3. Because of the mixing properties of the chaotic dynamics (4.1.1), the distribution of trajectories spreads in few turnover times all over the respective regions. After a time  $T := 7000 \times \frac{1}{\alpha}$ , we plot the distribution of trajectories with respect to the variable  $P$ . The result is displayed in Fig.(4.3.4). There is some arbitrariness in the choice of the values of  $\bar{P}$  to define the chaotic regions. The upper frontier of the chaotic region is defined as the value  $\bar{P}$  such that 80% of the trajectories starting in region 3 satisfy the relation  $P < \bar{P}$ . On the contrary, the lower frontier of a chaotic region is defined as the value  $\bar{P}$  such that 80% of the trajectories starting in region 1 satisfy the relation  $P > \bar{P}$ . In section 4.4, we will look for transitions of the system from region 1 to region 3. With the criterion defined above, we find the value  $\bar{P} = 0.7110$  for the upper frontier of region 3. The frontiers of chaotic regions are displayed in Fig.(4.3.4). The criterion of entrance into region 3 is thus

$$P(p, q, t) < 0.7110. \quad (4.3.5)$$

In the simulations of the dynamics (4.1.2), the frequencies depend on time, and thus the value  $\bar{P}$  of entrance into region 3 also changes. Yet, the amplitudes of frequency variations are quite small compared to the size of chaotic regions. (4.3.5) still holds and will be used in section 4.4.

### 4.3.5 The problem of first entrance times

In section 4.4, we will perform a set of numerical simulations of the dynamics of the spin axis of the Moonless Earth. The aim is to compute the probability of transitions between the three main chaotic regions 1,2 and 3 in phase space. Those transitions are very rare, and the numerical cost of the simulations is quite high because we have to integrate a lot of trajectories to obtain a good statistics for the transitions. I have thus chosen to focus only on the transitions from region 1 to region 3. We choose a time interval  $\Delta T$ . For  $N \gg 1$  trajectories, the flux  $J(t)$  can be estimated as the ratio  $\frac{n(t)}{N}$ , where  $n(t)$  is the number of trajectories that enter in region 3 between  $t$  and  $t + \Delta T$ . We will compute in section 4.4 three quantities of interest.

1. The flux  $J_{fix}(t)$  entering into region 3 for fixed values of the frequencies  $\nu_k(t)$ .
2. The flux  $J_{ref}(t)$  entering into region 3 for a given realization of the time-dependent frequencies  $\nu_k(t)$ . For this simulation, we will use the functions  $s_{1-4}(t)$  obtained in [56] with a complete simulation of the dynamics of the Solar system for 500 Myr. In particular, we will compare the average value of the fluxes  $\langle J_{ref} \rangle$  and  $\langle J_{fix} \rangle$  to see the influence of the variations of the frequencies.
3. The probability flux  $\langle J_{chaos} \rangle$  entering into region 3 averaged over a large number of realizations of the time-dependent frequencies  $\nu_k(t)$ . The realizations of the frequencies are computed with the auto-regressive model (4.2.1).

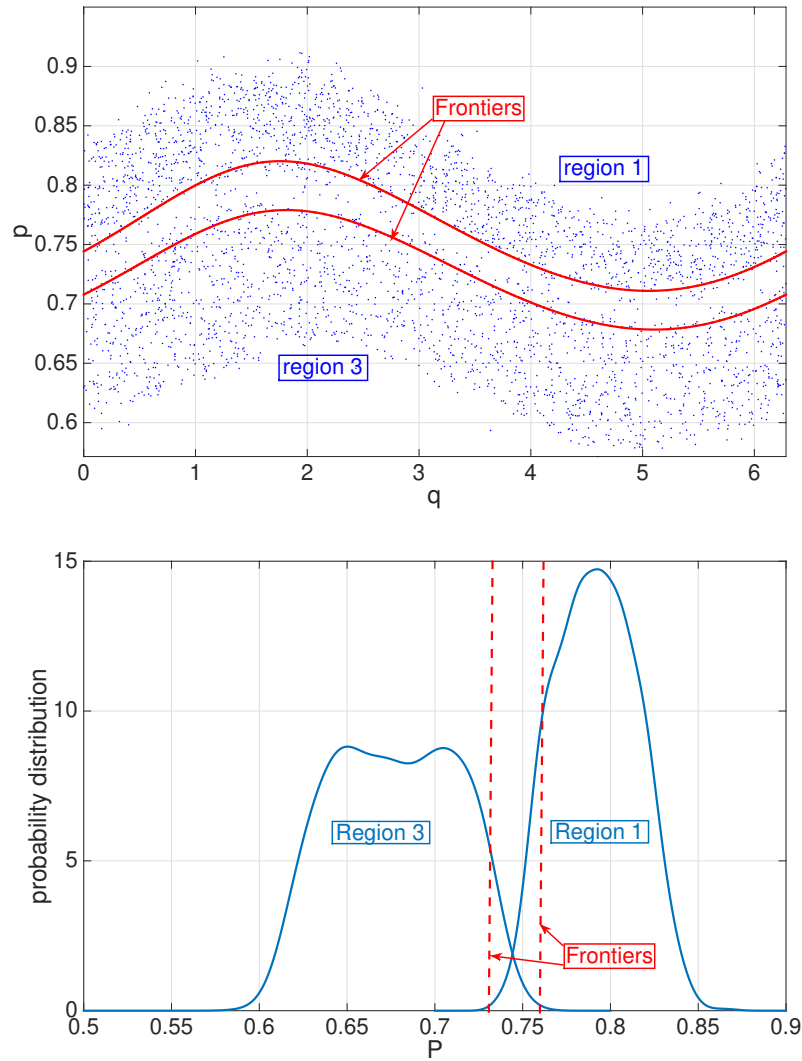


Figure 4.3.4: The left picture represents the trajectory distribution after a time  $T := 7000 \times \frac{1}{\alpha}$ . The trajectories starting in region 1 have spread but are still localized in region 1. 80% of them are above the frontier defined by the first red curve. The same happened in region 3, and 80% of the trajectories starting in region 3 are still localized under the second red curve. The right picture represents the trajectory distribution of the left picture according to the integral of first order  $P$ . The trajectories are localized in region 1 or 3 according to their value of  $P$ .

The aim of the numerical simulations is to emphasize the role of frequency chaotic variations in transport of the Earth obliquity.

All numerical simulations of part 4.4 are done with a Runge-Kutta 4 algorithm. The stochastic frequencies are simulated with the algorithm described in section 4.2.

## 4.4 Numerical integrations of the stochastic Hamiltonian dynamics

### 4.4.1 Integration with fixed values of the frequencies

In the first simulation, we have integrated 86688 trajectories with initial conditions inside the range  $0.75 < p < 1.0$ . The time step of integration is about 206 yr. The total time of integration is  $T = 247$  Myr. We record the value of  $J_{fix}(t)$  at each step of  $\Delta T = 8.241$  Myr such that the total integration time is 30 steps. The number of trajectories was not sufficient to get the precise value of  $J_{fix}(t)$ . The probability flux is close to zero for  $t < 164$  Myr because the system has not reached yet a quasistationary state. In the present problem, the quasistationary state is defined as the state when the distribution of trajectories is almost uniform over the whole region 1. The quasistationary state can be clearly seen in the simulation when the flux  $J_{fix}(t)$  fluctuates around its time averaged value. The quasistationary state seems to be reached for  $t \geq 206$  Myr, with between 1 and 8 trajectories entering into region 3 at each step. We therefore average the flux  $J_{fix}(t)$  over the period  $206 \leq t \leq 247$  Myr to get a reliable order of magnitude of the averaged probability flux entering into region 3 in quasistationary state. We find

$$\langle J_{fix} \rangle \approx 4.51 \times 10^{-6} \text{ Myr}^{-1} \pm 25\%. \quad (4.4.1)$$

### 4.4.2 Integration with the reference simulation of the frequencies

In the second simulation, we have integrated 10000 trajectories with uniform initial distribution on the line  $p = 0.84$  ( $\epsilon \approx 33^\circ$ ). The integration time step is about 129 yr. The integration ranges from  $t = -240$  to  $t = 239$  Myr, such that the total time of integration is about  $T = 479$  Myr. We record the value of  $J_{ref}(t)$  at each step  $\Delta T = 5.1529$  Myr. Four of the thirteen frequencies depend on time. The frequencies  $s_{1-4}$  (that correspond to the frequencies  $\nu_1, \nu_2, \nu_5$  and  $\nu_7$  in table (4.2)) depend on time following the numerical simulations of [65]. All other frequencies were kept constant.

Again, the number of trajectories was not sufficient to get a precise estimation for  $J_{ref}(t)$ . To be consistent with the first simulation, we only consider the interval where the system has reached a quasistationary state. We average the probability flux  $J_{ref}(t)$  over the period  $-34 < t < 239$  Myr. We find

$$\langle J_{ref} \rangle \approx 7.9 \times 10^{-6} \text{ Myr}^{-1} \pm 20\%. \quad (4.4.2)$$

The order of magnitude of the probability flux entering into region 3 with time dependent frequencies is about two times larger than the averaged flux (4.4.1) obtained with fixed values of the frequencies. The probability flux displays a significant increase at the end of the time interval. For  $170 < t < 239$  Myr, the averaged value of the flux is

$$\langle J_{ref} \rangle \approx 18.0 \times 10^{-6} \text{ Myr}^{-1}.$$

A glance at Fig.(4.1.3) shows that the frequencies  $s_3$  and  $s_4$  have exceptionally large variations in the same time interval. On the contrary, the variations of  $s_1$  and  $s_2$  do not seem to have

a significant impact on the probability flux. The simulation leads to the heuristic idea that the probability of transition from region 1 to 3 is dominated by exceptional variations of the frequencies  $s_3$  and  $s_4$ .

#### 4.4.3 Integration with a large number of realizations of the frequencies fluctuations

The aim of the last simulation is to compute probability flux entering into region 3 averaged over the frequencies variations. To this aim, we first generate 111 random realizations of the frequencies  $s_{1-4}(t)$  with the algorithm of section 4.2. For each realization of the secular frequencies  $s_{1-4}$ , we integrate 500 trajectories with uniform initial distribution over the line  $p = 0.84$  ( $\varepsilon \approx 33^\circ$ ). The integration time step is about 129 yr, and the integration ranges from  $t = -240$  to  $t = 224$  Myr. For each frequency realization  $n$ , we get the probability flux  $J_{chaos}^n(t)$ , with  $n = 1..111$ . We record the values  $J_{chaos}^n(t)$  at each step  $\Delta T = 51.529$  Myr. We then average the flux over the 5 last steps, that is, over the time interval  $-34 < t < 224$  Myr and we average over  $n$ . We get

$$\langle J_{chaos} \rangle \approx 42.9 \times 10^{-6} \text{ Myr}^{-1} \pm 10\%. \quad (4.4.3)$$

The averaged probability flux (4.4.3) entering into region 3 computed with a large number of realizations of the time dependent frequencies  $s_{1-4}(t)$  is almost ten times larger than the flux (4.4.1) obtained with fixed frequencies. It is also much larger than the flux value (4.4.2) obtained with the reference simulations of the frequencies  $s_{1-4}(t)$ . The value (4.4.3) should thus be considered with caution: It can be that we have overestimated the random term amplitude in the stochastic algorithm of section 4.2, and this could explain the discrepancy between the values (4.4.3) and (4.4.2).

#### 4.4.4 Discussion

The numerical results of section 4.4 confirm that the transition between region 1 and region 3, which corresponds to an obliquity variation from  $30^\circ$  to  $55^\circ$  of the Moonless Earth, is a very rare event. Each of the simulations of section 4.4 has required a few days on a standard computer. The very low value of probability transition in 250 Myr explains the very poor precision of the numerical values (4.4.1-4.4.2-4.4.3). Even with their imprecision, the results show that the chaotic variations of the secular frequencies  $s_{1-4}$  have a significant effect on the transition probability. The averaged value of the flux (4.4.3) obtained with many realizations of the functions  $s_{1-4}(t)$  is almost ten times larger than the simulation with fixed frequencies. The typical transition time from region 1 to region 3 can be estimated as

$$T_{chaos} := \frac{1}{\langle J_{chaos} \rangle} \approx 20 \text{ Gyr} (\pm 10\%),$$

which is much larger than the lifetime of the solar system. For the fictive Moonless Earth we consider in our model, the transition from  $30^\circ$  to  $55^\circ$  is so rare that there is no chance to observe this event for a single trajectory over 5 Gyr.

From a theoretical point of view, let us consider the transport mechanism from region 1 to region 3. The interval  $\Delta P$  of the gap between the two chaotic regions is of the order of  $\Delta P \approx 0.3$  (see Fig.(4.3.4)). As explained in section 4.3.1, the locations of chaotic regions depend on the frequency values. A variation of the frequencies could close the gap between regions 1 and 3 and allow for rapid transitions. Knowing the size of the gap in  $P$ -space, we can deduce the amplitude of frequency variations necessary to close it. Only a frequency variation of the order of  $\alpha \Delta P \approx 6''/\text{yr}$  could close the gap and allow rapid transitions from region 1 to region 3.

Fig.(4.1.3) shows that the chaotic fluctuations of the secular frequencies are of the order of  $\Delta\nu \approx 0.1 - 0.2''/yr$ . We conclude that the transport mechanism of the first type, that is, transport by slow displacement of the chaotic regions, does not explain alone the transition between chaotic region, and that the transport mechanism of the second type (transport inside the regular region) plays a major role.

The only way to observe a transition between chaotic regions in less than 5 Gyr would be a fluctuation of exceptional amplitude of a few arcsec/yr for one of the frequencies  $s_{1-4}$ , to close the gap between chaotic region. Such a fluctuation might be possible because of chaotic motion of the solar system, but is expected to be extremely rare. In fact, we could not observe such a large fluctuation in the 111 random simulations of the frequencies  $s_{1-4}$  performed in (4.4.3). Much more work would thus be required to compute precisely the probability of a rare transition from  $23^\circ$  to  $80^\circ$  in less than 5 Gyr for our fictive Moonless Earth. Given the very low probability of such an event, the analysis would require a special algorithm designed for the computation of rare event (see e.g. [82] in references therein). It should be emphasized that those conclusions do not hold when considering a more precise model of the Moonless Earth obliquity. Using the model of [78], it can be shown that transitions from  $23^\circ$  to  $80^\circ$  in less than 5 Gyr are much more frequent.<sup>1</sup> With a realistic model, one could expect to recover the rare event phenomenology when looking for transitions whithin a time much shorter than 5 Gyr.

In the last section 4.5, we study a Hamiltonian dynamics very similar to (4.1.2) but in a parameter regime for which transport of the first type is dominant. We will show how the local diffusive model of section 4.3.3 can be used to predict the transition probability between chaotic regions of phase space.

## 4.5 Numerical simulations

We propose to study a Hamiltonian with only four frequencies given by

$$H(p, q, t, \nu) = \frac{p^2}{2} + \sum_{k=1}^4 \cos \left( q - \int_0^t \nu_k(\epsilon s) ds - \varphi_k \right). \quad (4.5.1)$$

The Hamiltonian (4.5.1) is designed to have the same qualitative properties as the Hamiltonian (4.1.2). The frequencies are divided in two groups of two frequencies which create resonance overlap, and create two main mixing regions around  $p = 0$  and  $p = 10$ . The parameters  $\{\varphi_k\}_{k=1..4}$  are some initial phases, and  $\epsilon$  is a small parameter to model the timescale separation between the Hamiltonian dynamics and the stochastic dynamics of the frequencies. To complete our Hamiltonian model (4.5.1), we need to specify the stochastic process for the set of frequencies  $\nu$ . We choose for the variations of  $\nu$  an Ornstein-Uhlenbeck process defined as

$$\dot{\nu} = -(\nu - \nu^*) + \sqrt{2\sigma^2}\xi(t). \quad (4.5.2)$$

In Equation (4.5.2),  $\xi(t)$  is a 4-dimensional Gaussian white noise. For simplicity, in order to keep the size of the stochastic regions constant, we choose to prescribe the same noise for two frequencies of the same set, that is,  $\xi_1 \equiv \xi_2$  and  $\xi_3 \equiv \xi_4$ . The parameter  $\sigma$  quantifies the amplitude of the noise, it is the same for all frequencies. In the following, we perform numerical simulations for different values of  $\sigma$  to change the amplitude of the frequency variations. The term  $-(\nu - \nu^*)$  keeps the frequencies close to their averaged values defined by the set  $\nu^*$ .

The Hamiltonian (4.5.1) together with the stochastic equation (4.5.2) completely defines our model. In the simulations we have performed, the parameters  $\varphi_k$ , the timescale separation  $\eta$

---

<sup>1</sup>J.Laskar, private discussion.

frequencies $\nu_k^*$ ( $s^{-1}$ )	initial angles $\varphi_k$	timescale separation $\epsilon$
10.0	0.0	$10^{-2}$
9.9	$\pi$	
0.1	$\pi$	
0.0	0.0	

Table 4.3: Invariant parameters of the model (4.5.1-4.5.2)

and the mean frequencies  $\nu_k^*$  were fixed to the values given in Table (4.3), whereas the amplitude  $\sigma$  is a control parameter that we changed in the different simulations.

### 4.5.1 Simulations of the stochastic Hamiltonian model

We now present the numerical results obtained with the stochastic Hamiltonian model defined by Equations (4.5.1-4.5.2). The Hamiltonian (4.5.1) has the form  $A(p) + B(q, t)$  with

$$A(p) := \frac{p^2}{2},$$

$$B(q, t) := \sum_{k=1}^4 \cos \left( q - \int_0^t \nu_k(\epsilon s) ds - \varphi_k \right).$$

We have thus used the symplectic integrator of order 4  $SBAB_3$ . At each time step of integration, we integrate the frequencies from Equation (4.5.2) with a stochastic Euler algorithm. The parameter  $\eta$ , the mean frequencies  $\nu_k^*$  and the initial phases  $\varphi_k$  were fixed to their nominal values given in Table (4.3).

We are mainly interested in the first exit time  $\tau$  defined as the first time to leave the region  $p > 0$  starting from  $p = 10$ . We wanted to compute numerically its probability distribution function  $\rho(\tau)$ , and determine how it depends on the noise amplitude  $\sigma$  in Equation (4.5.2). To achieve this aim, we have performed a set of five numerical simulations using the values of  $\sigma$  given in Table 4.4. For each simulation, we ran 5000 trajectories all starting at the same point  $(p, q) = (10, 0)$ . Each trajectory is run with a different realization of the noise  $\xi(t)$ . When the system has a strictly negative momentum,  $p < 0$ , we stop the integration and we record the time at which this event has happened. We fixed a limited time for the simulation  $T_{max}$  because some trajectories take a time much too long to reach  $p = 0$ . The values of  $T_{max}$  for each simulation are given in Table 4.4. Let  $N = 5000$  be the total number of trajectories, and  $n$  be the number of trajectories that effectively reach  $p = 0$  within the time  $T_{max}$ . The software Matlab can then build a normalized histogram  $h(\tau)$  with the values of the first hitting times given by the simulation. The probability distribution  $\rho(\tau)$  can then be estimated with the relation  $\rho(\tau) = \frac{n}{N} h(\tau)$  for  $\tau < T_{max}$ . The results of the simulations are the different histograms displayed in Fig.(4.5.1). The histograms represent the distributions  $\rho(\tau)$  for each simulation.

### 4.5.2 Simulations of the local diffusive model

The local diffusive model is given by equations (4.3.2-4.5.2). We have to prescribe the values of the parameters  $\delta_1, \delta_2$  corresponding to the extensions of the diffusive patches  $\mathcal{R}_1, \mathcal{R}_2, \mathcal{R}_3$ .  $\delta_1$  and  $\delta_2$  should correspond to the effective extension of the strongly chaotic regions of the stochastic Hamiltonian model. The parameters  $\delta_1$  and  $\delta_2$  could be estimated from the Chirikov criterion of resonance overlap. However, the direct numerical simulations show that the size of the chaotic regions is smaller than the theoretical predictions of the Chirikov criterion. To obtain a better

agreement with the simulations, we prescribed the size of the diffusive patches with the following method.

To estimate the size of the chaotic region 1 (see Fig. 4.3.1), we ran a numerical simulation of Hamilton's equations with the Hamiltonian (4.5.1), except that we kept the frequencies fixed to their reference values  $\nu_i^*$ . We simulated 2000 trajectories with initial conditions  $p = \nu_1^*$  and  $q$  equally distributed over the range  $[0, 2\pi]$ , over a time  $T = 300 * \frac{2\pi}{\nu_1^*}$ . The final coordinates are then distributed over the chaotic region 1, and only very few of them are gone out of the region 1. We show as an illustration the typical histogram of final momenta we obtain in Fig. (4.5.2). We then define the boundaries of the chaotic region as the interval  $[p_1, p_2]$  in which 90% of the probability distribution is concentrated, and satisfying  $\frac{p_1+p_2}{2} = \frac{\nu_1^*+\nu_2^*}{2}$ . Then, the empirical estimate of  $\delta_1$  is  $\delta_1 \approx p_2 - p_1$ .

Using the same method, we have estimated the extension  $\delta_2$  of the chaotic region 2 corresponding to the resonances of second order. Then we have also estimated the extensions  $\delta_3, \delta_4$  of the chaotic regions around the resonances of third and fourth order. They are located around the values  $p = 3.3$ ,  $p = 6.6$  for the resonances of third order, and  $p = 2.5$  and  $p = 7.5$  for the resonances of fourth order. The values of the parameters  $\{\delta_i\}_{i=1..4}$  are gathered in Table (4.5).

We ran  $M = 1000$  simulations using for each simulation distinct realization of the stochastic process  $\nu(t)$  given by (4.5.2). For each of the realization  $\nu(t)$ , we could compute with (4.3.2) the probability density  $\rho_\nu(p, t)$  to find the system in  $p$  at time  $t$ . At the beginning, the system is in  $p = \nu_1^*$ , which corresponds to the initial condition  $\rho_\nu(p, 0) = \delta(p - \nu_1^*)$ . We want to compute the probability of first hitting time at  $p = 0$ . This means that we have to prescribe the boundary condition  $\rho_\nu(p < 0, t) = 0$ . In practice, this condition amounts to set  $\rho_\nu(p, t) = 0$  for  $p \in [\nu_4(t) - \delta_1/2, \nu_4(t) + \delta_1/2]$  because if the system enters in the diffusive patch  $\mathcal{R}_2$ , it is immediately transported across the patch and reaches  $p = 0$ .

The complete probability distribution  $\rho(p, t)$  is simply the average of  $\rho_\nu(p, t)$  over the realizations of the stochastic process  $\nu(t)$ . Let  $\{\nu^k(t)\}_{k=1..M}$  be the  $M$  realizations of  $\nu(t)$ , we have

$$\rho(p, t) = \frac{1}{M} \sum_{k=1}^M \rho_{\nu^k}(p, t).$$

And the probability of first hitting times  $\rho(\tau)$  is given by

$$\rho(\tau) = -\frac{d}{d\tau} \int_0^{+\infty} \rho(p, \tau) dp.$$

The simulations are performed with the set of parameters given in Table (4.4). The results are displayed on the different graphs of Fig.(4.5.1) together with the histograms obtained by the direct Hamiltonian simulations. The curves show the results of  $\rho(\tau)$  obtained with the simulations of the local diffusive model, whereas the histograms show the results for  $\rho(\tau)$  obtained with the simulations of the stochastic Hamiltonian model. On the simulations 1, 2 and 3, we only used the local diffusive model including the resonances up to order two. But on the simulations 4 and 5, there are two curves  $\rho(\tau)$ : the lower one is the distribution  $\rho(\tau)$  computed with the local diffusive model with resonances up to order two, but on simulation 4, we included the resonances up to order three in the local diffusive model, and in the simulation 5 the resonances up to order four. The results are displayed by the highest curves in simulations 4 and 5.

### 4.5.3 Discussion of the results

The different simulations in Fig.(4.5.1) aim to show which phenomenon governs the transport in phase space in the stochastic Hamiltonian model (4.5.1-4.5.2), and how the transport depends on the parameters of the model.

Simulation	$\sigma$ ( $s^{-3/2}$ )	$T_{max}$ ( $\frac{2\pi}{\nu_1} \cdot 10^4 s$ )
1	3.0	1.0
2	2.2	2.0
3	1.84	3.0
4	1.1	10.0
5	0.7	50.0

Table 4.4: Noise amplitudes and integration times of the five simulations in Fig.(4.5.1)

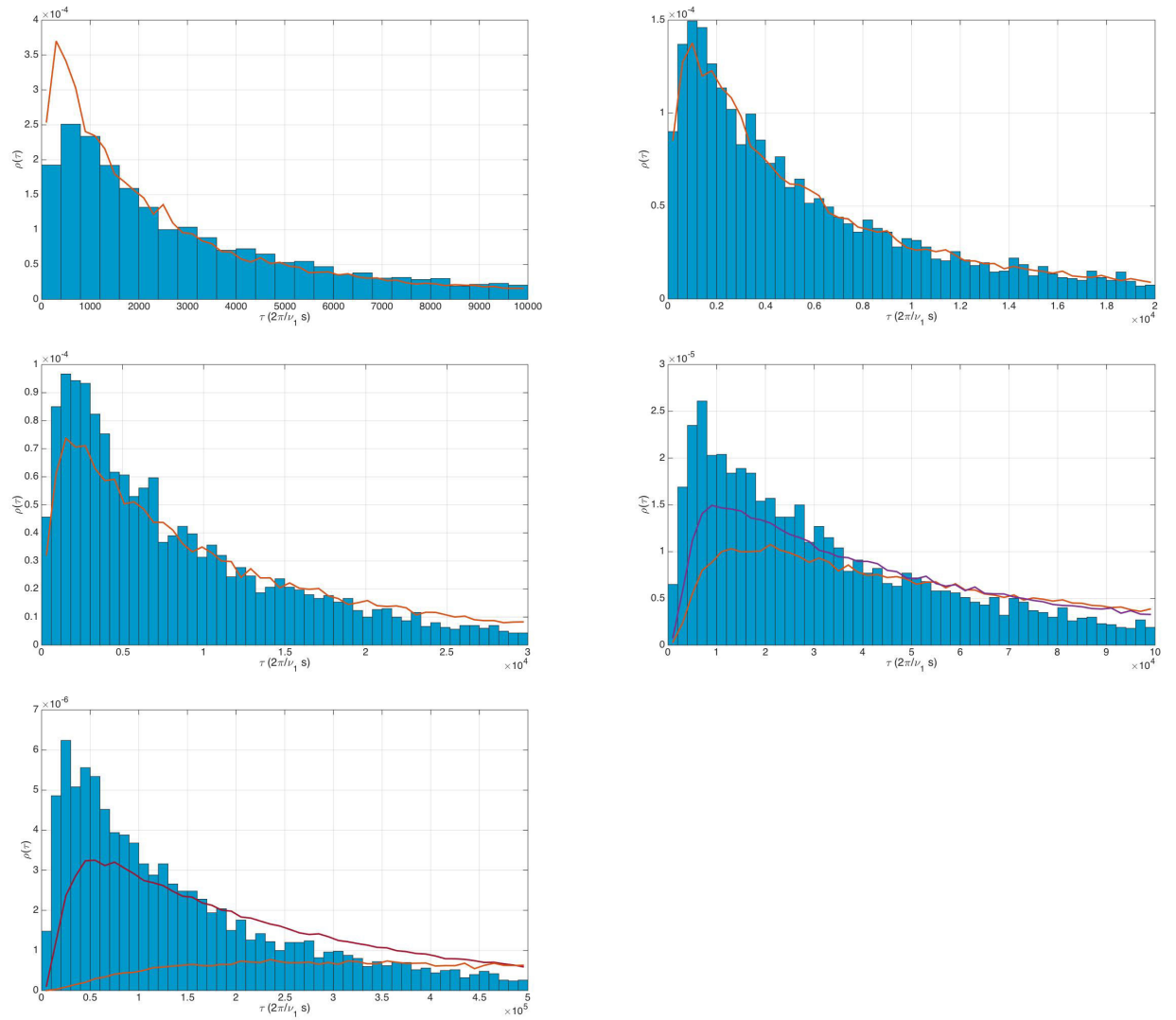


Figure 4.5.1: First exit time distributions for five simulations with different values of the noise amplitude. The histograms display the results of the simulations with the stochastic Hamiltonian model (4.5.1). The red curves display the results of the local diffusive model including second order resonances, the purple curves display the local diffusive model including third and fourth order resonances.

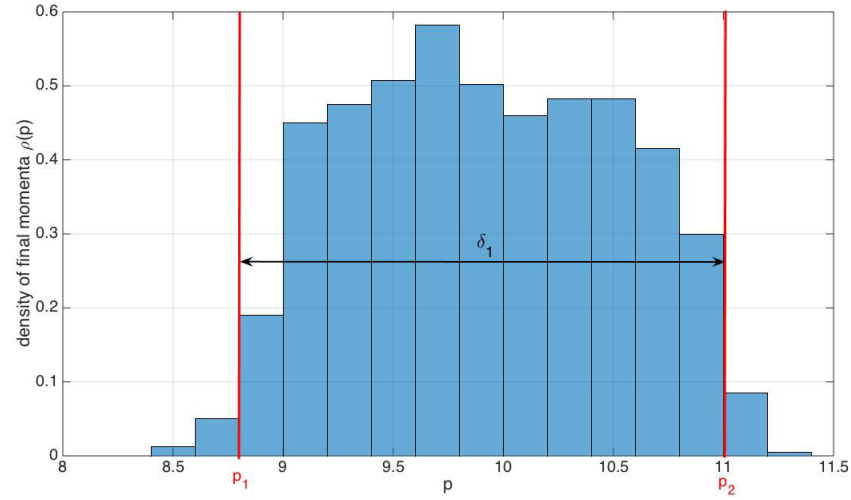


Figure 4.5.2: Representation of the chaotic region 1. The two red lines at  $p_1$  and  $p_2$  show the boundaries of the region. The region is centered at the value  $p = \frac{\nu_1^* + \nu_2^*}{2}$ . Its extension is given by  $\delta_1 = p_2 - p_1$ .

resonances	extension of the chaotic region	numerical estimation of $p_2 - p_1$
first order	$\delta_1$	2.25
second order	$\delta_2$	0.50
third order	$\delta_3$	0.28
fourth order	$\delta_4$	0.09

Table 4.5: Sizes of the diffusive patches of the local diffusive model.

One trivial but important conclusion of our numerical study is that the transport in a stochastic Hamiltonian model is very different from the transport with the same Hamiltonian (4.5.1) without stochastic variations of the frequencies. If the frequencies are fixed, the trajectories starting at  $p = \nu_1^*$  are just spread across the first chaotic region, and none of them reaches the value  $p = 0$  within the time  $T_{max}$  of our simulations. Transport with stochastic frequencies is thus a new mechanism that completely overcomes chaotic diffusion in deterministic chaotic Hamiltonian maps.

The qualitative shape of the distributions of first hitting times  $\rho(\tau)$  displayed in Fig.(4.5.1) is typical of a distribution of first exit times from a domain in a stochastic system. The probability distribution has a maximum  $\rho^*$  reached at  $\tau^*$ , that can be considered as the typical time for the exit event to occur. For times smaller than  $\tau^*$ , the probability distribution goes rapidly to zero. It is thus very rare for the system to reach  $p = 0$  in a time much smaller than the typical time  $\tau^*$ , because it corresponds to exceptionally large and fast random fluctuations of the stochastic frequencies  $\nu_i$ . For times larger than the typical time  $\tau^*$ , the probability distribution also goes to zero because it is also a rare event, called ‘‘persistence’’, that the system does not leave the domain  $p > 0$  in a large time.

The order of magnitude of  $\tau^*$  depends on the amplitude of the noise  $\sigma$  acting on the frequencies. For  $\sigma = 3.0$ , it is of the order of  $10^3 * \frac{2\pi}{\nu_1^*}$ , whereas for  $\sigma = 0.7$ , it is two orders of magnitude larger, of the order of  $10^5 * \frac{2\pi}{\nu_1^*}$ . The typical exit time  $\tau^*$  scales proportionally to the inverse of the time scale separation  $\eta$  of the frequencies variations. If  $\frac{1}{\epsilon}$  is one order of magnitude larger,  $\tau^*$  also grows by one order of magnitude. This scaling has been confirmed by additional numerical simulations that we did not display.

The local diffusive model presented in Section 4.3.3 can be seen as the averaging dynamics of the stochastic Hamiltonian model, for which transport outside of the principal resonant regions has been neglected. This is reflected in the local diffusive model by the fact that the diffusion coefficient is zero outside the diffusive patches  $\mathcal{R}_i$ . Therefore, the local diffusive model only takes into account transport of the first type occurring with the displacement of the mixing regions of resonance overlap. If the transport of this type is dominant, it is natural to expect that the local diffusive model reproduces well the results of the stochastic Hamiltonian model. If, on contrary, transport is mainly of the second type -due to stochastic diffusion in the regular regions of phase space-, then the exit rate at  $p = 0$  predicted by the local diffusive model is much slower than the real transport in the stochastic Hamiltonian model.

On Fig.(4.5.1), it can be seen that the local diffusive model is able to capture quite well the probability distribution of first exit times  $\rho(\tau)$ . For the three simulations with  $\sigma = 3.0/2.2/1.84$ , the local diffusive model with resonant regions up to second order gives excellent results. It reproduces qualitatively and quantitatively the histogram of  $\rho(\tau)$ , with the same location  $\tau^*$  of the maximal value, and reproduces the decrease of the distribution  $\rho(\tau)$  for long times. For the two simulations with  $\sigma = 1.1/0.7$  the local diffusive model of second order predicts a transport rate which is much smaller than the real transport. In particular for  $\sigma = 0.7$ , even the qualitative shape of  $\rho(\tau)$  for the Hamiltonian model is not reproduced, the typical time  $\tau^*$  is far overestimated. This means that for  $\sigma$  values below 1.84, transport through resonances of order higher than two can no longer be neglected. The local diffusive model with resonant regions up to order four is able to reproduce qualitatively the distribution of exit times  $\rho(\tau)$ , and gives also a good order of magnitude of the value of  $\rho(\tau)$ . This is illustrated by the two highest curves for the simulations 4 and 5 on Fig.(4.5.1). For values of  $\sigma$  below 0.7, the local diffusive model is no longer able to reproduce transport in phase space, even with resonant regions up to order four.

The relevance of the local diffusive model to predict transport depends on the balance between the amplitude  $\sigma$  of frequencies fluctuations and the distance to cross between two mixing regions. For example, in the local diffusive model of order two, the initial distance between two

neighboring diffusive patches is

$$\text{Dist}_{\mathcal{R}_1 \rightarrow \mathcal{R}_3} := \left( \frac{\nu_1^* + \nu_2^*}{2} - \frac{\delta_1}{2} \right) - \left( \frac{\nu_1^* + \nu_4^*}{2} + \frac{\delta_2}{2} \right) \approx 3.575.$$

The sum of the variances of the fluctuations of the diffusive patches  $\mathcal{R}_1$  and  $\mathcal{R}_3$  gives the typical amplitude of the fluctuations of the mixing regions

$$\sqrt{V_{\mathcal{R}_1} + V_{\mathcal{R}_3}} = \left( 1 + \frac{1}{\sqrt{2}} \right) \sigma$$

Therefore, the efficiency of the transport of the first type depends whether the parameter

$$\Delta := \frac{\text{Dist}_{\mathcal{R}_1 \rightarrow \mathcal{R}_3}}{\sqrt{V_{\mathcal{R}_1} + V_{\mathcal{R}_3}}} \simeq \frac{2.1}{\sigma}$$

is large or small compared to one.

This means that for the three simulations with  $\sigma = 3.0/2.2/1.84$ , the initial distance to cross between two diffusive patches is larger or of same order as the amplitude of the frequencies fluctuations. The jump between one diffusive patch to another is thus possible with “typical” fluctuations of the frequencies. Transport does not require an exceptionally large fluctuation. But this is no longer the case for  $\sigma = 1.1/0.7$ . Frequencies fluctuations are too small to pass directly from the first order resonant region to the second order resonant region (or equivalently, from  $\mathcal{R}_1$  to  $\mathcal{R}_3$ ), and transport is due to higher order resonances. For example, in the local diffusive model of fourth order, the initial distance to cross to jump from the diffusive patch  $\mathcal{R}_1$  to the next patch  $\mathcal{R}_3$  is  $\text{Dist}_{\mathcal{R}_1 \rightarrow \mathcal{R}_3} = \left( \frac{\nu_1^* + \nu_2^*}{2} - \frac{\delta_1}{2} \right) - \left( \frac{3\nu_1^* + \nu_4^*}{2} + \frac{\delta_4}{2} \right) \approx 1.28$ . On the other hand, the combined fluctuations of the two patches have a variance of  $\sqrt{V_{\mathcal{R}_1} + V_{\mathcal{R}_3}} = \left( 1 + \frac{\sqrt{10}}{4} \right) \sigma$ . Thus the parameter  $\Delta$  is of the order of  $\Delta \simeq \frac{1.28}{1 + \sqrt{10}/4} \frac{1}{\sigma} \simeq \frac{0.71}{\sigma}$ . This argument explains why the local diffusive model up to order four is able to predict the transport for values of  $\sigma$  of the order of 0.7, but fails for lower values of  $\sigma$ .

In the present section, we have shown how a system satisfying a Hamiltonian dynamics with stochastic frequencies can be transported slowly through phase space by the slow displacement of chaotic regions. We have shown that this kind of transport can be reproduced qualitatively and quantitatively by a completely stochastic Markovian model, the local diffusive model. The local diffusive model gives a representation of the strongly chaotic regions created by resonance overlap in the Hamiltonian by diffusive patches with infinite diffusion coefficient. The relevance of the Markovian model to predict transport rates in the stochastic Hamiltonian model mainly depends on the amplitude of the frequency stochastic variations. We have shown that for decreasing amplitudes of the variations, the local diffusive model should take into account resonances of higher and higher orders. In this Section, we presented a model including resonances up to order four. But one cannot expect the local diffusive model to be valid for all range of the amplitude fluctuations  $\sigma$ , even if we include resonances up to higher orders. The reason for that is that transport is also due to a stochastic diffusion in the regular regions, away from the resonances. If the amplitude of the fluctuations is too small, then transport is mainly due to diffusion in the regular regions, what we have called “transport of the second type”. We have shown that the transport is mainly of the first type in the stochastic Hamiltonian system if the typical frequency fluctuations are similar to the distance in phase space between two neighboring resonant regions. We have performed an other numerical simulation where the stochastic process for the variations of  $\nu$  is a jump process with exponential distribution of the jumps, and we found that the results are in accordance to the general picture we give in this section. This suggests that the transport mechanism is robust to other types of stochastic processes for the frequency evolution.

## 4.6 Conclusion

The secular dynamics of the Earth spin axis can be approximately modeled by a Hamiltonian that depends on time and on a set of slow chaotic frequencies. We have therefore studied the simple model of [51] for the Earth obliquity to reproduce qualitatively the main dynamical features observed in more realistic models [78]. For the obliquity of our fictive Moonless Earth, transitions from  $23^\circ$  to  $80^\circ$  are possible but extremely rare. We estimate the typical transition time to 20 Gyr in the present model. Given the simplicity of the present model, this time should not be considered as the realistic one for the Moonless Earth: simulations with the model of [78] show that transitions from  $23^\circ$  to  $80^\circ$  happen in fact in a shorter timescale. The important point is that our work reveals the significant effect of frequency fluctuations, a phenomenon that had been neglected in previous theoretical studies [67]. Without chaos in the solar system, the secular frequencies  $s_{1-4}$  would be constant and the transition time would be one order of magnitude larger.

Beside the particular problem of the dynamics of a Moonless Earth, our work has led to the discovery of a new transport mechanism in chaotic Hamiltonian systems depending on slow external frequencies. Even in the mathematical community, this kind of problem seems to have been neglected. We have shown that transport is created by the slow distortion of the phase space structure, and we have characterized the transport properties depending on the parameter regime. The timescale separation between the Hamiltonian dynamics and the frequency evolution allows us to perform a kind of averaging over the chaotic regions of phase space. The result of the procedure is a diffusive model that gives relevant predictions of transport rates in a regime where transport through displacement of the chaotic regions is dominant. This regime corresponds to large frequency fluctuations.

The dynamics of the Moonless Earth does not fall in this particular parameter regime, and the diffusive model cannot be used to predict large obliquity variations. However, large obliquity variations on a timescale smaller than one Gyr are only possible if an exceptionally large variations of one of the frequencies  $s_{1-4}$  closes the gap between the different chaotic regions. This kind of event is captured by the diffusive model. that's why we expect that the diffusive model would be relevant to describe rare events in the system.

## Chapter 5

# Instantons for Mercury's dynamics

### 5.1 Introduction: large variations of Mercury's eccentricity

The discovery that our solar system is chaotic with a Lyapunov time of about 10 Myr [47, 48] has again brought up the very old question of our solar system's long term stability. This question has been settled more recently by the team of Jacques Laskar at the IMCCE. Thanks to an extended numerical integration of 2500 trajectories of the solar system with close initial conditions, they have been able to show that about 1% of the trajectories led to collisions between planets, or between planets and the Sun within 5 Gyr [58]. This shows that our solar system is marginally stable, which means that it can be considered as stable for a time comparable to its age. For the vast majority of collisional trajectories, the collision happens between Mercury and Venus, or Mercury and the Sun, and leads thus to the disappearance of Mercury alone. But more rarely, the orbit of Mars can also be strongly perturbed and destabilize the four inner planets Mercury, Venus, the Earth and Mars [60].

In the question of the solar system's stability, there is a great difference between the inner solar system composed of the four small telluric planets Mercury, Venus, the Earth and Mars, and the external solar system composed of the four giant gaseous planets Jupiter, Saturn, Uranus and Neptune. It has been shown that the external solar system is in the so called *Nekhoroshev* regime [76, 73], and is thus stable for a time much larger than the age of the solar system. This is reflected by the fact that the giant planets' trajectories is very well predicted on the Gyr timescale by the Laplace–Lagrange secular equations. On the contrary, the Laplace–Lagrange equations fail to predict the small planets orbital elements after few tens of Myr. Among the small planets, the lightest one, Mercury, is also the most unstable one. It has been shown in the numerical simulations [58] that the chaotic disintegration of the inner solar system always happens through a very rapid and large increase in Mercury's eccentricity. In particular destabilization of other planets cannot be observed before Mercury's destabilization. This shows that Mercury's chaotic dynamics is the key element to understand any large structural changes in our solar system.

The fact that Mercury's eccentricity can reach very high values  $e > 0.7$  is related to a possible resonance between the precession frequency  $g_1$  of Mercury's perihelion and the frequency  $g_5$  of Jupiter. This resonance has been early noticed to be the main destabilizing factor of Mercury's orbit [6, 53, 58]. A simplified model for Mercury's secular dynamics perturbed by the  $g_5$  secular frequency also shows that the particular resonance  $g_1 - g_5$  is enough to reproduce the increase in Mercury's eccentricity beyond 0.7 as observed in the simulations [15]. The right panel of Fig.5.1.1 displays the time evolution of Mercury' eccentricity once the orbital conditions for

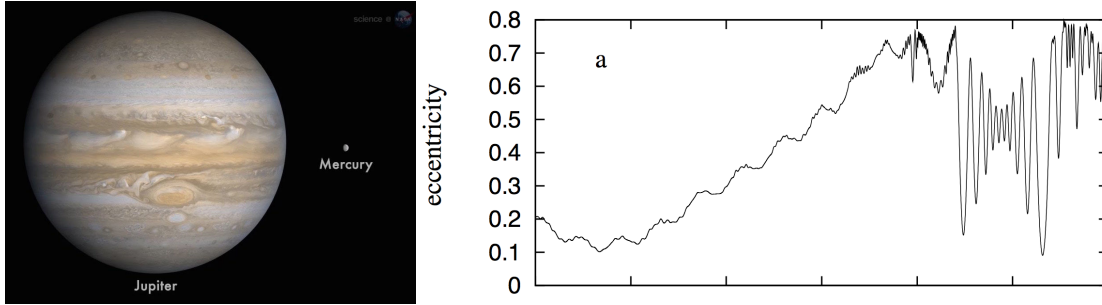


Figure 5.1.1: Right: the planet Jupiter compared to Mercury. Left: rapid increase in Mercury's eccentricity because of a resonance with Jupiter. The time unit on the abscissa is 1 Myr. [15]

resonance with Jupiter have been reached. The picture shows that the eccentricity increase occurs within only a few million year, which is very fast compared to the 10 Myr Lyapunov time of the solar system. The physical interpretation of this event is that the resonance allows the transfer of a large amount of angular momentum from Jupiter to Mercury [52]. As Jupiter's mass is about 5750 times larger than that of Mercury (see Fig.5.1.1), Jupiter's orbit has absolutely negligible changes due to interaction with Mercury. This is of course not the case for the small planet Mercury which trajectory becomes more and more elliptic when angular momentum is transferred. Once Mercury's orbit has become very elliptic, close encounters or collisions are allowed with Venus. The inner solar system enters in a regime of large scale chaos for which predictions become extremely hard.

Now that the destabilization mechanism of the inner solar system through the secular resonance  $g_1 - g_5$  between Mercury and Jupiter has been widely acknowledged, important questions remain: how do the system reach the orbital condition for this resonance? How much time would be necessary to reach the resonance? Is it possible to predict the probability distribution of the first time this resonance occurs? All these questions will be the central subject of the present chapter.

A lot of work has already been devoted to characterize the mechanism by which Mercury's orbital parameters slowly evolve until they reach the conditions for resonance. The long term evolution of Mercury's orbit is conditioned by the resonances of its secular motion with the characteristic frequencies of the solar system. In addition to the secular frequency  $g_5$ , it has been shown that the second mode (mainly associated to the presence of Venus), characterized by the frequencies  $g_2$  and  $s_2$  in the Laplace–Lagrange system, plays a crucial role [71]. All the previous observations have led the authors Konstantin Batygin, Alessandro Morbidelli and Matthew Holman to introduce a simplified model for Mercury's secular dynamics that should contain all necessary ingredients to drive Mercury into the  $g_1 - g_5$  resonance [7]. The model, that we will call from now for convenience the BMH model, predicts Mercury's destabilization through the stochastic dynamics of a non-trivial adiabatic invariant. With the stochastic dynamics, the authors have been able to predict the average lifetime of Mercury before it enters into the  $g_1 - g_5$  resonance. The BMH model is the starting point of the present work. After a general presentation of the model in section 5.2, we show in section 5.3 how stochastic averaging gives precisely the stochastic equation followed by the adiabatic invariant. In particular, we are able to predict theoretically the right order of magnitude for the diffusion coefficient of the stochastic process. The model thus gives access not only to the average, but to the full probability distribution of the first time of Mercury's destabilization. Finally, we show in section 5.4 that the instanton theory presented in section 1.4 can be applied to Mercury's secular

dynamics to predict its destabilization in a time smaller than the age of the solar system.

## 5.2 Simplified model for a Massless planet

In the present section, we present the simplified BMH model for Mercury's secular dynamics [7]. In particular, we remind which approximations are used to derive it and what are its limitations.

We recall in Fig.(5.2.1) the elliptical coordinates  $(a, e, i, \lambda, \varpi, \Omega)$  that are used to describe planetary orbital position.

- $a$  : semi-major axis.
- $e$  : eccentricity. If  $e = 0$ , the ellipse is a circle. If  $e = 1$ , the ellipse is flat.
- $i$  : inclination of the ellipse w.r.t a reference plane.
- $\lambda$  : mean longitude =  $\Omega + \omega + M$ .
- $\varpi$  : longitude of the perihelion =  $\Omega + \omega$ .
- $\Omega$  : longitude of the ascending node.

$M$  is called the *mean anomaly*. It is defined as the ratio between the shaded area covered by the trajectory in Fig.(5.2.1) and the total area of the ellipse, with a factor  $2\pi$ . Kepler's second law states that the mean anomaly is then proportional to the time. If the planet is at time  $t = 0$  at the perihelion, then Kepler's second law gives

$$M(t) = 2\pi \frac{t}{T},$$

where  $T$  is the Keplerian orbital period.

The elliptical coordinates  $(a, e, i, \lambda, \varpi, \Omega)$  are very convenient to characterize planetary trajectories, but are not canonical action-angle variables. The sets of canonical variables usually used in celestial mechanics are Delaunay variables, or Poincaré variables. They will be defined in section 5.2.1.

### 5.2.1 Secular Hamiltonian for Mercury including the three major resonances

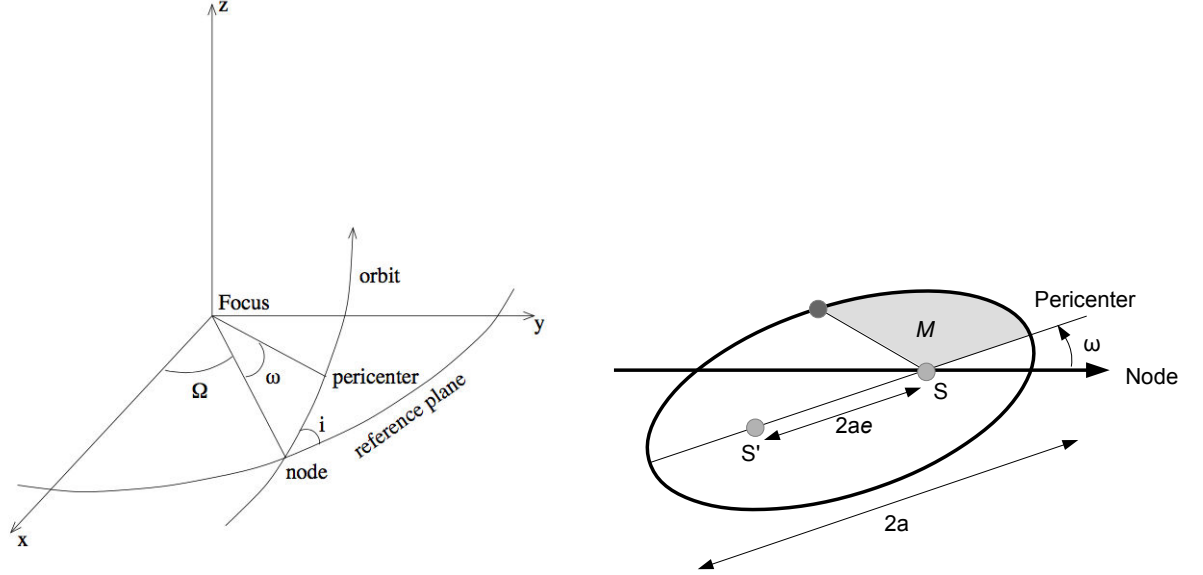
Let  $H$  be the Hamiltonian of the eight planets of the solar system. In heliocentric coordinates,  $H$  can be written as the sum of three terms [75, 72]

$$H = H_0 + T_1 + U_1. \quad (5.2.1)$$

In formula (5.2.1),  $H_0$  is the Hamiltonian of Kepler for the eight planets

$$H_0 = \sum_{p=1}^8 \frac{\tilde{r}_p^2}{2\beta_p} - \frac{\mathcal{G}\beta_p\mu_p}{|r_p|}, \quad (5.2.2)$$

where  $r_p$  is the position vector of planet  $p$  in heliocentric coordinates,  $\tilde{r}_p$  is the canonical variable conjugated to  $r_p$ ,  $\mathcal{G}$  is the gravitational constant,  $\frac{1}{\beta_p} := \frac{1}{M_S} + \frac{1}{m_p}$  is the reduced mass of planet  $p$  and  $\mu_p := M_S + m_p$ . The Hamiltonian (5.2.2) is the Hamiltonian of eight independent Kepler problems of a planet of mass  $m_p$  in interaction with the Sun of mass  $M_S$ . It is known since

Figure 5.2.1: Elliptical coordinates: definition of  $a, e, i, \omega, \Omega$  and  $M$ .

Newton that this problem is equivalent to a body of mass  $\beta_p$  orbiting around the fixed center of mass of the planet and the Sun.

A lot of work has been devoted in the *XIX<sup>th</sup>* century to find good action-angle variables to integrate the Kepler problem. We use in the present work the canonical Poincaré variables defined by

$$\begin{aligned} \Lambda &:= \beta\sqrt{\mu a} & \lambda &:= M + \omega + \Omega & (5.2.3) \\ I &:= \Lambda \left(1 - \sqrt{1 - e^2}\right) & -\varpi &:= -\omega - \Omega \\ J &:= \Lambda\sqrt{1 - e^2} (1 - \cos(i)) & -\Omega & \end{aligned}$$

In the present work, we have done a canonical change of variable in the secular Hamiltonian (5.2.8) to eliminate the  $\Lambda$  variable. In the following, the canonical variables  $I$  and  $J$  are dimensionless, and we have the relations  $I := 1 - \sqrt{1 - e^2}$  and  $J := \sqrt{1 - e^2} (1 - \cos(i))$ . The great advantage of the Poincaré variables compared to Delaunay ones is that for small eccentricity and inclination we have  $I \approx \frac{e^2}{2}$  and  $J \approx \frac{i^2}{2}$ . This means that  $I$  and  $J$  are small when  $e$  and  $i$  are small. In terms of Poincaré variables, the Kepler Hamiltonian can be written for each planet  $p$  as

$$H_0^p := \frac{\tilde{r}_p^2}{2\beta_p} - \frac{\mathcal{G}\beta_p\mu_p}{|r_p|} = -\frac{\mathcal{G}\beta_p^3\mu_p^2}{2\Lambda_p^2}.$$

Would the planetary mutual interactions be neglected, the Hamiltonian (5.2.1) would be reduced to the Hamiltonian  $H_0$ , that only depends on the action variable  $\Lambda$ . The perturbative function composed of the terms  $T_1$  and  $U_1$  gives a small deviation from the Keplerian orbits because planetary masses are much lower than the mass of the Sun. To leading order in planetary masses, the canonical equations of motion are simply for each planet

$$\dot{\lambda}_p = n(\Lambda_p), \quad (5.2.4)$$

with the Keplerian beating frequency  $n(\Lambda_p) = \frac{\mathcal{G}\beta^3\mu^2}{\Lambda_p^3}$ . All other variables are Keplerian constants of motion. When the perturbative function is added, the variables are no longer constant, but evolve slowly compared to the fast Keplerian motion. Their dynamics is accurately described by the secular equations, which we now describe.

The terms  $T_1$  and  $U_1$  in expression (5.2.1) represent the *perturbative function*, i.e the term coming from planetary mutual gravitational interaction.  $T_1$  is called the indirect part of the Hamiltonian, and comes from the fact that the origin of coordinates is not the center of mass of the system. The expression of  $T_1$  is

$$T_1 = \sum_{p' < p} \frac{\tilde{r}_{p'} \cdot \tilde{r}_p}{M_S}. \quad (5.2.5)$$

$U_1$  is called the direct part of the perturbative function. Its explicit expression is

$$U_1 = -\mathcal{G} \sum_{p' < p} \frac{m_p m_{p'}}{|r_{p'} - r_p|}. \quad (5.2.6)$$

Because of the timescale separation between the mean longitudes' dynamics (5.2.4), and that of the other variables  $\Lambda, I, J, \varpi$  and  $\Omega$ , the dynamics of the slow variables is very accurately described by the planetary Hamiltonian (5.2.1) averaged over the mean longitudes. The Kepler Hamiltonian  $H_0$  does not depend on the mean longitudes. The aim is thus to obtain the expression of the perturbative function  $\langle T_1 \rangle + \langle U_1 \rangle$  averaged over the fast angles  $\lambda_p$ .  $T_1$  and  $U_1$  are both periodic functions of the angles  $\Omega, \varpi, \lambda$ . They can thus be expressed as Fourier series of the canonical angles. In fact, it can be shown that  $T_1$  only contains periodic terms in  $\lambda$  and thus

$$\langle T_1 \rangle = 0.$$

The indirect part of the Hamiltonian gives no secular contribution. The secular Hamiltonian thus reduces to  $\langle U_1 \rangle$ .

It is not the aim of my work to describe precisely how to do the Fourier expansion for the disturbing function. The method can be found in all good textbooks of celestial mechanics, including [75, 72]. We will just give in the following the minimum of practical indications to manipulate the expansion of the perturbative function.

It is important to bear in mind that there are different methods to expand the perturbative function. The oldest one, that is also mostly used, is described in the book by Murray and Dermott [75]. It takes advantage of the fact that the planetary eccentricities and inclinations are very small, to classify the Fourier coefficients depending on their order in  $e$  and  $i$ . In particular, this kind of expansion breaks down if some of the planetary eccentricities or inclinations become large. Another way to perform the expansion has been proposed more recently by Jacques Laskar and Philippe Robutel in [64] leading to the same results, but with compact and explicit expressions for the coefficients. In particular, an explicit expansion of the secular Hamiltonian up to degree 4 in planetary eccentricities and inclinations can be found in [64]. Then, Jacques Laskar and Gwenaél Boué at IMCCE proposed a new method to expand explicitly the disturbing function to any order in eccentricity and inclination [55]. The expansion is done in series of the ratio of the semi-major axes and remains thus valid even for large values of  $e$  and  $i$ . Such an expansion is important for long-term predictions of planetary orbits as the eccentricity of Mercury can come close to  $e = 1$ . In the following paragraph, we describe briefly how the BMH model can be obtained using the perturbative function expansion presented in [75].

**The BMH model** The appendix B of the book by Murray and Dermott [75] presents the explicit expansion of the three-body disturbing function with all Fourier terms up to order 4 in

eccentricity and inclination. The two bodies position is described by their elliptical elements. The expansion uses the variable  $s := \sin\left(\frac{i}{2}\right)$  instead of  $i$ . The two bodies have semi-major axes respectively  $a$  and  $a'$  with  $a < a'$ . The Laplace coefficients are functions of  $\alpha := \frac{a}{a'}$ . The appendix gives the Fourier expansion of the function

$$\mathcal{R} := \frac{a'}{|r - r'|}.$$

To get the average of  $\mathcal{R}$  over  $\lambda$  and  $\lambda'$ -called the *secular part*-, one has to take the zeroth-order arguments of table B.1 with  $j = 0$ . The functions  $f_i$  are given in table B.3. (See also the explicit expansion of the secular part of the disturbing function in [64]).

The BMH model in [7] considers a massless planet Mercury in the gravitational field of the other planets. The secular motion of all other planets is given by the Laplace–Lagrange periodic solution. The only degrees of freedom in the model are thus Mercury's ones, with an additional time dependence in the Hamiltonian. The Hamiltonian to be computed for Mercury is thus

$$H := \sum_{p=2}^8 -\frac{\mathcal{G}m_1m_p}{a_p} \mathcal{R}^{sec}(e_1, s_1, \varpi_1, \Omega_1, e_p(t), s_p(t), \varpi_p(t), \Omega_p(t)), \quad (5.2.7)$$

where  $\mathcal{R}^{sec}$  is the perturbative function  $\mathcal{R}$  averaged over  $\lambda$ .

Then, the BMH model is built on the assumption that only the secular modes  $g_5, g_2, s_2$  have a significant impact on Mercury's dynamics. This assumption is not equivalent to saying that only Jupiter and Venus influence the dynamics, because all planetary trajectories have a component on the modes  $g_5, g_2, s_2$ . The aim is thus to replace all time dependent terms with  $(e_p(t), s_p(t), \varpi_p(t), \Omega_p(t))$  in (5.2.7) by their quasiperiodic decomposition on the modes  $g_5, g_2, s_2$ . This can be achieved with the formulae

$$\begin{aligned} e_p \cos(\varpi) &\approx e_{p5} \cos(g_5 t + \beta_5) + e_{p2} \cos(g_2 t + \beta_2), \\ e_p \sin(\varpi) &\approx e_{p5} \sin(g_5 t + \beta_5) + e_{p2} \sin(g_2 t + \beta_2), \end{aligned}$$

and

$$\begin{aligned} i_p \cos(\Omega) &\approx i_{p2} \cos(s_2 t + \gamma_2), \\ i_p \sin(\Omega) &\approx i_{p2} \sin(s_2 t + \gamma_2), \end{aligned}$$

where the coefficients  $e_{pp'}$  and  $i_{pp'}$  and the phases  $\beta_p$  and  $\gamma_p$  are given by the secular theory of Brouwer and Van Woerkom's in tables 7.1 and 7.2.

Finally, we must replace all elliptical coordinates  $e_1, s_1, \varpi_1, \Omega_1$  by the Poincaré canonical variables (5.2.3). The corrections due to general relativity has important stabilizing effects on Mercury [53] and must be added to the Hamiltonian (5.2.7) (see [96, 15, 7])

$$H_{GR} = -3 \frac{(\mathcal{G}M_S)^2 m_1}{a_1^2 c^2} \frac{1}{\sqrt{1 - e^2}}.$$

The result is the Hamiltonian of the BMH model (see [7] formula (41))

$$\begin{aligned} H &= \left(F_{GR} + F_e^{(1)}\right) I + F_e^{(3)} I^2 + F_i^{(1)} J + F_i^{(3)} J^2 + F_{ei} J J \\ &\quad + F_{e5}^{(2)} \sqrt{I} \cos(\varphi + g_5 t + \beta_5) \\ &\quad + F_{e2}^{(2)} \sqrt{I} \cos(\varphi + g_2 t + \beta_2) \\ &\quad + F_{i2}^{(2)} \sqrt{J} \cos(\psi + s_2 t + \gamma_2). \end{aligned} \quad (5.2.8)$$

In the Hamiltonian (5.2.8), we have dropped the subscripts 1 because its expression contains only Mercury's canonical variables.  $\varphi := -\varpi$  and  $\psi := -\Omega$  are the canonical angles conjugated resp. to  $I := 1 - \sqrt{1 - e^2}$  and  $J := \sqrt{1 - e^2} (1 - \cos i)$ . The coefficients are homogeneous to a frequency, and the Hamiltonian has thus the dimension of a frequency (arcsec/yr). In the present work, we have applied a canonical transformation  $t \leftarrow gt$  and  $H \leftarrow \frac{H}{g}$  such that the frequencies are directly expressed in arcsec/yr. The reader should thus be careful that the numerical values for the coefficients of  $H$  are not the same as in [7]. The numerical values for the coefficients of  $H$  are given in appendix C.

### 5.2.2 Resonance map in action space

The Hamiltonian of the BMH model (5.2.8) has one part that only depends on the actions

$$H_{action} := \left( F_{GR} + F_e^{(1)} \right) I + F_e^{(3)} I^2 + F_i^{(1)} J + F_i^{(3)} J^2 + F_{ei} I J. \quad (5.2.9)$$

Would the total Hamiltonian be reduced to the part (5.2.9), Mercury's dynamics would be integrable. The actions would be constant and the canonical angles would simply grow linearly with time according to the Hamilton equations

$$\begin{aligned} \dot{\varphi}(t) &= -g_1(I, J), \\ \dot{\psi}(t) &= -s_1(I, J). \end{aligned} \quad (5.2.10)$$

The frequencies  $g_1(I, J) := -\frac{\partial H_{action}}{\partial I}$ , and  $s_1(I, J) = -\frac{\partial H_{action}}{\partial J}$  are called the *fundamental frequencies* of the system (strictly speaking, they are not frequencies but beating frequencies). Note that the frequencies  $g_1$  and  $s_1$  are defined to correspond to the beating frequencies of  $\varpi$  and  $\Omega$ , hence the strange minus sign in (5.2.10). Equations (5.2.10) means that Mercury's elliptical orbit is not fixed: Mercury's perihelion precesses at frequency  $g_1$ , and Mercury's orbital plane oscillates at frequency  $s_1$  w.r.t the invariant reference plane. Equations (5.2.10) describe the secular variations of Mercury's orbit, that is, its orbital variations on a timescale of about 100000 yr. For example, the current value of  $g_1$  is about  $5.46''/yr$ , which corresponds to a period of about 237000 yr.

However, Hamiltonian (5.2.8) is not integrable because one part depends on the angles

$$H_{res} = F_{e5}^{(2)} \sqrt{I} \cos(\varphi + g_5 t + \beta_5) + F_{e2}^{(2)} \sqrt{I} \cos(\varphi + g_2 t + \beta_2) + F_{i2}^{(2)} \sqrt{J} \cos(\psi + s_2 t + \gamma_2). \quad (5.2.11)$$

The frequencies  $g_5, s_2, g_2$  are the three main resonances (or *resonances of first order*) in the system. Mercury reaches a resonance when the action values are such that the fundamental frequencies correspond to one of the resonances, that is when  $g_1 \approx g_5$ ,  $g_1 \approx g_2$  or  $s_1 \approx s_2$ . In that case, one of the angular terms in  $H_{res}$  (5.2.11) has a beating frequency close to zero, and the integrable dynamics is completely perturbed.

The dynamics defined by the Hamiltonian (5.2.8) is nonlinear. The nonlinearities can excite all Fourier harmonics which are linear combinations of the first order resonances  $(g_5, g_2, s_2)$ . The harmonics can have a major influence on the dynamics, because Mercury's fundamental frequencies  $g_1$  and  $s_1$  can be resonant with some of the harmonics, even if they are not resonant to first order with  $(g_5, g_2, s_2)$ . For example, the second order resonances are  $g_5 \pm g_2$ ,  $g_5 \pm s_2$  and  $g_2 \pm s_2$ . More generally, the system has reached a resonance if an equality of the form

$$n_1(g_1 - g_5) + n_2(g_1 - g_2) + n_3(s_1 - s_2) = 0 \quad (5.2.12)$$

is satisfied, for integer values of the coefficients  $n_1, n_2, n_3$ . The sum  $|n_1| + |n_2| + |n_3|$  is called the *order of the resonance*. The larger the order of the resonance, the smaller its impact on the dynamics.

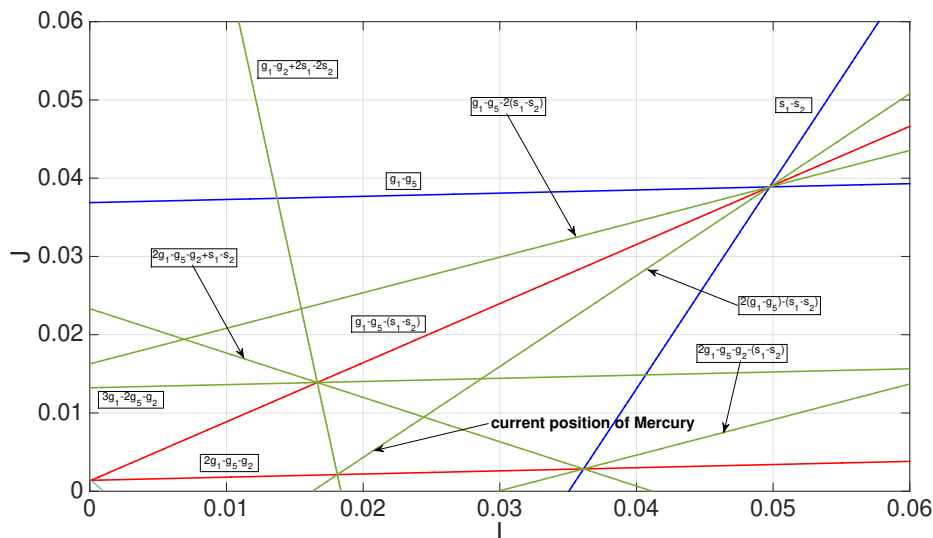


Figure 5.2.2: The resonance map in action space. The blue lines represent the first order resonances, the red lines to the second order resonances, and the green lines to third order. Mercury's current position is close to an intersection of many third order resonances.

Since the work of Chirikov [18], it is known empirically that chaotic motion arises because of overlap of resonant regions. Heuristically, this means that the dynamics is chaotic if at least two relations of the form of (5.2.12) are almost satisfied. On the contrary, a term depending on the canonical angles with a beating frequency far away from any resonance only creates a quasi-periodic perturbation on the dynamics, and does not break integrability. Those ideas can be formulated more rigorously with Lie transforms methods of the Hamiltonian, the interested reader is referred for example to [72]. Lie transforms methods are quite subtle, and yet the basic idea is very simple:

*A resonance of highest order creates a smaller perturbation in the dynamics.*

To understand which of the resonances (5.2.12) create chaotic motion in Mercury's dynamics, we have plotted in Fig.(5.2.2) the resonance network in action space  $(I, J)$  up to third order (for convenience, the actions have been divided by  $\Lambda$ ). The resonance lines are defined by all equations (5.2.12) for all triplets of integers  $(n_1, n_2, n_3)$  with  $|n_1| + |n_2| + |n_3| < 3$ . For our purpose, it can be considered that resonances of order higher than 3 can be neglected. The lines are drawn in action space close to the current position of Mercury. The resonance lines are straight lines because we stopped the expansion of the Hamiltonian to quadratic terms in  $I, J$  which corresponds to the fourth order in eccentricity and inclination. In Fig.(5.2.2), the blue lines correspond to the first order resonances, the red lines to the second order resonances, and the green lines to third order ones.

Fig.(5.2.2) is very important in the present context. It gives the qualitative structure of the dynamical system before doing any numerical integration of the equations of motion. Let us comment more precisely on Fig.(5.2.2). The blue line corresponding to the resonance  $g_1 - g_5$  defines the border of the interesting part of the domain in action space. Once Mercury reaches this line, resonance with Jupiter occurs and Mercury enters in a regime of large-scale chaos, as explained in section 5.1. We thus restrict the study to the domain below the line  $g_1 - g_5$ .

The first order resonance  $s_1 - s_2$  crosses the action domain, not so far from Mercury's current position. The term  $\cos(\psi + s_2 t + \gamma_2)$  in  $H_{res}$  (5.2.11) is close to resonance and can thus not be integrated out. The resonance line  $g_1 - g_2$  does not appear on Fig.(5.2.2) because it crosses the action space for negative values of  $J$ . The resonance  $g_1 - g_2$  can never be reached by Mercury (this is a consequence of the simplicity of the present model, as the resonance  $g_1 - g_2$  can actually be reached with the complete solar system's dynamics). The second order resonance  $2g_1 - g_5 - g_2$  has also a negligible influence because it lies at the border of the accessible domain. The frequency  $g_2$  is only resonant to third order.

This last point has an important consequence: even if the coefficients  $F_{e_5}^{(2)}, F_{e_2}^{(2)}, F_{i_2}^{(2)}$  in (5.2.11) are of same order of magnitude, the three angular terms do not have an equivalent impact on Mercury's dynamics. The term  $F_{e_2}^{(2)} \sqrt{I} \cos(\varphi + g_2 t + \beta_2)$  creates a large amplitude perturbation on the dynamics, but this perturbation is mostly quasiperiodic. Its contribution to chaotic motion only comes from the third order resonances  $2g_1 - g_5 - g_2 + s_1 - s_2 / g_1 - g_2 + 2s_1 - 2s_2$  and  $3g_1 - 2g_5 - g_2$  that cross the domain close to Mercury's position. Hence, the frequency  $g_2$  represents a small perturbation for Mercury's long-term motion. More precisely, there exists a canonical change of variables  $(I, J, \varphi, \psi) \rightarrow (\tilde{I}, \tilde{J}, \tilde{\varphi}, \tilde{\psi})$  such that the perturbation  $F_{e_2}^{(2)} \sqrt{I} \cos(\varphi + g_2 t + \beta_2)$  can be reduced to a term of much smaller amplitude. We do not give further details on this technique, because it will be precisely developed in section 5.3.1 to do stochastic averaging.

### 5.2.3 The truncated Hamiltonian as a slow variable

The remarkable intuition of BMH is to consider the resonance  $g_2 - g_5$  as a small perturbation for Mercury. Using this idea, they were able to find out a non trivial slow variable for the Hamiltonian dynamics (5.2.8). We now report the steps leading to the definition of the slow variable.

First, we integrate the time dependance  $g_5 t + \beta_5$  and  $s_2 t + \gamma_2$  in  $H_{res}$  with the canonical change of variable

$$\begin{aligned}\varphi &\leftarrow \varphi + g_5 t + \beta_5, \\ \psi &\leftarrow \psi + s_2 t + \gamma_2, \\ H &\leftarrow H + g_5 I + s_2 J.\end{aligned}$$

In the new canonical variables, the Hamiltonian (5.2.8) of the BMH model becomes

$$\begin{aligned}H &= \left( F_{GR} + F_e^{(1)} + g_5 \right) I + F_e^{(3)} I^2 + \left( F_i^{(1)} + s_2 \right) J + F_i^{(3)} J^2 + F_{ei} I J \\ &\quad + F_{e_5}^{(2)} \sqrt{I} \cos(\varphi) + F_{i_2}^{(2)} \sqrt{J} \cos(\psi) \\ &\quad + F_{e_2}^{(2)} \sqrt{I} \cos(\varphi + (g_2 - g_5) t + \beta_2 - \beta_5).\end{aligned}\tag{5.2.13}$$

The Hamiltonian part that only depends on the actions is

$$H_{action} := \left( F_{GR} + F_e^{(1)} + g_5 \right) I + F_e^{(3)} I^2 + \left( F_i^{(1)} + s_2 \right) J + F_i^{(3)} J^2 + F_{ei} I J.\tag{5.2.14}$$

We call  $\tilde{H}$  the first part of the Hamiltonian, excluding the resonance  $g_2$

$$\tilde{H} = \left( F_{GR} + F_e^{(1)} + g_5 \right) I + F_e^{(3)} I^2 + \left( F_i^{(1)} + s_2 \right) J + F_i^{(3)} J^2 + F_{ei} I J + F_{e_5}^{(2)} \sqrt{I} \cos(\varphi) + F_{i_2}^{(2)} \sqrt{J} \cos(\psi),\tag{5.2.15}$$

and  $H_{pert}$  the term with the  $g_2 - g_5$  frequency

$$H_{pert} = F_{e_2}^{(2)} \sqrt{I} \cos(\varphi + (g_2 - g_5)t + \beta_2 - \beta_5). \quad (5.2.16)$$

The term  $H_{pert}$  represents a small perturbation. Without this term, the truncated Hamiltonian  $\tilde{H}$  is conserved. The dynamics defined by  $\tilde{H}$  alone conserves the value of  $\tilde{H}$  because it is an autonomous Hamiltonian. The dynamics contains all resonances obtained with the combination of  $g_5$  and  $s_2$ . A look at Fig.(5.2.2) shows that 3 resonances give a contribution to chaotic motion: the second order resonance  $g_1 - g_5 - (s_1 - s_2)$  and the two third order resonances  $2(g_1 - g_5) - (s_1 - s_2)$  and  $g_1 - g_5 - 2(s_1 - s_2)$ . The dynamics defined by  $\tilde{H}$  is thus chaotic and we assume it is ergodic on the levels of constant  $\tilde{H}$  values.

With the perturbation (5.2.16), the truncated Hamiltonian  $\tilde{H}$  is no longer conserved, but evolves through the equation

$$\begin{aligned} \frac{d\tilde{H}}{dt} &= \{H, \tilde{H}\}, \\ &= \{H_{pert}, \tilde{H}\}, \end{aligned} \quad (5.2.17)$$

where  $\{F, G\}$  represent the canonical Poisson brackets. The time evolution equation (5.2.17) shows that the truncated Hamiltonian  $\tilde{H}$  has a time evolution with a typical amplitude given by  $H_{pert}$ . The variations of  $\tilde{H}$  are thus not small. However, most of those variations are quasiperiodic and give no long-term deviation. Only the third order resonant terms hidden in the Poisson bracket  $\{H_{pert}, \tilde{H}\}$  give a non-integrable variation of  $\tilde{H}$ . Averaging  $\tilde{H}$  variations over a frame of length about ten times the period of the large oscillations  $\frac{1}{g_1 - g_2}$  kills the quasiperiodic variations and leaves only the non-integrable component of the time evolution of  $\tilde{H}$ . We thus introduce a variable defined by

$$h := \langle \tilde{H} \rangle_\theta, \quad (5.2.18)$$

where the average  $\langle \rangle_\theta$  is a local time average over a frame of length  $\theta$ . The variable  $h$  defined by (5.2.18) is a slow variable for the BMH dynamics. Fig.(5.2.3) shows a numerical integration of the equation (5.2.17) together with the trajectory of the slow variable  $h$ . The time variations of  $\tilde{H}$  are reduced by more than a factor ten with local time averaging.

#### 5.2.4 Condition for Mercury's destabilization

We are now looking for the conditions for Mercury's destabilization. We have just shown in section 5.2.3 that the truncated Hamiltonian  $\tilde{H}$  defined in (5.2.15) (more precisely, its local time average  $h$ ), is a slow variable. Because of the presence of the second and third order resonances in the domain, the Hamiltonian dynamics defined by  $\tilde{H}$  is chaotic. We observed in the simulation that chaos has enough amplitude to carry the system all over accessible phase space in a few Myr. As we will see in the following, the slow variable  $h$  evolves over a typical timescale of 1 Gyr. At the slow variable's time scale, the dynamics defined by  $\tilde{H}$  satisfies the ergodic hypothesis.

Let us consider for the moment that  $\tilde{H}(I, J, \varphi, \psi)$  is constant. This amounts to neglecting the term  $H_{pert}$  coming from the  $g_2$  frequency in the BMH Hamiltonian. Fig.(5.2.4) displays the level curves of equation  $H_{action}(I, J) = C^{te}$  in action space, with  $H_{action}$  given by (5.2.14).  $H_{action}$  is the part of  $\tilde{H}$  that depends only on action variables. The function  $H_{action}(I, J)$  has the global structure of a saddle in the three dimensional space  $(I, J, H_{action})$ . The picture

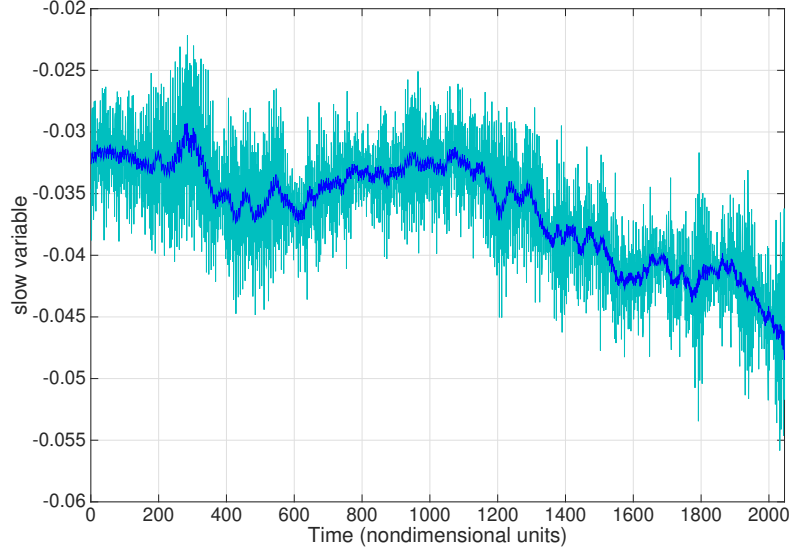


Figure 5.2.3: A trajectory  $\tilde{H}(t)$  (cyan) compared to the slow variable  $h(t)$  (blue). The local time averaging of  $\tilde{H}(t)$  suppresses the fast oscillations that do not correspond to long-term variations.

shows the existence of a critical value  $H_{cr}$  such that the curve of equation  $H_{action}(I, J) = H_{cr}$  separates four disjoint domains in phase space. Two of the domains are defined by the inequality  $H_{action} < H_{cr}$ . One of these two domains is confined to low values  $I$  and  $J$ , and another one is unbounded and extends to values for  $I$  and  $J$  close to 1.

Mercury is currently in the bounded part of phase space, with value  $H_{action} < H_{cr}$ . As long as the value of  $H_{action}$  remains lower than  $H_{cr}$ , the trajectory is confined in the bounded domain of phase space, with low eccentricity and inclination values. Of course,  $H_{action}$  is not conserved by the dynamics, and the system is thus not confined to a single level curve of  $H_{action}$ . For a given value of  $\tilde{H}$ ,  $H_{action}$  satisfies the inequalities

$$\tilde{H} - \left|F_{e5}^{(2)}\right| \sqrt{I} - \left|F_{i2}^{(2)}\right| \sqrt{J} < H_{action} < \tilde{H} + \left|F_{e5}^{(2)}\right| \sqrt{I} + \left|F_{i2}^{(2)}\right| \sqrt{J}. \quad (5.2.19)$$

In the stable domain of phase space,  $I < 0.05$  and  $J < 0.04$ . As a result  $H_{action}$  is bounded from below by the inequality

$$\tilde{H} - \sqrt{0.05} \left|F_{e5}^{(2)}\right| - \sqrt{0.04} \left|F_{i2}^{(2)}\right| < H_{action}. \quad (5.2.20)$$

We call  $H_{low} := \tilde{H} - \sqrt{0.05} \left|F_{e5}^{(2)}\right| - \sqrt{0.04} \left|F_{i2}^{(2)}\right|$  the lower bound of  $H_{action}$ . If the lower bound in (5.2.20) is larger than  $H_{cr}$ , Mercury's orbit is stable because it is confined in the bounded domain of phase space defined by the inequality  $H_{action} > H_{cr}$ .

Destabilization occurs when the value of  $\tilde{H}$  decreases such that the lower bound  $H_{low} := \tilde{H} - \sqrt{0.05} \left|F_{e5}^{(2)}\right| - \sqrt{0.04} \left|F_{i2}^{(2)}\right|$  reaches the critical value  $H_{cr}$ . Then the system can cross the level curve  $H_{action} = H_{cr}$  exactly at the saddle point and enter the unbounded region of phase space. Because of ergodicity, Mercury is brought very fast at high  $I$  and  $J$  values (and thus at

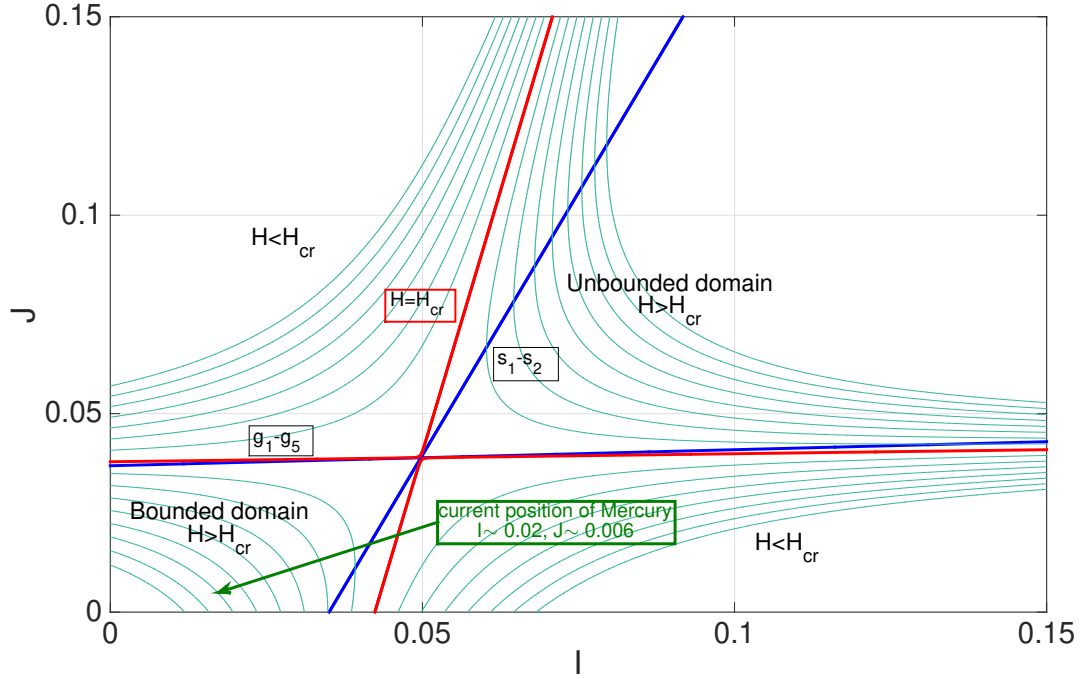


Figure 5.2.4: Level curves of  $H_{action}(I, J)$  in action space. The 3D surface of  $H_{action}$  has the structure of a saddle. The saddle is located exactly at the intersection of the two first order resonances  $g_1 - g_5$  and  $s_1 - s_2$ . To enter the unbounded domain of phase space, the system has to cross the saddle.

high eccentricity and inclination values) once it has crossed the saddle. The saddle point is the point where the gradient of  $H_{action}$  vanishes, which correspond to the equations

$$\begin{aligned} \frac{\partial H_{action}}{\partial I}(I, J) &= 0, \\ \frac{\partial H_{action}}{\partial J}(I, J) &= 0. \end{aligned} \quad (5.2.21)$$

Equations (5.2.21) are exactly equivalent to the conditions for the resonances  $g_1 - g_5$  and  $s_1 - s_2$  intersection. This is an interesting point: Fig.(5.2.4) shows that the condition  $H_{action} = H_{cr}$  for destabilization corresponds almost exactly to the resonance  $g_1 - g_5$ . It is reflected in the fact that the red line defined by  $H_{action} = H_{cr}$  is almost identical to the resonance line  $g_1 - g_5$ , and confirms that destabilization of Mercury's orbit occurs through a secular resonance with Jupiter. But destabilization also occurs when the system is in resonance with the  $s_2$  mode, because destabilization happens when the system crosses the saddle.

We have found a very simple and intuitive mechanism for the destabilization of Mercury's orbit. Mercury's dynamics is governed by a slow variable  $\tilde{H}$  obtained as the truncation of the secular Hamiltonian. The timescale for the variations of  $\tilde{H}$  is much larger than the typical period of secular motion. Fig.(5.2.5) illustrates the destabilization mechanism. The phase space of the system can be seen as two reservoirs of  $H_{action}$ , connected by a saddle. The variations of  $\tilde{H}(t)$  can be seen as the water level in the first reservoir that increases or decreases following

the variations of  $\tilde{H}(t)$ . If the water level increases (for example, when snow is melting...) and reaches the level of the saddle, water overflows and begins to fill the second reservoir.

A last point should be emphasized. The criterion  $H_{action} = H_{cr}$  for destabilization is not exact. Destabilization does not exactly occurs at the first time the equality  $H_{action} = H_{cr}$  is satisfied. Destabilization may occur a bit before or after the slow variable reaches the value  $H_{cr}$  because the dynamics takes some time to travel over the available phase space at constant value  $\tilde{H}$ . Also, destabilization depends somehow on the values of the angles  $\varphi$  and  $\psi$ . Let us define a critical time  $t_{cr}$  by the first time at which the equation

$$h(t_{cr}) = h_{cr}$$

is satisfied. The value  $h_{cr}$  is roughly related to  $H_{cr}$  by the relation  $h_{cr} - \sqrt{0.05} \left| F_{e5}^{(2)} \right| - \sqrt{0.04} \left| F_{i2}^{(2)} \right| = H_{cr}$ . For many independent realizations of the BMH dynamics, some trajectories may be destabilized a bit before the critical time  $t_{cr}$ , and some other a bit after  $t_{cr}$ . As we will see in section 5.3.4, the approximation that consists in identifying the first destabilization time on the one hand, and the first time  $t_{cr}$  the slow process  $h$  reaches the value  $h_{cr}$  on the other hand, leads to excellent results.

## 5.3 Diffusion process for the slow variable

The present section is much more technical than the previous ones. We put on a more formal basis the ideas presented in section 5.2.4 using Lie transforms of the Hamiltonian. The computation have been done with the software TRIP developed at the IMCCE by Jacques Laskar and Mickael Gastineau (<https://www.imcce.fr/trip/>), which is precisely devoted to the computation of series in celestial mechanics. In this section, we apply stochastic averaging to the dynamics of the slow variable  $h$  defined in (5.2.18), and we obtain a theoretical expression for the diffusion coefficient of the stochastic process.

### 5.3.1 Third order resonances amplitudes

The Hamiltonian of the BMH model can be written as

$$H = \tilde{H}(I, J, \varphi, \psi) + \epsilon H_{pert}(I, J, \varphi, \psi, gt), \quad (5.3.1)$$

where  $g := g_2 - g_5$ , with  $\tilde{H}$  given by (5.2.15) and  $H_{pert}$  given by (5.2.16). Table (C.1) gives the values to compute the order of magnitude of  $\epsilon$ . We find  $|\tilde{H}| \approx 3 \times 10^{-2}$  arcsec/yr, and  $\epsilon |H_{pert}| \approx 9 \times 10^{-3}$  arcsec/yr.  $\epsilon$  is a formal parameter that quantifies the ratio between the perturbative part and the principal part of the Hamiltonian. We give the value  $\epsilon = \frac{9 \cdot 10^{-3}}{3 \cdot 10^{-2}} = 0.3$ . The parameter  $\epsilon$  is used below to set the hierarchy of Lie transforms. The first part  $\tilde{H}$  contains the terms depending only on the action variables and the terms coming from the two frequencies  $g_5$  and  $s_2$ .  $H_{pert}$  contains the term coming from the frequency  $g_2$ . We have explained in section 5.2.3 that the resonance  $g_1 - g_2$  does not occur in the accessible domain of phase space. The term  $H_{pert}$  is nonresonant to first order in  $\epsilon$ . We can thus perform a canonical change of variables  $\{I, J, \varphi, \psi\} \rightarrow \{I', J', \varphi', \psi'\}$  with Lie transforms methods to average the term  $H_{pert}$  and all nonresonant harmonics. To perform the Lie transforms, we use as a kernel the part  $H_{action}$  (given by (5.2.14)) of the Hamiltonian, that does not depend on the angles. The procedure is described with all details in many references [74, 72]. The procedure leads to the so-called

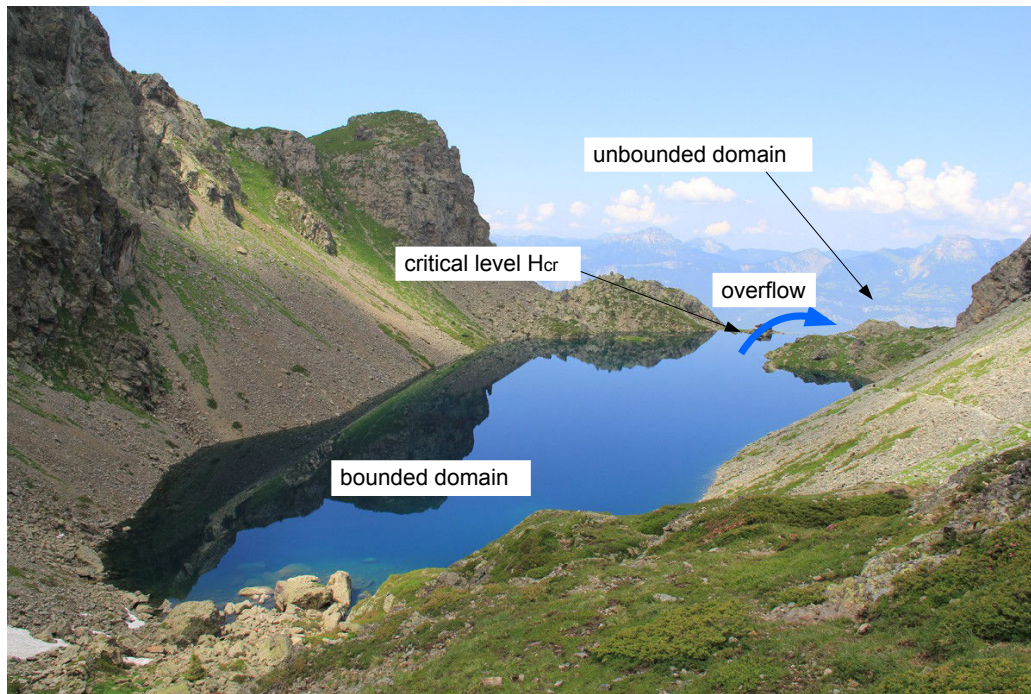


Figure 5.2.5: Lac du Crozet in the mountain of Belledonne (Grenoble). The lake with the mountain represent the dynamical structure of phase space for the BMH model. The water level represents the lower bound value  $H_{low}$ , and indirectly the value of  $\tilde{H}$ . When the value  $\tilde{H}(t)$  is above a critical level, the system travels in the accessible part of phase space (the lake), but remains in the bounded domain. If on the contrary the value  $\tilde{H}(t)$  reaches the critical level, the system can enter the unbounded domain. This is analogous to water overflowing the saddle. (picture from altituderando.com)

	resonance	angle
second order	$2g_1 - g_5 - g_2$	$2\varphi + gt$
third order	$3g_1 - 2g_5 - g_2$	$3\varphi + gt$
	$2g_1 - g_5 - g_2 + s_1 - s_2$	$2\varphi + \psi + gt$
	$g_1 - g_2 + 2s_1 - 2s_2$	$\varphi + 2\psi + gt$
	$2g_1 - g_5 - g_2 - (s_1 - s_2)$	$2\varphi - \psi + gt$

Table 5.1: Table of the perturbing resonances in the BMH model up to order 3.

*resonant normal form.* The Hamiltonian in resonant normal form only contains terms that can not be integrated out because they are resonant in the accessible domain.

For the BMH model, the resonances are displayed on the resonance map in Fig.(5.2.2). The map shows that there are 5 resonances in the domain that involve the  $g_2$  frequency. They are gathered in table (5.1). Each of these resonances is associated to a term depending on the angles in the Hamiltonian. The resonant angles are also gathered in table (5.1).

The computations of the Lie transforms up to order 3 in  $\epsilon$  are very tough. They can be done with a special algorithm designed by Jacques Laskar on the software TRIP. At each order in  $\epsilon$  in the Lie transforms, we keep all terms that involve at least one of the resonant angles listed in table (5.1). The algorithm gives the Hamiltonian of the BMH model written in terms of the new canonical variables. The new Hamiltonian can be put in the form

$$H(I', J', \varphi', \psi', t) := \tilde{H}^{(3)}(I', J', \varphi', \psi') + \epsilon^3 H_{res}^{(3)}(I', J', \varphi', \psi', gt) + O(\epsilon^4), \quad (5.3.2)$$

where  $\tilde{H}^{(3)}$  is the autonomous part of the Hamiltonian that gathers all terms that do not depend on the time angle  $gt$ , and  $H_{res}^{(3)}$  is the part of the Hamiltonian with all resonant angles of second and third order given in table (5.1). The part  $H_{res}^{(3)}$  has the form

$$\begin{aligned} \epsilon^3 H_{res}^{(3)}(I', J', \varphi', \psi', gt) &:= F_1(I', J') \cos(2\varphi' + gt) \\ &+ F_2(I', J') \cos(3\varphi' + gt) \\ &+ F_3(I', J') \cos(2\varphi' + \psi' + gt) \\ &+ F_4(I', J') \cos(\varphi' + 2\psi' + gt) \\ &+ F_5(I', J') \cos(2\varphi' - \psi' + gt). \end{aligned} \quad (5.3.3)$$

We have explicitly computed the coefficients  $F_1, F_2, F_3, F_4, F_5$  with TRIP. The expressions of those coefficients are given in appendix C. The order of magnitude of  $\epsilon^3 H_{res}^{(3)}$  is much lower than the order of magnitude of  $\epsilon H_{pert}$  because of the increased order in  $\epsilon$ .  $\epsilon^3 H_{res}^{(3)}$  is a small perturbation in the dynamics defined by the Hamiltonian (5.3.2). This means that the autonomous part  $\tilde{H}^{(3)}$  of the Hamiltonian is a slow variable for the dynamics. The time evolution of  $\tilde{H}^{(3)}$  is given by

$$\begin{aligned} \dot{\tilde{H}}^{(3)} &= \{H, \tilde{H}^{(3)}\} \\ &= \epsilon^3 \{H_{res}^{(3)}, \tilde{H}^{(3)}\}. \end{aligned} \quad (5.3.4)$$

Equation (5.3.4) is equivalent to equation (5.2.17). The difference is that equation (5.2.17) describing the time evolution of  $\tilde{H}$  still contains periodic terms that give no long-term variations of  $\tilde{H}$ . In equation (5.3.4), we have integrated out all periodic contributions, such that the time evolution of  $\tilde{H}^{(3)}$  is slow, and only contains nonintegrable terms.  $\tilde{H}^{(3)}$  is somehow the best slow

variable we can built for the dynamics, because it has irreducible long term variations due to the presence of resonances in the system.

The Hamiltonian (5.3.2) defines a slow-fast dynamical system. The fast dynamics is given by Hamilton's equations of motion defined by the Hamiltonian  $\tilde{H}^{(3)}$ . The slow dynamics is given by the time evolution of  $\tilde{H}^{(3)}$  in equation (5.3.4). The dynamics has thus the form of a fully coupled slow-fast system, because the fast variables  $\{I', J', \varphi', \psi'\}$  are coupled to the slow variable  $\tilde{H}^{(3)}$ . The dynamics defined by the Hamiltonian  $\tilde{H}^{(3)}$  is similar to that of  $\tilde{H}$ , because  $\tilde{H}$  and  $\tilde{H}^{(3)}$  only differ by terms of order larger than  $\epsilon$  from each other. In particular, the  $\tilde{H}^{(3)}$  is chaotic, with a Lyapunov time of the order of 10 Myr and we thus assume that it satisfies the mixing hypothesis. In the next section, we apply stochastic averaging to the dynamics (5.3.4) to find theoretically the order of magnitude for the long-term diffusion of  $\tilde{H}^{(3)}$ .

### 5.3.2 Stochastic averaging and order of magnitude for the diffusion coefficient

In the present section, we apply stochastic averaging to the dynamics (5.3.4) to find an order of magnitude for the diffusion of the slow variable  $\tilde{H}^{(3)}$ . To simplify the computations and to get an explicit expression for the diffusion coefficient, we have chosen to do rough but reasonable assumptions.

We first notice that the terms of largest amplitude in  $\tilde{H}^{(3)}$  are the terms that depend only on the action variables. To leading order, the expression of  $\tilde{H}^{(3)}$  reduces to

$$\tilde{H}^{(3)}(I', J', \varphi', \psi') \approx H_{action}(I', J', \varphi', \psi'),$$

with the expression of  $H_{action}$  given by (5.2.9). Using the above approximation in the right-hand side of (5.3.4), the dynamics of  $\tilde{H}^{(3)}$  reduces to

$$\dot{\tilde{H}}^{(3)} = -\epsilon^3 \frac{\partial H_{action}}{\partial I'} \frac{\partial H_{res}^{(3)}}{\partial \varphi'} - \epsilon^3 \frac{\partial H_{action}}{\partial J'} \frac{\partial H_{res}^{(3)}}{\partial \psi'}. \quad (5.3.5)$$

With the expression (5.3.3), equation (5.3.5) can be rewritten as

$$\begin{aligned} \dot{\tilde{H}}^{(3)}(I', J', \varphi', \psi', gt) &= \bar{F}_1(I', J') \sin(2\varphi' + gt) \\ &+ \bar{F}_2(I', J') \sin(3\varphi' + gt) \\ &+ \bar{F}_3(I', J') \sin(2\varphi' + \psi' + gt) \\ &+ \bar{F}_4(I', J') \sin(\varphi' + 2\psi' + gt) \\ &+ \bar{F}_5(I', J') \sin(2\varphi' - \psi' + gt). \end{aligned} \quad (5.3.6)$$

where  $\{\bar{F}_1, \bar{F}_2, \bar{F}_3, \bar{F}_4, \bar{F}_5\}$  are new coefficients obtained from the expression of  $\{F_1, F_2, F_3, F_4, F_5\}$ . They are given in section C. Stochastic averaging for the dynamics (5.3.6) states that the long-term evolution of  $\tilde{H}^{(3)}$  should be equivalent in law to a stochastic differential equation

$$\dot{\tilde{H}}^{(3)} = a\left(\dot{\tilde{H}}^{(3)}\right) + D\left(\dot{\tilde{H}}^{(3)}\right)\xi(t). \quad (5.3.7)$$

The drift term  $a\left(\dot{\tilde{H}}^{(3)}\right)$  comes from averaging (5.3.6) over the fast motion, and from the correlations between fast and slow motion as explained in section 1.3.3. There is no hope to find

any explicit expression for this term. Quite surprisingly, preliminary simulations done with the dynamics (5.3.6) seem to show that the drift is very small compared to the diffusion, and can be neglected. In the following, we focus on the diffusion coefficient  $D\left(\tilde{H}^{(3)}\right)$ .

The diffusion coefficient can be expressed with a Green-Kubo formula involving the correlation function of the driving term in (5.3.6) (see section 1.3.3). The complete expression is quite long. In this section, in order to get orders of magnitude, we assume that the cross correlations between different resonant angles give no appreciable contributions. For example, we neglect the correlation  $C_{12} := \langle \bar{F}_1(I(t), J(t)) \sin(3\varphi'(t) + gt) \bar{F}_2(I'(0), J'(0)) \sin(2\varphi'(0) + \psi'(0)) \rangle$ .

In the type of chaotic Hamiltonian systems we are studying, decorrelation is much faster on the angles than on action variables. This can be explained qualitatively by the fact that separation of action trajectories is enhanced on angle trajectories because of the Hamiltonian flow. In general, if decorrelation of action variables occurs over a timescale  $\tau_{action}$ , the angle variables decorrelate over a timescale of the order of  $(\tau_{action})^{1/3}$ . This phenomenon has already been noticed by many authors, including [46, 102]. We thus do not longer take into account the dependence on action variables in (5.3.6) and we systematically replace the functions  $\bar{F}_i(I(t), J(t))$  (for  $i = 1, 4$ ) by a constant corresponding to their order of magnitude. Fig.(5.3.2) shows that the accessible domain is centered around  $I \approx J \approx 0.02$ . We define an order of magnitude for  $\bar{F}_i$  by  $|\bar{F}_i| := \bar{F}_i(0.02, 0.02)$ . Among the five terms appearing in equation (5.3.6), two of them are equal to zero. The order of magnitude for the diffusion coefficient  $D\left(\tilde{H}^{(3)}\right)$  finally writes

$$D\left(\tilde{H}^{(3)}\right) \approx 2|\bar{F}_1|^2 \int_0^{+\infty} dt \langle \sin(2\varphi(t) + gt) \sin(2\varphi(0)) \rangle_{\tilde{H}^{(3)}} + 2|\bar{F}_3|^2 \int_0^{+\infty} dt \langle \sin(2\varphi(t) + \psi(t) + gt) \sin(2\varphi(0) + \psi(0)) \rangle_{\tilde{H}^{(3)}} \quad (5.3.8)$$

$$+ 2|\bar{F}_4|^2 \int_0^{+\infty} dt \langle \sin(\varphi(t) + 2\psi(t) + gt) \sin(\varphi(0) + 2\psi(0)) \rangle_{\tilde{H}^{(3)}}. \quad (5.3.9)$$

In formula (5.3.9), the notation  $\langle \cdot \rangle_{\tilde{H}^{(3)}}$  means that the average should be done with a fixed value for  $\tilde{H}^{(3)}$ .

A last approximation is done to compute the correlation functions of the sinus terms inside the integrals. The two angles  $2\varphi + \psi + gt$  and  $\varphi + 2\psi + gt$  are resonant right at the center of the accessible domain. Their average beating frequency is close to zero. On the contrary, the angle  $2\varphi + gt$  is only resonant at the domain boundaries. We choose to keep only the contribution from the resonant angles 3 and 4 of table (5.1). The two angles are chaotic functions, with a Lyapunov time  $\tau_L$ . We thus choose to do the approximation

$$2\varphi(t) + \psi(t) + gt \approx \varphi(t) + 2\psi(t) + gt \approx \theta + \omega t + W\left(\frac{t}{\tau_L}\right),$$

where  $W(t)$  is the standard Brownian motion (also called the *Wiener process*),  $\theta$  is a random variable with uniform probability distribution over  $[0, 2\pi]$ , and  $\omega$  is a typical beating frequency of the resonant angle. The resonant angle's frequency is not zero. It changes chaotically between positive and negative values, depending on the exact location in the domain. The relation between the Lyapunov exponent of a chaotic Hamiltonian dynamics with one degree of freedom and two resonances has been precisely studied by [67]. In the present case however, we do not know any simple relation between the resonant frequencies and the Lyapunov exponent. We have assumed without any further justification that we are in the regime where  $\tau_L \approx \frac{2\pi}{\omega}$ . The

expression (5.3.9) for the diffusion coefficient becomes

$$D\left(\tilde{H}^{(3)}\right) \approx 2\left(|\bar{F}_3|^2 + |\bar{F}_4|^2\right) \int_0^{+\infty} \mathbb{E}\left[\sin\left(\theta + \omega t + W\left(\frac{t}{\tau_L}\right)\right) \sin(\theta)\right] dt. \quad (5.3.10)$$

The computation of the integral in (5.3.10) is straightforward. The final result is

$$D\left(\tilde{H}^{(3)}\right) \approx \frac{1}{2}\left(|\bar{F}_3|^2 + |\bar{F}_4|^2\right) \frac{\tau_L}{1 + (2\pi)^2}. \quad (5.3.11)$$

The diffusion coefficient  $D$  does not depend on  $\tilde{H}^{(3)}$ . Such an expression can thus not be valid everywhere in phase space. In fact, expression (5.3.11) has been obtained with the implicit assumption that the two third order angles  $2\varphi + \psi + gt$  and  $\varphi + 2\psi + gt$  are resonant and cannot be integrated. Expression (5.3.11) is valid if the dynamics crosses the resonant lines  $2g_1 - g_5 - g_2 + s_1 - s_2$  and  $g_1 - g_2 + 2s_1 - 2s_2$ , which corresponds only to a fraction of the accessible domain. The domain of validity of expression (5.3.11) is discussed precisely in the section 5.3.4 where we define the diffusive model.

Finally, we have used the numerical value of the Lyapunov time  $\tau_L \approx 10$  Myr obtained with numerical simulations, and we have evaluated numerically the explicit expressions of  $\bar{F}_2$  and  $\bar{F}_3$  given in appendix C. The units are chosen such that the dimension of  $\tilde{H}^{(3)}$  is the *arcsec/yr*. We get the order of magnitude

$$D_{th} \approx 2.3 * 10^{-14} (\text{arcsec})^2 / \text{yr}^3 \quad (5.3.12)$$

Although the order of magnitude (5.3.4) has been obtained with very strong and questionable assumptions, the numerical value is in very good agreement with the one obtained in (5.3.23) with direct fitting of the numerical simulations results. This result confirms that the long-term diffusion of the slow variable  $h$  defined in (5.2.18) is due to the third order resonances, in particular the resonances  $2g_1 - g_5 - g_2 + s_1 - s_2$  and  $g_1 - g_2 + 2(s_1 - s_2)$ . Even if the coefficients of the stochastic differential equation for the slow variable cannot be computed analytically, Lie transforms method is a good way to define properly the slow and fast variables. For the BMH Hamiltonian, the complete Lie transforms up to third order are much too complex to be done with a usual software like mathematica or Maple, and the software TRIP is necessary to perform them. The theoretical order of magnitude (5.3.11) for  $D$  involves the complex functions  $\bar{F}_3(I', J')$  and  $\bar{F}_4(I', J')$  that can be expressed as rational fractions in  $I', J'$ . We have done the explicit computation of those functions in order to properly justify the order of magnitude (5.3.12). But the order of magnitude (5.3.12) can be obtained in a much more heuristic manner. We have proven that diffusion of the slow variable  $\tilde{H}^{(3)}$  is due to third order secular resonances, that come to order  $\epsilon^3$  in the Hamiltonian (5.3.2). The order of magnitude for  $\bar{F}_3(I', J')$  and  $\bar{F}_4(I', J')$  roughly corresponds to  $\epsilon^3 |\tilde{H}|^2$ . Using the definition of  $\epsilon$  given in (5.3.1), expression (5.3.11) can be written

$$D\left(\tilde{H}^{(3)}\right) \approx \frac{1}{2} \epsilon^6 |\tilde{H}|^4 \frac{\tau_L}{1 + (2\pi)^2}, \quad (5.3.13)$$

where  $|\tilde{H}|$  is the order of magnitude of the averaged BMH Hamiltonian. Evaluating expression (5.3.13) with  $\epsilon = 0.3$ ,  $|\tilde{H}| = 3.10^{-2}$  and  $\tau_L = 10 \times \frac{\pi}{180 * 3600}$  gives  $D \approx 3.5 \times 10^{-10}$  in renormalized time units and  $D \approx 1.7 \times 10^{-15} (\text{arcsec})^2 / \text{yr}^3$ , which is also in good qualitative agreement with (5.3.23).

### 5.3.3 Numerical evaluation of the probability distribution of Mercury's first destabilization time

We have done a numerical simulation to study the probability distribution of Mercury's first destabilization time, and compared the result with the theoretical predictions obtained with stochastic averaging. We have integrated numerically the Hamiltonian dynamics (5.2.13) for 127282 trajectories with close initial conditions. The current value of Mercury's orbital parameters are

$$e_0 \approx 0.205632, i_0 \approx 6.34046^\circ, \varphi_0 \approx -46.8061^\circ, \psi_0 \approx 237.27^\circ. \quad (5.3.14)$$

The initial values of  $e$  and  $i$  were unchanged, but the phases were chosen with uniform probability distribution in the ranges  $[\varphi_0, \varphi_0 + 0.573^\circ]$  and  $[\psi_0, \psi_0 + 0.573^\circ]$ . We had to choose a condition to check if Mercury's orbit was still stable, or if it had been destabilized. A look at Fig.(5.2.4) shows that the trajectory cannot have action values larger than 0.05 as long as it remains in the bounded domain. We thus chose arbitrarily the criterion  $\max(I, J) > 0.06$  to say that Mercury's orbit had been destabilized. The exact action value to set the destabilization criterion has no significant impact on the result because the trajectory fast reaches very high  $I$  and  $J$  values as soon as it has crossed the saddle.

We have integrated the trajectories and recorded for each trajectory the first time  $\tau$  at which the destabilization criterion was satisfied. We set a maximal integration time such that more than 50% of the trajectories had escaped. The reason why we did not choose a longer integration time is that we are mostly interested by destabilizations occurring for times short compared to the age of the solar system. The numerical integrations were done with a symplectic algorithm  $SBAB_2$  (it is not completely trivial to see why the Hamiltonian (5.2.13) can be integrated with a symplectic algorithm, but it can be!).

The red curve in Fig.(5.3.1) displays the numerical computation of the probability distribution  $\rho_{exp}(\tau)$ . The distribution has the general shape of a probability distribution of first exit times from a bounded domain for a stochastic process. The probability distribution  $\rho_{exp}$  decreases very fast to zero when  $\tau \rightarrow 0$ . This can be interpreted by the fact that the process needs some time to reach domain boundaries. To reach the boundary in short times, the process has to perform large jumps very fast, and this happens with very low probability. Mercury's fast destabilizations will be studied in more details in section 5.4. The present simulation has not enough trajectories to get a reliable estimation of  $\rho_{th}$  for short times, that's why the numerical curve in Fig.(5.3.1) begins at  $t \approx 200$ .

The probability has a maximum at the value  $\tau^*$ . It can be considered as the typical time for Mercury's destabilization. Most of the trajectories exit the domain within a time of the order of  $\tau^*$ . In the BMH model, the typical time for Mercury's destabilization is

$$\tau^* \approx 1.32 \times 10^9 yr. \quad (5.3.15)$$

The long time tail of the distribution, that is not represented in Fig.(5.3.1), corresponds to trajectories that remain stable for very long times in spite of chaotic motion. This kind of event also happens with small probability. For a stochastic process (for example a diffusion process), the long time tails of first exit times probability distribution has an exponential decay. We also expect in the present case exponential decay for  $\tau > \tau^*$ .

### 5.3.4 Theoretical predictions for the first destabilization time probability distribution

Section 5.3.1 has shown how to apply rigorously stochastic averaging to the Hamiltonian dynamics of the BMH model. Stochastic averaging shows that the truncated Hamiltonian  $\tilde{H}^{(3)}$

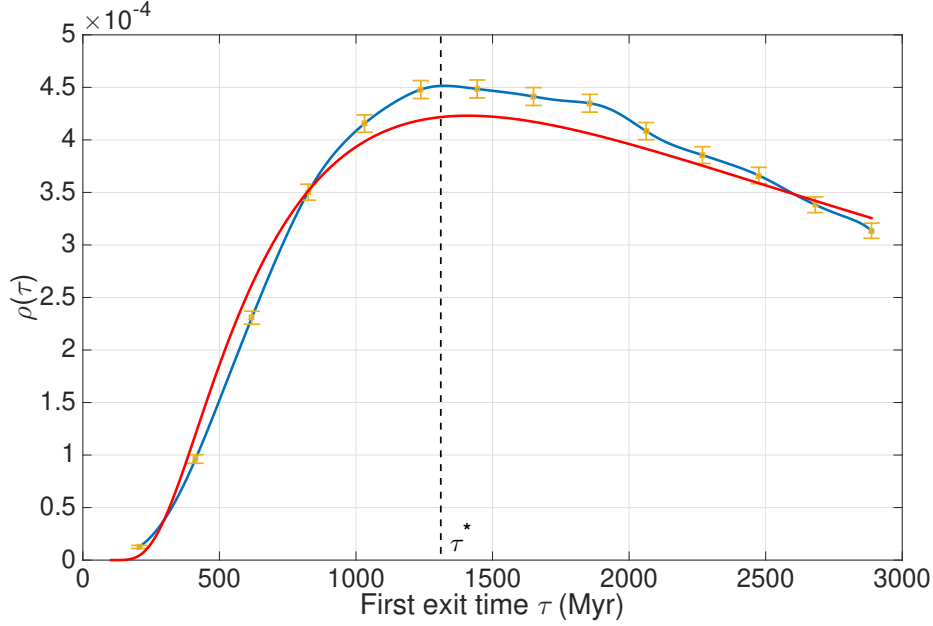


Figure 5.3.1: Probability distribution of Mercury's first destabilization time computed with a direct numerical simulation (blue curve) and with the theoretical prediction of the diffusive model (5.3.22) (red curve).

defined in (5.3.2) is a well-defined slow variable for the system, and follows a diffusion equation (5.3.7). The explicit expression for  $\tilde{H}^{(3)}$  is much too complex to be easily tractable in numerical simulations. We thus assume that the slow variable  $h$  defined in (5.2.18) is a good approximation of  $\tilde{H}^{(3)}$  and we identify the equations for  $\tilde{H}^{(3)}$  and for  $h$ . The stochastic differential equation for  $h$  thus writes

$$\dot{h} = D(h)\xi(t). \quad (5.3.16)$$

We have tried to compute theoretically the diffusion coefficient value  $D(h)$  in (5.3.11). However, the theoretical expression can only give an order of magnitude, not the precise value for  $D(h)$ . It is also very difficult to know how precisely the diffusion coefficient  $D(h)$  depends on  $h$ . In the following, we try to do reasonable assumptions to obtain a simpler stochastic equation for  $h$ .

In Fig.(5.3.2), we have plotted together the level curves of  $H_{action}$  and the two third order resonances  $2g_1 - g_5 - g_2 + s_1 - s_2$  and  $g_1 - g_2 + 2s_1 - 2s_2$  that are responsible for the slow diffusion of  $\tilde{H}$ . For small values of the action variables, Fig.(5.3.2) displays a small region defined by the inequality  $H_{action} > H_{sup}$  where the system does no longer cross the resonance lines. Fig.(5.3.2) shows that  $H_{sup}$  is defined by  $H_{sup} = H_{action}(0.0187, 0)$ . The inequality  $H_{action} > H_{sup}$  can be related to an inequality over  $\tilde{H}$  through relation (5.2.19). Let  $h_{sup}$  be the upper bound for  $\tilde{H}$ , then the value of  $h_{sup}$  roughly satisfies

$$H_{sup} = h_{sup} + \sqrt{0.0187} \left| F_{e5}^{(2)} \right|$$

As the resonances are responsible for the diffusion of  $\tilde{H}$  (or equivalently, for the diffusion of  $h$ ), diffusion is much slower in this region because it is created by resonances of order larger

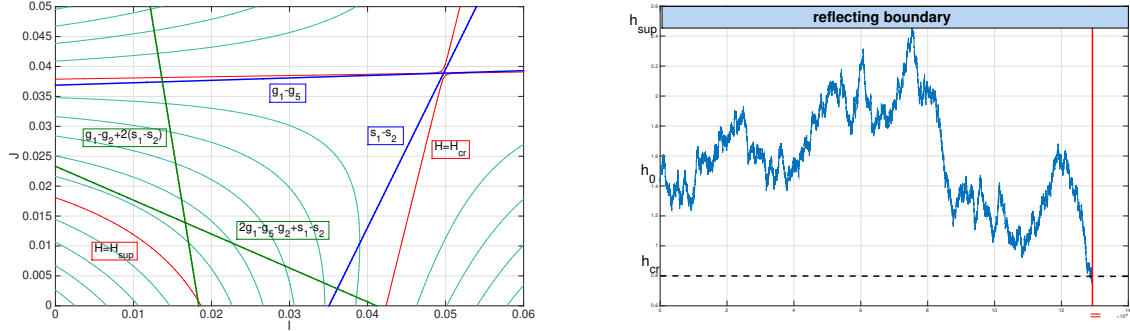


Figure 5.3.2: Left: Level curves of  $H_{action}(I, J)$ , together with the two third order resonances that are responsible for its long-term diffusion. The figure displays the existence of a small domain for  $H_{action} > H_{sup}$  of weak chaos amplitude. The upper bound for  $H_{action}$  is related to an upper bound  $h_{sup}$  for the diffusion process. The value  $h_{sup}$  is modeled by a reflecting boundary for the diffusion process. Right: Properties of the diffusion model for the slow variable. The problem is reduced to the computation of first exit time from the bounded domain  $[h_{cr}, h_{sup}]$ .

than three (the resonances of order larger than three are not represented in Fig.(5.3.2)). We therefore do the rough assumption

$$D(h) = 0 \text{ for } h > h_{sup}. \quad (5.3.17)$$

For  $h_{cr} < h < h_{sup}$ , the numerical simulations show that the system is always in contact with the two resonances  $2g_1 - g_5 - g_2 + s_1 - s_2$  and  $g_1 - g_2 + 2s_1 - 2s_2$  displayed in Fig.(5.3.2). We therefore do the second assumption that the diffusion coefficient is constant in the second region

$$D(h) \equiv D \text{ for } h_{cr} < h < h_{sup}. \quad (5.3.18)$$

Inequalities (5.3.17) and (5.3.18) define a diffusive model for the slow variable  $h$ . The probability distribution  $\mathbb{P}(h, t)$  follows the one dimensional diffusion equation

$$\frac{\partial \mathbb{P}}{\partial t} = D \frac{\partial^2 \mathbb{P}}{\partial h^2} \text{ for } h_{cr} < h < h_{sup}, \quad (5.3.19)$$

with the boundary conditions of zero probability flux at  $h = h_{sup}$  and absorbing boundary conditions at  $h = h_{cr}$

$$\begin{cases} \mathbb{P}(h, t) = 0 & \text{when } h = h_{cr}, \\ \frac{\partial \mathbb{P}}{\partial h}(h, t) = 0 & \text{when } h = h_{sup}. \end{cases} \quad (5.3.20)$$

The initial condition is chosen to be the value of  $\tilde{H}$  computed with Mercury's current orbital parameters defined by (5.3.14). Let  $h_0$  be the initial value of  $\tilde{H}$ , the initial condition for the diffusion equation (5.3.19) writes  $\mathbb{P}(h, 0) = \delta(h - h_0)$ .

The diffusion equation (5.3.19) can be solved explicitly using Fourier transforms. The resolution of equation (5.3.19) is detailed in appendix B. The solution can be expressed as a Fourier series depending on the parameters  $h_{cr}, h_{sup}, h_0$  and  $D$ . Among those parameters, the only one that cannot be precisely evaluated theoretically is the diffusion coefficient. We thus keep the

diffusion coefficient as the only fitting parameter in the model. The values of  $h_{cr}, h_{sup}, h_0$  are given by

$$h_{cr} = -0.048, h_{sup} = -0.028, h_0 = -0.032.$$

We are mainly interested in the probability distribution  $\rho_{th}(\tau)$  of the first exit times from the domain  $[h_{sup}, h_{cr}]$ . The distribution  $\rho_{th}(\tau)$  is related to the probability distribution  $\mathbb{P}(h, t)$  by the relation

$$\rho_{th}(\tau) = -\frac{d}{dt} \int_{h_{cr}}^{h_{sup}} \mathbb{P}(h, t) dh. \quad (5.3.21)$$

With relation (5.3.21), the explicit expression of  $\rho_{th}(\tau)$  is

$$\rho_{th}(\tau) = \frac{2\pi D}{(h_{sup} - h_{cr})^2} \sum_{n=0}^{+\infty} (-1)^n \left(n + \frac{1}{2}\right) \cos\left(\pi \left(n + \frac{1}{2}\right) \frac{h_0 - h_{cr}}{h_{sup} - h_{cr}}\right) \exp\left(-\pi^2 \left(n + \frac{1}{2}\right)^2 \frac{D\tau}{(h_{sup} - h_{cr})^2}\right). \quad (5.3.22)$$

The distribution  $\rho_{th}(\tau)$  can be compared to the probability distribution  $\rho_{exp}(\tau)$  of Mercury's first destabilization time that has been computed numerically in section 5.3.3 Fig.(5.3.1). The diffusion coefficient  $D$  is the only fitting parameter in the model. In order to have a better agreement with numerical results, we have chosen to translate the theoretical distribution from two times the Lyapunov time (this corresponds empirically to the time after which the trajectories have been uniformly distributed in the domain of constant  $\tilde{H}$ ), that is  $\rho_{th}(\tau) \leftarrow \rho_{th}(\tau - 2\tau_L)$ . We thus choose the value of  $D$  that gives the best fit of the probability distribution  $\rho_{exp}(\tau)$ . The value of  $D$  is then estimated as

$$D \approx 4.1 * 10^{-14} (\text{arcsec})^2 / \text{yr}^3. \quad (5.3.23)$$

Using the numerical value given by (5.3.23), the first exit times theoretical distribution  $\rho_{th}(\tau)$  given by the diffusive model gives a excellent qualitative agreement with the distribution  $\rho_{exp}(\tau)$  obtained with direct numerical simulations. The distribution  $\rho_{th}(\tau)$  is displayed in Fig.(5.3.1). We have two strong indications that Mercury's long-term dynamics can be accurately described by a diffusive model for the slow variable  $h$ : first, we have got a relatively good agreement between the distributions  $\rho_{th}$  and  $\rho_{exp}$ . Second, the order of magnitude for the diffusion coefficient  $D$  obtained in (5.3.23) corresponds to the value of  $D$  obtained in (5.3.12) with Lie transforms method and stochastic averaging. The aim of the next section (5.4) is to derive some interesting consequences of the diffusive model. In particular, we study in the next section Mercury's short-term destabilizations, with  $\tau \ll \tau^*$ , and we show that Mercury's dynamics follows the instanton theory.

As a conclusion of the present section, we discuss the limitations of the diffusive model (5.3.19). The first limitation concerns the boundary conditions (5.3.20) of the model. We have considered the value  $h_{sup}$  as a close boundary for the dynamics. This assumption is obviously not perfectly satisfied. Some trajectories can cross with small probability the value  $h_{sup}$  and are then trapped in very weakly chaotic region of phase space. Those trajectories remain thus in the domain  $h > h_{cr}$  for a longer time than predicted by the diffusive model (5.3.19). We expect the numerical distribution  $\rho_{exp}(\tau)$  to have longer tails than the distribution  $\rho_{th}(\tau)$  because the trajectories that are trapped in the regular region of phase space can still be destabilized, but on a much larger timescale than  $\tau^*$ .

The second limitation concerns the times  $\tau$  of same order as the Lyapunov time  $\tau_L$  of the chaotic dynamics. In the diffusive model, trajectories can exit the domain even within times  $\tau < \tau_L$ . This is obviously not true for the chaotic dynamics, because Mercury's trajectories are completely predictable for times smaller than the Lyapunov time. This means that the real first destabilization times probability distribution  $\rho(\tau)$  is zero for  $\tau < \tau_L$ , whereas  $\rho_{th}(\tau) > 0$  for all times.

$\tau$ (Myr)	$\mathbb{P}_{th}(\tau)$ (%)
500	1.3
200	$7.9 * 10^{-3}$
100	$2.4 * 10^{-6}$

Table 5.2: Theoretical value of the probability that Mercury’s destabilization occurs within a time shorter than  $\tau$ .

## 5.4 Instantons for Mercury

### 5.4.1 Short term destabilization probability

We now focus on the probability that Mercury’s orbit is destabilized for short times  $\tau_L \ll \tau \ll \tau^*$ . The expression (5.3.22) for the probability distribution  $\rho_{th}(\tau)$  shows that the fast decrease at short times in the distribution is dominated by the exponential term

$$\rho_{th}(\tau) \underset{\tau \rightarrow 0}{\asymp} e^{-\frac{\bar{\tau}}{\tau}}, \quad (5.4.1)$$

where  $\bar{\tau} = \frac{(h_0 - h_{cr})^2}{D} \approx 1.56 * 10^9$  yr is of same order of magnitude as  $\tau^*$ . The asymptotic behavior (5.4.1) means that the distribution  $\rho_{th}(\tau)$  follows a large deviation principle (defined in section 1.4) when  $\tau \rightarrow 0$ . The large deviation principle (5.4.1) has interesting physical consequences. It shows that the probability of Mercury’s short-term destabilizations is very small. Consider instead of  $\rho_{th}(\tau)$  the probability  $\mathbb{P}_{th}(\tau) := \int_0^\tau \rho_{th}(\tau') d\tau'$  that the destabilization of Mercury’s orbit occurs in the interval  $[0, \tau]$ . The large deviation principle (5.4.1) shows that  $\mathbb{P}_{th}(\tau/k) \approx (\mathbb{P}_{th}(\tau))^k$  for  $k > 0$ . This is a particular property of exponential decay. For example, the probability of destabilization in less than 500 Myr is about 1% in the present model, it is of the order of  $10^{-2}\%$  in 200 Myr and  $10^{-6}\%$  in 100 Myr. The table (5.2) gives some orders of magnitude for the probability distribution  $\mathbb{P}_{th}(\tau)$  for some values of  $\tau$ .

The large deviation principle (5.4.1) obtained in the small time limit is an indication that Mercury’s short -term destabilizations should follow a instanton phenomenology. As was explained in section 1.4.3, a rare event occurrence is not predictable but if it happens, the path chosen by the system to realize the rare event may be predictable. In the present case, the large deviation principle (5.4.1) shows that the short-term destabilization of Mercury’s orbit is a very rare event. The aim of the next two sections is to find an instanton phenomenology both for the diffusive model of section 5.3.4 and for the chaotic Hamiltonian dynamics of the BMH model.

### 5.4.2 Explicit formulae obtained with the diffusive model

The aim of this section is to find the explicit expression for instanton trajectories in the diffusive model (5.3.19-5.3.20). For the diffusive model (5.3.19-5.3.20), an instanton corresponds to a trajectory that reaches the absorbing boundary at  $h = h_{cr}$  in short time  $\tau \ll \tau^*$ . In general, an instanton trajectory can be computed by minimizing the large deviation action functional. The problem of a diffusion equation in a one dimensional domain is simple enough to be completely solved with explicit expressions if we neglect the reflecting boundary at  $h = h_{sup}$ . In particular we do not only obtain an equation for instanton trajectories and the exponential equivalent of the trajectories distribution, but we obtain explicitly the full distribution. The approximation that consists in neglecting the reflecting boundary does not affect the instanton equations because instanton trajectories go as fast as possible to the exit boundary  $h = h_{cr}$ . Trajectories that exit the domain in short after a reflexion at the boundary  $h_{sup}$  are very unlikely and their probability of occurrence can be neglected.

The aim is to compute the probability

$$\rho^{\tau_{ex}}(h, t) := \mathbb{P}(h, t | \{h_0, 0\} \cap \{\tau = \tau_{ex}\}) \quad (5.4.2)$$

to have a trajectory at location  $h$  at time  $t$  with the constraints that the trajectory starts at  $H_0$  and exits the domain at time  $\tau_{ex}$ . The inequality  $0 < t < \tau_{ex}$  should be satisfied. Using Bayes theorem and Markov property, the probability distribution (5.4.2) can be written as

$$\rho^{\tau_{ex}}(h, t) = \frac{\mathbb{P}(\tau = \tau_{ex} | h, t) \mathbb{P}(h, t | h_0, 0)}{\mathbb{P}(\tau = \tau_{ex} | h_0, 0)}. \quad (5.4.3)$$

All probability distributions in the right-hand side of (5.4.3) have explicit expressions. The probability  $\mathbb{P}(\tau = \tau_{ex} | h, t)$  to exit the domain starting at a given position can be obtained from equation (5.3.22) in the limit  $h_{sup} \rightarrow +\infty$ . We have thus

$$\begin{aligned} \mathbb{P}(\tau = \tau_{ex} | h, t) &= \frac{1}{\tau_{ex} - t} \frac{h - h_{cr}}{\sqrt{4\pi D(\tau_{ex} - t)}} e^{-\frac{(h - h_{cr})^2}{4D(\tau_{ex} - t)}}, \\ \mathbb{P}(\tau = \tau_{ex} | h_0, 0) &= \frac{1}{\tau_{ex}} \frac{h_0 - h_{cr}}{\sqrt{4\pi D\tau_{ex}}} e^{-\frac{(h_0 - h_{cr})^2}{4D\tau_{ex}}}. \end{aligned}$$

The last term  $\mathbb{P}(h, t | h_0, 0)$  is simply the solution of the free diffusion equation in an infinite domain, which is the classical result

$$\mathbb{P}(h, t | h_0, 0) = \frac{1}{\sqrt{4\pi Dt}} e^{-\frac{(h - h_0)^2}{4Dt}}.$$

After some algebra, we obtain the following explicit expression for  $\rho^{\tau_{ex}}(h, t)$  (valid for  $h > h_{cr}$  and  $0 < t < \tau_{ex}$ )

$$\rho^{\tau_{ex}}(h, t) = \frac{h - h_{cr}}{h_0 - h_{cr}} \left( \frac{\tau_{ex}}{\tau_{ex} - t} \right)^{3/2} \frac{1}{\sqrt{4\pi Dt}} \left\{ e^{-\frac{1}{4D\tau_{ex}s(1-s)}(h - h_{cr} - (1-s)(h_0 - h_{cr}))^2} - e^{-\frac{1}{4D\tau_{ex}s(1-s)}(h - h_{cr} + (1-s)(h_0 - h_{cr}))^2} \right\}, \quad (5.4.4)$$

where we have introduced the ratio  $s := \frac{t}{\tau_{ex}}$ . It can be quite easily checked that  $\int_{h_{cr}}^{+\infty} \rho^{\tau_{ex}}(h, t) dh = 1$ , because  $\rho^{\tau_{ex}}(h, t)$  is a probability density.

The instanton trajectory, and the variance of the distribution around the instanton can be obtained with the first and the second moments of the distribution (5.4.4). We define the average trajectory  $\{\bar{h}(t)\}_{0 < t < \tau_{ex}}$  as

$$\bar{h}(t) = \int_{h_{cr}}^{+\infty} h \rho^{\tau_{ex}}(h, t) dh. \quad (5.4.5)$$

There is a small difference between the average trajectory defined by (5.4.5) and the instanton trajectory  $\tilde{h}(t)$  which is the trajectory of highest probability. The trajectory of highest probability is the straight trajectory of equation

$$\tilde{h}(t) = \frac{t}{\tau_{ex}} h_{cr} + \left( \frac{\tau_{ex} - t}{\tau_{ex}} \right) h_0.$$

The distribution of trajectories that exit the domain for short times is more and more concentrated around the trajectory of highest probability when  $\tau_{ex}$  goes to zero. To first approximation,  $\tilde{h} \approx \bar{h}$  when  $\tau_{ex}$  is small compared to  $\tau^*$ . However, the average trajectory is a bit curved when  $t$  gets closer to  $\tau_{ex}$  because of the influence of the absorbing boundary condition. We represent in Fig.(5.4.1) the averaged trajectory instead of the instanton trajectory because it can more easily

be compared to numerical results. To study the trajectories dispersion around the instanton, we can also compute the standard deviation

$$\delta\bar{h}(t) := \left[ \int_{h_{cr}}^{+\infty} (h - \bar{h}(t))^2 \rho^{\tau_{ex}}(h, t) dh \right]^{1/2}. \quad (5.4.6)$$

Expressions (5.4.5) and (5.4.6) can be evaluated numerically. The result is displayed in Fig.(5.4.1) for  $\tau_{ex} = 443$  Myr. In order to compare the theoretical results (5.4.5-5.4.6) to numerical simulations of the BMH dynamics, we have chosen to adjust the value  $h(\tau_L)$  with the numerical results.  $\tau_L$  is the Lyapunov time of the BMH chaotic dynamics. We have done this correction to take into account that trajectories in the BMH dynamics are deterministic until the time  $\tau_L$  and can therefore not fit the Brownian trajectories. The next section presents the numerical results of a direct numerical simulation of the BMH dynamics, that we compare to the theoretical results at the level of instanton trajectories.

### 5.4.3 Comparison with the slow variable trajectories

We now want to find the instanton trajectories for the chaotic Hamiltonian dynamics of the BMH model (5.2.8). The aim is to compare the numerical simulations with the theoretical predictions of the diffusive model given by (5.4.5-5.4.6). We have therefore integrated 300000 trajectories of the BMH dynamics using the same symplectic algorithm  $SBAB_2$  as in section 5.3.3. The initial action values are the same for all trajectories, but the phases have been randomly chosen in an interval of 0.01 radian. We record the value of the slow variable  $h$  during the trajectory, and we define Mercury's "destabilization" with the criterion  $h < h_{cr}$  to be consistent with section 5.3.3. Mercury's typical destabilization time  $\tau^*$  has been evaluated to 1.32 Gyr in (5.3.15) We have looked at instanton trajectories for three different exit times  $\tau = 241$  Myr,  $\tau = 443$  Myr and  $\tau = 691$  Myr. For each given value of  $\tau$ , we record the trajectories that exit the domain  $[h_{cr}, +\infty]$  in the time interval  $[\tau - \delta\tau, \tau + \delta\tau]$ . The interval length  $2\delta\tau$  is chosen to obtain a sample containing at least 100 trajectories. In the present case,  $\delta\tau = 2$  Myr.

For each sample  $i = 1, 2, 3$ , we record the  $n_i$  trajectories of the slow variable  $h(t)$ , and we compute the average trajectory  $\bar{h}^{(i)}(t) := \frac{1}{n_i} \sum_{k=1}^{n_i} h_k(t)$ , and the standard deviation  $\delta\bar{h}^{(i)}(t) :=$

$\left[ \frac{1}{n_i} \sum_{k=1}^{n_i} (h_k(t) - \bar{h}^{(i)}(t))^2 \right]^{1/2}$ . Fig.(5.4.1) displays the numerical results obtained with the second sample with  $\tau = 443$  Myr, together with the theoretical predictions of the diffusive model. Fig (5.4.1) displays three curves. The intermediate curve is the average trajectory  $\bar{h}^{(2)}(t)$ . The two other curves are defined by  $\bar{h}^{(2)}(t) + \delta\bar{h}^{(2)}(t)$  and  $\bar{h}^{(2)}(t) - \delta\bar{h}^{(2)}(t)$  respectively. The theoretical curves have been obtained with equations (5.4.5) and (5.4.6), with the same value of  $D$  that has been obtained in (5.3.23) with direct fitting of the first destabilization time probability distribution.

Two differences between the numerical results and the theoretical predictions can be observed at the two trajectory extremities. For  $0 < t < \tau_L$ , the trajectories separate exponentially fast, but are still clustered together on the same deterministic path. Only for times larger than  $\tau_L$  can the trajectories be considered as independent realizations, and their distribution can be predicted by the diffusion equation. Second, the variance of the trajectories distribution do not follow the theoretical predictions for times close to  $\tau$ . The reason is that the local time average (5.2.18) does not suppress all fast oscillations of the chaotic dynamics. The consequence is that the numerical trajectory  $h(t)$  is defined with some uncertainty corresponding to the fast oscillations amplitude. The criterion  $h < h_{cr}$  cannot be considered as a rigorous criterion for such oscillating trajectories.

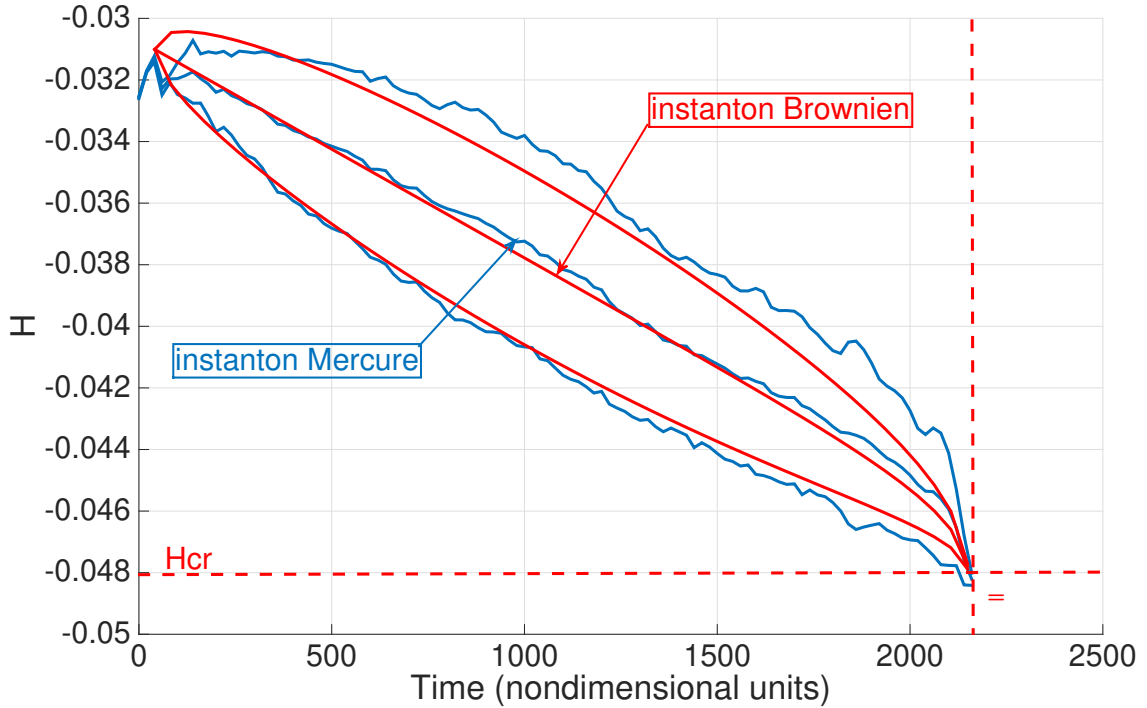


Figure 5.4.1: Numerical (blue curves) and theoretical (red curves) predictions of the instanton trajectories for the BMH model. The intermediate curves are the average trajectories. The two extremal curves define the variance of the trajectories distribution around the average.

Modulo the corrections due to the chaotic aspect of the BMH dynamics, the agreement between the diffusive model and the BMH model, at the level of instanton predictions, can be considered as excellent. This result is a second confirmation of the validity of the predictions obtained with stochastic averaging. It can thus be said that the diffusive model for the slow variable is consistent both for the prediction of Mercury's first destabilization time probability distribution, and for the prediction of instantons.

## 5.5 Conclusion and perspectives

The BMH model is a very attractive model because it reduces the very difficult question of desintegration of the inner solar system to the very simple problem of first exit times from a bounded domain for a Brownian trajectory. Within the framework of the BMH model, stochastic averaging allows to justify that a well-chosen slow variable follows a diffusion equation. It should be however kept in mind that the diffusion equation is only justified for the simple BMH dynamics.

For the full solar system's dynamics, numerical simulations by [59] have shown that the probability of Mercury's destabilization is about 1% in 5 Gyr. For the time being, this value is the only one to which the results presented in this work can be compared. Let us assume that the mechanism that triggers Mercury's destabilization is the same for the full solar system's

dynamics and for the BMH model. More precisely, let us assume that there exists a slow diffusive variable with a threshold and that Mercury's destabilization is simultaneous to the first crossing time of the threshold. We expect the probability distribution of Mercury's destabilization time to scale as

$$\rho(\tau) \underset{\tau \rightarrow 0}{\approx} \frac{1}{\tau} \sqrt{\frac{\bar{\tau}}{\pi\tau}} e^{-\frac{\tau}{\bar{\tau}}}. \quad (5.5.1)$$

The value of  $\bar{\tau}$  in the last expression is unknown. Assuming expression 5.5.1 is valid for the full solar system's dynamics, we deduce that a probability of 1% in 5 Gyr corresponds to a value of

$$\bar{\tau} \approx 16.6 \text{ Gyr}. \quad (5.5.2)$$

In the BMH model, the typical destabilization time  $\bar{\tau}$  is of the order of one Gyr (see section 5.3.3), whereas the simulations of [59] suggest a typical time  $\bar{\tau}$  of the order of 10 Gyr. This may be related to the fact that the critical eccentricity at which destabilization occurs is too small in the BMH model. The critical threshold  $h_{cr} = -0.048$  for destabilization corresponds to the value  $I \approx 0.05$  (see Fig.(5.2.4)) and consequently to  $e \approx 0.3$ . Simulations of [59] suggest that the destabilization threshold rather corresponds to  $e \approx 0.6$  (see Fig.(0.0.1)). The discrepancy between the values (5.5.2) and (5.3.15) could be attributed to an underestimated threshold value for instability.

The fact that the BMH model does not conserve the total angular momentum deficit (AMD) might be the reason of the discrepancy observed between the BMH model and the complete secular dynamics. Indeed, it has been shown that AMD is a key quantity to control the destabilization of planetary orbits (see [62]). The AMD conservation is expected to slow the diffusion process for the slow variable and a more realistic order of magnitude for  $\tau^*$  could certainly be obtained.

The question whether the destabilization of the inner solar system is controlled by the first exit time from a domain of some well-chosen slow variable, remains open. However, the instanton phenomenology described in section 5.4 should be observed in the full solar system's dynamics, because the instanton phenomenology is generic of rare events and can be observed in very different types of stochastic or deterministic dynamical systems. We are currently involved in a research project with the IMCCE to try to observe the instanton phenomenology with a more complete model for the solar system's secular dynamics.



# Conclusion

At the beginning of my PHD thesis, I was concerned with the distinction between a deterministic and a stochastic dynamics. I came out of my studies with the impression that some phenomena in nature can be described by deterministic sets of equations, while some others, because of their complexity, could only be tackled with statistical physics and with stochastic differential equations. The domain of deterministic phenomena and the one of stochastic phenomena appeared to me as two separated boxes with no possible connections between them. This issue has been an implicit concern in the last three years. I believe the work I have done shows, for some restricted classes of physical systems, how deterministic and stochastic descriptions are related to each other. I have learned how the concepts of ergodicity and mixing give a firm theoretical basis to the intuitive idea that a complex deterministic dynamics has no fundamental difference from a stochastic dynamics [29, 86, 23]. The choice to model a physical system with either deterministic or stochastic equations is related to the considered time or space scale [5]. In the present work, I have shown for some chaotic deterministic systems how the large scale evolution can be modeled by stochastic equations, with the benefit of a drastic reduction of the system's complexity. Although the fascinating ergodic theory is not the primary topic of this thesis, my work can be seen as a concrete illustration of the transition from deterministic equations to stochastic differential equations.

Chapter 1 gives the main theorems in averaging and stochastic averaging, with intuitive proofs of the results. The proofs are not presented in the manuscript just for sake of mathematical rigor. They use a mathematical formalism that is of real practical interest for physical problems. A mathematical theory can not be applied to concrete physical systems without a intuitive and flexible formalism that keeps the exactitude of results all along the calculations. For example, we owe to Leibniz the remarkable formalism for differential calculus that is now widely used in the physicists community. The stochastic method that consists in studying the asymptotic distribution of the slow increment  $\Delta X$  is not the method found in classical textbooks on multiscale systems [33, 79], but it is very intuitive. This method has been on the ground of physical applications found in chapters 3,4 and 5, and I believe I could not have derived all results presented in my thesis without it. The method of the increment  $\Delta X$  is also at the core of formal derivations of large deviation theorems, and surely will gain popularity among physicists in the near future.

The main goal of this thesis has been the description of rare events for some complex physical systems. Building on the work of [94], my aim was to describe the rare transitions in zonal jets dynamics. As explained in chapter 1, the dynamics of rare events first depends on the structure of the averaged dynamics, and the existence of attractors for the averaged dynamics. I have discovered that the averaged dynamics of zonal jets could partly be computed analytically in the limit of small scale and weak energy injection (inertial and small scale forcing limit). A numerical work by Eric Simonnet (private communication) has shown that rare transitions in the flow begin with the nucleation of a new jet at the extremum of one of the westward jets.

I have also studied the particular dynamics of westward jets and found that those jets are in a marginally stable state: it means that equilibration of the jet occurs through a competition between the averaged dynamics that forces the jet to grow, and an hydrodynamic instability that stops its growth. This could be an indication why nucleation of jets preferentially occurs at the westward extremum. A possible perspective of this work could be to look for analytical results about instanton dynamics in the inertial and small scale forcing limit.

Large deviation theory can be seen as a very large framework to predict rare events in complex systems independently of the underlying dynamics. A large part of the theory deals with dynamical systems perturbed by a small random term [26]. Because of a timescale separation between the asteroid's chaos and planetary chaos, the gravitational influence of asteroids on planetary dynamics can be seen as a small random perturbation for the system composed of the eight planets. Using stochastic averaging, the work of chapter 3 gives the physical properties of this noise. I have shown that the noise created by the asteroids is irrelevant to compute the probability of rare events in the solar system, because it is felt on a timescale on which chaos in planetary motion is already the dominant source of randomness. Therefore, the solar system should not be considered as an integrable dynamical system perturbed by a small random noise, but as a fully chaotic system in which chaos develops over many different timescales. Such a situation is much less understood than the simpler framework of dynamical systems with small random perturbations. The solar system is thus an example of a very complex slow-fast chaotic system.

Large deviation theory is a suitable tool to describe rare events in slow-fast dynamical systems. In celestial mechanics, large deviation theory may thus be applied to the secular evolution of the solar system, but it first requires the identification of a timescale separation in the dynamics, and a good slow variable. This task is a difficult part of the work toward the description of rare events, and can only be done with much experience in celestial mechanics. The work I have done in chapters 4 and 5 would not have been possible without all previous works of [53, 65, 15, 7] who showed the existence of rare events in the solar system, and identified the relevant slow variables for those events.

Building on these works, I have described rare and large variations of the obliquity of a Moonless Earth. I have discovered a new transport mechanism for chaotic Hamiltonians depending on slow external frequencies. In the regime of large variations of the frequencies, transport is mainly due to the displacement of chaotic mixing regions, and can be characterized by a diffusive model of transport. This transport mechanism is generic and can be found in other Hamiltonian dynamics depending on slow external parameters. I have also shown that the transport mechanism is fully equivalent to a simple diffusive model with space-dependent diffusion coefficient. The theoretical computation of rare event probabilities can be done for the diffusive model (this computation is not presented in the manuscript). Unfortunately, I have found that the Earth is not in a parameter regime in which the diffusive model gives fully relevant results. The numerical prediction of rare events probability for the real dynamics of a Moonless Earth thus remains a difficult challenge.

I believe the most important achievement of my thesis is the work of part 5 about Mercury. The puzzling secular dynamics of Mercury seems to perfectly correspond to the framework of large deviations in slow-fast dynamical systems. I have worked in chapter 5 on a simplified model of Mercury's secular dynamics for which the slow variable had already been identified by [7]. For this simplified dynamics, I have found that the fast destabilizations of Mercury's orbit follow an instanton phenomenology. The large deviation approach predicts the probability distribution of Mercury's short-term destabilizations, at least for the simplified dynamics. However, instanton phenomenology is robust to a change in the fast dynamics. I expect the instanton phenomenology to be valid even if the slow variable does not follow a diffusion equation, but follows instead

a more complex Markov process with a continuous increment distribution. A promising collaboration with the IMCCE is going on to look for the instanton phenomenology in a more realistic model of Mercury's dynamics that includes all planetary mutual interactions in the inner solar system. The BMH model predicts that Mercury's orbit becomes unstable when the slow variable crosses a threshold value that can be computed in terms of the current planetary orbital parameters. This mechanism opens wide perspectives: would the above criterion be valid for the real secular dynamics of the solar system, this would be a major step toward the understanding of the long-term solar system stability, and more generally toward the understanding of long-term stability of planetary systems. It would be very interesting to relate the criterion of the slow variable threshold with the criterion of AMD stability [62]. The criterion of the slow variable threshold could also be used to constrain the architecture of extra-solar systems.



# Bibliography

- [1] [https://www.nasa.gov/mission\\_pages/juno/images/index.html](https://www.nasa.gov/mission_pages/juno/images/index.html).
- [2] DG Andrews and ME McIntyre. Generalized Eliassen-Palm and Charney-Drazin theorems for waves on axisymmetric mean flows in compressible atmospheres. *Journal of the Atmospheric Sciences*, 35(2):175–185, 1978.
- [3] Louis Bachelier. *Théorie de la spéculation*. Gauthier-Villars, 1900.
- [4] Nikolaos Bakas and Petros Ioannou. A theory for the emergence of coherent structures in beta-plane turbulence. *preprint arXiv:1303.6435*, 2013.
- [5] Roger Balian. *Du microscopique au macroscopique: cours de physique statistique de l'École polytechnique*. Ecole Polytech. Palaiseau, 1982.
- [6] Konstantin Batygin and Gregory Laughlin. On the dynamical stability of the solar system. *The Astrophysical Journal*, 683(2):1207, 2008.
- [7] Konstantin Batygin, Alessandro Morbidelli, and Matthew J Holman. Chaotic disintegration of the inner solar system. *The Astrophysical Journal*, 799(2):120, 2015.
- [8] Michael Victor Berry. Regular and irregular motion. In *AIP Conference proceedings*, volume 46, pages 16–120. AIP, 1978.
- [9] Guido Boffetta and Robert E Ecke. Two-dimensional turbulence. *Annual Review of Fluid Mechanics*, 44:427–451, 2012.
- [10] Freddy Bouchet, Tobias Grafke, Tomás Tangarife, and Eric Vanden-Eijnden. Large deviations in fast-slow systems. *Journal of Statistical Physics*, 162(4):793–812, 2016.
- [11] Freddy Bouchet and Hidetoshi Morita. Large time behavior and asymptotic stability of the 2d Euler and linearized Euler equations. *Physica D: Nonlinear Phenomena*, 239(12):948–966, 2010.
- [12] Freddy Bouchet, Cesare Nardini, and Tomás Tangarife. Kinetic theory of jet dynamics in the stochastic barotropic and 2d Navier-Stokes equations. *Journal of Statistical Physics*, 153(4):572–625, 2013.
- [13] Freddy Bouchet, Cesare Nardini, and Tomas Tangarife. Kinetic theory and quasilinear theories of jet dynamics. *arXiv preprint arXiv:1602.02879*, to be published in the book *Zonal Flows*, edited by Boris Galperin, and to be published by Cambridge University Press., 2016.
- [14] Freddy Bouchet and Eric Simonnet. Random changes of flow topology in two-dimensional and geophysical turbulence. *Physical Review Letters*, 102(9):094504, 2009.

- [15] Gwenaël Boué, Jacques Laskar, and François Farago. A simple model of the chaotic eccentricity of mercury. *Astronomy & Astrophysics*, 548:A43, 2012.
- [16] Dirk Brouwer. On the accumulation of errors in numerical integration. *The Astronomical Journal*, 46:149–153, 1937.
- [17] B Caroli, C Caroli, and B Roulet. Diffusion in a bistable potential: The functional integral approach. *Journal of Statistical Physics*, 26(1):83–111, 1981.
- [18] Boris V Chirikov. A universal instability of many-dimensional oscillator systems. *Physics reports*, 52(5):263–379, 1979.
- [19] Navid C Constantinou. Formation of large-scale structures by turbulence in rotating planets. *arXiv preprint arXiv:1503.07644*, 2015.
- [20] Navid C Constantinou, Petros J Ioannou, and Brian F Farrell. Emergence and equilibration of jets in beta-plane turbulence. *arXiv preprint arXiv:1208.5665*, 2012.
- [21] Alexandre CM Correia and Jacques Laskar. The four final rotation states of venus. *Nature*, 411(6839):767, 2001.
- [22] J-P Eckmann and David Ruelle. Ergodic theory of chaos and strange attractors. In *The Theory of Chaotic Attractors*, pages 273–312. Springer, 1985.
- [23] JP Eckmann. J.-p. eckmann and d. ruelle, rev. mod. phys. 57, 617 (1985). *Rev. Mod. Phys.*, 57:617, 1985.
- [24] Brian F Farrell and Petros J Ioannou. Structure and spacing of jets in barotropic turbulence. *Journal of the Atmospheric Sciences*, 64(10):3652–3665, 2007.
- [25] A Fienga, J Laskar, T Morley, H Manche, P Kuchynka, C Le Poncin-Lafitte, F Budnik, M Gastineau, and L Somenzi. Inpop08, a 4-d planetary ephemeris: from asteroid and time-scale computations to esa mars express and venus express contributions. *Astronomy & Astrophysics*, 507(3):1675–1686, 2009.
- [26] M.I. Freidlin and A.D. Wentzell. *Random Perturbations of Dynamical Systems*. Springer-Verlag, 3dr ed. New York, 2012.
- [27] Yanning Fu and Jacques Laskar. Frequency analysis and the representation of slowly diffusing planetary solutions. *arXiv preprint arXiv:1701.07108*, 2017.
- [28] Giovanni Gallavotti. Chaotic hypothesis. 3(1):5906, Scholarpedia.
- [29] Giovanni Gallavotti and E GD Cohen. Dynamical ensembles in stationary states. *Journal of Statistical Physics*, 80(5):931–970, 1995.
- [30] Boris Galperin, Semion Sukoriansky, and Huei-Ping Huang. Universal  $n-5$  spectrum of zonal flows on giant planets. *Physics of Fluids (1994-present)*, 13(6):1545–1548, 2001.
- [31] Boris Galperin, Roland MB Young, Semion Sukoriansky, Nadejda Dikovskaya, Peter L Read, Andrew J Lancaster, and David Armstrong. Cassini observations reveal a regime of zonostrophic macroturbulence on jupiter. *Icarus*, 229:295–320, 2014.
- [32] Ricardo García-Herrera, José Díaz, Ricardo M Trigo, Jürg Luterbacher, and Erich M Fischer. A review of the european summer heat wave of 2003. *Critical Reviews in Environmental Science and Technology*, 40(4):267–306, 2010.

- [33] C. W. Gardiner. *Handbook of stochastic methods for physics, chemistry and the natural sciences*. Springer Series in Synergetics, Berlin: Springer, |c1994, 2nd ed. 1985. Corr. 3rd printing 1994, 1994.
- [34] Adrian E Gill. *Atmosphere-ocean dynamics*, volume 30. Academic press, 1982.
- [35] Seymour L Hess and HA Panofsky. The atmospheres of the other planets. In *Compendium of meteorology*, pages 391–398. Springer, 1951.
- [36] Jérôme Idier. Traitement numérique du signal. deuxième partie: algorithmes. In <http://pagesperso.ls2n.fr/~idier-j/teachFR.html>. 2004.
- [37] Andrew P Ingersoll. Atmospheric dynamics of the outer planets. *Science*, 248(4953):308–315, 1990.
- [38] Andrew P Ingersoll, Reta F Beebe, Jim L Mitchell, Glenn W Garneau, Gary M Yagi, and Jan-Peter Müller. Interaction of eddies and mean zonal flow on jupiter as inferred from voyager 1 and 2 images. *Journal of Geophysical Research A*, 86(A10):8733–8743, 1981.
- [39] Takashi Ishihara, Toshiyuki Gotoh, and Yukio Kaneda. Study of high–reynolds number isotropic turbulence by direct numerical simulation. *Annual Review of Fluid Mechanics*, 41:165–180, 2009.
- [40] Y Kaspi, E Galanti, WB Hubbard, DJ Stevenson, SJ Bolton, L Iess, T Guillot, J Bloxham, JEP Connerney, H Cao, et al. Jupiter’s atmospheric jet streams extend thousands of kilometres deep. *Nature*, 555(7695):223, 2018.
- [41] David Kelly, Ian Melbourne, et al. Smooth approximation of stochastic differential equations. *The Annals of Probability*, 44(1):479–520, 2016.
- [42] R Z Khasminskii. On an averaging principle for ito stochastic differential equations. *Kybernetika*, 4:260–279, 1968.
- [43] Yuri Kifer. Averaging principle for fully coupled dynamical systems and large deviations. *Ergodic Theory and Dynamical Systems*, 24(03):847–871, 2004.
- [44] Yuri Kifer. *Large deviations and adiabatic transitions for dynamical systems and Markov processes in fully coupled averaging*. American Mathematical Soc., 2009.
- [45] Masahide Kimoto and Michael Ghil. Multiple flow regimes in the northern hemisphere winter. part i: Methodology and hemispheric regimes. *Journal of the Atmospheric Sciences*, 50(16):2625–2644, 1993.
- [46] Khanh-Dang Nguyen Thu Lam and Jorge Kurchan. Stochastic perturbation of integrable systems: a window to weakly chaotic systems. *Journal of Statistical Physics*, 156(4):619–646, 2014.
- [47] Jacques Laskar. A numerical experiment on the chaotic behaviour of the solar system. *Nature*, 338(6212):237, 1989.
- [48] Jacques Laskar. The chaotic motion of the solar system: a numerical estimate of the size of the chaotic zones. *Icarus*, 88(2):266–291, 1990.
- [49] Jacques Laskar. Frequency analysis for multi-dimensional systems. global dynamics and diffusion. *Physica D: Nonlinear Phenomena*, 67(1-3):257–281, 1993.

- [50] Jacques Laskar. Large-scale chaos in the solar system. *Astronomy and Astrophysics*, 287:L9–L12, 1994.
- [51] Jacques Laskar. Large scale chaos and marginal stability in the solar system. *Celestial Mechanics and Dynamical Astronomy*, 64(1-2):115–162, 1996.
- [52] Jacques Laskar. Large scale chaos and the spacing of the inner planets. *Astronomy and Astrophysics*, 317:L75–L78, 1997.
- [53] Jacques Laskar. Chaotic diffusion in the solar system. *Icarus*, 196(1):1–15, 2008.
- [54] Jacques Laskar. <https://www.obspm.fr/mercury-mars-venus-and-the.html>. 2009.
- [55] Jacques Laskar and Gwenael Boué. Explicit expansion of the three-body disturbing function for arbitrary eccentricities and inclinations. *Astronomy & Astrophysics*, 522:A60, 2010.
- [56] Jacques Laskar, Agnes Fienga, Mickaël Gastineau, and Herve Manche. La2010: a new orbital solution for the long-term motion of the earth. *Astronomy & Astrophysics*, 532:A89, 2011.
- [57] Jacques Laskar, Claude Froeschlé, and Alessandra Celletti. The measure of chaos by the numerical analysis of the fundamental frequencies. application to the standard mapping. *Physica D: Nonlinear Phenomena*, 56(2-3):253–269, 1992.
- [58] Jacques Laskar and Mickaël Gastineau. Existence of collisional trajectories of mercury, mars and venus with the earth. *Nature*, 459(7248):817, 2009.
- [59] Jacques Laskar and Mickaël Gastineau. Existence of collisional trajectories of mercury, mars and venus with the earth. *Nature*, 459(7248):817–819, 2009.
- [60] Jacques Laskar and Mickael Gastineau. Mercure, mars, vénus, la terre : le choc des planètes ! <http://www2.cnrs.fr/presse/communiquel/1614.htm?theme1=6debut=72>, 2009.
- [61] Jacques Laskar, Mickaël Gastineau, Jean-Baptiste Delisle, Ariadna Farrés, and Agnes Fienga. Strong chaos induced by close encounters with ceres and vesta. *Astronomy & Astrophysics*, 532, 2011.
- [62] Jacques Laskar and Antoine Petit. Amd-stability and the classification of planetary systems. *Astronomy & Astrophysics*, 2017.
- [63] Jacques Laskar and Philippe Robutel. The chaotic obliquity of the planets. *Nature*, 361(6413):608–612, 1993.
- [64] Jacques Laskar and Philippe Robutel. Stability of the planetary three-body problem. *Celestial Mechanics and Dynamical Astronomy*, 62(3):193–217, 1995.
- [65] Jacques Laskar, Philippe Robutel, Frédéric Joutel, Mickaël Gastineau, ACM Correia, and Benjamin Levrard. A long-term numerical solution for the insolation quantities of the earth. *Astronomy & Astrophysics*, 428(1):261–285, 2004.
- [66] Thibault Lestang, Francesco Ragone, Charles-Edouard Bréhier, Corentin Herbert, and Freddy Bouchet. Computing return times or return periods with rare event algorithms. *Journal of Statistical Mechanics: Theory and Experiment*, 2018(4):043213, 2018.

- [67] Gongjie Li and Konstantin Batygin. On the spin-axis dynamics of a moonless earth. *The Astrophysical Journal*, 790(1):69, 2014.
- [68] Liming Li, Andrew P Ingersoll, and Xianglei Huang. Interaction of moist convection with zonal jets on jupiter and saturn. *Icarus*, 180(1):113–123, 2006.
- [69] Allan J Lichtenberg and Michael A Lieberman. *Regular and stochastic motion*, volume 38. Springer Science & Business Media, 2013.
- [70] Jack J Lissauer, Jason W Barnes, and John E Chambers. Obliquity variations of a moonless earth. *Icarus*, 217(1):77–87, 2012.
- [71] Yoram Lithwick and Yanqin Wu. Theory of secular chaos and mercury’s orbit. *The Astrophysical Journal*, 739(1):31, 2011.
- [72] Alessandro Morbidelli. *Modern celestial mechanics: aspects of solar system dynamics*. 2002.
- [73] Alessandro Morbidelli and Antonio Giorgilli. Superexponential stability of kam tori. *Journal of statistical physics*, 78(5-6):1607–1617, 1995.
- [74] Alessandro Morbidelli and Antonio Giorgilli. On the role of high order resonances in normal forms and in separatrix splitting. *Physica D: Nonlinear Phenomena*, 102(3-4):195–207, 1997.
- [75] Carl D Murray and Stanley F Dermott. *Solar system dynamics*. Cambridge university press, 1999.
- [76] Nikolai Nikolaevich Nekhoroshev. An exponential estimate of the time of stability of nearly-integrable hamiltonian systems. *Russian Mathematical Surveys*, 32(6):1–65, 1977.
- [77] Takahiro Nemoto, Freddy Bouchet, Robert L. Jack, and Vivien Lecomte. Population-dynamics method with a multicanonical feedback control. *Physical Review E*, 93(6):062123, 2016.
- [78] Olivier Néron de Surgy and Jacques Laskar. On the long term evolution of the spin of the earth. *Astronomy and Astrophysics*, 318:975–989, 1997.
- [79] Grigorios A Pavliotis and Andrew Stuart. *Multiscale methods: averaging and homogenization*. Springer Science & Business Media, 2008.
- [80] J. Pedlosky. *Geophysical fluid dynamics*. New York and Berlin, Springer-Verlag, 1982. 636 p., 1982.
- [81] Carolyn C Porco, Robert A West, Alfred McEwen, Anthony D Del Genio, Andrew P Ingersoll, Peter Thomas, Steve Squyres, Luke Dones, Carl D Murray, Torrence V Johnson, et al. Cassini imaging of jupiter’s atmosphere, satellites, and rings. *Science*, 299(5612):1541–1547, 2003.
- [82] Francesco Ragone, Jeroen Wouters, and Freddy Bouchet. Computation of extreme heat waves in climate models using a large deviation algorithm. *Proceedings of the National Academy of Sciences*, page 201712645, 2017.

- [83] Jean-Marie Robine, Siu Lan K. Cheung, Sophie Le Roy, Herman Van Oyen, Clare Griffiths, Jean-Pierre Michel, and François Richard Herrmann. Death toll exceeded 70,000 in Europe during the summer of 2003. *Comptes Rendus Biologies*, 331(2):171–178, February 2008.
- [84] John H Rogers. *The giant planet Jupiter*, volume 6. Cambridge University Press, 1995.
- [85] Joran Rolland, Freddy Bouchet, and Eric Simonnet. Computing transition rates for the 1-d stochastic Ginzburg-Landau equation for finite-amplitude noise with a rare event algorithm. *Journal of Statistical Physics*, 162(2):277–311, 2016.
- [86] David Ruelle. Measures describing a turbulent flow. *Annals of the New York Academy of Sciences*, 357(1):1–9, 1980.
- [87] Colette Salyk, Andrew P Ingersoll, Jean Lorre, Ashwin Vasavada, and Anthony D Del Genio. Interaction between eddies and mean flow in Jupiter’s atmosphere: Analysis of Cassini imaging data. *Icarus*, 185(2):430–442, 2006.
- [88] JM Sancho, M San Miguel, and D Dürr. Adiabatic elimination for systems of Brownian particles with nonconstant damping coefficients. *Journal of Statistical Physics*, 28(2):291–305, 1982.
- [89] T. Schneider and J. Liu. Formation of jets and equatorial superrotation on Jupiter. *Journal of Atmospheric Sciences*, 66:579–+, 2009.
- [90] Carles Simó. On the analytical and numerical approximation of invariant manifolds. In *Les Méthodes Modernes de la Mécanique Céleste. Modern methods in celestial mechanics*, pages 285–329, 1990.
- [91] Yakov Grigor’evich Sinai. Dynamical systems with elastic reflections. *Russian Mathematical Surveys*, 25(2):137–189, 1970.
- [92] Kaushik Srinivasan and WR Young. Reynolds stress and eddy diffusivity of  $\beta$ -plane shear flows. *Journal of the Atmospheric Sciences*, 71(6):2169–2185, 2014.
- [93] GJ Sussman and J. Wisdom. Chaotic evolution of the solar system. *Science*, 257(5066):56, 1992.
- [94] Tomás Tangarife. *Kinetic theory and large deviations for the dynamics of geophysical flows*. PhD thesis, Ecole normale supérieure de Lyon-ENS LYON, 2015.
- [95] Hugo Touchette. The large deviation approach to statistical mechanics. *Physics Reports*, 478(1-3):1–69, 2009.
- [96] JR Touma, S Tremaine, and MV Kazandjian. Gauss’s method for secular dynamics, softened. *Monthly Notices of the Royal Astronomical Society*, 394(2):1085–1108, 2009.
- [97] Margit Vallikivi, Bharath Ganapathisubramani, and AJ Smits. Spectral scaling in boundary layers and pipes at very high Reynolds numbers. *Journal of Fluid Mechanics*, 771:303–326, 2015.
- [98] Ashwin R Vasavada and Adam P Showman. Jovian atmospheric dynamics: An update after Galileo and Cassini. *Reports on Progress in Physics*, 68(8):1935, 2005.
- [99] A Yu Veretennikov. On large deviations in the averaging principle for SDEs with a "full dependence". *Annals of Probability*, pages 284–296, 1999.

- [100] Angelo Vulpiani, Fabio Cecconi, Massimo Cencini, Andrea Puglisi, and Davide Vergni. Large deviations in physics. *The Legacy of the Law of Large Numbers (Springer, 2014)*, 2014.
- [101] Heinz Wanner, Stefan Brönnimann, Carlo Casty, Dimitrios Gyalistras, Jürg Luterbacher, Christoph Schmutz, David B Stephenson, and Eleni Xoplaki. North atlantic oscillation—concepts and studies. *Surveys in geophysics*, 22(4):321–381, 2001.
- [102] Eric Woillez and Freddy Bouchet. Long-term influence of asteroids on planet longitudes and chaotic dynamics of the solar system. *Astronomy & Astrophysics*, 607:A62, 2017.
- [103] Eric Woillez and Freddy Bouchet. Theoretical prediction of reynolds stresses and velocity profiles for barotropic turbulent jets. *EPL (Europhysics Letters)*, 118(5):54002, 2017.
- [104] PK Yeung, XM Zhai, and Katepalli R Sreenivasan. Extreme events in computational turbulence. *Proceedings of the National Academy of Sciences*, 112(41):12633–12638, 2015.
- [105] Ashraf Youssef and Philip S Marcus. The dynamics of jovian white ovals from formation to merger. *Icarus*, 162(1):74–93, 2003.
- [106] MV Zagarola and AJ Smits. Scaling of the mean velocity profile for turbulent pipe flow. *Physical review letters*, 78(2):239, 1997.



# Appendix A

## Computation of the diffusion coefficient

We want to give an order of magnitude of the diffusion coefficient (3.3.4) for the semi-major axis of Mars feeling the perturbation of a large asteroid of the asteroid belt. The perturbative function writes

$$G(\Lambda, \lambda - \varphi) = \frac{-1}{|\Lambda^2 e^{i(\lambda - \varphi)} - a|}$$

where  $\Lambda$  is the conjugated momentum of the mean longitude  $\lambda$ . In the following, we will always assume that  $\Lambda^2 < a$ . The Fourier expansion of  $G$  has been given in the general case by [55], and writes in our simplified model

$$\begin{aligned} \widehat{G}(k) &= \frac{1}{\Lambda_0^2} \sum_{q=k}^N \left( \frac{\Lambda_M}{\Lambda_0} \right)^{4q-2k} f_{2q-k,q} \\ f_{n,q} &= \frac{(2q)!(2n-2q)!}{2^{2n}(q!)^2[(n-q)!]^2} \end{aligned} \quad (\text{A.0.1})$$

where  $N$  is a cut off to stop the Fourier expansion. In our calculations, we took  $N = 20$ .

We have the Fourier decomposition of  $G$  in the form  $G = \sum_k \widehat{G}(k) e^{ik(\lambda - \varphi)}$ . Our aim is to evaluate the quantity  $\mathbb{E} \left[ \frac{\partial G}{\partial \lambda}(t) \frac{\partial G}{\partial \lambda}(0) \right]$  where for simplicity we use the shortcoming  $G(t) = G(\Lambda, \lambda(t) - \varphi(t))$ . The reader should bear in mind that  $\lambda(t)$  is given by the *unperturbed* dynamics, because to compute the fast motions we have to “freeze” the slow variables. If we freeze  $\Lambda$  in the dynamics of  $\lambda$ , we simply get the Keplerian motion. Therefore  $\lambda(t) = \lambda_0 + nt$ . The chaotic dynamics of the asteroid is modeled by  $\varphi(t) = \varphi_0 + \nu_a t + \delta\varphi(t)$  where  $\delta\varphi$  should account for the chaotic diffusion on a time scale  $\tau_\varphi$ . We will give its expression later on. We thus have

$$\begin{aligned} \mathbb{E} \left[ \frac{\partial G}{\partial \lambda}(t) \frac{\partial G}{\partial \lambda}(0) \right] &= \sum_{k,k'} k k' \widehat{G}(k) \widehat{G}(k')^* \mathbb{E} \left[ e^{i(k\lambda(t) - k'\lambda(0))} e^{-i(k\varphi(t) - k'\varphi(0))} \right] \\ &= \sum_{k,k'} k k' \widehat{G}(k) \widehat{G}(k')^* e^{ikt(n - \nu_a)} \dots \\ &\quad \dots \mathbb{E} \left[ e^{i(\lambda_0 - \varphi_0)(k - k')} \right] \mathbb{E} \left[ e^{-ik\delta\varphi(t)} \right]. \end{aligned}$$

We have two averages to perform. The invariant measure for the initial conditions  $\lambda_0$  and  $\varphi_0$  is the uniform measure over the range  $[0, 2\pi]$ . Thus the term  $\mathbb{E} \left[ e^{i(\lambda_0 - \varphi_0)(k - k')} \right] = \delta_{k - k'}$ . What

is then the Esperance of  $e^{-ik\delta\varphi}$  ? For a general chaotic trajectory, it should be a complicated function, decreasing with the time scale  $\tau_\varphi$ . We chose for  $\delta\varphi$  the Brownian motion  $W\left(\frac{t}{\tau_\varphi}\right)$  which has a Gaussian statistics. It comes

$$\begin{aligned}\mathbb{E}\left[e^{-ik\delta\varphi(t)}\right] &= \frac{1}{\sqrt{2\pi t/\tau_\varphi}} \int dx e^{-ikx} e^{-\frac{x^2}{2t/\tau_\varphi}} \\ &= e^{-\frac{t}{2\tau_\varphi}k^2}.\end{aligned}$$

Finally, the expression of our correlation function is

$$\mathbb{E}\left[\frac{\partial G}{\partial \lambda}(t)\frac{\partial G}{\partial \lambda}(0)\right] = \sum_k k^2 \left|\widehat{G}(k)\right|^2 e^{-\frac{t}{2\tau_\varphi}k^2} e^{ik(n-\nu_a)t}.$$

It remains to integrate this expression over time according to (3.3.4), and we obtain

$$D(\Lambda) = \sum_k k^2 \left|\widehat{G}(k)\right|^2 \frac{1}{(\nu_a - n)^2 \tau_\varphi} \frac{1}{\left(\frac{k}{2(\nu_a - n)\tau_\varphi}\right)^2 + 1}. \quad (\text{A.0.2})$$

Expressions (A.0.1) and (A.0.2) allow to compute the magnitude of the diffusion coefficient and then to estimate the diffusion time scale of the mean longitude of Mars.

## Appendix B

# Resolution of the diffusion equation

It has been shown in section 5.3.4 that the long-term secular dynamics of Mercury's orbit can be reduced to the stochastic dynamics of a Brownian particle in a bounded domain. The situation is displayed in the right panel of Fig.(5.3.2). Within the framework of this diffusive model, the orbital destabilization occurs when the particle exits the domain. In the present section, we show how to derive the probability distribution function (5.3.19) of the first exit time from the domain.

Let  $G(h, t) := \int_{h_{cr}}^{h_{sup}} \mathbb{P}(h', t|h, 0) dh'$  be the probability that the Brownian particle starting at  $h$  is still in the domain  $[h_{cr}, h_{sup}]$  at time  $t$ . It can be shown that the distribution  $G(h, t)$  satisfies the same diffusion equation as  $\mathbb{P}(h', t|h, 0)$  (see [33])

$$\frac{\partial G}{\partial t} = D \frac{\partial^2 G}{\partial h^2}. \quad (\text{B.0.1})$$

At time  $t = 0$ , the particle is inside the domain, which means that  $G(h, 0) = 1$  for all  $h \in [h_{cr}, h_{sup}]$ . The boundary conditions (5.3.20) can be equivalently expressed with the distribution  $G$  as

$$\text{for all } t > 0, \begin{cases} G(h_{cr}, t) & = 0 \\ \frac{\partial G}{\partial h}(h_{sup}, t) & = 0 \end{cases}. \quad (\text{B.0.2})$$

We solve the problem (B.0.1-B.0.2) by decomposing the solution into proper modes. Let us introduce the standard scalar product

$$\langle f, g \rangle := \frac{2}{h_{sup} - h_{cr}} \int_{h_{cr}}^{h_{sup}} f(h)g(h)dx.$$

It can be checked that the family of functions

$$e_n(h) := \cos \left( \pi \left( n + \frac{1}{2} \right) \frac{h - h_{sup}}{h_{cr} - h_{sup}} \right) \text{ with } n \in \mathbb{N}$$

form an orthonormal basis of all functions  $G(x, t)$  satisfying the boundary conditions (B.0.2). The solution of (B.0.1-B.0.2) can thus be expressed as the Fourier series

$$G(h, t) = \sum_{n=0}^{+\infty} g_n(t) e_n(h), \quad (\text{B.0.3})$$

where the coefficients  $g_n(t)$  are defined as the projection of  $G$  on the orthonormal basis, that is  $g_n(t) := \langle G(h, t) e_n(h) \rangle$ . Using the Fourier decomposition (B.0.3), we find that  $G$  is solution of (B.0.1) if and only if

$$g_n(t) = g_n(0) e^{-\pi^2 \left(n + \frac{1}{2}\right)^2 \frac{D}{(h_{sup} - h_{cr})^2} t}.$$

The value  $g_n(0)$  can be found with the initial condition  $G(h, 0) = 1$ . We get

$$g_n(0) = \langle G(h, 0) e_n(h) \rangle = \frac{1}{n + \frac{1}{2}}.$$

Finally, the solution  $G(h, t)$  can be expressed explicitly as

$$G(h, t) = \sum_{n=0}^{+\infty} \frac{1}{n + \frac{1}{2}} \cos \left( \pi \left( n + \frac{1}{2} \right) \frac{h - h_{sup}}{h_{cr} - h_{sup}} \right) e^{-\pi^2 \left( n + \frac{1}{2} \right)^2 \frac{D}{(h_{sup} - h_{cr})^2} t}.$$

The time derivative of the above formula gives the expression (5.3.22) for the probability distribution of first exit times.

## Appendix C

# Explicit expression of the resonant part $H_{res}^{(3)}$ of the BMH Hamiltonian

$F_{GR} + F_e^{(1)} + g_5$	-1.68964
$F_e^{(3)}$	-0.905766
$F_i^{(1)} + s_2$	-1.54396
$F_i^{(3)}$	-8.55372
$F_{ei}$	45.2859
$F_{e5}^{(2)}$	0.0730504
$F_{i2}^{(2)}$	0.0421457
$F_{e2}^{(2)}$	0.0643625
$g_2$	7.4559
$g_5$	4.2575

Table C.1: Numerical value (in arcsec/yr) of the coefficients of the BMH Hamiltonian (5.2.13).

```

explicit expression of the coefficients {F1,F2,F3,F4,F5} in part 5 of the manuscript

with ican=sqrt(I'), jcan=sqrt(J')
mu1=nu[1,0,1]=1.508759999999999 + 45.2859*jcan**2 -1.811532*ican**2 mu2=-mu1
mu3=nu[1,1,1]=- 0.03520000000000056 +28.17846*jcan**2 +43.474368*ican**2 mu4=-mu3

F2=0
F5=0

F3=
  0.02438288399395212*mu2**(-2)*mu4**(-2)*jcan*ican**2
+ 0.02438288399395212*mu1**(-2)*mu4**(-2)*jcan*ican**2
- 0.002032019170805752*mu2**(-3)*mu4**(-1)*jcan*ican**2
+ 0.002032019170805752*mu1**(-3)*mu4**(-1)*jcan*ican**2
+ 0.002032019170805752*mu3**(-1)*mu2**(-3)*jcan*ican**2
+ 0.02438288399395212*mu3**(-2)*mu2**(-2)*jcan*ican**2
- 0.002032019170805752*mu3**(-1)*mu1**(-3)*jcan*ican**2
+ 0.02438288399395212*mu3**(-2)*mu1**(-2)*jcan*ican**2

F4=
  0.009118002832963379*mu2**(-2)*mu4**(-2)*jcan**2*ican
+ 0.009118002832963379*mu1**(-2)*mu4**(-2)*jcan**2*ican
+ 0.02930727686987127*mu2**(-3)*mu4**(-1)*jcan**2*ican
- 0.02930727686987127*mu1**(-3)*mu4**(-1)*jcan**2*ican
- 0.02930727686987127*mu3**(-1)*mu2**(-3)*jcan**2*ican
+ 0.009118002832963379*mu3**(-2)*mu2**(-2)*jcan**2*ican
+ 0.02930727686987127*mu3**(-1)*mu1**(-3)*jcan**2*ican
+ 0.009118002832963379*mu3**(-2)*mu1**(-2)*jcan**2*ican

F1=
+ 0.00212932288596471*mu2**(-2)*ican**2
+ 0.00212932288596471*mu1**(-2)*ican**2

```

Figure C.0.1: Explicit expressions of the coefficients  $F_1, F_2, F_3, F_4$  and  $F_5$  in (5.3.3), given in a fortran file.

```

and explicit expression for the driving term {Hres,Haction}

- 0.04356180561465252*mu2**(-2)*mu4**(-2)*jcan**2*ican*sin( g*t + 2*psi + phi)
- 0.04356180561465252*mu1**(-2)*mu4**(-2)*jcan**2*ican*sin( g*t + 2*psi + phi)
- 0.1400172736824222*mu2**(-3)*mu4**(-1)*jcan**2*ican*sin( g*t + 2*psi + phi)
+ 0.1400172736824222*mu1**(-3)*mu4**(-1)*jcan**2*ican*sin( g*t + 2*psi + phi)
+ 0.1400172736824222*mu3**(-1)*mu2**(-3)*jcan**2*ican*sin( g*t + 2*psi + phi)
- 0.04356180561465252*mu3**(-2)*mu2**(-2)*jcan**2*ican*sin( g*t + 2*psi + phi)
- 0.1400172736824222*mu3**(-1)*mu1**(-3)*jcan**2*ican*sin( g*t + 2*psi + phi)
- 0.04356180561465252*mu3**(-2)*mu1**(-2)*jcan**2*ican*sin( g*t + 2*psi + phi)
+ 0.1009455917237942*mu2**(-2)*mu4**(-2)*jcan**4*ican*sin( g*t + 2*psi + phi)
+ 0.1009455917237942*mu1**(-2)*mu4**(-2)*jcan**4*ican*sin( g*t + 2*psi + phi)
+ 0.324461448371882*mu2**(-3)*mu4**(-1)*jcan**4*ican*sin( g*t + 2*psi + phi)
- 0.324461448371882*mu1**(-3)*mu4**(-1)*jcan**4*ican*sin( g*t + 2*psi + phi)
- 0.324461448371882*mu3**(-1)*mu2**(-3)*jcan**4*ican*sin( g*t + 2*psi + phi)
+ 0.1009455917237942*mu3**(-2)*mu2**(-2)*jcan**4*ican*sin( g*t + 2*psi + phi)
+ 0.324461448371882*mu3**(-1)*mu1**(-3)*jcan**4*ican*sin( g*t + 2*psi + phi)
+ 0.1009455917237942*mu3**(-2)*mu1**(-2)*jcan**4*ican*sin( g*t + 2*psi + phi)
- 0.007195578242082825*mu2**(-2)*ican**2*sin( g*t + 2*phi)
- 0.007195578242082825*mu1**(-2)*ican**2*sin( g*t + 2*phi)
- 0.1200427897943848*mu2**(-2)*mu4**(-2)*jcan*ican**2*sin( g*t + psi + 2*phi)
- 0.1200427897943848*mu1**(-2)*mu4**(-2)*jcan*ican**2*sin( g*t + psi + 2*phi)
+ 0.01000411806247771*mu2**(-3)*mu4**(-1)*jcan*ican**2*sin( g*t + psi + 2*phi)
- 0.01000411806247771*mu1**(-3)*mu4**(-1)*jcan*ican**2*sin( g*t + psi + 2*phi)
- 0.01000411806247771*mu3**(-1)*mu2**(-3)*jcan*ican**2*sin( g*t + psi + 2*phi)
- 0.1200427897943848*mu3**(-2)*mu2**(-2)*jcan*ican**2*sin( g*t + psi + 2*phi)
+ 0.01000411806247771*mu3**(-1)*mu1**(-3)*jcan*ican**2*sin( g*t + psi + 2*phi)
- 0.1200427897943848*mu3**(-2)*mu1**(-2)*jcan*ican**2*sin( g*t + psi + 2*phi)
+ 0.1928566065630185*mu2**(-2)*jcan**2*ican**2*sin( g*t + 2*phi)
+ 0.1928566065630185*mu1**(-2)*jcan**2*ican**2*sin( g*t + 2*phi)
+ 1.791272967569936*mu2**(-2)*mu4**(-2)*jcan**3*ican**2*sin( g*t + psi + 2*phi)
+ 1.791272967569936*mu1**(-2)*mu4**(-2)*jcan**3*ican**2*sin( g*t + psi + 2*phi)
- 0.1492809878909753*mu2**(-3)*mu4**(-1)*jcan**3*ican**2*sin( g*t + psi + 2*phi)
+ 0.1492809878909753*mu1**(-3)*mu4**(-1)*jcan**3*ican**2*sin( g*t + psi + 2*phi)
+ 0.1492809878909753*mu3**(-1)*mu2**(-3)*jcan**3*ican**2*sin( g*t + psi + 2*phi)
+ 1.791272967569936*mu3**(-2)*mu2**(-2)*jcan**3*ican**2*sin( g*t + psi + 2*phi)
- 0.1492809878909753*mu3**(-1)*mu1**(-3)*jcan**3*ican**2*sin( g*t + psi + 2*phi)
+ 1.791272967569936*mu3**(-2)*mu1**(-2)*jcan**3*ican**2*sin( g*t + psi + 2*phi)
+ 0.8093163750785887*mu2**(-2)*mu4**(-2)*jcan**2*ican**3*sin( g*t + 2*psi + phi)
+ 0.8093163750785887*mu1**(-2)*mu4**(-2)*jcan**2*ican**3*sin( g*t + 2*psi + phi)
+ 2.601321749319975*mu2**(-3)*mu4**(-1)*jcan**2*ican**3*sin( g*t + 2*psi + phi)
- 2.601321749319975*mu1**(-3)*mu4**(-1)*jcan**2*ican**3*sin( g*t + 2*psi + phi)
- 2.601321749319975*mu3**(-1)*mu2**(-3)*jcan**2*ican**3*sin( g*t + 2*psi + phi)
+ 0.8093163750785887*mu3**(-2)*mu2**(-2)*jcan**2*ican**3*sin( g*t + 2*psi + phi)
+ 2.601321749319975*mu3**(-1)*mu1**(-3)*jcan**2*ican**3*sin( g*t + 2*psi + phi)
+ 0.8093163750785887*mu3**(-2)*mu1**(-2)*jcan**2*ican**3*sin( g*t + 2*psi + phi)
- 0.007714673092514846*mu2**(-2)*ican**4*sin( g*t + 2*phi)
- 0.007714673092514846*mu1**(-2)*ican**4*sin( g*t + 2*phi)
+ 1.015860097047052*mu2**(-2)*mu4**(-2)*jcan*ican**4*sin( g*t + psi + 2*phi)
+ 1.015860097047052*mu1**(-2)*mu4**(-2)*jcan*ican**4*sin( g*t + psi + 2*phi)
- 0.08465968146213604*mu2**(-3)*mu4**(-1)*jcan*ican**4*sin( g*t + psi + 2*phi)
+ 0.08465968146213604*mu1**(-3)*mu4**(-1)*jcan*ican**4*sin( g*t + psi + 2*phi)
+ 0.08465968146213604*mu3**(-1)*mu2**(-3)*jcan*ican**4*sin( g*t + psi + 2*phi)
+ 1.015860097047052*mu3**(-2)*mu2**(-2)*jcan*ican**4*sin( g*t + psi + 2*phi)
- 0.08465968146213604*mu3**(-1)*mu1**(-3)*jcan*ican**4*sin( g*t + psi + 2*phi)
+ 1.015860097047052*mu3**(-2)*mu1**(-2)*jcan*ican**4*sin( g*t + psi + 2*phi)

```

Figure C.0.2: Explicit expressions of the driving term  $\tilde{H}_{res}^{(3)}$  in (5.3.6), given in a fortran file.